



**HAL**  
open science

# Pathways towards efficiency improvement of Kesterite based solar cell

Md Abdul Aziz Suzon

► **To cite this version:**

Md Abdul Aziz Suzon. Pathways towards efficiency improvement of Kesterite based solar cell. Mechanics of materials [physics.class-ph]. Université Grenoble Alpes, 2018. English. NNT: 2018GREAI085 . tel-02017690

**HAL Id: tel-02017690**

**<https://theses.hal.science/tel-02017690>**

Submitted on 13 Feb 2019

**HAL** is a multi-disciplinary open access archive for the deposit and dissemination of scientific research documents, whether they are published or not. The documents may come from teaching and research institutions in France or abroad, or from public or private research centers.

L'archive ouverte pluridisciplinaire **HAL**, est destinée au dépôt et à la diffusion de documents scientifiques de niveau recherche, publiés ou non, émanant des établissements d'enseignement et de recherche français ou étrangers, des laboratoires publics ou privés.

## THÈSE

Pour obtenir le grade de

### **DOCTEUR DE LA COMMUNAUTE UNIVERSITE GRENOBLE ALPES**

Spécialité : **2MGE : Matériaux, Mécanique, Génie civil,  
Electrochimie**

Arrêté ministériel : 25 mai 2016

Présentée par

**Md Abdul Aziz SUZON**

Thèse dirigée par **Henri (phys) MARIETTE, CNRS**  
et codirigée par **Louis GRENET, CEA**

préparée au sein du **Laboratoire CEA Grenoble / LITEN**  
dans **l'École Doctorale I-MEP2 - Ingénierie - Matériaux,  
Mécanique, Environnement, Energétique, Procédés,  
Production**

## **Amélioration des performances des cellules solaires à base de Kesterite**

Thèse soutenue publiquement le **3 décembre 2018**,  
devant le jury composé de :

**Monsieur Hubert RENEVIER**

Professeur, Grenoble INP. Président du jury.

**Monsieur Edgardo SAUCEDO**

Directeur de recherche, IREC (Espagne). Rapporteur.

**Madame Charlotte PLATZER-BJÖRKMAN**

Professeur, Université d'Uppsala (Suède). Rapporteur.

**Monsieur Henri MARIETTE**

Directeur de recherche, CNRS. Directeur de thèse.

**Monsieur Muhammad Monirul ISLAM**

Professeur assistant, Université de Tsukuba (Japon). Examineur.

**Monsieur Louis GRENET**

Ingénieur de recherche, CEA-LITEN. Co-directeur de thèse.





The more original a discovery  
the more obvious it seems afterwards.

— Arthur Koestler

To my parents. . .



# Acknowledgements

I would first like to express my gratitude to all the members of the jury: Thanks to Dr. Edgardo SAUCEDO and Dr. Charlotte PLATZER-BJÖRKMAN for evaluating my manuscript, to Dr. Hubert RENEVIER, president of the jury and to Dr. Muhammad Monirul ISLAM for taking a long trip to attend my defense.

Working on my thesis was a long journey which I would never have been to accomplish had I not received kind help along the way. In December 2014, I was desperately looking for a Ph.D. position when Louis GRENET replied to my inquiries about a possible Ph.D. position. After going through several interviews for the position, I was happy to accept that position and I moved to Grenoble right away. Today, I can say that this has been the best decision I have ever made in my entire life! Therefore, I want to extend special thanks to my supervisor Louis GRENET, both for this opportunity and for his support. He was always there to point me in the right direction and give me feedback to better myself. I would also like to thank my thesis director Henri MARIETTE for sharing his wisdom and encouraging me to seek a better understanding of the physics behind my work.

I also want to express my gratitude to the LANEF consortium and CEA-LITEN for providing the necessary funding for conducting this thesis work.

A warm thanks to the photovoltaic team at LRME. You have been part of my life for the whole duration of my Ph.D. Thank you, Fabrice, for always providing the best technical solution [every time a machine break] and for being such a good friend with whom I was able to share my thoughts both professional and personal. If I ever was confused, I knew I could rely on Frédéric and Arnaud to discuss on photovoltaic. When I started my thesis I was feeling quite lonely and friendless having just moved to a new city. Thankfully, I was very fortunate to be surrounded by wonderful colleagues which I came to see as good friends: Thanks to Noé, Agathe, Sophie, Antoine, Lina for being there to make me feel better. I also want to thank Sébastien, Ulrich, Nicolas, Helga, Cédric, Géraldine for being actively present at the right moments. Last but not least, I want to offer my special thanks to Emmanuel Ollier who was always available to help me with the administrative papers, to listen to my requests and to solve my problems right away.

---

Assistance provided by researchers from other institutes for their help in characterization was greatly appreciated. First of all, I would like to thank Frédérique DUCROQUET for making it possible for me to visit Tallinn University of Technology twice for experiments. This experience not only allowed me to visit Tallinn but also to meet many researchers. Taavi RAADIK and Mati DANILSON from Tallinn University of Technology were particularly helpful and conducted experiments for me during my visit.

I also wish to acknowledge the help provided by CEA researchers. I am very grateful to Eric de VITO for his help with ToF-SIMS analysis and Auger mapping; Claude CHABROL patiently taught me about XRD which I had just discovered and listened to my questions during these three years of experiments. Advices given by Denis ROUCHON on Raman setup and the several experiments he performed for me were greatly appreciated. I would also like to thank Stephanie POUGET for performing GIXRD, which was crucial for one part of my study.

My research would have been impossible without the aid and support of all my friends outside of my Ph.D. environment. Thanks to Manuel for always being there as my emotional support all these years. I can still remember some Friday evenings, he was there to cheer me up. I had faced many failed experiments, and he was there to remind me that in science, failure is also a result and that I should keep working towards success. Richard and Laura also need to be mentioned for being such good friends during this period, as well as Sai and Rasha for being always there when I needed them the most. Many thanks to the Bangladeshi community in Grenoble for their warm gatherings, which made me feel closer to my country. I cannot forget to mention all of my friends from Bangladesh, especially Minar for supporting me emotionally. Last but not the least I would like to thank my family without whom it would not have been possible for me to come until here. A special thanks to Sandra, without whom it would be impossible for me to finish my manuscript. Thanks for helping me to prepare for the defense and for taking care of me while I was writing my manuscript.

I received so much help that it would be quite impossible to thank everyone personally. To those of you, I didn't mention by name, please know that I appreciated your kindness immensely.

## Résumé

Le but de ce travail est d'étudier et de développer des voies pour améliorer l'efficacité des cellules solaires à base de Kesterite. La première partie de ce manuscrit traite du développement d'un procédé de base : le mécanisme de formation de l'absorbeur est étudié en fonction des conditions de croissance du composé  $\text{Cu}_2\text{ZnSnS}_4$  (CZTS à base de soufre pur) et  $\text{Cu}_2\text{ZnSnSe}_4$  (CZTSe à base de sélénium pur). Un procédé séquentiel en deux étapes a été utilisé pour synthétiser l'absorbeur en Kesterite. Différentes optimisations du procédé sont réalisées pour améliorer la microstructure et les performances des dispositifs. Dans le cas du dispositif à base de CZTSe, le meilleur rendement de conversion photovoltaïque obtenu est de 7.6% en utilisant un profil de température en deux étapes et un suscepteur fermé. Pour les cellules solaires à base de CZTS, la meilleure performance obtenue est de 5.9% grâce à l'optimisation de la température et de la pression partielle en soufre : Les performances des dispositifs augmentent avec la pression partielle en soufre.

L'incorporation de Na (Sodium) et de Sb (Antimoine) dans les absorbeurs Kesterite en pur soufre a été testée comme la première stratégie pour améliorer les performances des dispositifs à base de CZTS. L'incorporation de Sb n'entraîne pas d'amélioration en termes de propriétés des matériaux ou des dispositifs, tandis que le co-dopage avec Na et Sb a montré une morphologie améliorée des absorbeurs. D'autre part, la contamination intentionnelle avec du Na s'est avérée bénéfique pour les cellules solaires, particulièrement pour la tension en circuit ouvert. Par conséquent, l'efficacité des dispositifs avec une teneur en Na optimisée est doublée (> 4,5%) par rapport à celle des échantillons de référence sans Na.

La seconde étude pour améliorer les performances des cellules solaires à base de Kesterite concerne l'introduction de gradients de chalcogènes (S/Se) dans l'épaisseur de l'absorbeur. Le but est d'obtenir des gradients de bande interdite afin d'augmenter la longueur de collection des porteurs et de diminuer les phénomènes de recombinaison. Dans ce but, deux procédés sont développés pour réaliser des gradients simples (en face avant ou en face arrière de l'absorbeur). Ces procédés consistent en des recuits successifs (sulfuration/sélénisation) d'empilements de précurseurs. Pour obtenir un gradient en face avant, un recuit de sulfuration à différentes températures et durées est appliqué après un recuit de sélénisation standard.

---

Une température plus importante entraîne un gradient plus marqué. Pour obtenir un gradient en face arrière, un recuit de sulfurisation à différentes températures avant un recuit de séléni-sation standard a été utilisé. A faible température de sulfurisation, des absorbeurs avec une bonne morphologie ont été obtenus mais sans gradient de composition en chalcogène tandis que l'utilisation de températures de sulfurisation plus importantes ont entraîné l'apparition de gradients de composition mais ont détérioré la morphologie des absorbeurs. Ainsi, les voies et limites pour réaliser des absorbeurs de Kesterite à gradient de bande interdite sont proposées.



# Scientific Production

## Journal Papers

- L. Grenet, M. A. A. Suzon, F. Emieux, and F. Roux, “*Analysis of failure modes in kesterite solar cells,*” **ACS Applied Energy Materials**, vol. 1, no. 5, pp. 2103–2113, 2018.
- L. Grenet, M. A. A. Suzon, F. Emieux, and F. Roux, “*Comparing strategies for improving efficiencies in vacuum processed Cu<sub>2</sub>ZnSnSe<sub>4</sub> solar cells,*” **Journal of Renewable and Sustainable Energy**, vol. 10, no. 4, p. 043503, 2018.

## Conference

- **7th European Kesterite Workshop**, Leuven, Belgium 2016, poster presentation.
- **8th European Kesterite Workshop**, Barcelona, Spain 2017, oral presentation.
- **Journées Nationales du Photovoltaïque**, Dourdan, France 2017, oral presentation.
- **PV couches minces et concepts avancés**, Grenoble, France, 2017, oral presentation.

# Contents

<b>1</b>	<b>Introduction</b>	<b>1</b>
1.1	Global warming and energy crisis . . . . .	1
1.2	Photovoltaic (PV) technology . . . . .	3
1.2.1	Solar radiation . . . . .	3
1.2.2	Photovoltaic effect . . . . .	5
1.2.3	Thin film technology . . . . .	6
1.2.4	CZTSSe technology . . . . .	8
<b>2</b>	<b><math>\text{Cu}_2\text{ZnSn}(\text{S}_x\text{Se}_{1-x})_4</math> solar cell</b>	<b>10</b>
2.1	CZTSSe solar cell . . . . .	10
2.2	CZTSSe material properties . . . . .	12
2.2.1	Crystal structure . . . . .	12
2.2.2	Secondary phases . . . . .	14
2.2.3	Defects . . . . .	16
2.2.3.1	Effect of defects . . . . .	17
2.2.4	Bandgap . . . . .	18
2.3	Possible solution for improved PCE . . . . .	19
2.3.1	Inclusion/doping of different elements . . . . .	20
2.3.2	Bandgap grading . . . . .	20
2.4	Context and structure of the thesis . . . . .	21
<b>3</b>	<b>Experimental procedure</b>	<b>22</b>
3.1	Device preparation . . . . .	23
3.1.1	Substrate . . . . .	23
3.1.2	Back contact . . . . .	23
3.1.3	Absorber . . . . .	24
3.1.3.1	Precursor deposition by DC sputtering . . . . .	24
3.1.3.2	Annealing reactor . . . . .	25

---

3.1.4	Deposition of Buffer Layer . . . . .	27
3.1.5	Deposition of (ZnO+ZnO:Al) window layer . . . . .	28
3.1.6	Front Contact . . . . .	28
3.1.7	Equipment used for doping study . . . . .	29
3.1.7.1	Barrier . . . . .	29
3.1.7.2	Evaporation deposition . . . . .	29
3.2	Material characterization techniques . . . . .	30
3.2.1	Scanning electron microscopy (SEM) . . . . .	30
3.2.2	Energy dispersive X-ray spectroscopy (EDX) . . . . .	31
3.2.3	X-ray florescence spectrometry (XRF) . . . . .	32
3.2.4	X-Ray diffraction (XRD) . . . . .	33
3.2.4.1	General principle and uses . . . . .	33
3.2.4.2	Analysis using XRD data . . . . .	34
3.2.4.3	Limitations . . . . .	35
3.2.4.4	Grazing incident X-ray diffraction (GIXRD) . . . . .	35
3.2.5	Raman spectroscopy (RS) . . . . .	36
3.2.6	Time of flight- secondary ion mass spectroscopy (ToF-SIMS) . . . . .	38
3.2.7	Glow discharge spectroscopy (GDS) . . . . .	39
3.3	Device characterization techniques . . . . .	40
3.3.1	Current density-voltage measurement . . . . .	40
3.3.1.1	Under illumination . . . . .	40
3.3.1.2	In the dark . . . . .	42
3.3.2	External quantum efficiency (EQE) measurement . . . . .	43
3.3.3	Capacitance-voltage measurement . . . . .	45
3.3.4	e-ARC (optical simulation) . . . . .	47
<b>4</b>	<b>Development of CZTSe and CZTS absorber</b>	<b>52</b>
4.1	State of the art . . . . .	53
4.1.1	CZTSe . . . . .	53
4.1.2	CZTS . . . . .	54
4.2	CZTSe synthesis process . . . . .	55
4.2.1	Selenization . . . . .	55
4.2.2	Optimization of the micro-structure . . . . .	56
4.2.2.1	Influence of cation composition . . . . .	57
4.2.2.2	Influence of selenization condition . . . . .	61
4.2.2.3	Summary . . . . .	65

## Contents

---

4.2.3	Electrical properties of CZTSe . . . . .	66
4.2.4	Formation mechanism of CZTSe . . . . .	70
4.3	CZTS synthesis process . . . . .	74
4.3.1	Sulfurization . . . . .	74
4.3.2	Effect of annealing temperature . . . . .	76
4.3.3	Effect of sulfur vapor pressure . . . . .	77
4.3.4	Device properties . . . . .	79
4.3.5	Formation mechanism of CZTS . . . . .	82
4.4	Conclusion . . . . .	87
<b>5</b>	<b>Strategies and effects of Na and Sb incorporation on CZTS absorber</b>	<b>89</b>
5.1	State of the art . . . . .	90
5.1.1	Effects of Na and Sb incorporation . . . . .	90
5.1.2	Na and Sb incorporation method from literature . . . . .	92
5.2	Na and Sb incorporation strategy . . . . .	94
5.3	Experimental results on Na and Sb incorporation . . . . .	95
5.3.1	ToF-SIMS analysis . . . . .	95
5.3.1.1	Evaluation of Na and Sb depth profile . . . . .	96
5.3.2	Effect on material properties . . . . .	103
5.3.2.1	Effect on macro structural properties . . . . .	103
5.3.2.2	Effect on micro-structural properties . . . . .	105
5.3.2.3	XRD analysis . . . . .	109
5.3.2.4	Raman analysis . . . . .	111
5.3.3	Effects of Na and Sb on device properties . . . . .	112
5.3.3.1	Light J-V Measurements . . . . .	112
5.3.3.2	Dark J-V measurements: . . . . .	113
5.3.3.3	C-V measurements: . . . . .	114
5.3.3.4	EQE measurements . . . . .	116
5.4	Simulation using e-ARC . . . . .	118
5.4.1	Effect of Na incorporation on Carrier Diffusion Length . . . . .	123
5.5	Conclusion . . . . .	124
<b>6</b>	<b>Bandgap grading</b>	<b>126</b>
6.1	State of the Art . . . . .	126
6.2	Front Grading . . . . .	128
6.2.1	Experimental Procedure . . . . .	128

6.2.2	Results and discussions . . . . .	130
6.2.2.1	Effects on morphology . . . . .	130
6.2.2.2	Effects on material properties . . . . .	132
6.2.2.3	Device properties . . . . .	141
6.3	Back Grading . . . . .	143
6.3.1	Experimental Procedure . . . . .	143
6.3.2	Result and discussion . . . . .	144
6.3.2.1	Effects on morphology . . . . .	144
6.3.2.2	Effects on material properties . . . . .	144
6.4	General discussion and conclusion . . . . .	151
<b>7</b>	<b>Conclusion and Perspective</b>	<b>154</b>
7.1	Perspectives . . . . .	155
	<b>Bibliography</b>	<b>174</b>
	<b>Appendix</b>	<b>175</b>
.1	Sensitivity analysis of e-ARC . . . . .	175
.2	Dark J-V and C-V measurements of Sb-doped CZTS device . . . . .	176



# 1 Introduction

## Contents

---

<b>1.1 Global warming and energy crisis</b> . . . . .	<b>1</b>
<b>1.2 Photovoltaic (PV) technology</b> . . . . .	<b>3</b>
1.2.1 Solar radiation . . . . .	3
1.2.2 Photovoltaic effect . . . . .	5
1.2.3 Thin film technology . . . . .	6
1.2.4 CZTSSe technology . . . . .	8

---

## 1.1 Global warming and energy crisis

The term 'Global warming' refers to the rise in the average temperature of earth's climate system that has been observed in a century scale. While comparing the average global temperature anomaly between 1901-2016 and the most recent period of 1986-2016 (figure 1.1 on the left), an increase of up to  $\sim 0.7^{\circ}\text{C}$  can be observed. Furthermore, this anomaly of temperature is not confined to one region of earth, but rather is a global phenomenon that can be witnessed anywhere of the globe (figure 1.1(right)). Despite all the misconceptions and political movement rejecting the global warming phenomenon, there is no denying that it is indeed happening.

## Chapter 1. Introduction

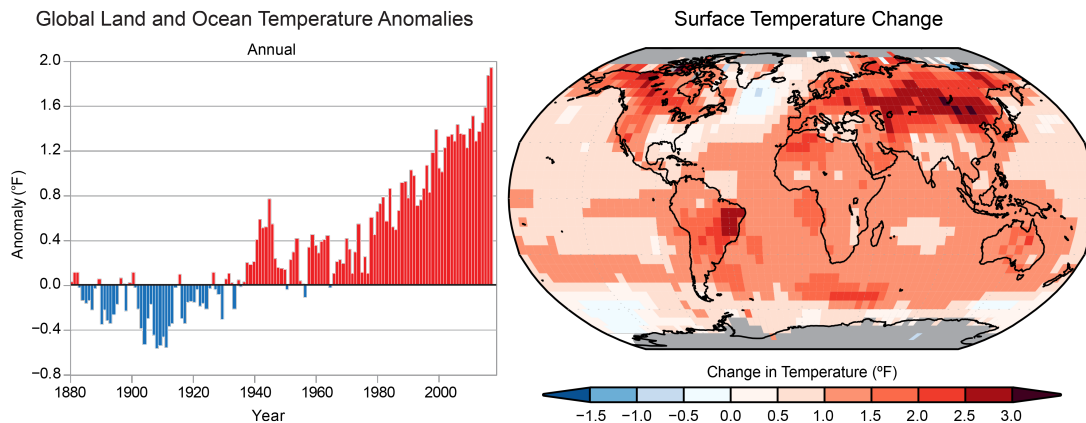


**Figure 1.1:** (left) Global annual average temperature has increased by more than 1.2°F (0.7°C) for the period 1986–2016 relative to 1901–1960. Red bars show temperatures that were above the 1901–1960 average, and blue bars indicate temperatures below the average. (right) Surface temperature change (in °F) for the period 1986–2016 relative to 1901–1960. Gray indicates missing data [1].

Certain gases (greenhouse gas) in the atmosphere, because of their infrared absorption properties, prevent the heat from escaping. Carbon dioxide (CO<sub>2</sub>) is one such gases. Burning fossil fuel for energy harvesting is the main culprit for CO<sub>2</sub> emission in the atmosphere [1]. Global warming is the consequence of the human activity of burning fossil fuel and it will impact in the following ways-

- It will cause an increase of the sea level because of the melting of ice glaciers. Between 1880 and now, the total sea level increased by approximately 225 mm and it is currently increasing at a rate of roughly 3.2 mm each year [2].
- The average precipitation will increase, according to the projection made by NASA for year 2000 to 2100 [2].
- The frost-free season will be increasingly longer, an anomaly that will affect the ecosystem and bring many flora and fauna to extinction [2].
- Natural disasters such as droughts, heat waves, hurricanes, etc. will occur more often.

The Paris climate agreement COP21, signed by 196 countries, was a pledge to work toward the common goal of reducing the greenhouse gas emission by 40% [3] within 2030. This endeavor makes it imperative to find sources of energy (renewable energy/green energy) that will both meet our present and future needs and helps us to cut down the green house gas emission drastically. Thus, in the said agreement, most participating countries agreed that at least 27% of their energy mix should consist of renewable energy. But, up until 2015 more than ~85% of the global primary energy supply was from fossil fuel(oil/gas/coal) (figure 1.2). Consequently, to meet the goal of 27% share of renewable energy and to reduce greenhouse gases, more

renewable energy sources are needed. Amongst all the renewable sources of energy, solar and wind energy have the lowest LCOE(levelized cost of electricity)/KWh. Thanks to the technological advancement and the mass production of solar energy technology, LCOE of solar energy has been consistently reduced. It has been recently pointed out that, the cost of producing solar energy is lower when compared to that of fossil fuels; and that cost is predicted to drop even more (figure 1.3).

Nonetheless, to make the solar technology more acceptable, it is essential that its cost be brought down further. Thus, continuous research in alternative technologies like kesterite solar cells are needed to provide clean and sustainable energy at low costs in the future.

## 1.2 Photovoltaic (PV) technology

### 1.2.1 Solar radiation

The surface temperature of the Sun is 5800K. The spectrum of electromagnetic radiation emitted by the sun is therefore roughly equivalent to that of a black body at the same temperature. The irradiance of this radiation reaching the Earth's atmosphere (Total Solar Irradiance, TSI) is  $1366 \text{ W/m}^2$ .

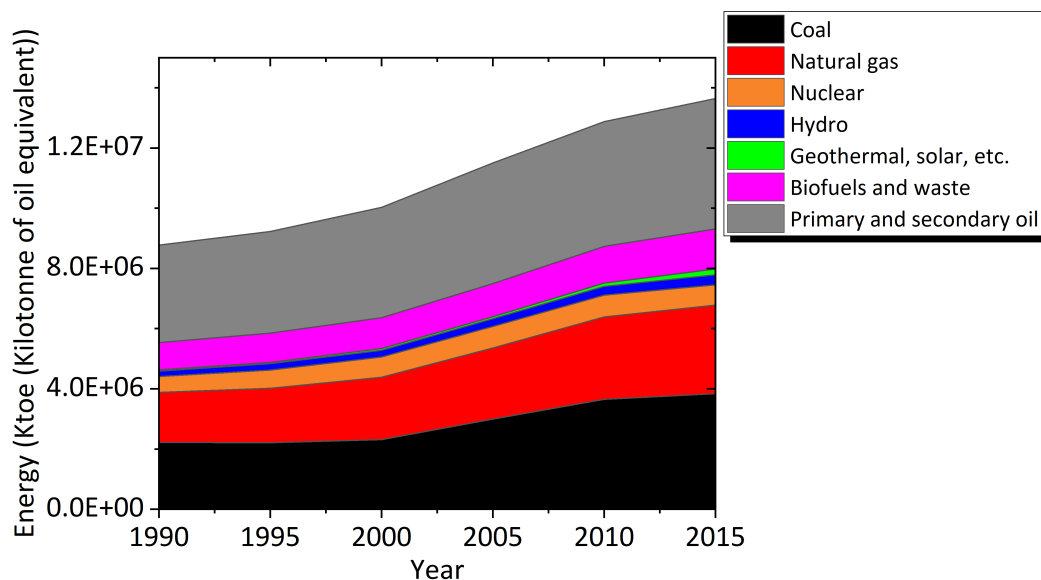


**Figure 1.2:** Global total primary supply of energy by different sources from 1990 to 2015 (Excluding electricity and heat trade) [4].

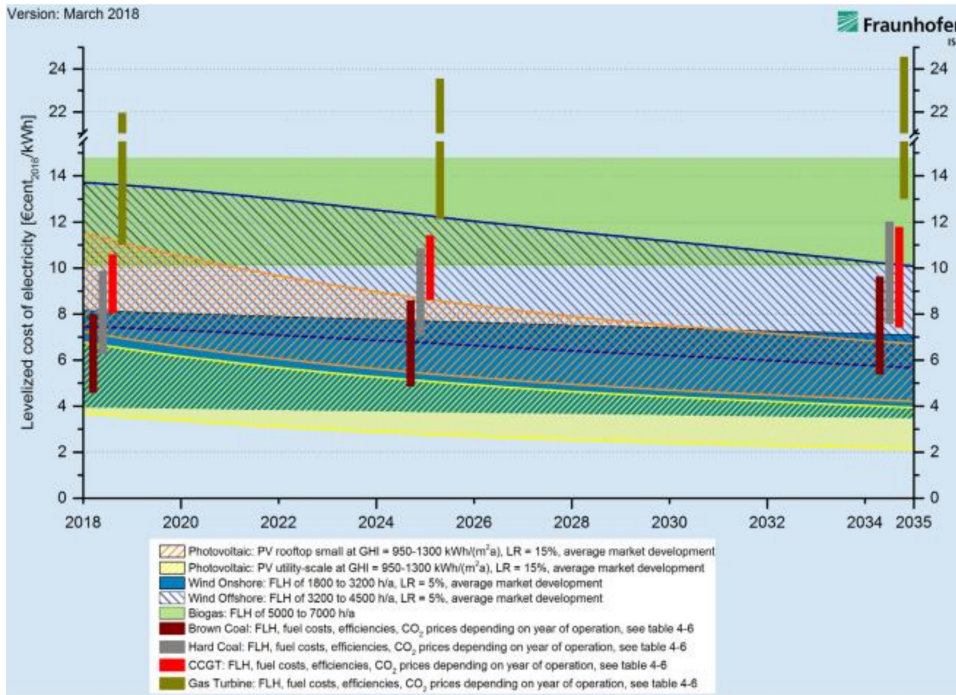


**Figure 1.3:** Learning-curve based predictions of the LCOE of renewable energy technologies and conventional power plants in Germany by 2035. [5].

However, upon crossing the atmosphere, a part of the spectrum is absorbed by the various gases (O<sub>3</sub>, H<sub>2</sub>O and CO<sub>2</sub> in particular) or particles present. As a result, the solar energy available on Earth's surface is reduced, as a function of the traveling distance of radiation through the atmosphere. This distance is called air mass and can be expressed as:

$$AM = \frac{1}{\cos\theta} \quad (1.1)$$

Here,  $\theta$  is the angle from the vertical or zenith angle. To standardize the measurement methods, a spectrum has been defined as an international reference. The AM 1.5G (Global) spectrum, corresponding to an air mass of 1.5 and an angle of 48.2°. Global, here, means that the spectrum takes both direct and diffuse radiation into account. The extraterrestrial (AM0) and reference spectra with air mass (AM1.5G) are compared in Figure 1.4.

As a result, the total usable irradiance on Earth's surface is reduced to about 1000 W.m<sup>-2</sup>, in the form of radiation with wavelengths from 280 nm to approximately 2500 nm.

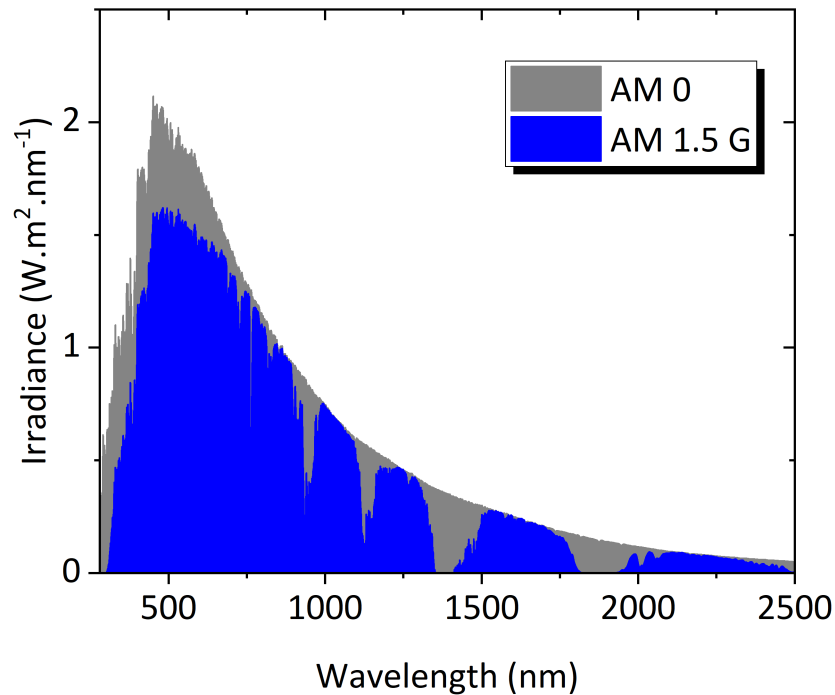


**Figure 1.4:** AM0 (extraterrestrial) and AM1.5G (terrestrial reference) solar radiation spectra (from NREL).

### 1.2.2 Photovoltaic effect

Photovoltaic energy is based on the semiconductor material properties. Semiconductors are capable of absorbing photons whose energy  $E_{\text{photon}} = h\gamma$  ( $h$  is Planck's constant and  $\gamma$  is the frequency of light) is greater than the bandgap ( $E_g$ ) of that material. When the energy of the photon is absorbed by the semiconductor, the energy of an electron in the valence band is transferred into the conduction band. Its absence in the valence band is modeled by a hole, positive charge carrier. The absorption of the photon thus generates an electron-hole pair. If the energy of the photon is higher than the band gap of the material, the excess energy is released by the electron in the form of phonon (thermalization). A semiconductor material alone, however, cannot generate electrical current. Using a semiconductor only, an electron-hole pairs can not be collected and they all recombine after a time period  $\tau$  (life time of the carriers).

To generate a current, a p-n junction is used instead of a simple semiconductor. The electric field formed by this junction separates electrons and holes, that are collected in the respective

electrode. Generally, in a solar cell only one of the two components of the junction (p or n) is used as a light-absorbing material. Photovoltaic cells are therefore designed with one absorbent layer much thicker than the other layer forming the junction. The basic structure of a photovoltaic solar cell is shown in Figure 1.5. In order to harvest photons efficiently while minimizing shadow, the front contact is made with a metal grid. The rear contact, conversely, occupies the entire back of the cell. Depending on the technology used, other layers are added to this basic structure.

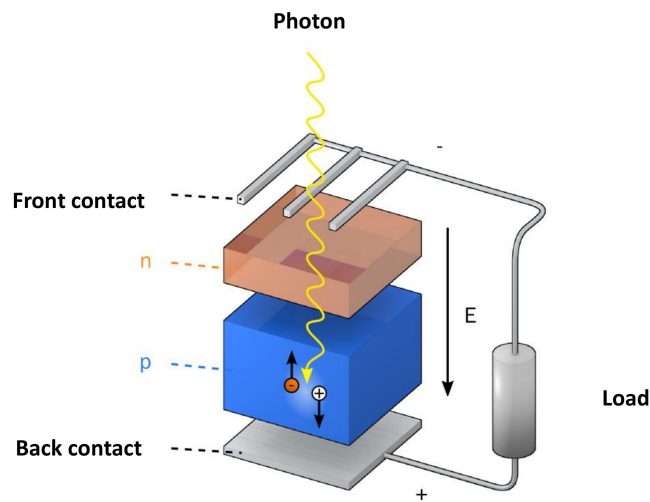


**Figure 1.5:** Basic structure of a PV solar cell with a p-type absorber connected with a load.

### 1.2.3 Thin film technology

The first generation of solar cells used crystalline silicon (Si) (monocrystalline or polycrystalline) as the absorbent material. Si has the advantage of being very abundant in the earth's crust. Besides, the physics and technology of semiconductor using Si are extremely well developed thanks to its use in microelectronics. The global market for photovoltaic is currently dominated by cells of this type (more than 80% of shares [6]). One of the main limitation with this technology is that it requires the use of a very pure Si with a thickness of approximately  $200\ \mu\text{m}$ , due to the indirect bandgap of Si. In order to reduce material usage and create new applicability, a second generation of solar cell has emerged, based on thin film materials. The principle of thin film cells is to use an absorber material with a high absorption coefficient compared to the crystalline Si. For this purpose, materials with direct bandgap are generally used. This creates a possibility to use much thinner absorbent materials, around  $2\ \mu\text{m}$  thick (100x less than Crystalline Si), thus reducing the amount of raw material required. The main materials used as thin film absorbers are amorphous Si (a-Si), microcrystalline Si, CdTe,

## 1.2. Photovoltaic (PV) technology

Cu(In<sub>1-x</sub>Ga<sub>x</sub>)Se<sub>2</sub> (CIGS), perovskite and Cu<sub>2</sub>ZnSn(S,Se)<sub>4</sub> (CZTSSe). Excellent performances have also been demonstrated with thin layers of GaAs. Table 1.1 summarizes the record yields achieved based on single junction c-Si and thin film materials.

**Table 1.1:** Record efficiency achieved by different c-Si and thin film technology as photovoltaic cell and module [7].

Type	Absorber	Cell efficiency (%)	(approx.)Area (cm <sup>2</sup> )	Module efficiency (%)	(approx.)Area (cm <sup>2</sup> )
mono c-Si	Si	26.7±0.5	79	24.4±0.5	13177
poly c-Si	Si	22.3±0.4	4	19.9±0.4	15143
TF	CIGS	22.9±0.5	1	15.7±0.5	9703
TF	CdTe	21±0.4	1	18.6±0.5	7039
TF	a-Si	11.9±0.3	1	9.1±0.5	14300
TF	GaAS	28.8±0.9	1	25.1±0.8	867
TF	perovskite	20.9±0.7	1	11.7±0.4	703

While crystalline silicon technology is most mature and dominant technology, thin film technology, as of 2012, represented a market share (all technologies combined) of approximately 15%, with a decrease to 5% in 2017 [6]. Their complexity of implementation and the lack of knowledge about the materials used (in comparison with the Si) suggest that these technologies need to be the subject of research for a while longer in order to be more developed. In spite of this economic scenario, thin film technology can be beneficial for to several reasons:

- Due to the high absorption coefficient of thin film material, a thin layer of 1-2  $\mu\text{m}$  is sufficient for absorbing 99% of solar radiations. Thus, it could be used as absorber for multifunction solar cells.
- Energy payback time of thin-film technology is lower compared to c-Si technology [6].
- Due to low thickness of the absorber it allows to have flexible solar cell and module.
- It can be the perfect candidate for building integrated photovoltaic (BIPV) application, as it allows many customization of the module (size, shape, color, transparency etc).
- Lastly, the practical upper limit of efficiency for thin film technology is higher compared to the c-Si technology, due to the direct bandgap nature [8]. Thus, it is possible to achieve efficiency higher than c-Si technology.

Some applications of thin film photovoltaic are shown in figure 1.6.

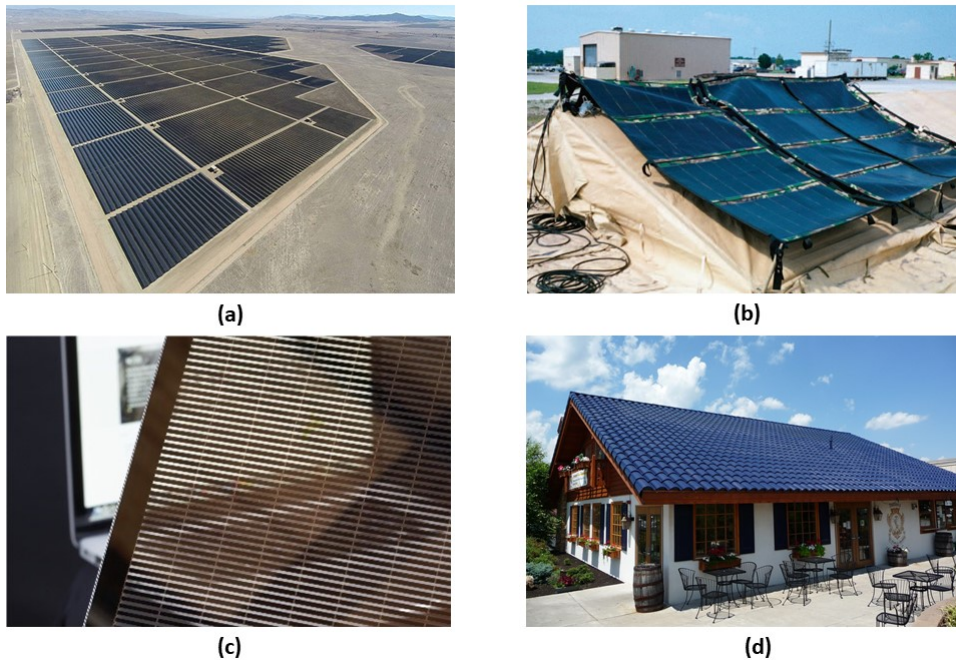


**Figure 1.6:** Illustration of the application possibilities offered by thin film PV: (a) Topaz solar power plant, consisting of CdTe devices from First Solar, (b) lightweight and flexible CIGS modules from Global Solar, (c) semitransparent CIGS module from Nexcis and (d) solar tile roof from SRS Energy using amorphous silicon technology.

### 1.2.4 CZTSSe technology

CZTSSe( $\text{Cu}_2\text{ZnSn}(\text{S}_x\text{Se}_{1-x})_4$ ) based absorbers have become more popular than other thin film absorbers in the last couple of years for multiple reasons:

- First, thin film technologies such as CIGS or CdTe uses scarce (In, Ga, Te etc) and toxic materials (Cd) [9, 10]. Although, the efficiency of these technologies can be comparable with c-Si technology, these drawbacks are believed to be problematic for gigawatt scale production [11]. Kesterite absorber, on the other hand, uses only earth abundant materials such as (Cu, Zn, Sn and S) [9, 10].
- The absorption coefficient of this material is  $>10^4 \text{ cm}^{-1}$ , which is sufficient to absorb 99% of usable sunlight using 1-2  $\mu\text{m}$  thick material [12].
- Tunable bandgap of this material from 1.0 eV (pure Se CZTSe) to 1.5 eV (pure S CZTS), makes it a perfect candidate for bandgap tuning to achieve high efficiency. Theoretically, the highest efficiency can be achieved within this bandgap range (figure 1.7).

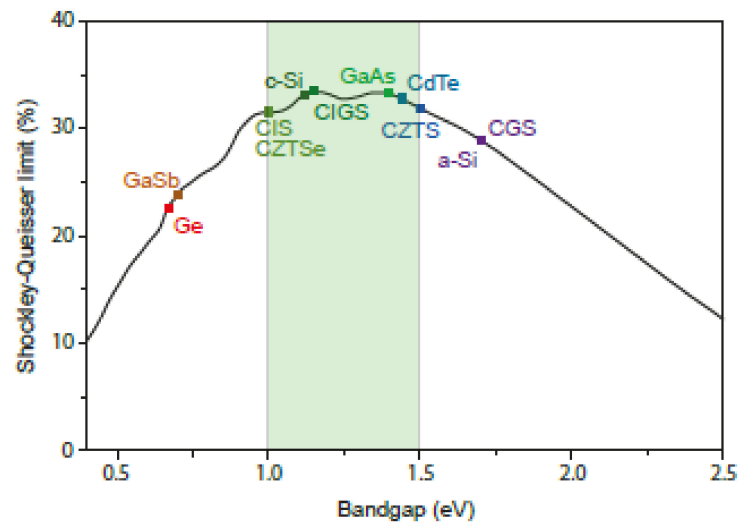


**Figure 1.7:** Theoretical maximum efficiency for a single-junction solar cell depending on the absorber bandgap [13].

Despite all the advantages of kesterite material, the highest power conversion efficiency (PCE) reached so far is 12.6% [14]. To be considered as economically sound as PV technology, CZTSSe absorbers need to achieve an even higher PCE. Therefore, this study is focused on finding ways to improve this absorber material and reach higher PCE.

## 2 $\text{Cu}_2\text{ZnSn}(\text{S}_x\text{Se}_{1-x})_4$ solar cell

### Contents

---

<b>2.1 CZTSSe solar cell</b> . . . . .	<b>11</b>
<b>2.2 CZTSSe material properties</b> . . . . .	<b>13</b>
2.2.1 Crystal structure . . . . .	13
2.2.2 Secondary phases . . . . .	15
2.2.3 Defects . . . . .	17
2.2.4 Bandgap . . . . .	19
<b>2.3 Possible solution for improved PCE</b> . . . . .	<b>20</b>
2.3.1 Inclusion/doping of different elements . . . . .	21
2.3.2 Bandgap grading . . . . .	21
<b>2.4 Context and structure of the thesis</b> . . . . .	<b>22</b>

---

This chapter will present the operating principle of CZTSSe solar cells. It also summarizes the main topics needed to understand the work described in the subsequent chapters.

### 2.1 CZTSSe solar cell

In its most common configuration, a CZTSSe solar cell is formed by a stack of several thin-film materials deposited successively on a substrate. The structural design of CZTSSe solar cell is mainly inspired by those of CIGS-based technology. The substrate is generally a soda-lime glass (SLG) with the standard structure shown in figure 2.1.

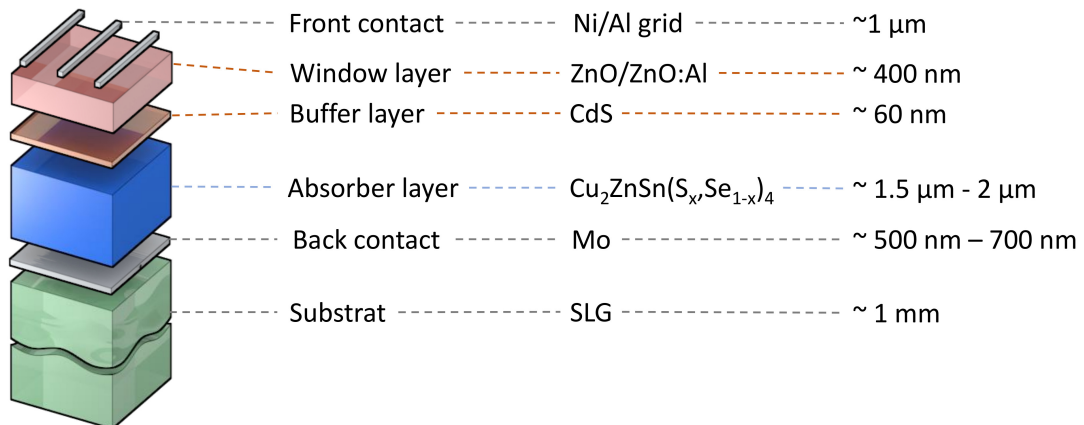


**Figure 2.1:** Standard structure of CZTSSe solar cell.

The first layer deposited on the substrate is the back contact electrode. Its main role is to collect the charges generated in the cell. This layer is composed of molybdenum (Mo) and its thickness is approximately 500 nm to 700 nm. The layer directly above the back contact is composed of absorber material, the CZTSSe. It is a p-type semiconductor that forms the first part of the p-n heterojunction. A majority of photons are absorbed in this layer to form the electron-hole pairs. The thickness of this layer is about 1.0  $\mu\text{m}$  to 2  $\mu\text{m}$ . The p-n heterojunction with CZTSSe is formed by adding a layer called "buffer layer". Currently, the best yields are obtained by using buffer layers of cadmium sulphide (CdS). It is the most commonly used material for buffer layers. The typical thickness of a CdS buffer layer is about 60 nm. The most common method of CdS deposition for CIGS/CZTSSe solar cell, is chemical bath deposition (CBD) [15]. After that, the buffer layer is covered with a layer called window Layer. This layer consists of 50 nm deposition of zinc oxide (ZnO) and 350 nm deposition of Al doped ZnO as transparent conductive oxide (TCO). The ZnO layer is resistive and serves to limit short-circuit formation in areas with imperfect overlaps of the CZTSSe by the buffer layer [16]. The TCO allows the window layer to act partially as the front contact of the photovoltaic cell while being transparent to solar energy for the thin film covered by it. The final layer (front contact) is made by adding a stacked grid that will collect the electrons generated by the device. This grid is composed of a layer of Nickel and a layer of aluminium (Al). Ni serves as a barrier and prevents oxidation of Al related to the underlying presence of TCO. The grids are generally deposited by evaporation using a deposition mask.

## 2.2 CZTSSe material properties

### 2.2.1 Crystal structure

The most common semiconductor used for photovoltaic applications is from the IV column of the periodic table. This element has 4 valence electrons and crystallizes in the diamond crystalline structure (mesh). The formation of  $\text{I}_2\text{-II-IV-VI}_4$  compounds like CZTSSe can be achieved from a II-VI semiconductor by sequential replacement of cations in which the octet rule is respected and the total charge remains neutral (see Figure 2.2).

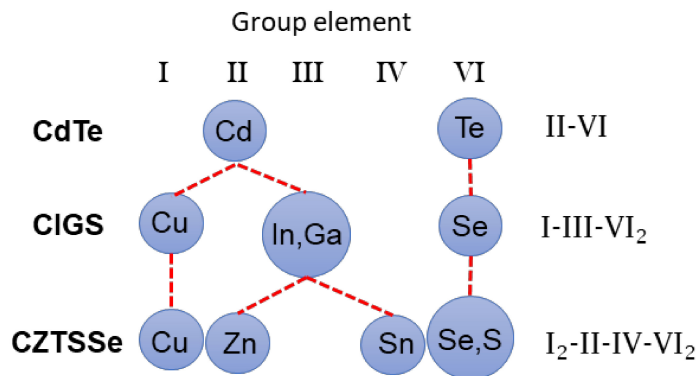


**Figure 2.2:** Formation of CZTSSe ( $\text{I}_2\text{-II-IV-VI}_4$ ) compounds by sequential replacement of cations.

The CZTSSe crystal structure follows the same crystal structure as CdTe (zincblende). Schematic of CZTSSe crystal structure and cation substitution phenomena is shown in figure 2.3 [17]. Additionally, CZTSSe can be crystallized as kesterite (space group  $\bar{I}4_2m$ ) or stannite (space group  $\bar{I}4_2m$ ). Kesterite and stannite structures differ by the cations stacking sequences on the axis  $c$  [18, 19]. Figure 2.3 shows a stack of the type ( ...-[CuSn]-[CuZn]-[CuSn]-[CuZn]-... ) for the kesterite structure, while the stack for the stannite structure is of the type ( ...-[ZnSn]-[Cu<sub>2</sub>]-[ZnSn]-[Cu<sub>2</sub>]-). Both structures are very likely to be found in a material because their formation energy differs very little (about 3 meV per atom). But, the kesterite structure has the lowest formation energy and would be the most stable one [20].

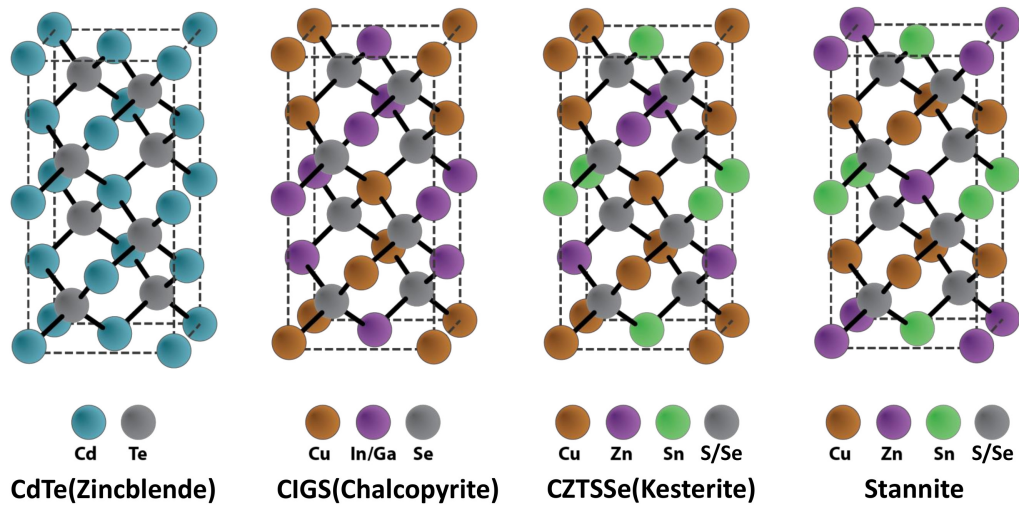


**Figure 2.3:** Elemental cells of CdTe (zincblende), CIGS (chalcopyrite) and CZTSSe (kesterite and stannite) structure, showing the development of each structure by the cationic substitution of the previous structure.

Finally, it is also possible to encounter disordered kesterite crystal structure. CZTSSe is composed of the alternation of two cationic planes along the  $c$  axis of the mesh (see figure 2.4): - The Cu and Sn planes located at  $z=0$  and  $z=1/2$ . - The planes of Cu and Zn located at  $z=1/4$  and  $z=3/4$ . Each of these planes are separated by anion planes. The  $\text{Cu}_{\text{Zn}}$  and  $\text{Zn}_{\text{Cu}}$  anti-sites have low enthalpies of formation due to the similar size of the cations. It follows that a kesterite structure exists in which Cu and Zn sites are occupied in a random way by atoms of Cu/Zn [21]. This disordered structure is highlighted by Schorr et al. [19] using neutron diffraction measurements. The degree of disordered state in the absorber depends on the metal ratio (especially  $[\text{Cu}]/[\text{Zn}+\text{Sn}]$ ) and the heating or cooling profile used during the synthesis [22]. A transition from partially ordered to disordered kesterite occurs at  $260^\circ\text{C}$  for CZTS (pure sulfur-based kesterite) [23] and  $200^\circ\text{C}$  for CZTSe (Pure selenium-based kesterite) [24] compounds. Completely disordered kesterite shows lower bandgap compared to more ordered kesterite. But, it is still under debate if this is the main reason behind the lower efficiency of CZTSSe solar cell.

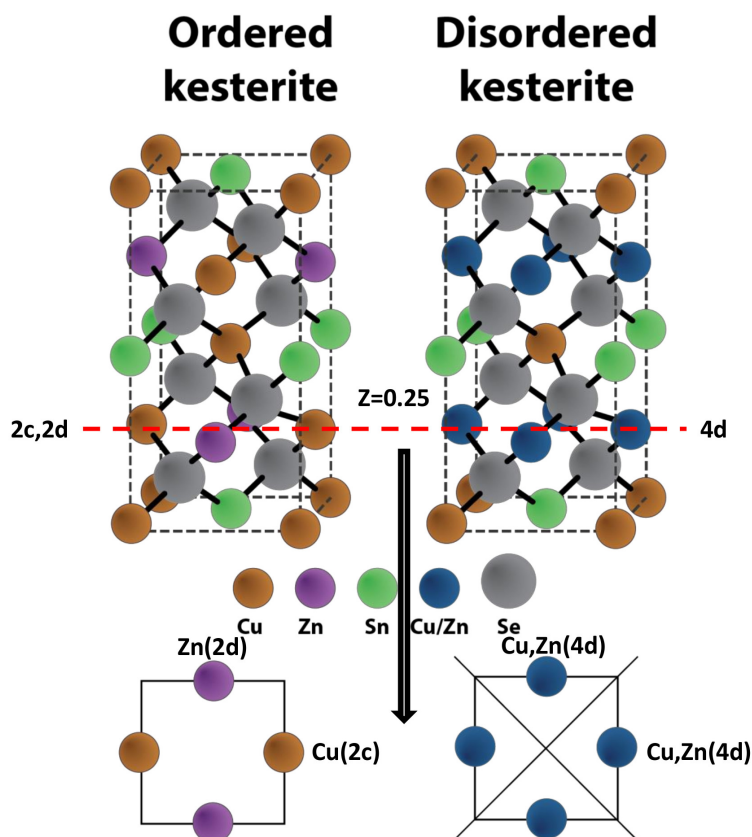
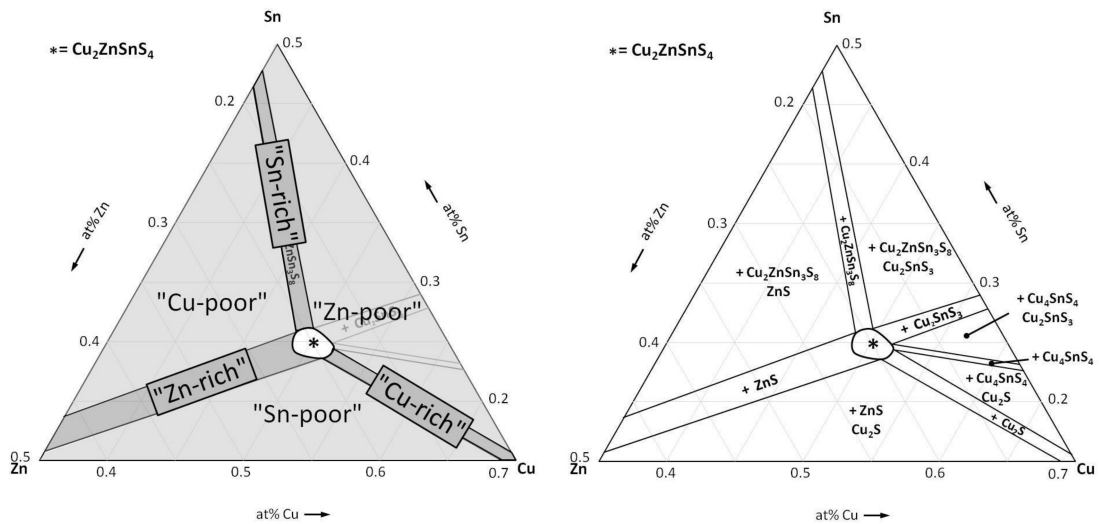


**Figure 2.4:** Crystalline structure of disordered kesterite phase, adapted from [25].

### 2.2.2 Secondary phases

The study of the composition of CZTSSe can be presented using the composition value of the cationic elements: copper, tin and zinc and anionic elements: sulfur and selenium. The composition of CZTSSe is usually represented in a ternary diagram. It is a section of the quaternary diagram in three dimensions with fixed anion compositions and only variable cation compositions. A ternary diagram of CZTS is shown in Figure 2.5(a). Each side of the triangle indicates the atomic percentage of one of the three cations of CZTS. At each point on the diagram, summation of cations values are unity. The area in the center is noted by an asterisk represents the area of existence of CZTS phase. Experimentally, achieving a pure CZTSSe absorber is highly challenging, due to a narrow zone of existence. A thermodynamic calculation by Scragg et al [26], explains the decomposition of the kesterite phase at elevated temperature, resulting in the formation of secondary phases. Beside this relatively narrow zone, six zones are observable in which minor crystalline phases are formed alongside with CZTS. These zones are identified in figure 2.5(a), as Zn-rich, Cu-poor, Sn-poor etc. These

labels will be used throughout this study to define a compositional position of an absorber material.



(a) Ternary phase diagram defining the compositional labels used throughout this report.

(b) Ternary phase diagram showing the possible secondary phases at 400°C for defined compositional positions

**Figure 2.5:** Ternary diagram to define the compositional position of CZTS absorber and the possible secondary phases arise from the position, adapted from Scragg et al, [27].

Figure 2.5 (b) present a ternary diagram of pure CZTS at different compositional position, adapted from Scragg et al, [27]. In all the region except the small region of CZTS (indicated by an asterisk), up to two additional secondary phases are present along with the CZTS absorber. Similar secondary phases for CZTSe or CZTSSe compound is also possible for similar compositional position. The optimal cation composition for highly efficient CZTSSe solar cells was experimentally determined as Cu-poor and Zn-rich ( $[Cu]/[Zn+Sn]=0.8$  and  $[Zn]/[Sn]=1.2$ ) [28]. One of the reasons for achieving best efficiency in this region is due to the probability of inducing ZnS(e) secondary phase, which is less detrimental in nature compared to other secondary phases. The possible secondary phases during fabrication of CZTSSe absorber and their effects are listed in table 2.1.

## Chapter 2. $\text{Cu}_2\text{ZnSn}(\text{S}_x\text{Se}_{1-x})_4$ solar cell

**Table 2.1:** List of secondary phases and their impact on solar cell performance adapted from [29,30]

Compound	Bandgap	Electrical properties	Impact on solar cell performance
Zn(S,Se)	2.7-3.7 eV	Insulator	Due to the higher bandgap compared to absorber material, it does not affect the PCE in case of presence in lower amount. In case of presence in higher amount, it reduces the active area and increases the series resistance of the device.
$\text{Cu}_2(\text{S,Se})$	1.2 eV	Metal like (p-type)	In case of pure S based absorber, $\text{Cu}_2\text{S}$ shows lower bandgap than the absorber, which is detrimental for the device by limiting the open circuit voltage. Furthermore, due to the metal like electrical properties, it can also shorten the layers of the device.
$\text{Sn}(\text{S,Se})_2$	1.0-2.5 eV	Semiconductor (n-type)	Due to the n-type nature of this material, it forms diodes, that is detrimental for carrier collection.
$\text{Cu}_2\text{Sn}(\text{S,Se})_3$	0.8-1.35 eV	Semiconductor p-type	Due to the lower bandgap compared to the absorber material, it limits the open circuit voltage of the finished solar device.

### 2.2.3 Defects

In addition to the secondary phases, a variety of other defects can be observed in CZTSSe absorber, such as vacancies, antisite, interstitials and complexes [31]. These defects and defect complexes form shallow donor level, shallow acceptor levels, mid gap states and deep trap states within the bandgap of the absorber. Those can work as a recombination center inducing reduced PCE. In figure 2.6 possible intrinsic defects and low energy intrinsic defects and defect complexes of CZTSe absorber are shown. The enthalpy of defect formation can be calculated by density function theory, depending on the atomic chemical potential of the cation present in the crystals. The top of figure 2.6 shows these enthalpies for 7 different chemical potentials (A to G) and corresponds to the limits of the single phase domain, adapted from Chen et al, [31]. The p-doped  $\text{Cu}_{\text{Zn}}$  antisite is identified to be the most likely point defect for any growth condition of the material from this analysis. But Han et al, [32] showed that the hole concentration is controlled by  $V_{\text{Cu}}$  due to the shallower acceptor level (50 meV) compared to  $\text{Cu}_{\text{Zn}}$  (100 meV) (see lower part of figure 2.6). These intrinsic defects can also act as a defect complex together. The top of figure 2.6 shows the formation energy of different defect clusters. Here,  $(\text{Cu}_{\text{Zn}}+\text{Zn}_{\text{Cu}})$  has the lowest formation energy and can be the main defect complex in CZTSSe absorber. In addition Dimitrievska et al. showed the effect of Cu-substitutional defects, namely  $[V_{\text{Cu}}+\text{Zn}_{\text{Cu}}]$  is mainly on  $V_{\text{OC}}$  [33]. It is possible to modify the value of  $V_{\text{OC}}$  by modifying the amount of  $[V_{\text{Cu}}+\text{Zn}_{\text{Cu}}]$  defects. Cu poor condition during synthesis induce the ordering of Cu/Zn (001) planes by increasing the  $[V_{\text{Cu}}+\text{Zn}_{\text{Cu}}]$  cluster, which in turn widen the band-gap and increase the  $V_{\text{OC}}$  of final device [34].

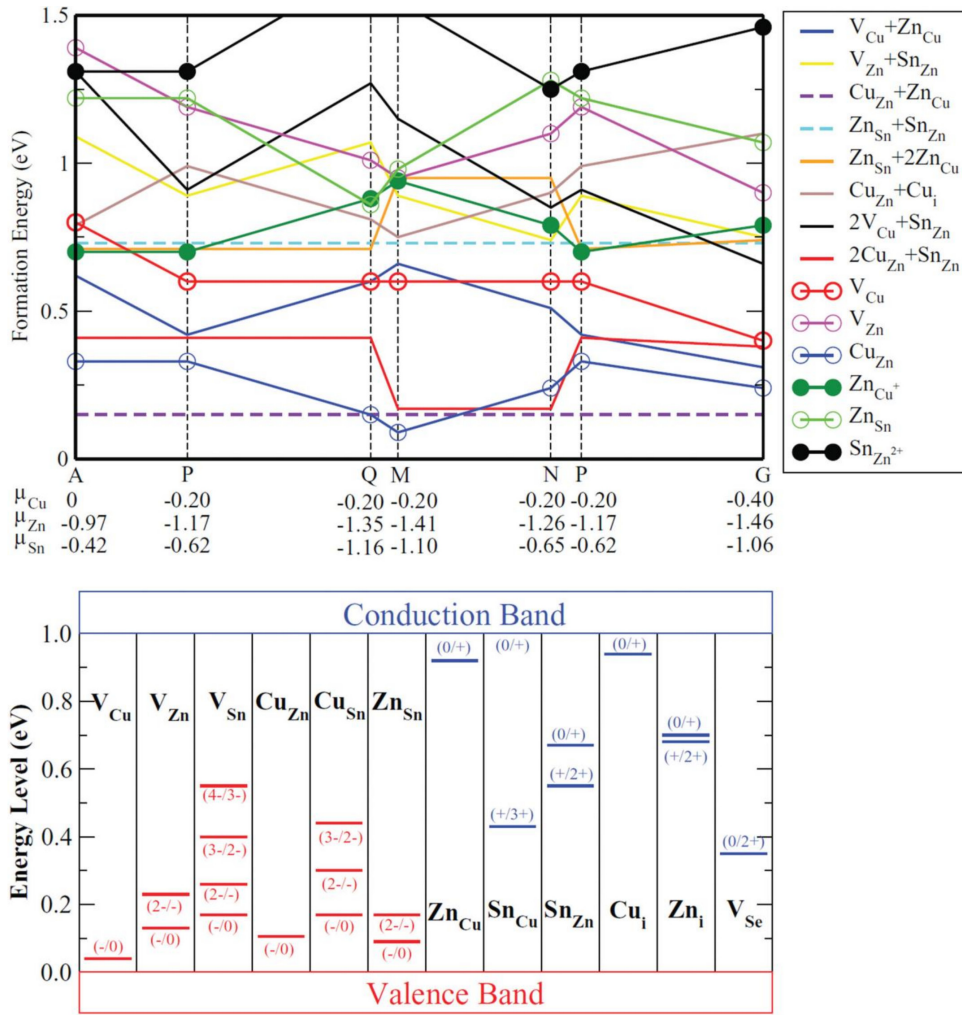


**Figure 2.6:** Upper panel: The formation energy of low-energy defects in  $\text{Cu}_2\text{ZnSnSe}_4$  as a function of the chemical potential of the cations. The Fermi energy is assumed to be at the top of the valence band (strong p-type conditions), and all donor defects are fully ionized. Lower panel: The ionization levels of intrinsic defects in the bandgap of  $\text{Cu}_2\text{ZnSnSe}_4$ . The red bars show the acceptor levels and the blue bars show the donor levels, with the initial and final charge states labeled in parentheses. This figure is adapted from [31].

### 2.2.3.1 Effect of defects

The main reason for having lower efficiency in CZTSSe is the  $V_{\text{OC}}$  deficit. Highest  $V_{\text{OC}}$  obtained by kesterite technology is 60% lower than the maximum achievable  $V_{\text{OC}}$  for the particular bandgap, lower than the  $V_{\text{OC}}$  for CIGS or CdTe technologies (see figure 2.7). Generally, the main cause for  $V_{\text{OC}}$  deficit is the recombination of the photogenerated charge carrier in the bulk of the material and at the surface. Bourdais et al. [25], concluded that deep defects and electrically active grain boundaries are the prominent candidates for causing high non-

radiative recombination and as a result high  $V_{OC}$  deficits. Short minority carrier lifetime (originated from band gap fluctuation) and presence of band tails are also identified as the main culprits for the  $V_{OC}$  deficit [35].

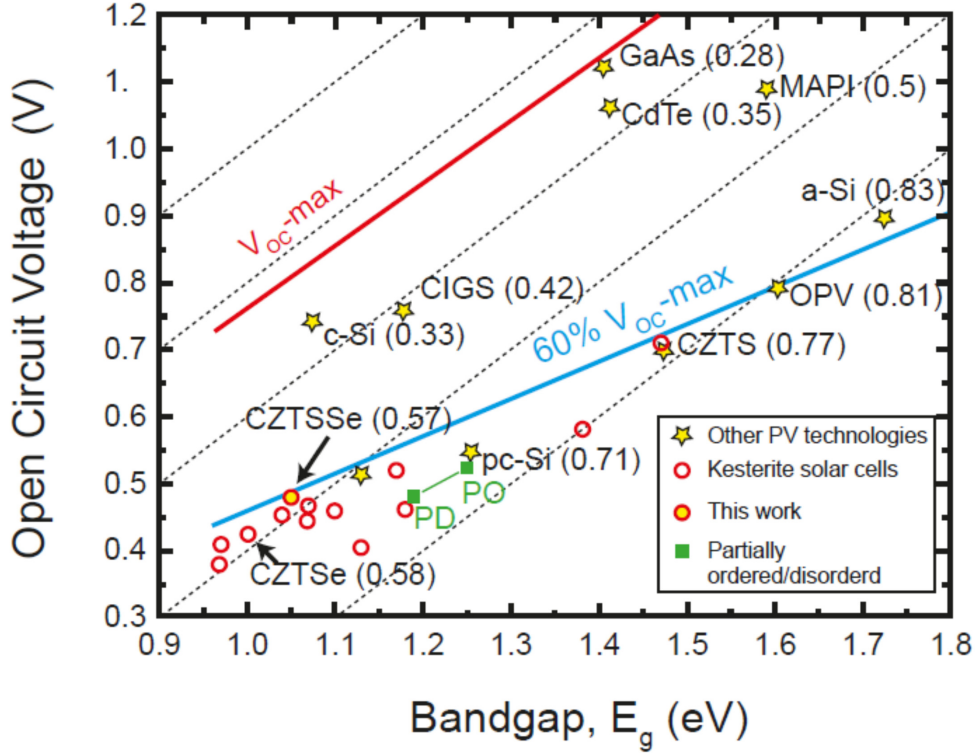


**Figure 2.7:**  $V_{OC}$  as function of bandgap for different technologies. Kesterite technology shows less than 60% of the maximum  $V_{OC}$ , which is lower compared to other technologies. [25].

### 2.2.4 Bandgap

The chalcogen (S/Se) concentration into CZTSSe compound gives the opportunity of band gap tuning to adapt the material for a given application. Calculations of the electronic band alignment of  $\text{Cu}_2\text{ZnSn}(\text{S}_x\text{Se}_{1-x})_4$  compound by density function theory shows a direct bandgap increasing nearly linear manner from 1.0 eV (pure CZTSe) to 1.5 eV (pure CZTS) [17, 36], according to the equation below.

$$E_g(x) = (1 - x)E_{g_{\text{CZTSe}}} + xE_{g_{\text{CZTS}}} - bx(1 - x) \quad (2.1)$$

Here  $b$  is the bowing parameter and it is found to be approximately 0.1 eV [36]. From equation

2.1, it is possible to calculate the bandgap from the value of  $x$  ( $x=[S]/[S+Se]$ ).

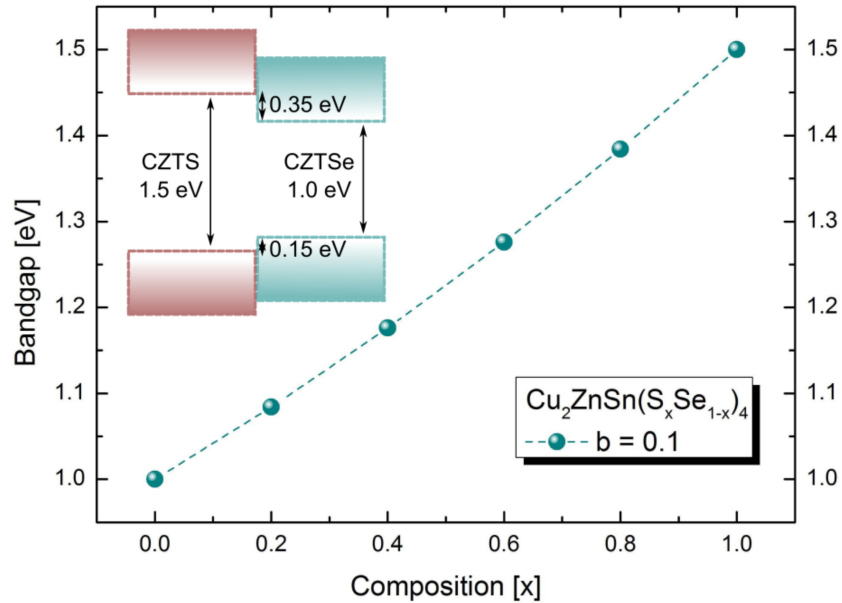


**Figure 2.8:** Bandgap variation of  $\text{Cu}_2\text{ZnSn}(\text{S}_x\text{Se}_{1-x})_4$  compound as a function of the composition ( $x$ ). In the inset the type I band alignment between CZTS and CZTSe [37].

The alignment between CZTS and CZTSe is of type I, where  $E_C$  offset (CBO-0.35 eV) is larger than  $E_V$  offset (VBO-0.15 eV) [36], shown in figure 2.8. It confirms the importance of  $x$  variation on  $E_C$  instead  $E_V$ .

### 2.3 Possible solution for improved PCE

Theoretically the efficiency of CZTSSe solar cell can be as high as that of CIGS solar cells. But, experimentally it is not the case due to a  $V_{OC}$  deficit. CIGS solar cell underwent many processes to achieve high efficiency and amongst them inclusion of alkali (Na, K) and bandgap grading are the two major processes. As CZTSSe devices share similar opto-electrical properties as CIGS, possible solution towards overcoming the  $V_{OC}$  deficit and increasing the efficiency of CZTSSe technology could be [25, 38]:

- Alloying or doping of CZTSSe with other elements to avoid detrimental defects;
- Tuning of anion composition/band gap engineering;

For this study we will exploit these two possibilities to find the pathway for improved PCE of CZTSSe solar cell.

### 2.3.1 Inclusion/doping of different elements

Different elements were exploited in the search for improving the CZTSSe device performance until now. Giraldo et al. [39] reported the beneficial effect of introducing tiny (10 nm) amount of Ge by improving the grain growth, long wavelength light collection and  $V_{OC}$  without changing the bandgap of the material. Substitution of Cu by Ag also showed improved grain growth, higher  $V_{OC}$  and reduced intrinsic defect concentration [40]. Several other studies could be also found, showing substitution of Cu with Li, Zn with Cd or Mn etc that showed beneficial effects [38].

The beneficial effect of sodium (Na) "contamination" on CIGS was discovered by Hedström and co-workers in 1993 [41]. Since then, numerous works have been done (still going on) on the electrical and structural impact of alkali on CIGS and CZTSSe material. Additionally, use of thin Antimony (Sb) layer during CIGS absorber synthesis was found to promote grain growth and improves PCE [42], only in the presence of Na. Na and Sb doping was found to have some positive effects on opto-electrical and microstructural properties of CZTSSe technology [43–45]. However, few works have been done to study the effect of Na and co-doping of Na and Sb on CZTSSe.

### 2.3.2 Bandgap grading

The bandgap tuning ability of CZTSSe absorber has already been discussed earlier. Using this principle, it is possible to have variable bandgap throughout the absorber by having different anion composition. Recently, bandgap grading was the subject of numerous studies in the field of CZTSSe. Four types of bandgap grading may be used in CZTSSe (see figure 2.9). In the first case- no gradient is present (a) therefore electron transport is not particularly influenced by the band structure. In the case of a front grading (b), the bandgap on the back contact side ( $E_g$ ) is smaller than the bandgap on the front contact side ( $E_{g1}$ ). A front grading increases the open circuit voltage of a solar cell while keeping the short circuit current unchanged compared to no grading. Additionally, a front gradient with a notch within the space charge region (SCR) similar to figure 2.9 (b) shows higher PCE than a linear gradient from front to back [46]. In the case of a back grading (c), the gap on the back contact side ( $E_{g2}$ ) is larger than the gap on the front contact side ( $E_g$ ). The induced potential difference thus facilitates electron transport to the SCR. In addition, the recombinations can be also reduced because of the presence of a larger gap at the rear contact. More information on bandgap grading can be found in [46, 47]. The fourth gap profile is called the double gradient (d). With this configuration, it will utilize the benefit of both front grading and back grading. As a result it will give improved  $V_{OC}$  and

$J_{SC}$ . Hence, applying bandgap gradient can be a way to increase the PCE of CZTSSe solar cell without improving the material quality. Even though, the potentiality of bandgap grading has been known for long, it has still not been possible to realize experimentally.

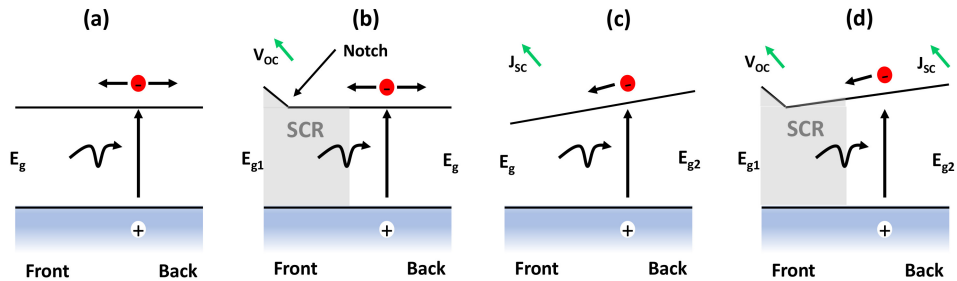


**Figure 2.9:** Main types of bandgap gradient of  $\text{Cu}_2\text{ZnSn}(\text{S}_x\text{Se}_{1-x})_4$  compound: (a) no grading, (b) front grading with notch inside SCR, (c) back grading and (d) double grading with notch inside SCR.

## 2.4 Context and structure of the thesis

The aim of this thesis is to examine ways to overcome the most important challenges of CZTSSe solar cell. These are  $V_{OC}$  deficit, defects and realization of bandgap grading. Accordingly, the structure of this work will be the following:

- Synthesis of pure CZTS and CZTSe absorber with near state of art PCE as a platform for further experiment and analysis (chapter 4);
- Process development and effects of Na and Sb inclusion on CZTS absorber to exploit the possibility of improved PCE (chapter 5);
- Realization and reaction mechanism of bandgap grading using elemental metal precursor (chapter 6);

# 3 Experimental procedure

## Contents

---

<b>3.1 Device preparation</b> . . . . .	<b>24</b>
3.1.1 Substrate . . . . .	24
3.1.2 Back contact . . . . .	24
3.1.3 Absorber . . . . .	25
3.1.4 Deposition of Buffer Layer . . . . .	28
3.1.5 Deposition of (ZnO+ZnO:Al) window layer . . . . .	29
3.1.6 Front Contact . . . . .	29
3.1.7 Equipment used for doping study . . . . .	30
<b>3.2 Material characterization techniques</b> . . . . .	<b>31</b>
3.2.1 Scanning electron microscopy (SEM) . . . . .	31
3.2.2 Energy dispersive X-ray spectroscopy (EDX) . . . . .	32
3.2.3 X-ray florescence spectrometry (XRF) . . . . .	33
3.2.4 X-Ray diffraction (XRD) . . . . .	34
3.2.5 Raman spectroscopy (RS) . . . . .	37
3.2.6 Time of flight- secondary ion mass spectroscopy (ToF-SIMS) . . . . .	39
3.2.7 Glow discharge spectroscopy (GDS) . . . . .	40
<b>3.3 Device characterization techniques</b> . . . . .	<b>41</b>
3.3.1 Current density-voltage measurement . . . . .	41
3.3.2 External quantum efficiency (EQE) measurement . . . . .	44
3.3.3 Capacitance-voltage measurement . . . . .	46
3.3.4 e-ARC (optical simulation) . . . . .	48

---

## 3.1 Device preparation

The preparation method of the layers of a CZTS(e) solar cell is described in the following subsections.

### 3.1.1 Substrate

Soda-lime glass (SLG) is generally used as a substrate for fabricating CZTS(e) solar cells. SLG contains significant amounts of alkali elements, such as Na<sub>2</sub>O (~12% by mass) and little amount of K<sub>2</sub>O (~1-2% by mass). For all the experiments in this study, SLG of 5×5 cm<sup>2</sup> and 1 mm of thickness is used as the substrate. All the substrates have been cleaned by automatic ultrasonic bath with detergent prior to rinsing with de-ionized water using Pluritan USC120 MK4 from Novatec.

### 3.1.2 Back contact

The material used as back contact during this study is Molybdenum (Mo). This material is deposited by magnetron sputtering in direct current (DC). An Alliance Concept equipment (ProCIGS) is used for the deposition, designed for in-line sequential development of CIGS device. For this thesis, only the chamber dedicated to the Mo deposition is used. In this chamber, a cryogenic pump reaches an ultimate vacuum of  $1.33 \times 10^{-4}$  Pa. The substrates are placed via an airlock on a rectilinear motion tray, which travels back and forth under a 12.7×38.1 cm<sup>2</sup> rectangular target (Plansee, 3N purity), with a speed of 1 cm.s<sup>-1</sup>.

Two different recipes of back contact (BC) have been used for fabricating kesterite-based solar cell during this study. For the first recipe, the Ar pressure is set at 0.4 Pa, the power density is set at 2.1 W/cm<sup>2</sup> and the target-substrate distance is set at 6 cm. With a deposition time of 15 min, the deposits have a thickness of approximately 520 nm and a layer resistance of 0.35 Ω/□. This recipe will be called single layer Mo recipe or standard recipe throughout this study. For the second recipe, A tri-layered Mo is deposited: a first 500 nm layer is sputtered at 0.4 Pa and 2 W/cm<sup>2</sup> to ensure electrical conductivity, a 200 nm low density layer is then deposited at 1 Pa and 0.5 W/cm<sup>2</sup> to limit the MoSe<sub>2</sub> formation while a 20 nm sacrificial layer is sputtered at 0.1 Pa and 2 W/cm<sup>2</sup> to improve the CZTSe/Mo electrical contact. This recipe will be called three layer Mo recipe in the following chapters. During both recipes no intentional heating is used.

### 3.1.3 Absorber

The absorber layer is made using kesterite material ( $\text{Cu}_2\text{ZnSnSe}_4$ ,  $\text{Cu}_2\text{ZnSnS}_4$ ,  $\text{Cu}_2\text{ZnSn}(\text{S}_x\text{Se}_{1-x})_4$ ). A two step process or sequential process is used to synthesize this absorber layer: the first step is the deposition of precursor using DC magnetron based sputtering and the second step is the annealing of the precursor under Se or S, to synthesize CZTS(e). The choice of sputtering based processing is justified as it demonstrates high PCE during different works (see table 4.1) and it is compatible with industrial production. The sputtering deposition technique compared with other techniques also has the advantages of uniformity, stability and speed [48].

Both steps of sequential processes are described briefly below.

#### 3.1.3.1 Precursor deposition by DC sputtering

DC sputtering consists of a plasma in a vacuum chamber generating from a neutral gas Ar (Argon) by applying a direct voltage between two electrodes. Ar atoms are ionized ( $\text{Ar}^+$ ) by the discharge and accelerated towards the cathode, and the electrons towards the anode. The material to be deposited is present in the form of a sputtering target inside the chamber as a cathode. The  $\text{Ar}^+$  are accelerated towards the target and separate atoms from the target. These separated atoms then settle on the surface of the substrate under the target, allowing the material to deposit. The principle of this process is shown in Figure 3.1.

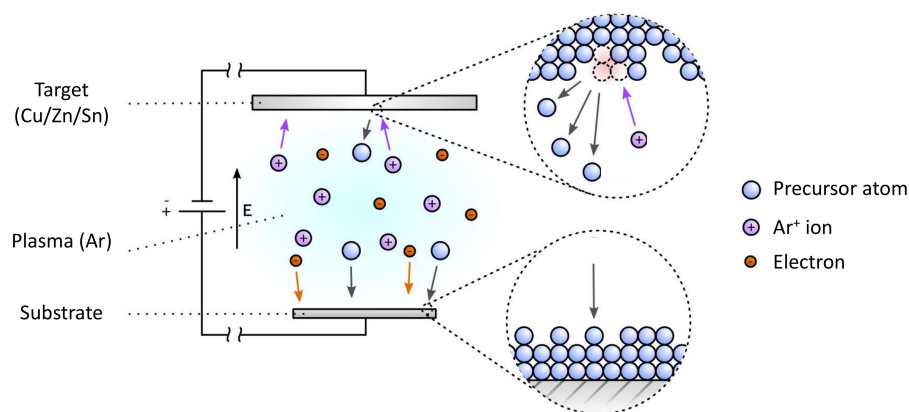


**Figure 3.1:** Schematic of DC sputtering deposition procedure using plasma of Argon.

Precursor deposition by sputtering is carried out in a Perkin Elmer frame (retrofit Plassys) (figure 3.2). The secondary vacuum of the chamber (approximately  $2.7 \times 10^{-6}$  Pa) is obtained with a cryogenic pump. Ar's pressure in the enclosure during the deposition (of the order

### 3.1. Device preparation

of a few Pa) is controlled by the opening of the rolling valve, as well as the argon flow rate (via a gas flow controller). Substrates are positioned on substrate holders (PS), which are placed on a turntable. Two PS can be used simultaneously. Both have a surface of  $15 \times 15 \text{ cm}^2$  and can therefore accommodate 9 substrates of  $5 \times 5 \text{ cm}^2$ . However, to avoid problems of inhomogeneity, only 2 substrates are inserted in the center of the PS for each deposition. The tray turns at a frequency of 4 round per minute. Three circular target of Copper (Cu), Zinc (Zn) and Tin (Sn) with 8 inches of diameter and 3N purity are used in the chamber.

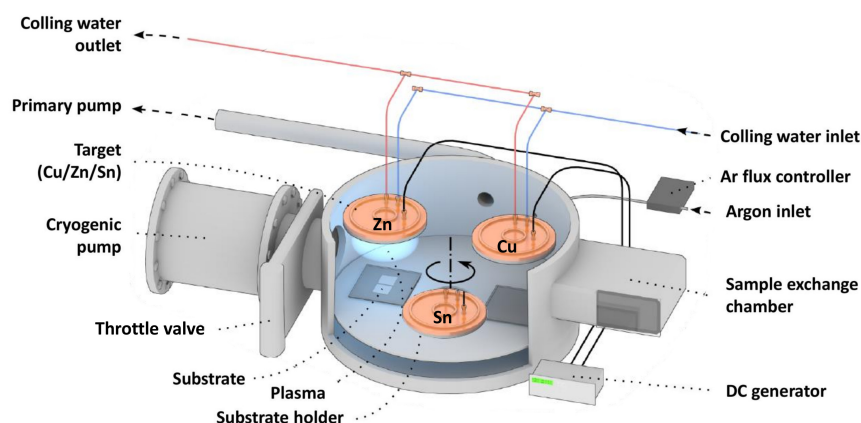


**Figure 3.2:** Schematic of the equipment (Perkin-Elmer) used for DC sputtering deposition of precursors (Cu/Zn/Sn).

Two different stack orders are used in this study: for the first stack order Zn ( $160 \text{ nm} \pm 10$ )/Sn ( $245 \text{ nm} \pm 20$ )/Cu ( $190 \text{ nm} \pm 10$ ) are deposited on Mo coated SLG and for the second stack order Cu ( $5 \text{ nm} \pm 2$ )/Sn ( $245 \text{ nm} \pm 20$ )/Cu ( $190 \text{ nm} \pm 10$ )/Zn ( $160 \text{ nm} \pm 10$ ) are deposited. The thickness of the precursor is used to tune the stoichiometry of the cation in the compound, and the value of thickness given here is related to the optimized thickness for achieving Cu-poor and Zn-rich stoichiometry. Power density of  $1.33 \text{ W.cm}^{-2}$  for Cu and Zn, and  $1.14 \text{ W.cm}^{-2}$  for Sn is used during sputtering deposition. Ar gas flow and pressure of 30 sccm and 0.2 Pa are used respectively for all the depositions. The deposition rate of material mainly depends on the applied power by the DC generator. The Ar pressure also has effects on several properties of the deposited layer.

#### 3.1.3.2 Annealing reactor

Two types of annealing reactor are used during this study. A semi-open and a closed annealing reactor for selenization and sulfurization process respectively.

### Selenization reactor

We used a semi-open reactor for selenization process: this type of reactor interacts with the outside on a much higher rate compared to a closed reactor. A tubular furnace is used as the selenization reactor and annealing occurred under Ar atmosphere with static Ar pressure (see figure 3.3 (a)). It is made of a quartz tube where the pressure inside can be changed by adjusting the Argon inlet and the pump. The precursor is placed on a graphite susceptor that is connected with a thermocouple in order to measure and control the temperature profile. The Selenium is provided in the form of pellets (two pellets - average weight of each pellet is  $45 \pm 5$  mg), placed in close proximity of the precursor stack to assure proper selenization. A quartz bell jar is placed on top of the susceptor to keep the Se vapor during annealing (figure 3.3 (b)). Out diffusion of selenium from graphite stand to the tubular furnace can still be observed during annealing. This setup of graphite stand will be called semi-open susceptor in later sections.

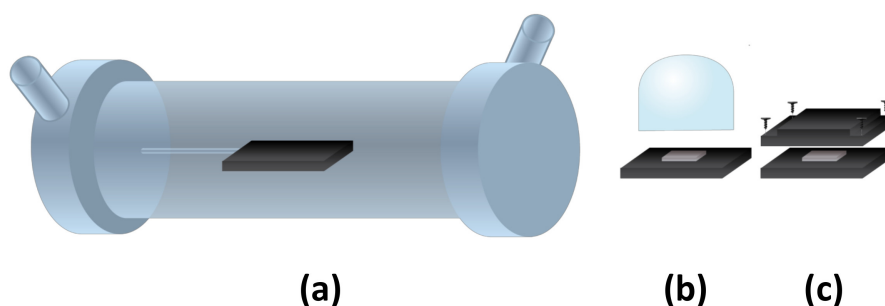


**Figure 3.3:** Tubular furnace used for the selenization process(a) the semi-open susceptor consists of a graphite sample holder and a quartz bell jar on top (b) and the closed susceptor consists of a graphite holder that can be closed using graphite screws (c).

Another type of susceptor used consists of a closable graphite box, that can be closed by four graphite screws (figure 3.3 (c)). In this case, the out-diffusion of Se is substantially reduced during the annealing procedure. This setup will be called closed susceptor in the later sections. A  $2.5 \times 2.5$  cm<sup>2</sup> precursor sample is used for annealing in both cases.

### Sulfurization reactor

A two zone tubular furnace has been used for the sulfurization process. One zone is dedicated for sulfur evaporation and another zone is used for the annealing of precursor stacks (see figure 3.4). The distance between both zone is 40 cm. Internal volume of the furnace is 3240 cm<sup>3</sup>, which is capable of working under  $1 \times 10^{-3}$  mbar pressure and Ar flow. An Ar flow of 2 L/min is used during the annealing process to diffuse evaporated sulfur from sulfur zone to the sample. Excess amount of sulfur is kept in the sulfur zone to ensure continuous sulfur supply

### 3.1. Device preparation

during annealing. The temperature of both zones is controlled by two different thermocouples. A resistive coil is used for the heating of both sides.

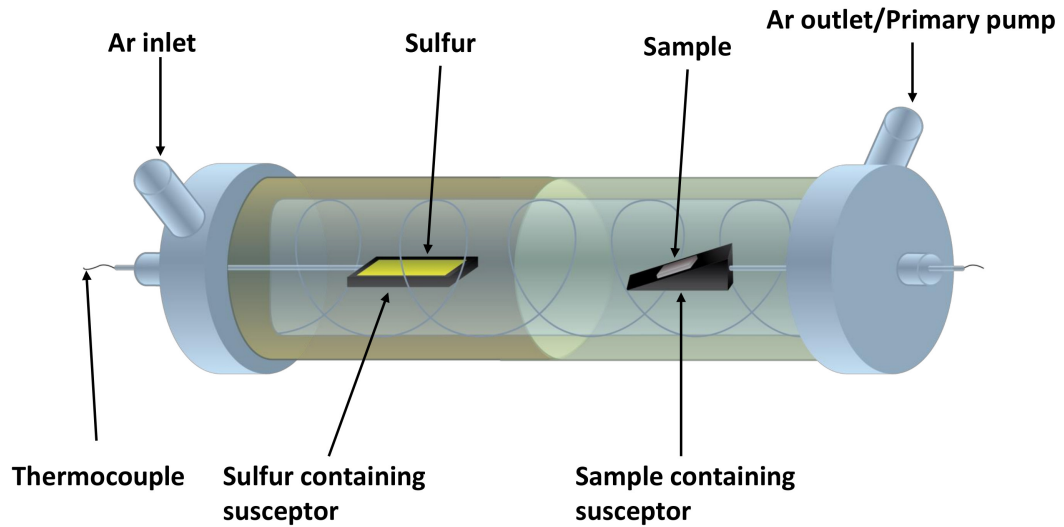


Figure 3.4: Schematic of the sulfurization reactor.

#### 3.1.4 Deposition of Buffer Layer

Cadmium sulfide (CdS) is used as a buffer layer in this study. The CdS layer is deposited in a chemical bath on the chemistry bench (figure 3.5). The solution used for CdS chemical bath contains Cadmium acetate ( $\text{Cd}(\text{CH}_3\text{COO})_2$ ) (1mM), thiourea ( $\text{SC}(\text{NH}_2)_2$ ) (5.1mM), ammonium acetate ( $\text{NH}_4\text{CH}_3\text{COO}$ ) (20mM) and ammonia ( $\text{NH}_4\text{OH}$ ) (0.3mM), which are mixed together in a double-walled beaker and stirred at 600 rpm.



Figure 3.5: Equipment used for chemical bath deposition of CdS buffer layer.

## Chapter 3. Experimental procedure

---

The beaker containing the solution is heated up to 80°C, then the sample is introduced into the solution. A CdS layer of about 60 nm forms on the sample in 15 min, accompanied by a yellowing of the solution. The sample is then rinsed with deionized water and dried with nitrogen.

### 3.1.5 Deposition of (ZnO+ZnO:Al) window layer

Unintentionally doped ZnO (ZnO-i, 50 nm) and ZnO:Al (350 nm) are sputtered using an MRC 603 equipment by radio-frequency (RF) magnetron sputtering. RF sputtering is used to deposit insulating materials. The principle is the same as for DC sputtering but this time the voltage between the target and the specimen holder is alternated at high frequency (13.56 MHz). This allows the plasma electrons (more mobile than ions) to neutralize the positive charges that accumulate on the target during sputtering, which will enable the plasma to sputter the target. A limit vacuum of  $5 \times 10^{-4}$  mTorr is achieved by a cryogenic pump. ZnO-i is deposited with a ZnO target of 4N purity and  $12.1 \times 37.8$  cm<sup>2</sup> dimension. During deposition, the RF power density is 1.2 W.cm<sup>-2</sup> and the pressure is set at 5.5 mTorr by introducing Ar with a flow of 17.5 sccm and 1% diluted O<sub>2</sub>.

ZnO:Al is deposited from a ZnO target containing 2% Al<sub>2</sub>O<sub>3</sub> by weight, 4N purity and the same dimensions as the pure ZnO target. During deposition, the RF power density is 1.9 W.cm<sup>-2</sup> and the pressure is set at 3.5 mTorr by introducing Ar with a flow rate of 21 sccm, along with 0.5% diluted O<sub>2</sub>. For both layers, the target-substrate distance is 1 cm and the scrolling speed of the substrate holder is 7 cm/min. The sample is not intentionally heated. The TCO layer resistance is between 25 and 35 Ω/□. A carrier density of  $3 \times 10^{20}$  cm<sup>-3</sup> and a typical mobility between 15 and 16 cm<sup>2</sup>/(V-s) are measured by Hall effect for a thickness of 350 nm. The optical transmittance of the 350 nm ZnO:Al layer on a 1.1 mm borosilicate glass substrate is 82% at 550 nm wavelength.

### 3.1.6 Front Contact

To collect the charges while limiting the shading of the cells, metal grids composed of 50 nm Ni (in contact with ZnO:Al) and 500 nm Al are deposited through a mechanical mask by e-beam evaporation in a Balzers BAK1052 frame. The grids cover about 10% of the cell surface. Lastly, the 0.5×0.5 cm<sup>2</sup> cells are mechanically scribed from the structure to the Mo-CZTS(e) interface. To form backside contact, a part of the structure is also etched at the edge of the sample to free a Mo surface on which a soldering iron In pad is placed. A total of either six or nine cells

of  $0.5 \times 0.5 \text{ cm}^2$  are made on the same sample. No anti-reflecting coating has been used during this study.

#### 3.1.7 Equipment used for doping study

##### 3.1.7.1 Barrier

Silicon nitride ( $\text{SiN}_x$ ) is used as a diffusion barrier between Mo and the substrate to stop material diffusion from the glass. This layer is deposited on the glass by plasma assisted chemical vapor deposition (PECVD) in a STS 310PC reactor. This technique consists of generating a plasma to the precursor gases introduced into the reactor. Free radicals formed by dissociation of molecules in plasma react with each other to grow the layer on the substrate. Ammonia ( $\text{NH}_3$ ) and silane ( $\text{SiH}_4$ ) diluted at 2% in argon are introduced into the reactor with respective flows of 20 sccm and 1000 sccm to deposit  $\text{SiN}_x$ . The pressure in the reactor during deposition is 1.1 Torr. The plasma is generated by applying an RF electrical voltage (13.56 MHz) between the reactor top wall and the substrate holder with a power of 50 W. During deposition, the substrate is at  $300^\circ\text{C}$  to promote dense layer growth [49]. A 300 nm thick layer is deposited in 20 min. The X-ray diffractogram (not shown here) of this layer do not show any peaks, indicating that the deposited material is amorphous.

##### 3.1.7.2 Evaporation deposition

The NaF and Sb depositions are carried out by evaporation technique in a homemade evaporation chamber composed of a Bloc Edwards vacuum chamber, an Annealsys RTP furnace and Riber evaporation sources (figure 3.6). Evaporation is achieved under a secondary vacuum (ultimate vacuum of approximately  $6.7 \times 10^{-5} \text{ Pa}$ , obtained with a pump turbo-molecular). No intentional heating of the sample is used during the deposition. To measure the temperature of the substrate, a thermocouple is placed in direct contact with it. The sources made of PBN cylindrical crucibles are filled with elements (99.999% purity). Each of the sources is equipped with a shutter allowing to precisely control the evaporation. Typical temperatures (measured by a thermocouple in contact with the crucible) are respectively  $730^\circ\text{C}$  for NaF and  $160^\circ\text{C}$  for Sb.

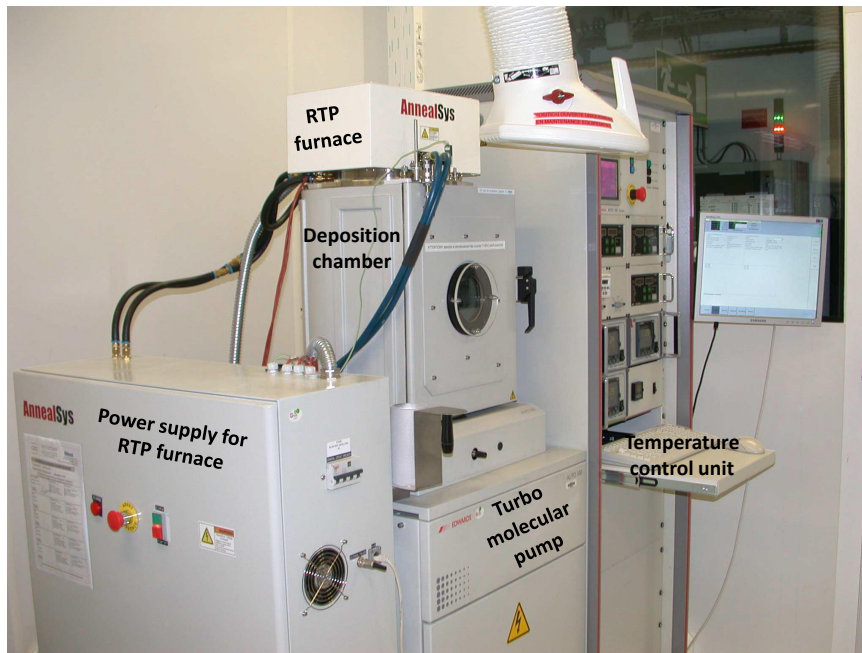
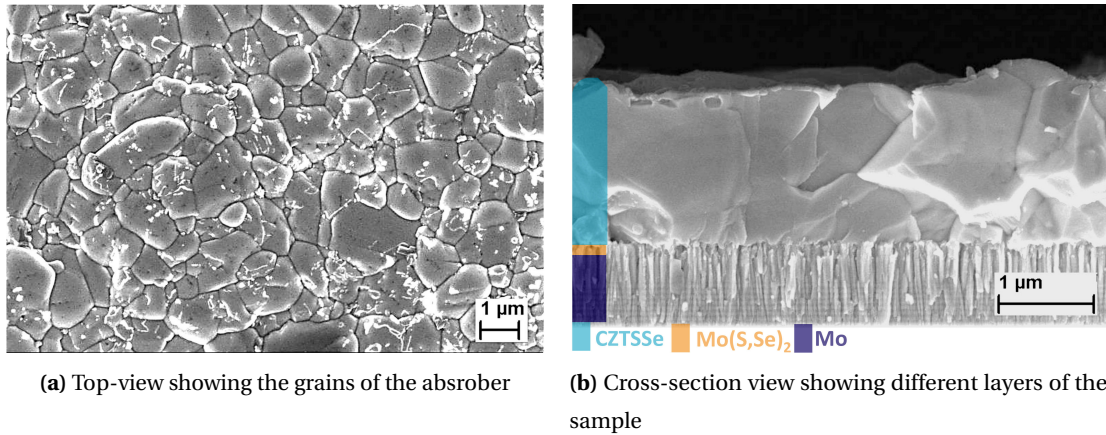


Figure 3.6: Evaporation equipment used for NaF and Sb deposition.

## 3.2 Material characterization techniques

### 3.2.1 Scanning electron microscopy (SEM)

The microstructures of the thin film are analyzed by Scanning Electron Microscopy (SEM) with a Zeiss LEO 1530 microscope, equipped with a Field Effect Gun (FEG). When the sample surface is bombarded by the electron beam, successive collisions cause the emission of secondary electrons. These electrons are detected to access the topography of the sample. An advanced description of cell characterization techniques by electron microscopy is given in [50]. The samples are observed from above or from the cross-section during the analysis. The first mode is used to see the pinholes and grain sizes while the second mode is used to see the grain size, layer roughness and voids between each layer. To see the surface, no previous metal coating is used as kesterite is a semiconductor material. To observe the cross-section of the sample, however, platinum coating ( $\sim 5$  nm) is used prior to the observation. This coating reduces the charging effects (occurs due to the insulating nature of SLG) from the substrate. For all the SEM images taken during this study, an excitation voltage of 5 keV is used. An example of the SEM image of surface (top-view) and the cross-section of a CZTSSe absorber is shown in figure 3.7.



**Figure 3.7:** SEM surface (top-view)(a) and cross-section(b) image of an annealed CZTSSe absorber synthesized on Mo coated SLG.

#### 3.2.2 Energy dispersive X-ray spectroscopy (EDX)

Energy dispersive X-ray spectrometry (EDX) measurements are performed using the same equipment as SEM measurement (Zeiss LEO 1530). It is an analytical technique used for the elemental analysis of all the elements present in the sample. In the scanning electron microscope a flow of primary electrons is focused onto the sample surface, resulting in a number of different particles or waves being emitted (secondary electrons, back-scattered electrons, X-rays, photons, Auger electrons etc.) from the sample. The secondary and backscattered electrons are used for SEM while the X-rays give characteristic chemical information of the emitting atoms. The depth of this analysis during EDX can be calculated by Castaing's formula as equation 3.1.

$$Z_m = 0.033(E_0^{1.7} - E_C^{1.7}) \frac{A}{\rho Z} \quad (3.1)$$

Here,  $Z_m$  is the x-ray generation depth ( $\mu\text{m}$ ),  $E_0$  is acceleration voltage (kV),  $E_C$  is the minimum emission voltage KeV,  $A$  is the the atomic mass of the compound,  $\rho$  is the density of the compound ( $\text{kg}/\text{m}^3$ ) and  $Z$  is the atomic number.

Different important points are taken into account during the analysis. First, each element has a certain minimum acceleration voltage to be excited for the measurement. All the anions and cations can be detected using 5 kV acceleration voltage, except Tin (Sn). Sn requires minimum

### Chapter 3. Experimental procedure

---

10 kV acceleration voltage to be detected. Thus, for elemental mapping of the sample surface, at least 10 keV acceleration voltage is used.

Second, for detecting anions on sample containing S, care needed to be taken as S and Mo have same signal and can not be distinguished using EDX. At 20 keV, the calculated depth of the measurement is  $\sim 1.2 \mu\text{m}$  to  $1.3 \mu\text{m}$  depending on the density of the material. In order to detect only S without reaching up to Mo, 20 keV excitation voltage is used (as the thickness of absorber varies from  $\sim 1.4 \mu\text{m}$  to  $1.5 \mu\text{m}$ ).

Third, for detecting cations, a 30 keV excitation voltage is used. The x-ray generation depth using this excitation voltage is between  $2.3 \mu\text{m}$  to  $2.5 \mu\text{m}$ , higher than the absorber thickness. This can ensure a better integrated measurement of cations in the sample. The amount of cations are indicated as an atomic percentage of cations considering  $[\text{Cu}+\text{Zn}+\text{Sn}]=100\%$  during this study.

Finally, the analysis is done on the surface of  $100 \mu\text{m} \times 100 \mu\text{m}$ , to reduce the non homogeneity effect forming in different places of a sample. In addition, one reference sample is used to determine the percentage of error, by measuring same sample in five different points (selected randomly). The error percentage is found out to be  $\pm 0.5\%$ .

#### 3.2.3 X-ray fluorescence spectrometry (XRF)

X-ray fluorescence spectrometry (X-Ray Fluorescence, XRF) is used to quantify the chemical composition of CZTS(e) absorber and also to estimate the thickness of the Mo and CZTSe layers. The measurement consists of exciting the core electrons of the atoms with an X-ray beam and analyzing the X-ray spectrum re-emitted by fluorescence. This spectrum is linked to the de-excitation of atoms by radiative electronic transitions and is therefore characteristic of atoms present in the layer. The equipment used is an energy dispersive X-ray fluorescence spectrometer (XDV-SDD, Fischer model). An acceleration voltage of 50 kV and a current of 1 mA are applied to emit X-rays from an anti cathode of W (line  $K_{\alpha}$ ,  $\lambda = 0.021 \text{ nm}$ ). A counting time of 30 s is used and the measurement is calibrated with a reference sample. The probe surface during measurement was  $3 \text{ mm}^2$ .

### 3.2.4 X-Ray diffraction (XRD)

#### 3.2.4.1 General principle and uses

This technique is based on the diffraction of an X-ray beam by the crystallographic structure of the material. An incident X-ray beam is diffracted in a specific direction depending on the incident angle. By detecting the angle of the diffracted beam, while knowing the angle of the incident beam, it is possible to study the crystalline properties of the materials. The presence of CZTS(e) can be detected along with the presence of secondary phases.

To analyze the orientation of the planes parallel to the sample surface, the measurements are performed in mode  $\theta$ - $2\theta$  in a D8 Advance Bruker AXS. This mode consists of tilting the detector by  $2\theta$  and the sample by  $\theta$  with respect to the incident beam. An XRD diffractogram of a CZTS absorber grown on Mo (figure 3.8) shows the Bragg peaks corresponding to CZTS phases and Mo.

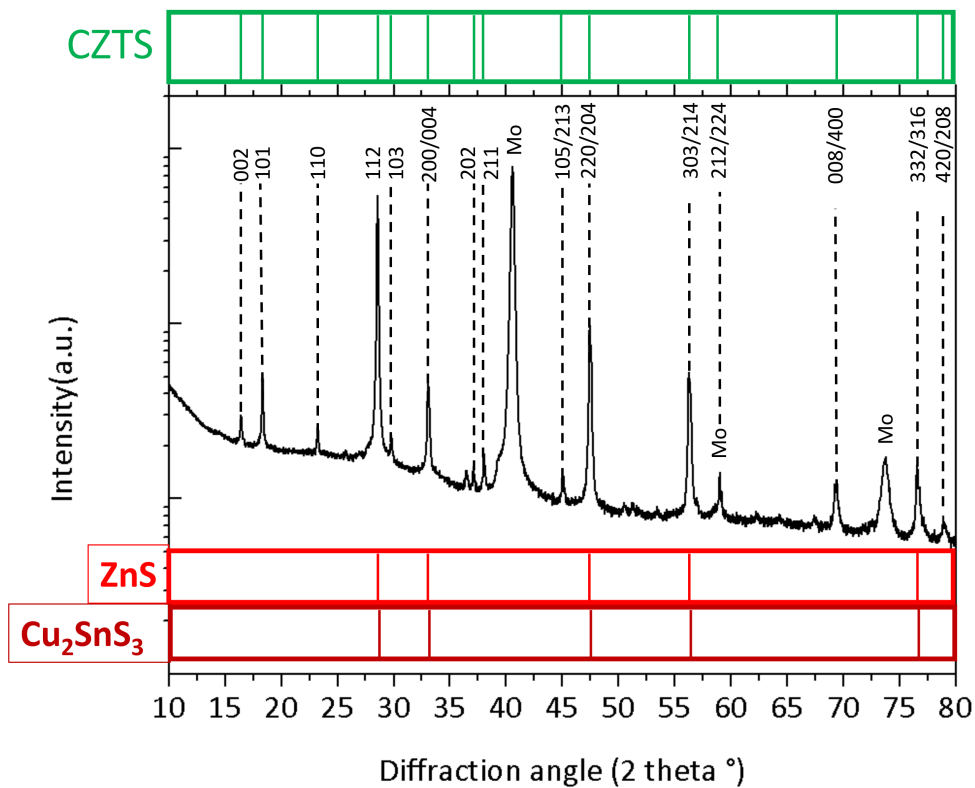


**Figure 3.8:** An XRD diffractogram of CZTS absorber on Molybdenum [51, 52].

### 3.2.4.2 Analysis using XRD data

**First of all**, The XRD diffractograms of all the samples are analyzed by fitting the peak(112), (220/204) and Mo via pseudo-voigt function according to equation 3.2, which is a linear combination between a Gaussian and Lorentzian function.

$$y = y_0 + A[m_u \frac{2}{\pi} \frac{w}{4(x - x_c)^2 + w^2} + (1 - m_u) \frac{\sqrt{4 \ln 2}}{\sqrt{\pi} w} e^{-(\frac{4 \ln 2}{w^2})(x - x_c)^2}] \quad (3.2)$$

Here,  $y_0$  is an offset,  $x_c$  is a peak center,  $A$  is the area under the peak,  $w$ =FWHM,  $m_u$  is the shape factor (the ratio indicating the percentage of Gaussian profile detected for the peak of interest).

**Secondly**, The Scherrer's equation is used to calculate the mean crystallite size  $D$  as,

$$D = \frac{0.9\lambda}{\beta_{mat} \cos \theta} \quad (3.3)$$

Here,  $\lambda$  is the wavelength of X-ray used ( $1.5406\text{\AA}$ ),  $\beta_{mat}$  is the width of the peak in radians (in this case peak (112)) at half of its intensity (FWHM) and  $\theta$  is the bragg angle ( $2\theta$  position of the peak (112)/2).

Before the crystallite size extraction from the width of the peak, instrumental contribution needs to be subtracted using the following equation,

$$\beta_{mat} = \sqrt{\beta_{experimental}^2 - \beta_{instrumental}^2} \quad (3.4)$$

Here,  $\beta_{experimental}$  and  $\beta_{instrumental}$  correspond to the FWHM of the same peak position from experimental sample and from the instrumental data sheet respectively.

**Finally**, The anion composition can be calculated using Vegard's law from the position of the peak of CZTSSe. This is an empirical heuristic stating that the lattice parameter of a solid solution of two constituents is approximately equal to a rule of mixtures of the two constituents lattice parameters at the same temperature [53]. Using this rule, the anion composition of

CZTSSe can be calculated using following equation-

$$A_{Cu_2ZnSn(S_xSe_{1-x})_4} = xB_{Cu_2ZnSnS_4} + (1-x)C_{Cu_2ZnSnSe_4} \quad (3.5)$$

Here,  $A_{Cu_2ZnSn(S_xSe_{1-x})_4}$  is the position of any selected peak (for this study peak (112) is used) from a CZTSSe sample,  $B_{Cu_2ZnSnS_4}$  is the position of same peak for CZTS (~28.44° [52]),  $A_{Cu_2ZnSnSe_4}$  is the position of same peak for CZTSe (~27.16° [54]) and x is the anion composition.

### 3.2.4.3 Limitations

Minor phases such as ZnS(e) or  $Cu_2SnS(e)_3$  are difficult to identify using XRD as the diffraction peaks overlap with the peaks of CZTS(e) [51, 52, 55] (see figure 3.8). Nonetheless, there are a few peaks with low intensity for the tetragonal kesterite phase with lower symmetry, which allow one to clearly identify the kesterite phase. These are for instance the peaks at 17.4°, 22.1°, 28.3°, 35.2°, and 36.1° corresponding respectively to diffraction planes (101), (110), (103), (202), and (121), respectively for CZTSe [56].

### 3.2.4.4 Grazing incident X-ray diffraction (GIXRD)

Grazing incidence XRD (GIXRD) uses small and fixed incident angles for the incoming X-ray beam for the XRD analysis as a function of the sample depth. The principle is based on controlling the incident angle of X-ray to limit the XRD measurement up to a certain depth. X-ray beam is applied on the sample with a fixed angle higher than the critical angle of material to get integrated XRD pattern until a certain depth of the material. The penetration depth of X-ray mainly depends on the incident angle and material properties.

The penetration depth for different incident angles can be calculated using the method described by Dimitrievska et al, [57]. Using this calculation method, penetration depth of a sample is calculated for different incident angles and shown in figure 3.9 as an example. Thus, certain incident angles gives information of the integrated signal up to the depth of penetration. Measurements are performed with a Rigaku SmartLab diffractometer mounted on a Copper rotating anode ( $\lambda_{K\alpha 1} = 1.54056 \text{ \AA}$ ,  $\lambda_{K\alpha 2} = 1.54443 \text{ \AA}$ ) and equipped with a Göbel mirror and a 0.114° vertical Soller collimator.

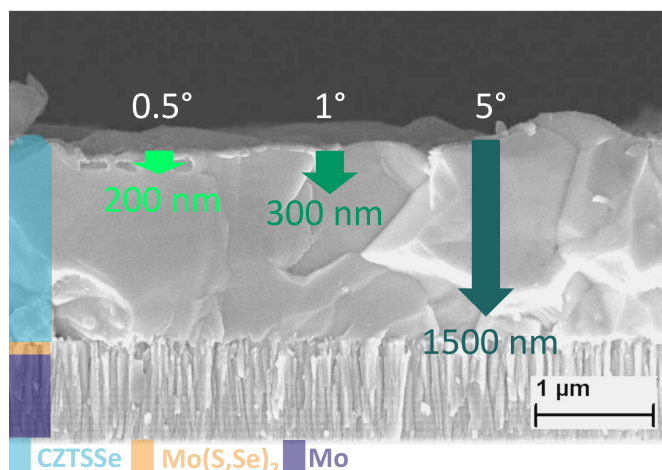


**Figure 3.9:** Illustration of an X-ray penetration depth for incident angle of 0.5°, 1° and 5° during GIXRD. To assist the depth perspective, it is drawn on the SEM cross-section image of the sample.

### 3.2.5 Raman spectroscopy (RS)

Raman spectroscopy is a non-destructive methods of characterizing the molecular composition and external structure of a material. It exploits the physical phenomenon whereby a medium slightly changes the frequency of the light flowing through it, by emitting or absorbing phonons. This frequency offset, called the Raman effect, corresponds to an energy exchange between the light beam and the medium. Raman spectroscopy consists of sending monochromatic light (usually from a laser in visible, near infra-red or near ultra-violet range) onto the sample and analyzing the scattered light. The analysis of the shift of spectral lines due to the Raman effect can give information on the molecular structure, inter-molecular interaction and chemical composition of the sample.

During this study, a in-Via confocal Raman microscope from Renishaw is used. Backscattering configuration is used with a green laser (532 nm excitation wavelength) and a red laser (632 nm excitation wavelength). Raman analysis is used mainly to determine the presence of minor phases along with that of kesterite material. The Raman analysis of a CZTS absorber is shown as an example in figure 3.10 indicating all the possible minor phases along with CZTS peaks.

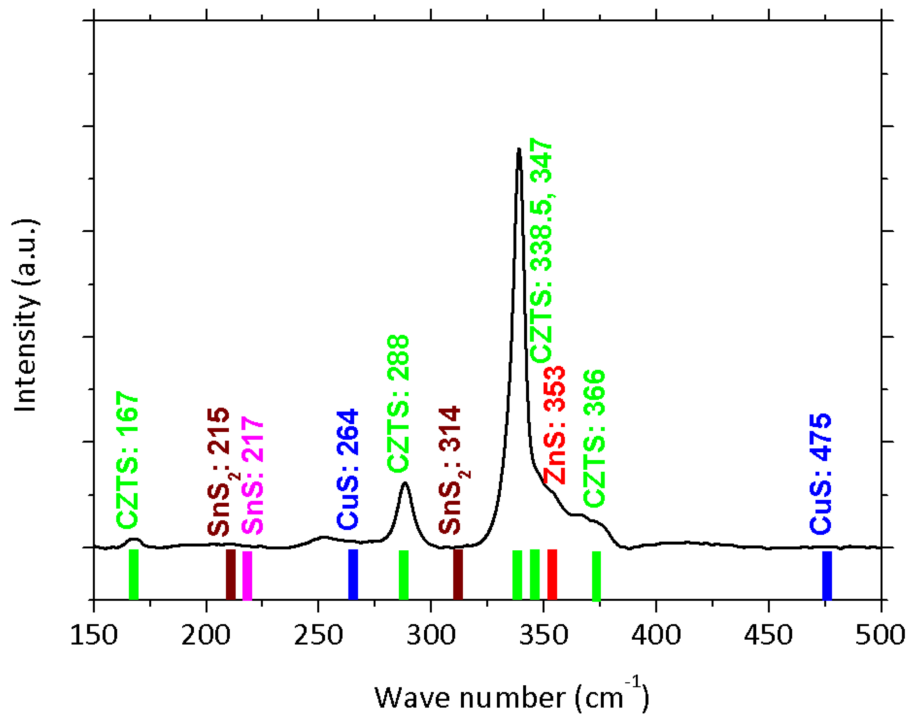


**Figure 3.10:** Raman peaks of CZTS and peak position of different secondary phases observed with 532nm excitation wavelength [51, 52, 58].

Different issues are taken into account during this characterization: first, Raman analysis is a local analysis that gives information only from the place excited by the laser (typical diameter of laser spot size used during this experiment is 800 nm- 2 $\mu$ m). As a result, the characterization results can be different depending on the sample inhomogeneity.

Second, depending on the laser wavelength, the measurement can show information from different depths of the absorber according to the penetration depth of laser (penetration depth increase with increasing laser wavelength for a given material). This phenomenon is shown in figure 3.11.

Finally, the minor phase of ZnS(e) or Cu<sub>2</sub>SnS(e)<sub>3</sub> is much sensitive while using UV or red laser respectively. But, using a green laser it can not be detected properly, due to the unfavorable pre-resonant condition at this wavelength [51, 52, 58].

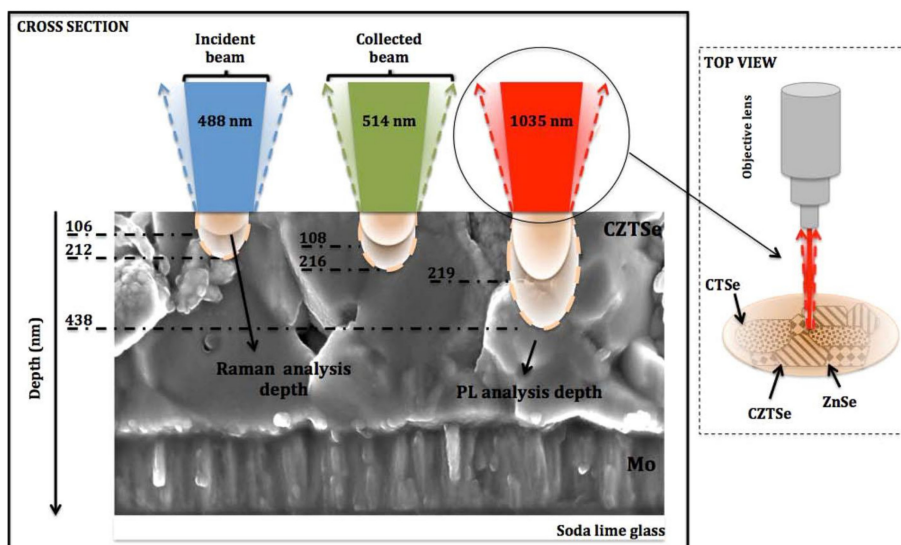


**Figure 3.11:** Scheme of the Raman analysis depth for the laser wavelengths of 488, 514 and 1035 nm, adapted from [54].

### 3.2.6 Time of flight- secondary ion mass spectroscopy (ToF-SIMS)

ToF-SIMS (Time of flight-Secondary Ion Mass Spectrometry) analysis is used to characterize the presence and distribution of the elements in CZTS(e). This characterization makes it possible to obtain the concentration profiles of different elements as a function of depth. In addition, it has a high sensitivity (in the ppm range), that is particularly useful for the study of impurities.

In ToF-SIMS analysis, a solid surface is bombarded by primary ions (usually  $\text{Cs}^+$ ) of some KeV energy that emitted ions (secondary ion) of different elements. Mass separation and detection of the emitted ions are performed using the difference in time-of-flight (time-of-flight is proportional to the square root of the weight). ION-TOF ToF-SIMS equipment is used in both negative and positive mode for this characterization. 2 kV  $\text{Cs}^+$  ion sputtering and 2 KV ( $\text{O}_2$ ) ion sputtering are used as primary ion for negative and positive mode respectively.  $300\mu\text{m} \times 300\mu\text{m}$  area of the surface is sputtered for this experiment on each sample. For analysis, the primary beam of LMIG  $\text{Bi}^{3+}$  used with 25 keV, cycle time  $80\mu\text{s}$ , and a raster size of  $87.5\mu\text{m}^2$ .

This kind of dual mode is useful to identify variable materials with preferred ionization condition for better ionization efficiency or higher count rates. The ionization efficiency becomes an important factor when experimental sample have trace amount (near the detection limit of SIMS analysis) of impurities (e.g. Sb have better ionization efficiency in negative secondary ion mode, therefore negative secondary ion mode will be better for Sb detection). Preferential



### 3.3 Device characterization techniques

#### 3.3.1 Current density-voltage measurement

##### 3.3.1.1 Under illumination

The reference method for measuring the performance of a solar cell is the J-V measurement under standard temperature (25°C) and illumination condition (AM 1.5 G and 1000 W/m<sup>2</sup>). These measurements were made on a Spectranova bench equipped with a CTA-XS 101 solar simulator, calibrated with a reference monocrystalline Si solar cell, whose properties have been certified by the Fraunhofer ISE Institute. In addition, a correction is applied to account for the difference between the actual irradiance, measured by a photo diode, and the standard irradiance of 1000 W/m<sup>2</sup>. The J-V characteristic is measured with 4 point probe system.

The principle of J-V measurement under illumination consists of measuring the current supplied by the cell as a function of the voltage applied to its terminals, by submitting this one to an illumination simulating solar radiation. The current generated by the cell is proportional to its surface. In order to work with independent values of the cell surface S, the quantity used is the current density  $J = I/S$ , expressed in A.cm<sup>-2</sup>. Figure 3.14 shows a J-V curve measured from a CZTSe cell on SLG glass. In the simplest approximation, a solar cell can be represented by a diode (p-n junction) in parallel with a current source (photogenerated current) (see figure 3.13). The curve obtained is the sum of the contributions corresponding to these two components, for each voltage value. The J-V measurement under illumination makes it possible to extract many parameters: the  $V_{OC}$  or open circuit voltage (voltage at 0 current density),  $J_{SC}$  or short circuit current density (current density at 0 voltage), FF and efficiency of a solar cell (see figure 3.14). The power density  $P = J \times V$  of the cell can be also calculated for each voltage applied.

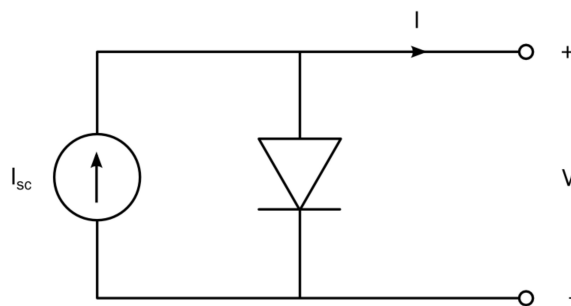


**Figure 3.13:** Electrical model of an ideal photovoltaic cell representing p-n junction.

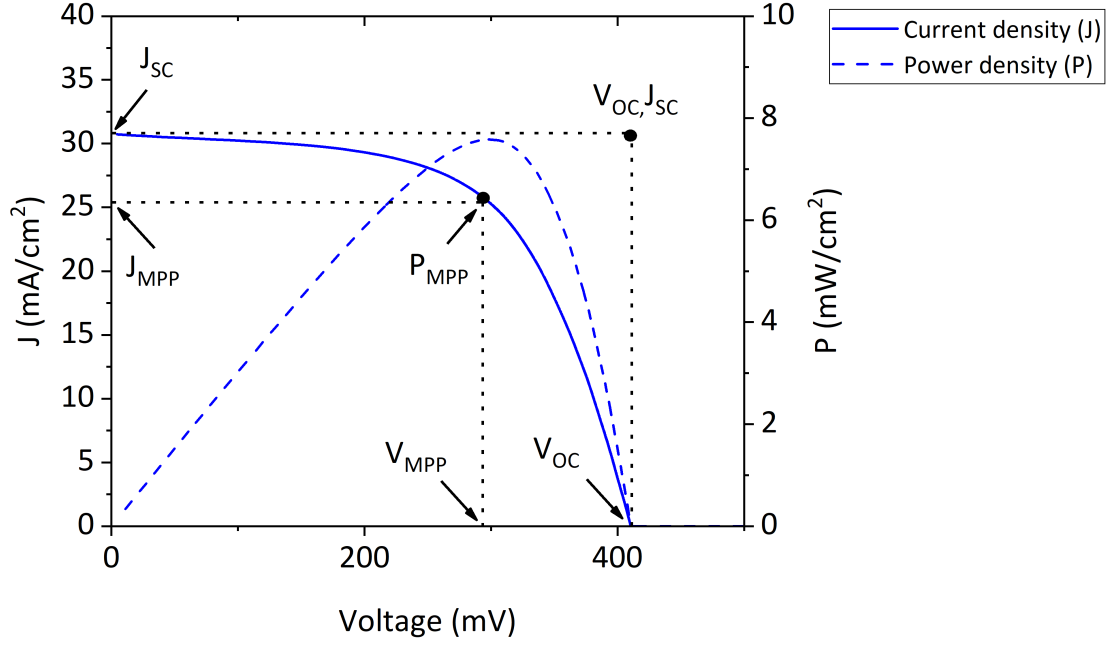


**Figure 3.14:** J-V and P-V curve of a CZTSe-based solar cell measured under AM 1.5G illumination.

Power shows a single maximum (Maximum Power Point, MPP),  $P_{MPP}$ , for a given curve where  $J_{MPP} < J_{SC}$  and  $V_{MPP} < V_{OC}$ . This difference is partly due to the loss mechanisms present within the device. The relationship between  $P_{MPP}$ ,  $J_{SC}$  and  $V_{OC}$  is called Fill Factor (FF) and is therefore:

$$FF = \frac{J_{MPP} V_{MPP}}{J_{SC} V_{OC}} \quad (3.6)$$

The efficiency of a solar cell is the ratio between the maximum power that it can deliver ( $P_{MPP}$ ) and the power of incident solar radiation ( $P_{in}$ ). The parameters extracted from a J-V measurement make it possible to determine the yield of a cell, equal to :

$$\eta = \frac{P_{MPP}}{P_{in}} = \frac{J_{SC} V_{OC} FF}{P_{in}} \quad (3.7)$$

The fill factor depends on the different loss mechanisms in the cell. In addition to recombinations, losses are also due to parasitic resistance phenomena. Figure 3.15 shows the electrical

### Chapter 3. Experimental procedure

circuit equivalent to a solar cell with these parasitic effects. The expression of the current under illumination becomes in this case:

$$J = J_{ph} - J_0 \left[ \exp\left(\frac{qV - qJR_S}{nKT}\right) - 1 \right] - \frac{V - R_S J}{R_{Sh}} \quad (3.8)$$

First, the different interfaces and layers of the device (notably the contact and window layer) have a resistance. The sum of these contributions is electrically manifested by a resistance in series ( $R_S$ ). The  $R_S$  influences the slope of the curve J-V around the  $V_{OC}$ . In the case of good quality CZTS(e) cells,  $R_S$  is generally on the order of few tenths of  $\Omega \cdot \text{cm}^2$ . An increase in  $\Omega \cdot \text{cm}^2$  can have significant effects on the fill factor.

Shunt resistance ( $R_{Sh}$ ) is the second parasitic effect taken into account in this model. It can be caused by faults in the cover of the rear contact by the CZTS(e) (short circuit CdS-Mo), by the secondary phases and more generally because of the problems related to the adhesion of certain layers. In contrast to series resistance, it must therefore be as high as possible. When  $R_{Sh}$  is on the order of  $\text{k}\Omega \cdot \text{cm}^2$  and above, its effect on the fill factor is limited. However, if the order of magnitude lower than  $\text{k}\Omega \cdot \text{cm}^2$ , the effect of short circuits can influence the cell's performance.

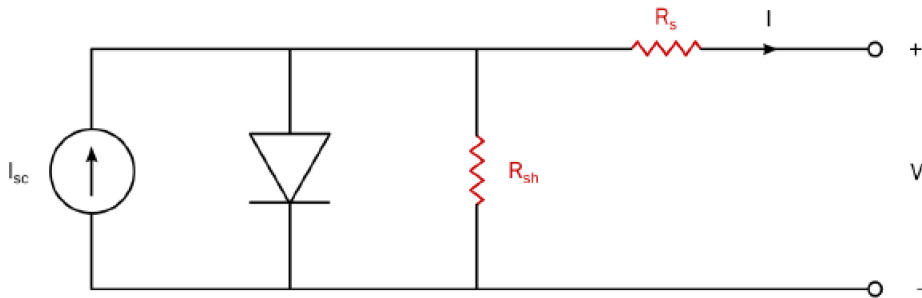


**Figure 3.15:** Electrical model of an ideal photovoltaic cell representing p-n junction with parasitic resistance  $R_S$  and  $R_{Sh}$ .

#### 3.3.1.2 In the dark

The J-V measurements under dark makes it possible to extract the parameters of the diode (the saturation current  $J_0$  and the ideality factor  $n$ ), as well as the resistance values  $R_S$  and  $R_{Sh}$ . Figure 3.16 shows a J-V curve measured under dark on a CZTSe cell. The principle is to apply different voltages on the solar cell under dark (acts as a diode) and to measure the current

responses. The simplest method of parameter extraction is to perform an interpolation for each area of the curve made from current-voltage data. The parallel resistance ( $R_{Sh}$ ) can thus be extracted by performing a linear regression of the curve around 0V. The series resistance ( $R_S$ ) is obtained with linear regression at high voltage values. Finally, the parameters of diode ( $J_0$  and  $n$ ) are obtained by interpolation of the exponential part (linear in scale) of the curve using Shockley's law. The dark J-V measurements were performed with a Keithley 2601A source meter using 4 point probe configuration at 25°C.

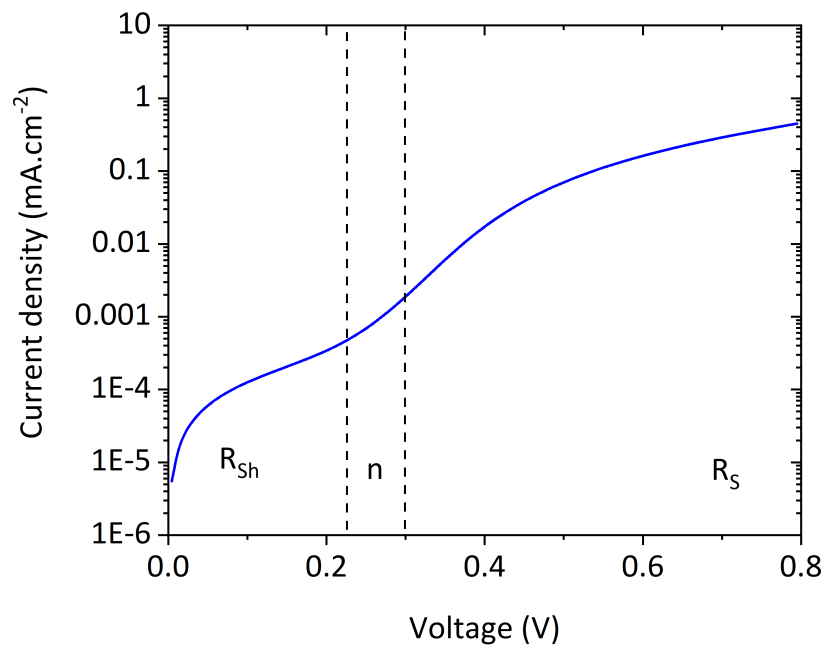


**Figure 3.16:** J-V curve of a CZTSe-based solar cell measured in dark. The vertical black dotted lines indicate the domains dominated by the different components: Shunt resistance ( $R_{Sh}$ ), diode ideality factor ( $n$ ) and series resistance ( $R_S$ ).

#### 3.3.2 External quantum efficiency (EQE) measurement

The external quantum efficiency (EQE) of the solar cell is a measure of the ratio between the number of charges collected in the device and the number of incident photons (i.e. the efficiency of conversion of photons into electrical current by the solar cell). It is represented as a function of the light wavelength.

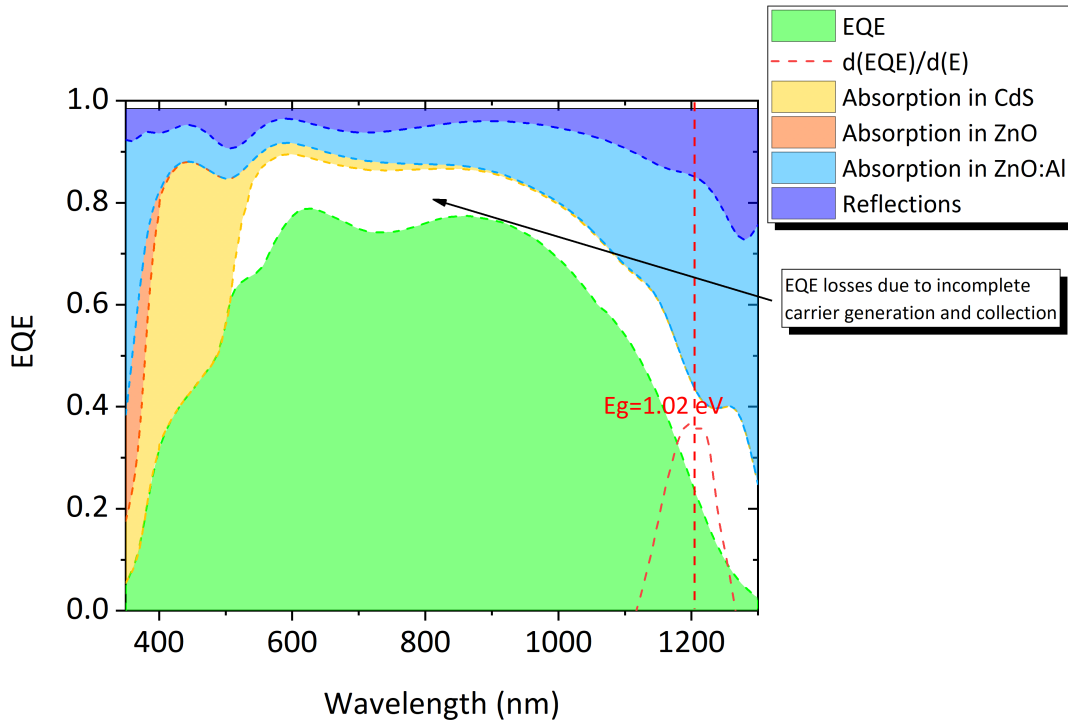


**Figure 3.17:** External quantum efficiency of a CZTSe cell with a gap of 1.02 eV. The different colored areas represent the different optical and electronic losses in the device. The dotted vertical line corresponds to the gap of the CZTSe, determined by the maximum of  $d(\text{EQE})/dE$ .

Figure 3.17 shows the EQE curve of a CZTSe cell with a gap of 1.02 eV. The corresponding curves represent the different optical and electronic loss mechanisms.

EQE measurements are performed on a 'Spequest' bench. During a measurement, the cell is illuminated over a circular area with 2 mm in diameter by the radiation of a tungsten filament lamp chopped by a mechanical chopper and filtered by a monochromator. The current delivered by the cell is measured via two points (one in contact with the rear contact and the other with the metal grid) for wavelengths between 350 and 1300 nm with a 10 nm step. A synchronous signal amplifier is used to increase the signal-to-noise ratio of the current measurement, modulated at the light chopping frequency. The EQE of the illuminated area is calculated from the measured current and the current delivered by an illuminated calibration diode under the same conditions with known spectral response. The measurements are taken at 25°C and at zero voltage. According to Merdes et al [60], the bandgap of the absorber can be determined from the maximum of its EQE derivative with respect to the photon energy.

### 3.3.3 Capacitance-voltage measurement

The capacitance-voltage measurements (C-V), or admittance measurements allows to determine the density of free carriers in the kesterite absorber, as well as the depletion region width [61]. The capacitance is a physical quantity that represents the ability to store electrical charges. The capacitance is defined by:

$$C = \frac{Q}{V} \quad (3.9)$$

where Q is a charge and V is a potential. The principle is to measure the capacitance of the diode at different values of applied voltage, which has the effect of varying the width of depletion region W.

To interpret a C-V measurement, it is necessary to model the photovoltaic cell. As a first approximation, the Shockley hypothesis is used to describe the p-n junction. It consists of the assumption that, there are no free carrier in the space charge region/depletion region. The depletion region is supposed to contain only positive charges. In this way, the p-n junction can be assimilated to a flat capacitor, the depletion region representing the dielectric medium. As a first approximation, the cell capacity is given by [62]:

$$C = \frac{1}{\frac{W_a}{\epsilon_a} + \frac{W_b}{\epsilon_b} + \frac{W_w}{\epsilon_w}} \quad (3.10)$$

Where  $\epsilon$  is the dielectric constant ( $\epsilon = \epsilon_r \epsilon_0$  with  $\epsilon_r$  as the relative dielectric constant and  $\epsilon_0$  as the permittivity of vacuum), and W is the width of the depletion region, that varies with the applied voltage. a, b and w mean "absorber" for the CZTS(e), "buffer" for the CdS buffer layer, and "window" for the window layer respectively. The thickness of the buffer layer is very low, compared to absorber layer. The assumption  $W_b \ll W_a$  can be made. In addition, the window layer being heavily doped, it is assumed that  $W_w$  is negligible respect to  $W_a$ . In this case, the depletion region extends exclusively into the CZTS(e) and therefore  $W_a$  is the only contribution to C. The situation is equivalent to having an  $n^+ - p$  hetero-junction. In this case,

### Chapter 3. Experimental procedure

---

the expression of the capacitance can be simplified by applying  $\epsilon=\epsilon_a$  and  $W=W_a$ :

$$C = \frac{\epsilon}{W} \quad (3.11)$$

and  $W$  can be described as [46]:

$$W = \sqrt{\frac{2\epsilon}{qN}(V_D - V)} \quad (3.12)$$

Here,  $q$  is the elementary charge,  $N$  is the acceptor concentration levels in the CZTS(e) (assuming that they are all ionized),  $V_D$  is the diffusion potential of the junction and  $V$  is the voltage applied to the device. Now, capacitance can be expressed as a function of acceptor density by combining the equations 3.11 and 3.12:

$$\frac{1}{C^2} = \frac{2}{\epsilon q N} (V_D - V) \quad (3.13)$$

Equation 3.13 shows that the graphical representation of  $1/C^2V$  is a line of slope inversely proportional to  $N$ . The value for  $1/C^2=0$  gives the diffusion voltage  $V_D$  of the p-n junction. C-V measurement can be used under these conditions to determine  $N$  and  $V_D$ . In the case where the  $N$  concentration is not uniform in the active layer, the  $1/C^2$  is not a straight line. In this case,  $N(W)$  can be determined for each value of  $W$ . Thus, equation 3.13 can be differentiated as:

$$\frac{d(C^{-2})}{dV} = \frac{2}{q\epsilon N(W)} \quad (3.14)$$

Thus, the acceptor defect density profile is obtained by representing  $N$  as a function of  $W$  where  $N$  is calculated from the derivative of  $1/C^2$  and  $W$  is obtained from the value of the capacity  $W=\epsilon/C$ .

This measurement method is used to determine the doping profile of CZTS(e) cells. The C-V

measurements were performed in the dark at ambient temperature, with an Agilent HP E4980A Precision LCR Meter. The frequency used during C-V measurement is 110kHz with a voltage oscillation of 50mV.

#### 3.3.4 e-ARC (optical simulation)

The e-ARC<sup>1</sup> is a simulation software developed by AIST in Japan. It can be used to calculate reflection, absorption and recombination losses for thin film photovoltaic by using EQE analysis. The carrier losses induced by absorber interface and bulk region can be roughly estimated.

First, the model of the CZTS solar cell is constructed with various layers according to the real device scenario (see figure 3.18).



**Figure 3.18:** Schematic of the thin film layers used for the EQE construction modeling.

To construct the optical modeling, the optical constants ( $n$  and  $k$  parameter as a function of wavelength) of all the layers (ZnO:Al, ZnO, CdS, CZTS MoS<sub>2</sub> and Mo) are defined for the calculation of absorption and reflection in each layer (see figure 3.19). The optical constants of ZnO:Al and ZnO are taken from an ellipsometry measurements using the same experimental material deposited on SLG. On the other hand, the optical constants of CdS, Mo and MoS<sub>2</sub> are taken from the literature [63, 64]. The optical constants of CZTS absorber are taken from the work of Li et al, [65], where the author used a  $797 \pm 28$  nm thick absorber. Lastly, the reflectance of each sample is measured separately and used as reflectance data for the simulation.

Having all the optical constants for each layer along with the reflectance spectra of the complete device, the information on the photon absorption for each layer can be determined. In

<sup>1</sup><https://unit.aist.go.jp/rcpv/cie/index.html>

### Chapter 3. Experimental procedure

---

the e-ARC software, the EQE spectrum is simply calculated by equation 3.15.

$$EQE(\lambda) = A_{absorber}(\lambda)H(\lambda) \quad (3.15)$$

Here,  $A_{absorber}(\lambda)$  is the photon absorption of the CZTS absorber layer as a function of wavelength and  $H(\lambda)$  is the carrier collection efficiency as a function of wavelength. In this model,  $H(\lambda)$  is calculated by the following equation 3.16.

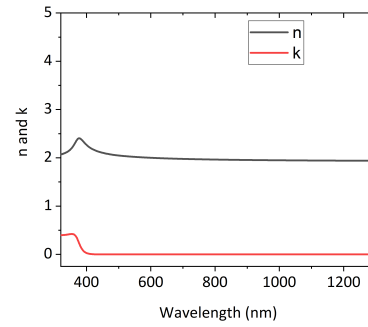
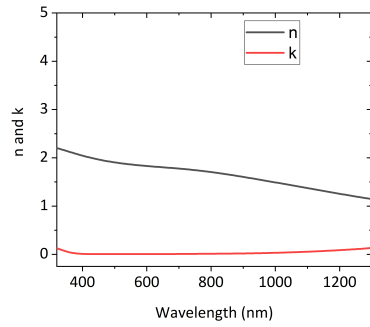
$$H(\lambda) = 1 - \exp[-\alpha(\lambda)L_C] \quad (3.16)$$

Here,  $\alpha(\lambda)$  denotes the absorption coefficient of the absorber layer and  $L_C$  denotes the carrier collection length. Therefore, we can estimate the carrier collection length of a solar cell by fitting the EQE spectrum with the calculated one. Also, from this model short-circuit current density of absorber layer can be calculated according to equation 3.17, which can provide information on the amount of current loss (absorption or recombination) induced by each layer of the CZTS solar cell device.

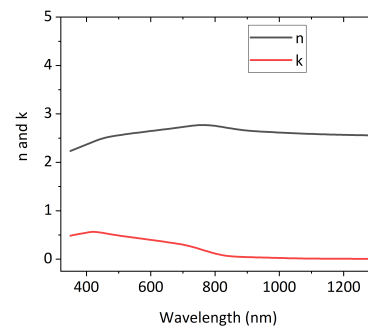
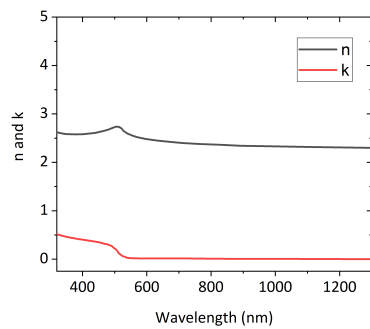
$$J_{SC} = \frac{e\lambda}{2\pi\hbar c} \int EQE(\lambda)F(\lambda)d\lambda \quad (3.17)$$

Where,  $e$ ,  $\hbar$  and  $c$  are the charge of the electron, the Planck constant and the speed of light respectively.  $F(\lambda)$  indicates the solar irradiance under AM 1.5G.

### 3.3. Device characterization techniques

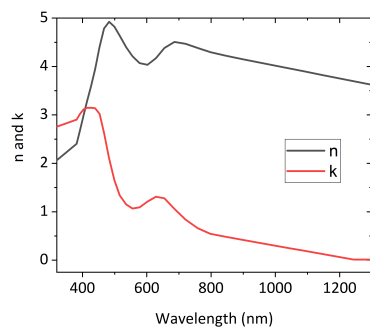


(a) n and k parameter of ZnO:Al (experimental) (b) n and k parameter of ZnO (experimental)

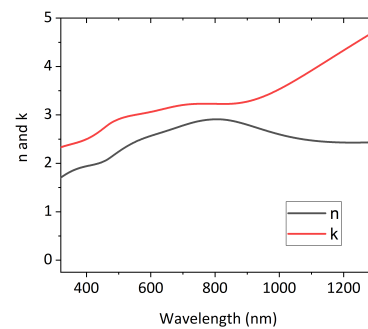


(c) n and k parameter of CdS [63]

(d) n and k parameter of CZTS [65]



(e) n and k parameter of MoS2 [64]



(f) n and k parameter of Mo [63]

**Figure 3.19:** Representation of optical parameter used as input for the simulation.

During the fitting, only the thickness of each layer (except thickness Mo) and the carrier collection length are adjusted to have a proper fitting of EQE spectra. The reason for not having Mo layer thickness as a parameter is that, the optical confinement effect induced by the back side reflection and the resulting multiple light reflection is neglected by this model. The fitting agreement can be evaluated by minimizing the mean-square error (MSE) generated

### Chapter 3. Experimental procedure

by the software according to equation 3.18.

$$MSE = \frac{1}{N} \sum_{i=1}^N (EQE_{ex,i} - EQE_{cal,i})^2 \quad (3.18)$$

where  $EQE_{ex,i}$ ,  $EQE_{cal,i}$  and  $N$  are experimental EQE, calculated EQE and a total number of data points respectively.

The flow chart of the fitting procedure is shown in Figure 3.20. The best fitting is achieved by selecting the proper parameter respecting the lowest MSE possible and the limitations applied (see table 3.1).

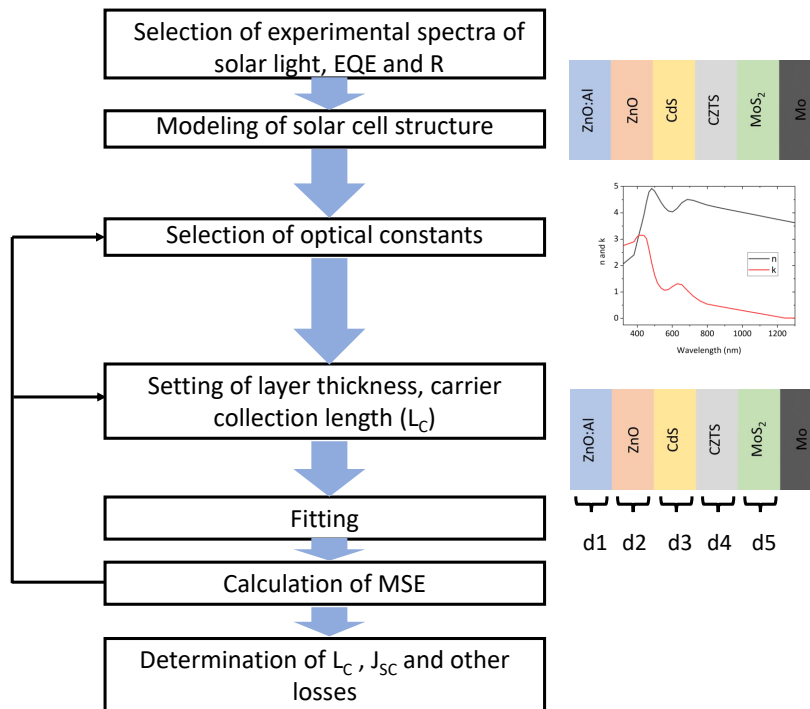


**Figure 3.20:** Flow-chart of the fitting procedure of the e-ARC simulation process.

### 3.3. Device characterization techniques

Device layer	Limit of thickness (nm)	Source of optical constants
ZnO:Al	400±50	Experimental
ZnO	60±20	Experimental
CdS	60±20	Hara et al, [63]
CZTS	Experimental (SEM)	Li et al, [65]
MoS <sub>2</sub>	100±30	Yim et al, [64]
Mo	N/A	Hara et al, [63]

**Table 3.1:** The list of device layers showing the thickness limitations and the optical constants used during simulation.

The sensitivity analysis of each changeable parameter is done and shown in the appendix.

# 4 Development of CZTSe and CZTS absorber

## Contents

---

<b>4.1 State of the art</b> . . . . .	<b>54</b>
4.1.1 CZTSe . . . . .	54
4.1.2 CZTS . . . . .	55
<b>4.2 CZTSe synthesis process</b> . . . . .	<b>56</b>
4.2.1 Selenization . . . . .	56
4.2.2 Optimization of the micro-structure . . . . .	57
4.2.3 Electrical properties of CZTSe . . . . .	67
4.2.4 Formation mechanism of CZTSe . . . . .	71
<b>4.3 CZTS synthesis process</b> . . . . .	<b>75</b>
4.3.1 Sulfurization . . . . .	75
4.3.2 Effect of annealing temperature . . . . .	77
4.3.3 Effect of sulfur vapor pressure . . . . .	78
4.3.4 Device properties . . . . .	80
4.3.5 Formation mechanism of CZTS . . . . .	83
<b>4.4 Conclusion</b> . . . . .	<b>88</b>

---

The baseline process of synthesizing pure Se based kesterite absorber ( $\text{Cu}_2\text{ZnSnSe}_4$  (CZTSe)) and pure sulfur based Kesterite absorber ( $\text{Cu}_2\text{ZnSnS}_4$  (CZTS)) will be discussed in this chapter. Additionally, the systematic optimization of the annealing procedure along with the material and optoelectrical properties will be discussed. A set of ex-situ characterizations will be also analyzed to determine the reaction mechanism of CZTS and CZTSe absorber synthesis.

## 4.1 State of the art

### 4.1.1 CZTSe

The potentiality of kesterite as a suitable absorber for photovoltaic devices was first demonstrated as early as 1988 [66]. However, pure Se based CZTSe synthesized by sputtering based precursor did not spark interest until 2009. Since then, the PCE of pure CZTSe grew quite fast and the most recent PCE record of CZTSe solar cell device is 11.6% by co-evaporation [67]. Figure 4.1 illustrates the highest PCE of CZTSe absorbers achieved by different methods over the years. Although the best efficiency of 11.6% was achieved by co-evaporation [67], the sputtering based process recently reached PCE of 11.4% [68]. Using a thin Ge layer during sputtering based synthesis of CZTSe enhanced this result with a PCE of 11.8% PCE [39], which is the highest one for CZTSe.

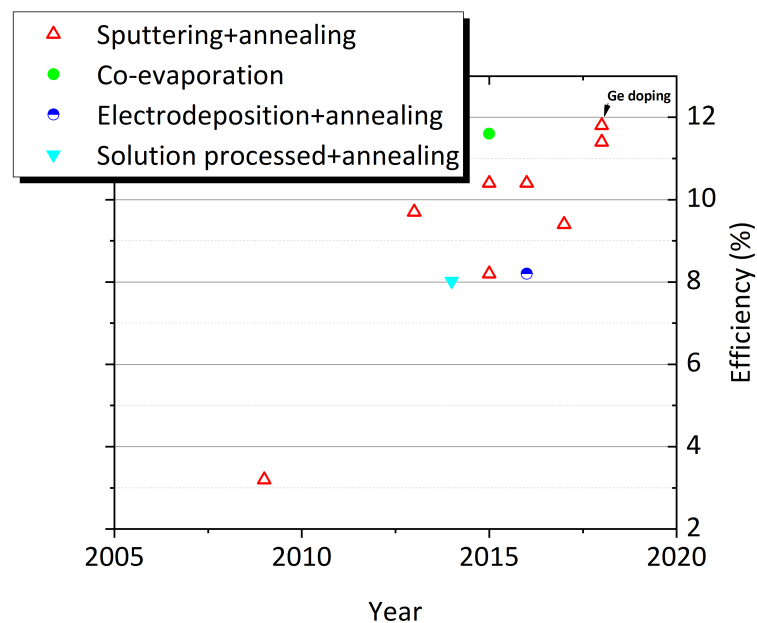


**Figure 4.1:** The PCE evolution of CZTSe devices using a sputtering technique along with the highest efficiency achieved by other methods.

Additional information on the PCE evolution of CZTSe solar cell devices is shown in table 4.1.

## Chapter 4. Development of CZTSe and CZTS absorber

**Table 4.1:** Details on synthesis process and optoelectronic properties of the work shown in figure 4.1.

Precursor deposition	Precursor stack order	Selenium usage mode	Annealing type	Voc [mV]	Jsc [mA/cm <sup>2</sup> ]	FF [%]	PCE [%]	Year
Sputtering	Multi-layer	Se pellet	One step	359	20.7	43.0	3.2	2009 [69]
Sputtering	Mo/Cu <sub>10</sub> Sn <sub>90</sub> /Zn/Cu	H <sub>2</sub> Se	One step	408	38.9	61.4	9.7	2013 [70]
Sputtering	Mo/Cu/Sn/Cu/Zn	Se pellet+Sn	Two step	392	32.4	62.1	8.2	2015 [71]
Sputtering	Mo/Cu <sub>10</sub> Sn <sub>90</sub> /Zn/Cu	H <sub>2</sub> Se	One step	395	39.7	66.2	10.4	2015 [72]
Sputtering	Mo/Zn/Cu/Sn/Cu	Se vapor	Two step	419	38.5	64.8	10.4	2016 [73]
Co-sputtering	N/A	Se cap+Se pellet	One step	440	34.0	63.0	9.4	2017 [74]
Sputtering	Mo/Zn/CuSn/Zn	No information	Single step	443	38.1	68.0	11.4	2018 [68]
Sputtering	Mo/Cu/Sn/Cu/Zn/Ge	Se pellet+Sn	Two step	463	38.3	66.3	11.8	2018 [39]
Electro-deposition	Mo/Cu/Sn/Zn	Se pellet+Sn	Two step	440	31.3	60.0	8.2	2016 [75]
Co-evaporation	N/A	No information	Two step	423	40.6	67.3	11.6	2015 [67]
Solution processed	N/A	Se pellet	One step	408	33.4	58.8	8.0	2015 [76]

### 4.1.2 CZTS

The research on kesterite first started with CZTS. The first known working solar cell was made by Katagiri et al. in 1997 [77], and achieved an efficiency of 0.66% by sequential process. Further improvements were made during the following years and the record PCE of 11% was achieved recently by a CZTS solar cell device using a co-sputtering process [78]. CZTS absorber is drawing a lot of attention recently as a research topic for two main reasons: First, sulfur is a much more abundant material compared to selenium and second, CZTS absorbers have large band-gap (> 1.5 eV [79]), which can be used in tandem solar devices with lower band-gap material [80]. Similar to the PCE evolution of CZTSe, CZTS also achieved high PCE using sputtering based precursors (figure 4.2).

Table 4.2 adds complementary information on the work showed in figure 4.2. Here, the best efficiencies are achieved using a compound precursor. Also, most of the highest PCEs are achieved by using H<sub>2</sub>S as a sulfur source. However, closed reactors are used for most of the best efficiency devices, in order to use H<sub>2</sub>S safely. This procedure can be complicated to apply to industrial production. Therefore using an open reactor along with elemental S for CZTS fabrication can be beneficial for transferring the process to industry. However, few works were done using an open reactor with elemental S to synthesize CZTS based absorber [81].

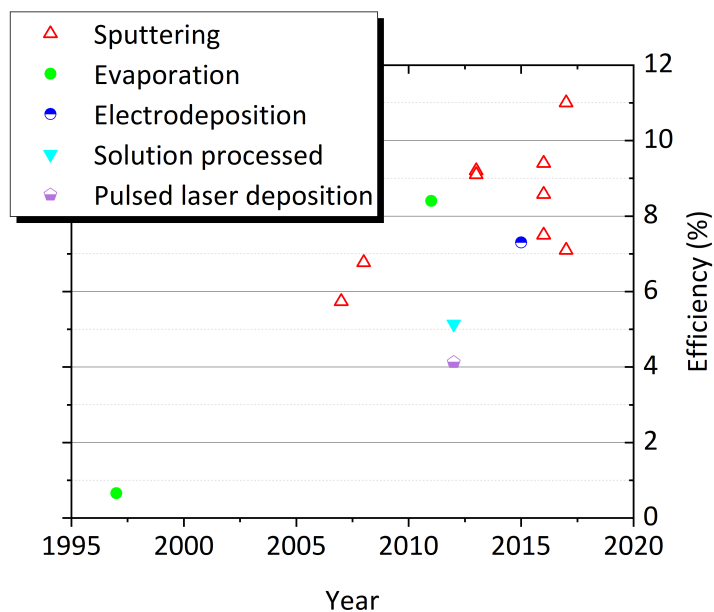


**Figure 4.2:** Evolution of CZTS solar cell devices in terms of PCE using sputtering technique along with the highest efficiency achieved by different method.

**Table 4.2:** Details on synthesis process and device properties of the work shown in figure 4.2.

Precursor deposition	Precursor stack order	Sulfur usage mode	Annealing type	Voc [mV]	Jsc [mA/cm <sup>2</sup> ]	FF [%]	PCE [%]	Year
Evaporation	Mo/Cu/Sn/Zn	H <sub>2</sub> S	One step	400	6.0	27.7	0.7	1997 [77]
Sputtering	Mo/ZnS/SnS/Cu	H <sub>2</sub> S	One step	662	15.7	55.0	5.7	2007 [82]
Co-sputtering	N/A	H <sub>2</sub> S	One step	610	17.9	62.0	6.8	2008 [83]
Sputtering	No information	H <sub>2</sub> S	No information	708	21.6	60.1	9.2	2013 [48]
Sputtering	Mo/ZnS/Sn/Cu/ZnS	H <sub>2</sub> S	One step	700	20.6	62.5	9.1	2013 [84]
Sputtering	Mo/CZTS/Cu/Sn/ZnS	H <sub>2</sub> S	Two step	700	21.3	63.0	9.4	2016 [85]
Sputtering	Mo/ZnS/SnS/Cu	Elemental S	One step	632	19.3	61.6	7.5	2016 [86]
Sputtering	Mo/ZnS/SnS <sub>2</sub> /Cu	H <sub>2</sub> S	Two step	625	21.1	65.1	8.6	2016 [87]
Co-sputtering	N/A	elemental S	One step	783	14.1	63.2	7.1	2017 [88]
Co-sputtering	Not applicable	S	One step	731	21.7	69.3	11.0	2017 [78]
PLD	No information	H <sub>2</sub> S	One step	700	10.0	59.0	4.1	2012 [89]
Solution processed	No information	H <sub>2</sub> S	One step	517	18.9	52.8	5.1	2012 [90]
Electrodeposition	CuZn/CuSn	elemental S	Two step	567	22.0	58.1	7.3	2015 [91]

## 4.2 CZTSe synthesis process

### 4.2.1 Selenization

To synthesize CZTSe absorber, metallic precursors (Cu, Zn and Sn) are deposited on a SLG substrate and transferred to a selenization reactor for annealing. At the beginning of the study,

the temperature profile used during annealing is a single step (570°C for 30 minutes with 60°C/minute ramp under 850 mbar of Ar pressure), followed by a natural cooling. Figure 4.3(a) is showing this single step temperature profile.

Later, a double step annealing profile is used to optimize the annealing (see figure 4.3(b)). The double step annealing procedure consists of: a first step under low pressure (1 mbar) at 320°C for 20 minutes with a 1°C/s ramp and a second step under nearly atmospheric pressure (850 mbar) at 520°C and 1°C/s ramp. In figure 4.3(b), at 305°C the temperature ramp is slowed down, to reduce the mismatch between the temperature programmed and the temperature achieved at the end of the ramp. Natural cooling is used at the end of annealing.

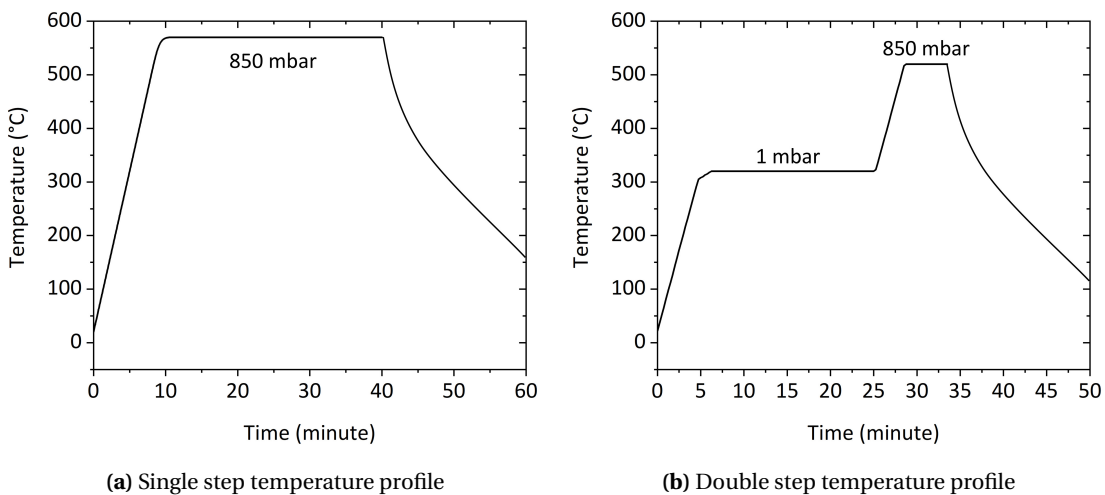


**Figure 4.3:** Temperature profiles used for selenization.

The following sections describe the optimization of CZTSe absorber and the reaction mechanism for the optimized process.

### 4.2.2 Optimization of the micro-structure

The objective of this section is to describe the synthesis process to achieve a CZTSe sample with big grains and a pinhole free surface with reduced roughness. At the beginning of the process development, the effect of the cation composition on the micro-structural properties of the final absorber is analyzed. Later, an optimized cation composition is selected to further optimize the microstructure using different selenization conditions.

### 4.2.2.1 Influence of cation composition

The samples are prepared with different compositions to assess the effect of stoichiometry on microstructural and material properties using a semi-open susceptor and one step annealing profile (figure 4.3(a)). The cation compositions of all these samples are shown on the ternary diagram (figure 4.4). Amongst them five samples are selected for further analysis and the cation compositions of those five samples are shown by big circles on the ternary diagram.

**SEM cross-section** image of these selected samples is shown in figure 4.4. Here, Cu-rich sample shows comparatively big grains, as observed in [92]. On the other hand, Cu-poor sample also showed big grains but smoother surface than Cu-rich growth. These big grains during Cu-poor growth are the result of Cu-Se phase forming relatively early in the selenization process, thus facilitate the grain growth.

Zn-poor/Sn-rich sample shows improved average grain size, a similar effect was observed by Malerba et al. [79]. In contrast, Zn-rich/Sn-poor growth showed smaller grain size, which can be attributed to the lack of Sn content. Finally, near stoichiometric absorber showed a moderate grain size with much smooth morphology compared to the Zn-rich/Sn-poor sample.

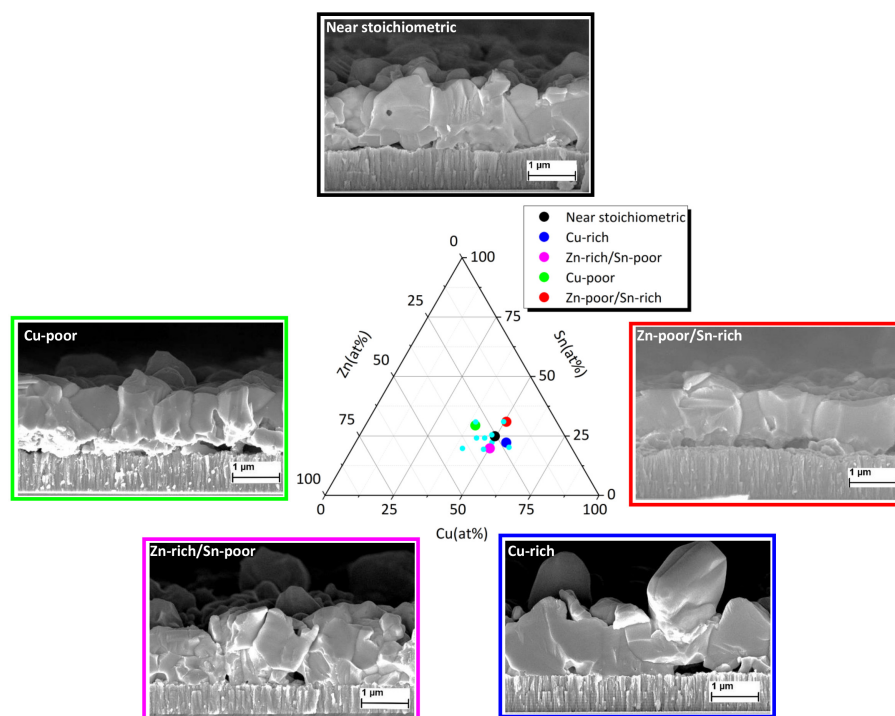


**Figure 4.4:** Effects of the cation composition on the micro-structural properties of a CZTSe based absorber : The ternary diagram in the middle shows the cation composition of different CZTSe absorbers. The big circles with different colors indicate the cation compositions of the sample related to the SEM cross-section images shown around the ternary diagram.

The **XRD analysis** on these five samples shows different secondary phases, depending on the composition (see figure 4.5). First of all, the near stoichiometric ( $[Cu]/[Zn+Sn]=0.98$ ,  $[Zn]/[Sn]=1.03$ ) sample does not show any obvious secondary phases that can be detected by XRD. Secondly, the Cu-rich ( $[Cu]/[Zn+Sn]=1.2$ ,  $[Zn]/[Sn]=1.03$ ) absorber shows peaks of Cu-Se ( $Cu_2Se$ ) secondary phase at  $26.2^\circ$ ,  $44.8^\circ$  and  $53.1^\circ$  with weak intensity (shown in the top-right corner of figure 4.5). It has been pointed out by Redinger et al. [55] that during Cu-rich growth of CZTSe by co-evaporation, Cu-Se secondary phase remains on the surface which can be detected accurately using grazing incident XRD. Therefore, for the experimental Cu-rich absorber, due to the smaller presence of Cu-Se secondary phase in the bulk, the detection is weak using XRD. The Zn-rich/Sn-poor ( $[Cu]/[Zn+Sn]=1.01$ ,  $[Zn]/[Sn]=1.52$ ) sample also showed similar Cu-Se secondary phase, a consequence of Cu being present in excess compared to Sn ( $Cu/Sn=2.6$ ). Therefore, the value of Cu in respect to Sn ( $Cu/Sn$  ratio) is important to understand the situation of the absorber stoichiometry.

Moreover, the Zn-poor/Sn-rich ( $[Cu]/[Zn+Sn]=1.03$ ,  $[Zn]/[Sn]=0.6$ ) sample shows a Sn-Se secondary phase, as well as the Cu-poor ( $[Cu]/[Zn+Sn]=0.67$ ,  $[Zn]/[Sn]=1.04$ ) sample due

to the presence of excess Sn. The main XRD peaks related to Sn-Se secondary phase are at  $14.43^\circ$  (SnSe<sub>2</sub>) and  $31.15^\circ$  (SnSe) [93], and can be seen for the Zn-poor/Sn-rich and the Cu-poor samples in figure 4.5. Here, the Cu-poor sample only showed a SnSe secondary phase, while the Zn-poor/Sn-rich sample showed both SnSe and SnSe<sub>2</sub> secondary phases. In case of a Sn excess, SnSe<sub>2</sub> is formed first and then decomposed into SnSe at high temperature [93]. Thus, if the amount of Sn is high enough, both phases can be detected.

Finally, the FWHM of CZTSe peak (112) is also shown for all samples (see bottom right corner of figure 4.5). Here, the Cu-rich sample has the lowest FWHM, indicating improved crystalline quality, while the Zn-rich/Sn-poor sample has the highest FWHM.

This preliminary study on stoichiometry leads to some criteria for the current work. Cu-rich sample showed pinholes detrimental for device performance due to a high degree of roughness. The presence of Cu-Se phase is also detrimental for the final device [92, 94]. Therefore, the Cu-rich condition will not be considered as a viable condition for improved micro-structure growth of CZTSe absorber. The Zn-rich/Sn poor sample showed the highest FWHM and the worst micro-structural properties, while the Zn-poor/Sn-rich sample showed better micro-structural properties along with Sn-Se secondary phases, which is detrimental for device properties [95]. Thus, Cu-poor and slightly Zn-rich composition is considered optimum towards improving micro-structural properties, with no or minimum Cu or Sn-based secondary phases. This choice is consistent with previously published results [96], showing that Cu-poor and Zn-rich samples give the best efficiencies.

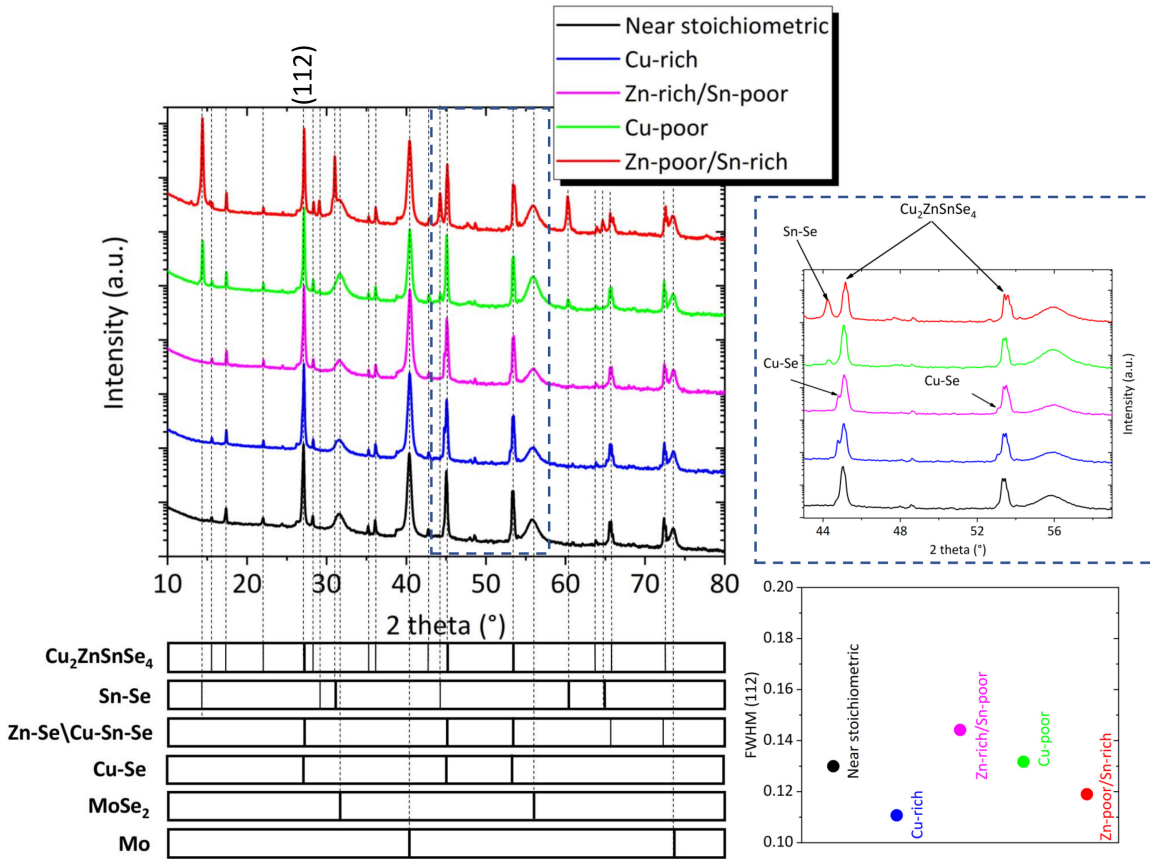


**Figure 4.5:** XRD diffractogram of a sample synthesized with different cation compositions. The top right corner is showing the enlarged view of the XRD diffractogram (43° to 59°). The bottom right corner is showing the FWHM of the peak (112).

Finally, a sample is fabricated maintaining the Cu-poor and Zn-rich cation composition, which will be called Sample A. For all the analyses in this work, the same cation composition of precursor as sample A has been used for synthesis of other CZTSe absorber. An XRD of sample A (figure 4.6) shows all the peaks of CZTSe with no peaks of Sn-Se or Cu-Se secondary phases. Also, the SEM surface and cross-section images show a grain size smaller than 500 nm and an irregular surface (see figure 4.6). Macro inhomogeneities, detrimental for the final device properties [74], are observed on the surface of the sample (not shown here). These macro inhomogeneity can be related to the fact that one pellet of 50mg Se is used on one side of the sample. Thus, the side near the pellet came in contact first with the Se vapor during annealing. To further improve the microstructural properties of the absorber, an optimization of the selenization condition is performed, as described in following section.

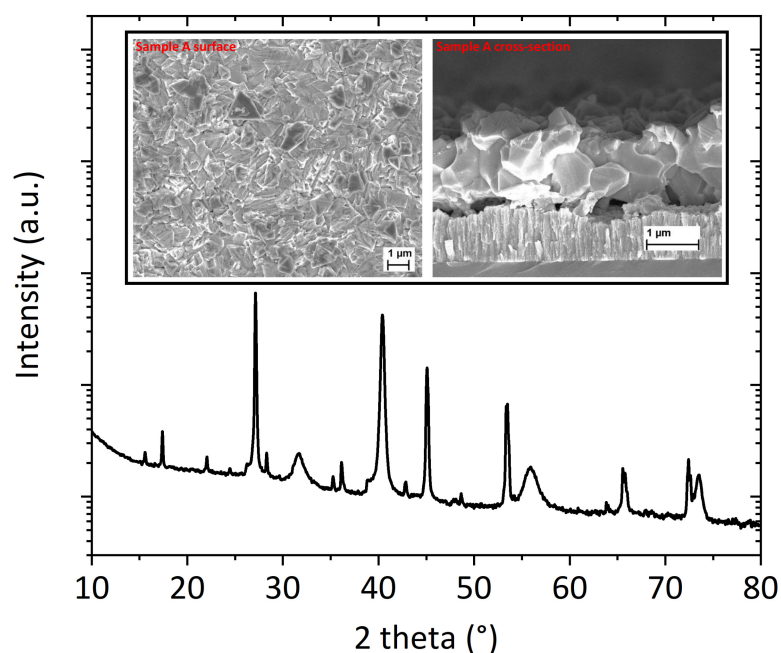


**Figure 4.6:** XRD diffractogram of sample A, along with the surface and cross-section SEM image in the inset.

#### 4.2.2.2 Influence of selenization condition

After optimizing the stoichiometry, we tried to optimize the selenization condition. These optimizations include- ways of introducing Se, temperature profile, susceptor and back contact. A complete list of all these optimizations is shown in table 4.3.

**Table 4.3:** List of different samples associated with different experiments for building the baseline process of a CZTSe based solar cell. Here, the cation ratio of the samples are measured by XRF from the synthesized absorber.

Sample name	Mo structure	Stack order	Selenium type	Graphite susceptor type	Annealing type	[Cu]/[Zn+Sn]	[Zn]/[Sn]
A	Single layer	Mo/Zn/Sn/Cu	50mg Se pellet	Semi-open	Single step	0.78	1.23
B	Single layer	Mo/Zn/Sn/Cu	Se cap+50 mg Se pellet	Semi-open	Single step	0.75	1.21
C	Single layer	Mo/Zn/Sn/Cu	Se cap+50mg Se pellet	Semi-open	Double step	0.74	1.18
D	Single layer	Mo/Cu/Sn/Cu/Zn	Se cap+50 mg Se pellet	Semi-open	Double step	0.73	1.17
E	Single layer	Mo/Cu/Sn/Cu/Zn	Se cap+50 mg Se pellet	Closed	Double step	0.75	1.12
F	Three layer	Mo/Cu/Sn/Cu/Zn	Se cap+50 mg Se pellet	Closed	Double step	0.74	1.08
F(etch)	Three layer	Mo/Cu/Sn/Cu/Zn	Se cap+50 mg Se pellet	Closed	Double step	0.75	1.07

After each optimization, we carefully observed the material properties of the absorber using SEM and XRD followed by accessing the PV properties to choose the best possible annealing condition in terms of- grain size, pin-hole free surface, homogeneity, MoSe<sub>2</sub> growth and PCE

(which is one of the consequence of the improved microstructural properties).

To reduce the effect of macro inhomogeneities, a 300nm Se capping layer has been deposited by evaporation on top of the precursor prior to annealing (see table 4.3) to create sample B. The absorber synthesized this way showed better macro homogeneity. However, an observation using SEM (figure 4.7 (a) and (d)), shows an irregular grain size (Variable grain size with bigger than  $1 \mu$  max.) and a rough surface with pinholes. Moreover, a significant amount of void and  $\text{MoSe}_2$  formation near the back contact can be observed (figure 4.7 (d)). Thus, longer annealing at higher temperature has two adverse effects on the absorber: First, high temperature and pressure (for this experiment 850 mbar Ar pressure was used) for a long time during annealing can promote the formation of a thicker  $\text{MoSe}_2$  layer [97]. Second, Se used during the reaction will diffuse away more at higher temperature and longer annealing duration. At the end of annealing the Se vapor pressure becomes low, resulting in Sn loss and void formation via decomposition of the absorber [26].

In other words, to have better crystallization higher temperature annealing is needed [98], which also has adverse effect on the absorber. This suggests relatively shorter duration, high temperature annealing. Therefore, a two-step annealing process (shown in 4.3(b)) has been adopted for sample C, from the work of Neuschitzer et al. [71]. During the two-step annealing, the first step consists of  $320^\circ\text{C}$  (for 20 min), to induce alloying and formation of a CZTSe phase, and the second step consists of  $520^\circ\text{C}$ (for 5 min), to induce crystallization. A better crystallinity and reduced  $\text{MoSe}_2$  can be seen from the cross-section SEM image of sample C in figure 4.7 (e). The pinholes and roughness are still present on the absorber surface (see figure 4.7 (b)). The Sn loss, however, compared to sample A has decreased, demonstrating the feasibility of a two-step annealing procedure. It also indicates that less Sn loss might be related to better morphology.

All the high-efficient sputtering based procedures have different precursor stack order, the one common feature being that Sn was never used as the top layer because of its volatility at high temperature [99]. Consequently, to decrease further Sn loss a different stack order is adopted: Mo/Cu/Sn/Cu/Zn similar to Neuschitzer et al. [71] for sample D. This stacking order was preferred for the following reasons [100]:

1. The first Cu layer improves the morphology of Sn layer, which can reduce the roughness of the final absorber;
2. Sn as a second layer can reduce the Sn loss during the annealing process;
3. Cu as a middle layer between Sn and Zn would increase the alloying between Sn by

forming bronze and Zn by forming brass;

4. Finally, Zn as a top layer could promote the Zn-Se secondary phases (due to using Zn-rich precursor) on the surface, which can be removed by an additional etching process after absorber synthesis.

The SEM cross-section of sample D shows a reduced roughness and a better morphology (see figure 4.7 (f)). A significant amount of pinhole reduction can be observed from the SEM surface image (4.7 (c)) compared to the previous samples. However, the voids near the Mo back contact similar to sample C and some of the pinholes are still present on the surface of sample D. It should also be noted that the cation ratio of the absorber in table 4.3, shows almost no difference between sample C and D.

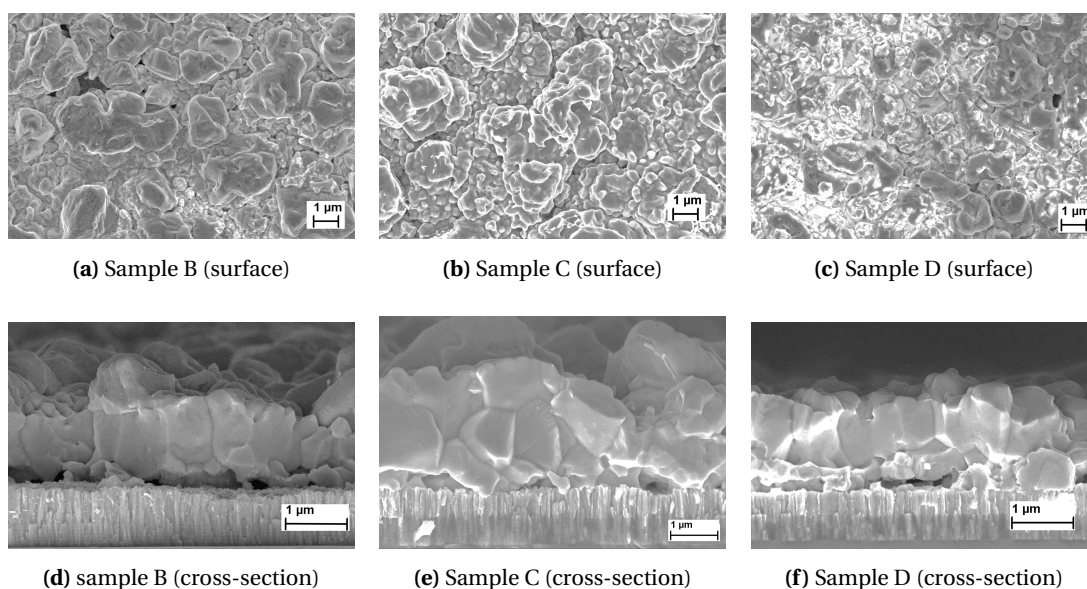


**Figure 4.7:** SEM image of samples using semi-open susceptor and different configurations (sample B- Selenium capping evaporated on precursor before annealing, sample C- Double step annealing procedure, sample D- different stack order of precursor).

Therefore, in an attempt to further improve the morphology of the absorber, a different susceptor is used, which is described in section 3.1.3.2 as a closed susceptor. Here, a limited amount of Se is used for each experiment and a significant amount of Se could escape by diffusion from the semi-open susceptor, therefore, a relatively closed susceptor is thought to be a way to decrease the out-diffusion of Se. Thus, Sample E is prepared using a closed susceptor, while keeping the other parameter identical to the previous sample. Annealing inside a closed susceptor shows a pin-hole free surface morphology (figure 4.8 (a,b)). However, this sample shows much thicker  $\text{MoSe}_2$  (around 670nm) (figure 4.8 (c,d)), which can be detrimental to

## Chapter 4. Development of CZTSe and CZTS absorber

the electrical properties of the final device [26]. Nonetheless, the Sn loss is further reduced compared to the previous sample.

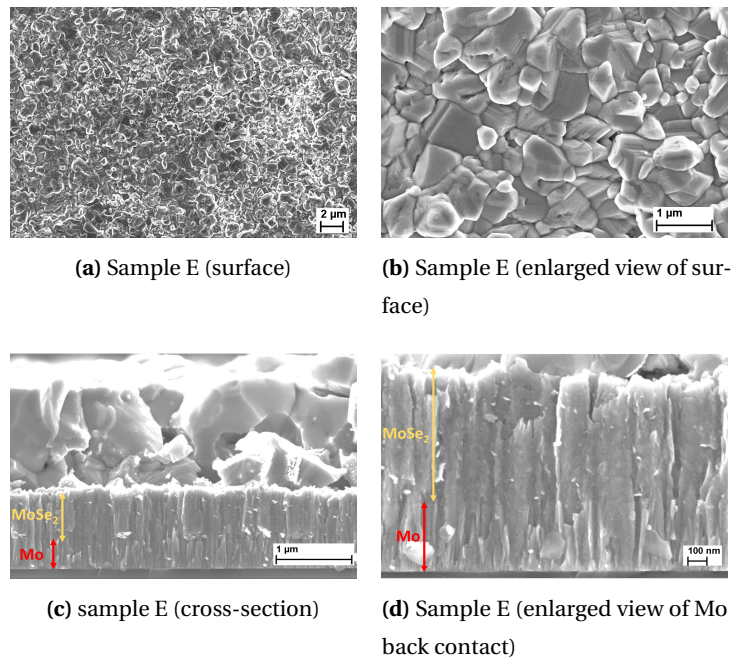


**Figure 4.8:** SEM image of the sample synthesized using closed susceptor.

To reduce the formation of MoSe<sub>2</sub>, a three-layer Mo back contact is used for sample F. Where the first layer is designed to ensure electrical conductivity, the second layer with low density to limit the formation of MoSe<sub>2</sub> and the third as a sacrificial layer. This three-layer Mo is described in section 3.1.2. The SEM surface and cross-section image of sample F (figure 4.9) show a significant improvement in the morphology. This absorber exhibits 1-2 μm big grains and less MoSe<sub>2</sub> compared to sample E.

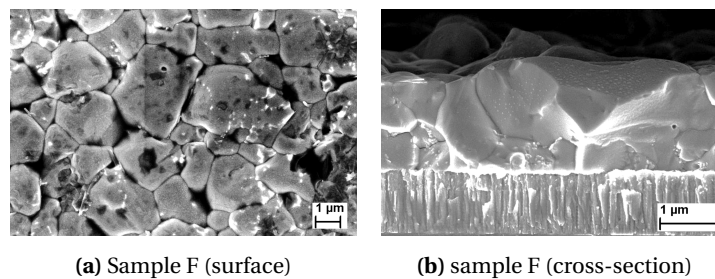


**Figure 4.9:** SEM image of the sample using three-layer Mo deposition as back contact during annealing.

A comparative GDOES depth profiling between sample D (synthesized by semi-open susceptor) and sample F (synthesized by closed susceptor) is shown in figure 4.10. At a first glance, all the cation profiles (Cu, Zn and Sn) show less variation throughout the absorber in the case of sample F compared to sample D. Furthermore, Zn shows an increase near the Mo back contact in the case of semi-open susceptor (sample D), while Zn shows a slight increase at the front surface for the closed susceptor. This is an indicator of the position of potential Zn-Se secondary phase in each case.

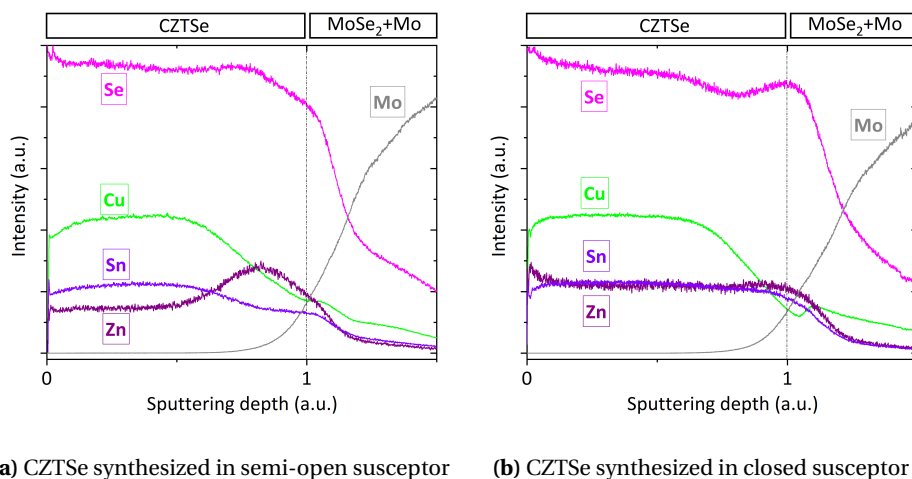


**Figure 4.10:** GDOES depth profiling of absorber synthesized in a semi-open susceptor (sample D) and closed susceptor (sample F), showing the material distribution along the depth of the absorber.

#### 4.2.2.3 Summary

The evolution and effect of the different synthesis processes have been discussed in terms of morphology and material properties. From the above discussion, some conclusions can be made:

1. A Cu-poor and Zn-rich cation composition is most favorable in terms of microstructural properties and formation of unwanted secondary phases;
2. The stack order is important for the absorber synthesis using elemental metal precursor, as Sn is a volatile metal and need to be placed at the bottom of the stacks.
3. It is highly important to ensure sufficient Se vapor pressure during annealing to reduce Sn loss and void formation in the CZTSe/Mo interface;

### 4.2.3 Electrical properties of CZTSe

The absorbers discussed in the previous section have been completed as solar cells by depositing the rest of the layers (Mo/CZTSe/CdS/ZnO:Al/Front grid) as described in chapter 3.

The light J-V parameters of all the samples are shown in figure 4.11. Here, the J-V parameter showed improvement with improved morphology. More specifically, there are two points where the PCE has almost doubled: one is during the use of two-step process instead of a one-step process and another is with the use of a closed susceptor and improved back contact.

Secondary phases such as ZnSe and SnSe at the absorber/buffer layer interface have been identified (in literature [95, 101]) to be one of the main reason for performance limitation. Their removal, therefore, is crucial for the final device performance. For this reason, HCl etching is used on a sample, prepared using the same recipe as for sample F, to remove the ZnSe secondary phase as shown by Fairbrother et al [102]. Using selective etching of Zn-Se, sample G shows an improved 7.6% efficiency.

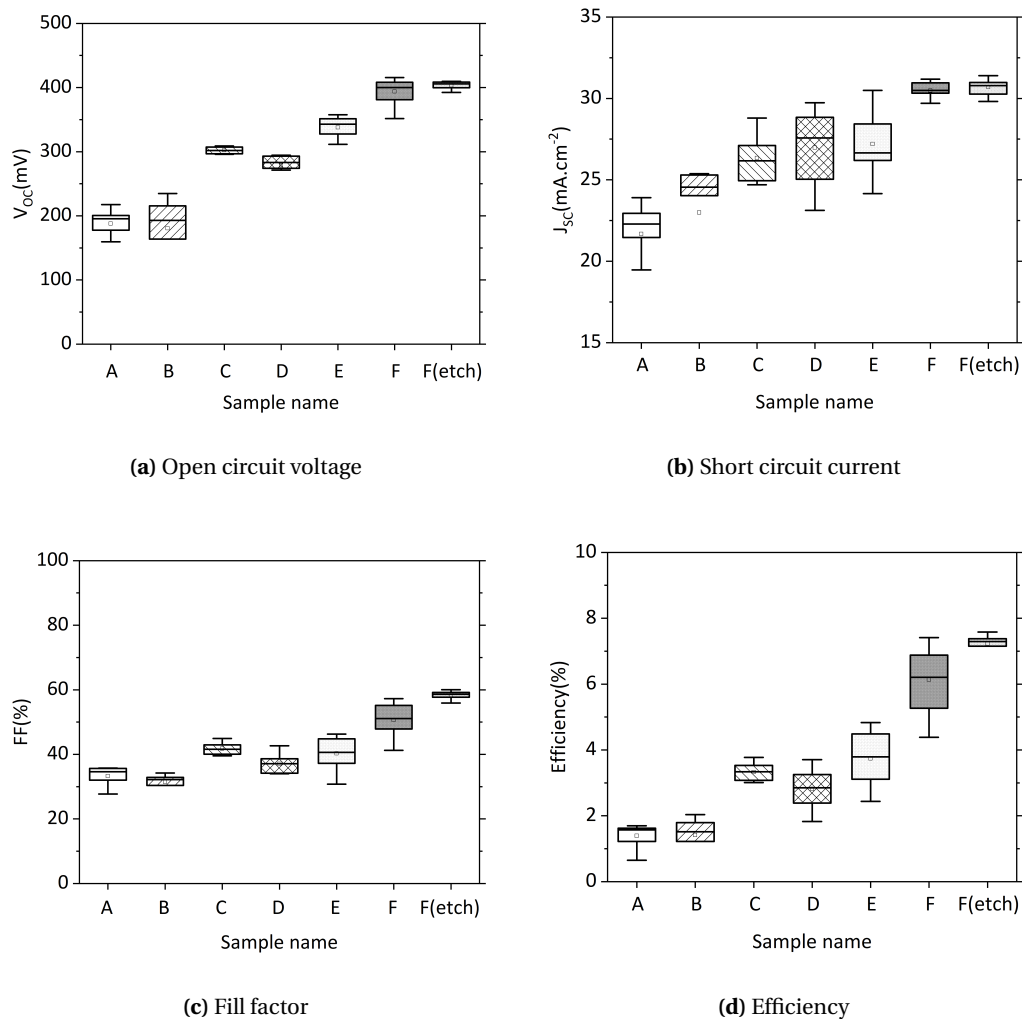


**Figure 4.11:** Light J-V parameters of all the samples prepared with different methods described in table 4.3 under 1.5G illumination condition.

The dark J-V parameters of all the samples are shown in figure 4.12. An evolution in the improvement can be seen from this characterization, very similar to those already observed with the light J-V parameter. Here, sample A and B are suffering from low shunt resistance and high series resistance, induced by bad crystallization resulting in pinholes and a thick  $\text{MoSe}_2$  formation. However, the highest series resistance was obtained with sample E, due to the highest thickness of its  $\text{MoSe}_2$  layer. In the case of sample F, series resistance decreases significantly by using three-layer Mo back contact as a result of the reduced  $\text{MoSe}_2$  thickness. An additional decrease in  $R_S$  and a significant increase in  $R_{Sh}$  are obtained with the HCl etching process, where the final absorber (sample F(etich)) shows a higher decrease in series resistance

compared to the non etched sample (sample F).

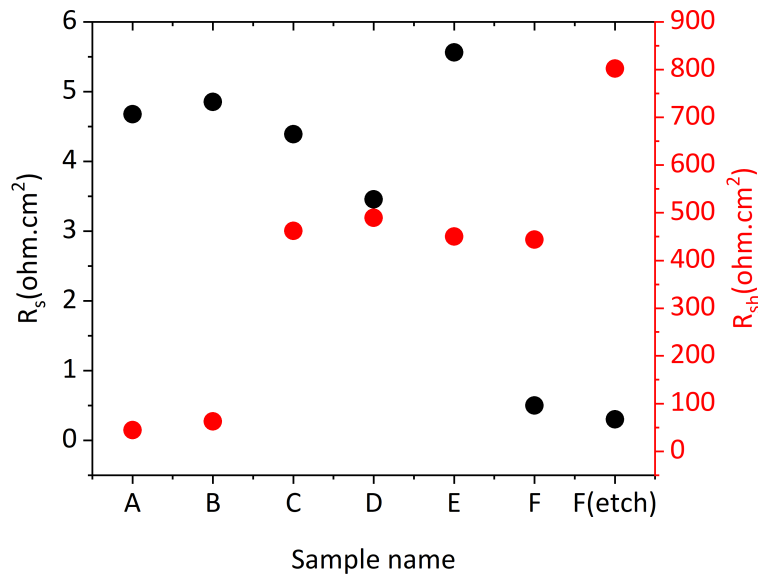
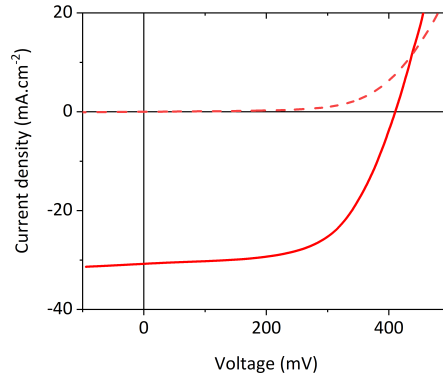
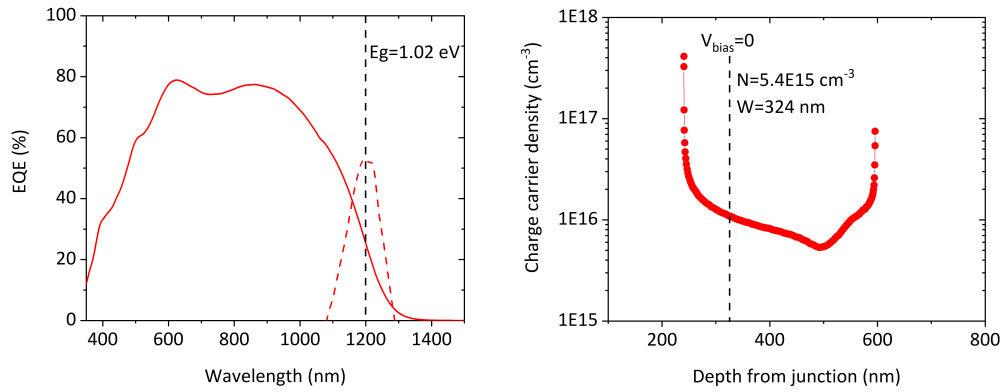


**Figure 4.12:** Dark J-V parameters ( $R_s$  and  $R_{sh}$ ) of all the samples prepared with different methods described in table 4.3.

The optoelectronic properties (dark and light J-V, EQE and C-V) of the best CZTSe device from this work are illustrated in figure 4.13. The parameters extracted from dark and light J-V are shown in table 4.4, which indicates  $V_{OC}$  of 410 mV and a maximum PCE of 7.6%. The EQE in figure 4.13 (b) indicates a band-gap of 1.02 eV, deducted from the maximum of the derivative of the EQE spectrum. The maximum EQE is found to be around 80%, which indicates that room for optimization is still present, particularly by reducing reflection using an anti-reflection coating such as  $MgF_2$  (not tested in this thesis). The apparent carrier concentration is  $5.4E15 \text{ cm}^{-3}$ , with a depletion region width ( $W$ ) of 324 nm (at 0 V bias), calculated from room temperature C-V measurement.



(a) Light and dark J-V curve of the best sample (sample F(etch))



(b) EQE response of best sample (sample F(etch)) (c) Apparent carrier concentration vs SCR width of best sample (sample F(etch))

**Figure 4.13:** Optoelectronic properties of the best CZTSe sample in this work. Light J-V (measured under AM 1.5G illumination) (solid line) and dark J-V (dashed line)(a) EQE reveals a band-gap of 1.02 eV derived from maximum of the derivative of EQE spectra (b) and apparent carrier concentration derived from room temperature C-V measurement(c).

**Table 4.4:** All electrical parameters of best CZTSe sample synthesized during this work.

Light J-V				Dark J-V		C-V		EQE		
$V_{OC}$ (mV)	$J_{SC}$ (mA.cm <sup>-2</sup> )	FF (%)	Efficiency (%)	$R_S$ (ohm.cm <sup>2</sup> )	$R_{Sh}$ (ohm.cm <sup>2</sup> )	$N_{C-V}$ (cm <sup>-3</sup> )	W (nm)	$J_{SC}(EQE)$ (mA.cm <sup>-2</sup> )	$E_g$ (eV)	$V_{OC}$ deficit (mV)
410	31.0	60	7.6	0.4	802	5.4E15	324	31.8	1.02	610

In conclusion, the highest efficiency of 7.5% is achieved by CZTSe based solar device from this work. A record PCE of 9.4% [103] has been achieved using additional etching and post-deposition annealing process along with the procedure described above. As this is out of the

scope of this thesis, it will not be further discussed.

### 4.2.4 Formation mechanism of CZTSe

An ex-situ characterization process has been performed on the selenization process to understand the formation mechanism of CZTSe. Figure 4.14 shows the temperature profile and the different temperatures where the process is stopped for the ex-situ experiments (blue points), covering the full temperature and time range for the selenization procedure.

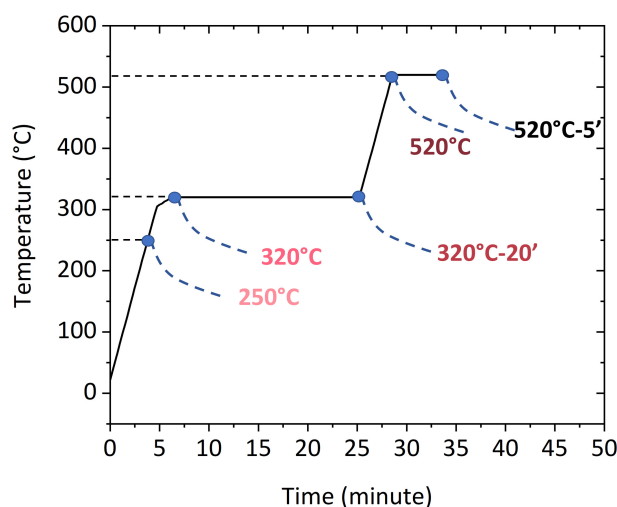


**Figure 4.14:** Temperature profile with the different points where the annealing was stopped for ex-situ characterization to determine the formation mechanism of CZTSe absorber.

In order to investigate the formation mechanism, an XRD analysis has been performed on all the samples at different temperatures points (see figure 4.15). At 250°C, formation of bronzes (Cu-Sn alloy), brasses (Cu-Zn alloy) and ZnSe is detected. It was already mentioned earlier that the main peaks of CZTSe, ZnSe and  $\text{Cu}_2\text{SnSe}_3$  coincide at room temperature. While it impedes the discrimination between ZnSe and  $\text{Cu}_2\text{SnSe}_3$  secondary phases, the absence of peaks at lower  $2\theta$  for the tetragonal kesterite phase exclude the presence of the CZTSe phase. At 250°C, the peak at  $27.2^\circ$  and  $45.2^\circ$  are attributed to the ZnSe phase, since the formation temperature for CZTSe is higher than 250°C [104, 105]. During the plateau of 320°C, relatively weak CZTSe peaks at  $17.4^\circ$  and  $36.1^\circ$  can be detected, thus showing that CZTSe is formed at this temperature along with other secondary phases such as Cu-Se.

Sn-Se secondary phase can only be seen at 520°C from the XRD, but after a 5 minutes plateau, it can no longer be detected. Finally, Cu-Se, Zn-Se and Sn-Se phases completely reacts at the 520°C plateau and form a more stable CZTS phase. Carolin et al, [105] reached a similar

conclusion, stating that CZTSe start to form above 280°C and co-exist with other secondary phases. Also, to maximize the formation of CZTSe compared to those binary or ternary phases, temperature higher than 450°C is needed.

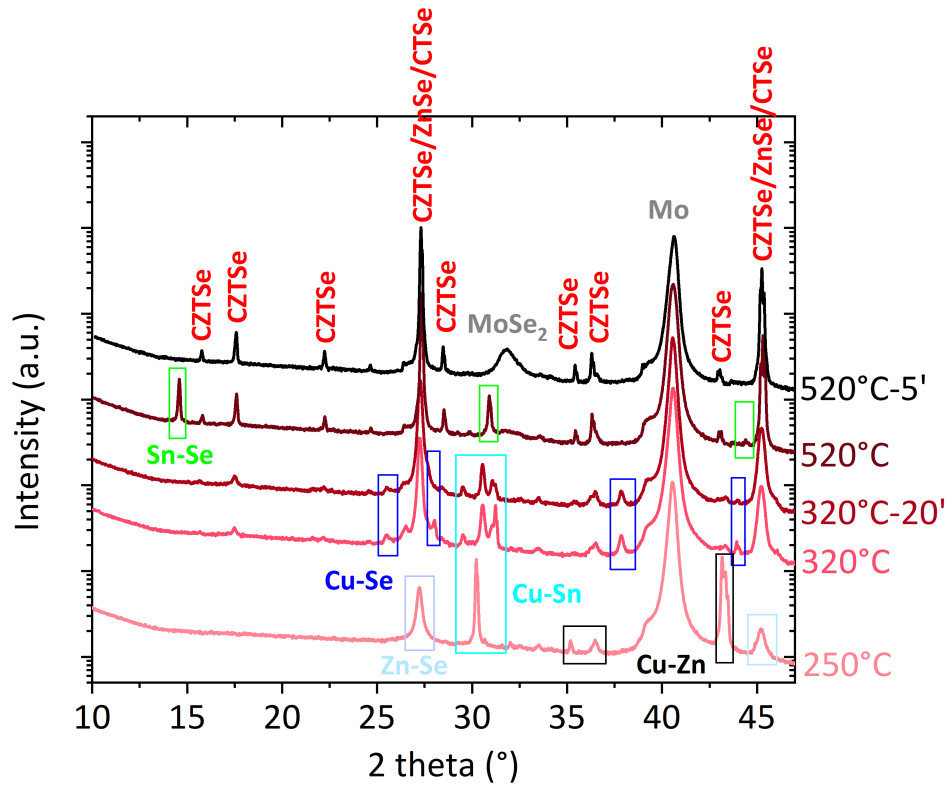


**Figure 4.15:** XRD diffractograms of samples at different annealing points of selenization as described in figure 4.14.

This conclusion is further confirmed by the Raman spectra of these samples (figure 4.16). Using green laser excitation for Raman spectra makes it difficult to detect ZnSe and  $\text{Cu}_2\text{SnSe}_3$  secondary phases [56]. Therefore, it is difficult to make a conclusion about the formation of ZnSe and CTSe. Nonetheless, the FWHM of CZTSe A mode peak is decreasing with increasing temperature, which indicates that the crystallization of the CZTSe phase improves at higher temperature. Also, Cu-Se secondary phase can not be detected at 320°C and 20 minutes plateau, although the XRD showed the presence of Cu-Se secondary phase at this stage of the process.

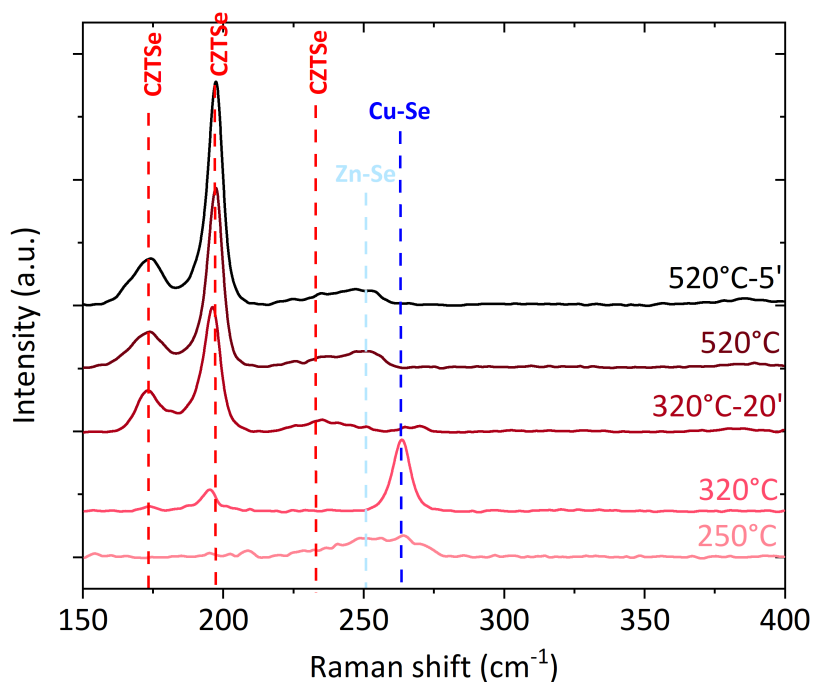


**Figure 4.16:** Raman spectra of different points during annealing described in figure 4.14, using 532 nm laser wavelength.

To investigate this point, SEM surface image of the sample at 320°C and after a 20 minutes plateau is shown in figure 4.17. The big grains on the surface of 320°C sample are identified as Cu-Se secondary phase by the EDX line scan (see figure 4.18). But, after a 20 min wait period at the same temperature, these big grains can not be seen on SEM image. This is the reason why the Cu-Se secondary phase for this sample was not detected by Raman spectroscopy, as this characterization is limited to the surface of the sample.

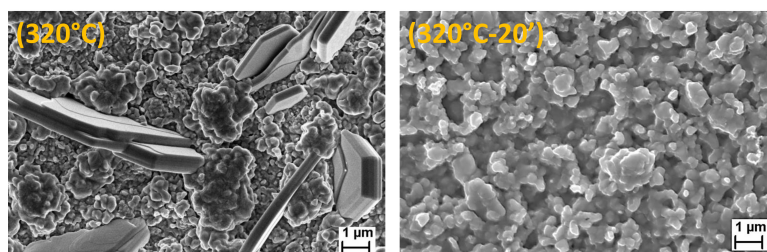


**Figure 4.17:** SEM surface of a sample annealed at 320°C before (left) and after (right) 20 minutes plateau.

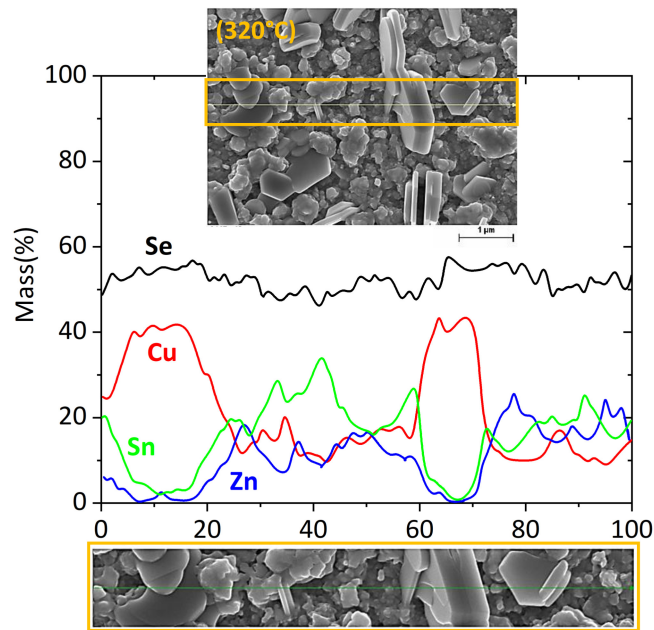


**Figure 4.18:** EDX line-scan performed on a sample annealed at 320°C before the 20 minutes plateau. Big grains on the surface can be clearly detected as Cu-Se secondary phase from the line scan.

SEM image of the sample surface annealed at 520°C is shown in figure 4.19. Two different zones with distinct crystal shape can be identified and are indicated as zone 1 and zone 2. By comparing the atomic concentration measured by EDX of both zones, Sn-Se secondary phase can be identified in zone 2. This also confirms the presence of the Sn-Se secondary phase at 520°C.

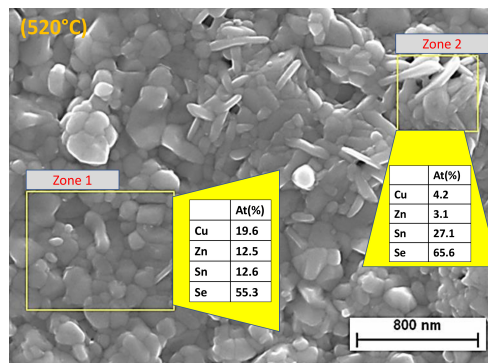


**Figure 4.19:** EDX analysis performed on the sample annealed at 520°C without wait time: Sn-Se secondary phase formation can be identified in zone 2 by comparing the cation composition achieved from zone 1.

Lastly, an EDX line-scan is performed on a finished absorber (see figure 4.20) and proved the presence of Zn-Se secondary phase near the surface. The Zn-Se secondary phase has a higher

bandgap than CZTSe and shows a bright contrast compared to CZTSe grains during SEM. This might be a way to effectively detect this phase by SEM imaging.

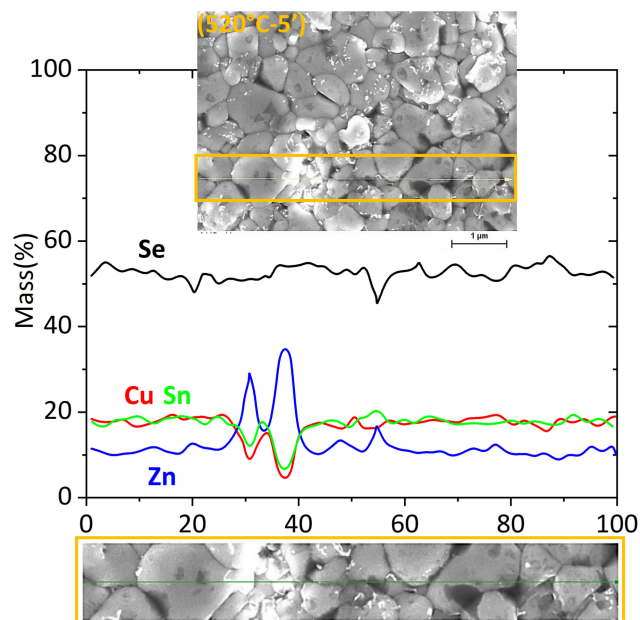


**Figure 4.20:** EDX line-scan on a finished CZTSe absorber.

**In summary**, the reaction path for the CZTSe synthesis shows the formation of a binary compound first prior to the formation of CZTSe compounds. However, Cu-Sn-Se phase was not identified due to lack of proper characterization.

Nonetheless, according to Hernandez-Martinez et al [56], the reaction pathway towards CZTSe using metallic precursor happens through binary compounds under low chalcogen pressure. As this is the case for our CZTSe synthesis, it can be concluded that the reaction pathway is following from the binary compounds to kesterite compound route.

### 4.3 CZTS synthesis process

#### 4.3.1 Sulfurization

CZTS absorber is fabricated by annealing the metallic precursor in a sulfurization reactor. The experimental sulfurization reactor is a two zone open reactor, that was described in section 3.1.3.2. During annealing, the sample zone used the ramp of 10°C/min, while the sulfur zone used the ramp of 20°C/min, followed by Natural cooling. However, the cooling rate of the sulfurization reactor is much slower compared to the selenization reactor. No

### 4.3. CZTS synthesis process

pressure controller is used during the annealing process, therefore pressure inside the chamber changed with the temperature evolution. Nonetheless, between two different runs of same recipe, the change of pressure are similar. A typical scenario of temperature in both zones and chamber pressure evolution as a function of time during the annealing are shown in figure 4.21. The amount of evaporated sulfur and sulfur vapor pressure during different sulfur zone temperatures is shown in table 4.5.

Temperature	Amount of evaporated S (mg)	S vapor pressure (mbar)
170°C	221±33	9E-3
200°C	565±47	3E-2
230°C	976±69	1E-1

**Table 4.5:** Amount of evaporated sulfur and sulfur vapor pressure at different sulfur zone temperature

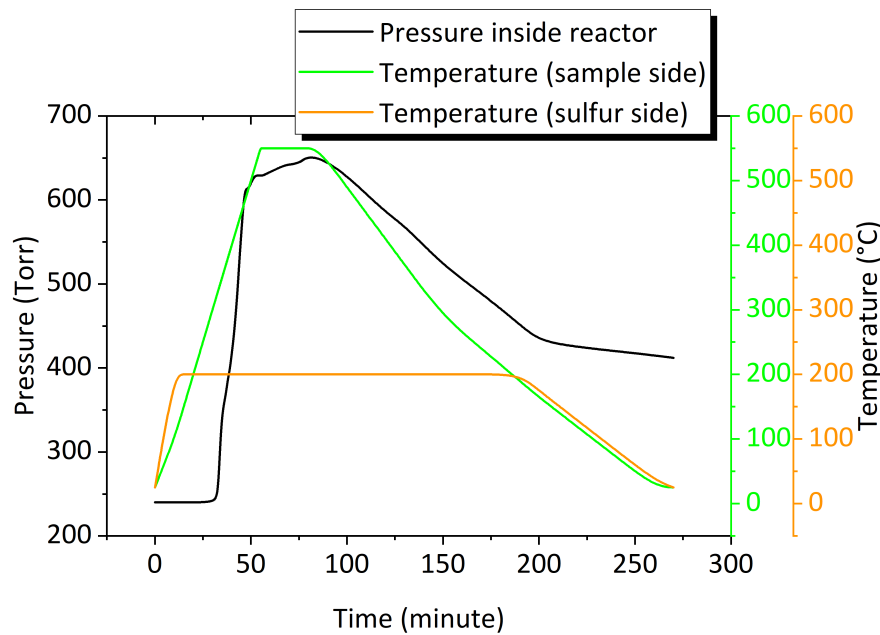


**Figure 4.21:** Pressure and temperature profile as a function of time during a typical sulfurization process.

Process optimization is performed by optimizing the temperature on both zone of the reactor. For this purpose, annealing temperature in the sample zone is varied from 520°C to 580°C, while keeping the sulfur zone temperature constant (200°C) for different samples. Later, the temperature of the sulfur zone is varied from 170°C to 230°C, while keeping the sample zone temperature constant for different runs. The experimental plan along with the cation composition of the associated absorber is shown in table 4.6.

## Chapter 4. Development of CZTSe and CZTS absorber

**Table 4.6:** List of different samples associated with different experiments for building baseline process of a CZTS based solar cell. Here, the cation ratio of the sample is measured by EDX from the synthesized absorber.

Experiment name	Sample name	Sample side temp.	Sulfur side temp.	[Cu]/[Zn+Sn]	[Zn]/[Sn]	[Cu]/[Sn]	[Zn]/[Cu+Sn]
A	CTZS <sub>520°C</sub>	520°C	200°C	0.72	1.15	1.55	0.45
	CTZS <sub>550°C</sub>	550°C	200°C	0.74	1.21	1.62	0.46
	CTZS <sub>580°C</sub>	580°C	200°C	0.75	1.28	1.72	0.47
B	S <sub>170°C</sub>	550°C	170°C	0.74	1.24	1.67	0.47
	S <sub>200°C</sub>	550°C	200°C	0.74	1.21	1.62	0.46
	S <sub>230°C</sub>	550°C	230°C	0.68	1.18	1.47	0.47

### 4.3.2 Effect of annealing temperature

To optimize the annealing temperature of the sulfurization process, three samples have been synthesized using three different temperatures (520°C, 550°C, 580°C) for sample zone. This set of experiments will be called experiment A in later sections.

Experiment A shows that the amount of Sn in the absorber decreases with increasing temperature (table 4.6). It has been attributed to an increased Sn loss during annealing with increased temperature. Indeed, it is well known that decomposition of CZTS can occur during thermal processing especially when low pressure and high temperature are used resulting in loss of S and SnS [99]. This decomposition mainly formulates by the relatively facile change of Sn(IV) to Sn(II) in a chalcogen environment, which is an underlying characteristic of Sn chemistry.

The SEM surface and cross-section images of these three samples are shown in figure 4.22. From this, several observations can be made:

1. Grain size and crystallization are improved with higher temperature;
2. More voids are present at the Mo/CZTS interface with increased temperature;
3. Pin-holes can be observed from the surface SEM of the sample synthesized with high temperature (580 °C).

Increasing annealing temperature leads to the formation of voids in the back absorber region due to the reaction between CZTS and Mo. This reaction forms MoS<sub>2</sub> along with other secondary phases, while evaporation of Sn-S based secondary phase occurs due to the aforementioned reason. This explanation is also supported by different works [26, 101].

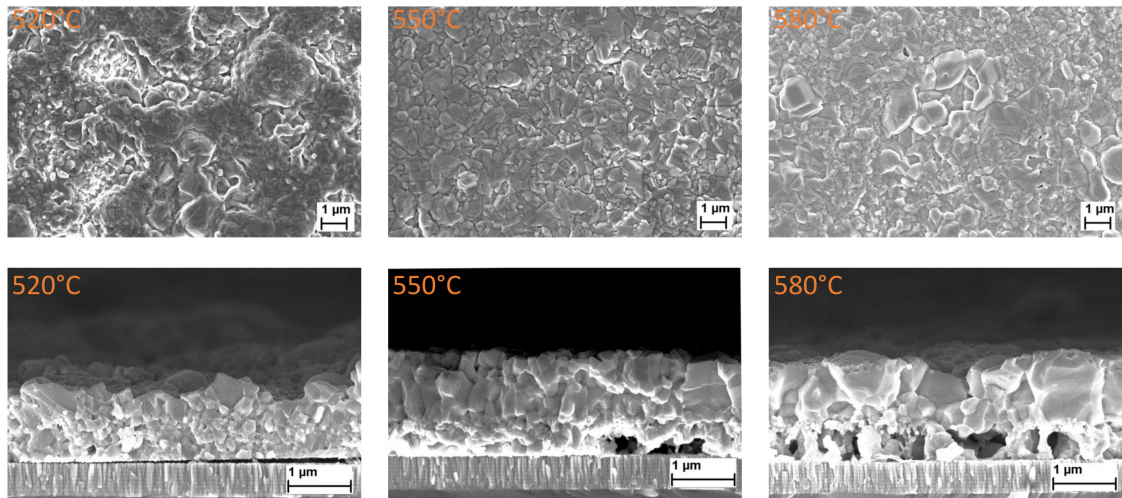


**Figure 4.22:** SEM representation of experiment A: surface (top left) and cross-section (bottom left) of sample CTZS<sub>520°C</sub> sulfurized under 520°C; surface (top middle) and cross-section (bottom middle) of sample CTZS<sub>550°C</sub> sulfurized under 550°C; surface (top right) and cross-section (bottom right) of sample CTZS<sub>580°C</sub> sulfurized under 580°C.

The XRD pattern of the three samples from experiment A are shown in figure 4.23. A SnS<sub>2</sub> based secondary phase can be detected for the sample prepared at 520°C but cannot be seen at higher temperatures. The presence of a SnS<sub>2</sub> secondary phase at this temperature only suggest that 520°C is not sufficient for CZTS absorber synthesis. Moreover, the FWHM of peak(112) as a function of temperature (the top left corner of figure 4.23) shows a decrease of FWHM with increased temperature, which indicates better crystallinity during high-temperature process.

#### 4.3.3 Effect of sulfur vapor pressure

Three samples are prepared with three different sulfur zone temperatures (170°C, 200°C and 230°C), which will provide higher amount of sulfur vapor pressure at higher annealing temperature (table 4.5). These experiments will be called experiment B, later in this section.

The first effect of the S zone temperature can be seen from table 4.6. Here, Sn content increases with increased sulfur zone temperature, meaning that Sn loss can be reduced with increased sulfur vapor pressure. This result is consistent with the results of Scragg et al, [99].

No noticeable difference can be observed from SEM image of these three samples, except the lower amount of void formation for higher temperature (230°C) (not shown here).

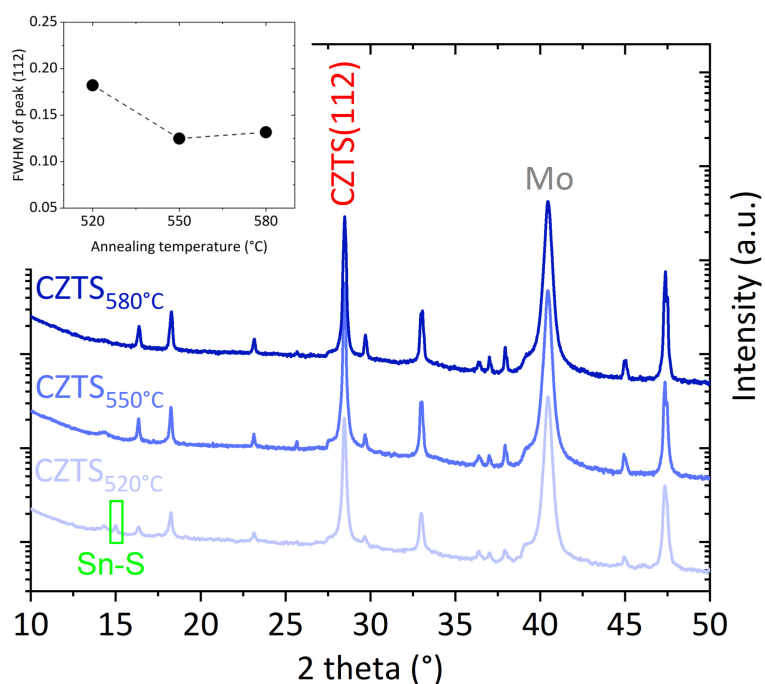


**Figure 4.23:** XRD representation of samples from experiment A: CZTS absorber prepared under three different temperatures to observe the effect of temperature on the material properties. In the inset, the FWHM of peak (112) is given as a function of temperature.

The XRD of these samples showed highly crystallized CZTS peaks with no peaks associated with Sn-S or Cu-S phase (see figure 4.24 (a)). No noticeable difference can be seen from the XRD of these samples.

In addition, the Raman spectra of all the samples associated with experiment B are shown in figure 4.24 (b). The sample synthesized with sulfur side temperature at 170°C shows a broadening of the 339  $\text{cm}^{-1}$  peak, as well as a large decrease in peak intensity at around 288  $\text{cm}^{-1}$ . Both effects have been attributed to a higher Cu/Zn disorder according to Scragg et al, [23], although, one must consider the effect of cation composition of the samples, which is directly related to the Cu/Zn-ordering as well. It can also affect the peak intensity and broadening of Raman spectrum [33]. For this experiment the sample annealed under the highest amount of sulfur pressure showed the lowest amount of Cu content, because of less Sn loss. Indeed, Cu poor condition during synthesis induces the ordering of Cu/Zn (001) planes by increasing the  $[V_{\text{Cu}}+\text{Zn}_{\text{Cu}}]$  cluster [34].

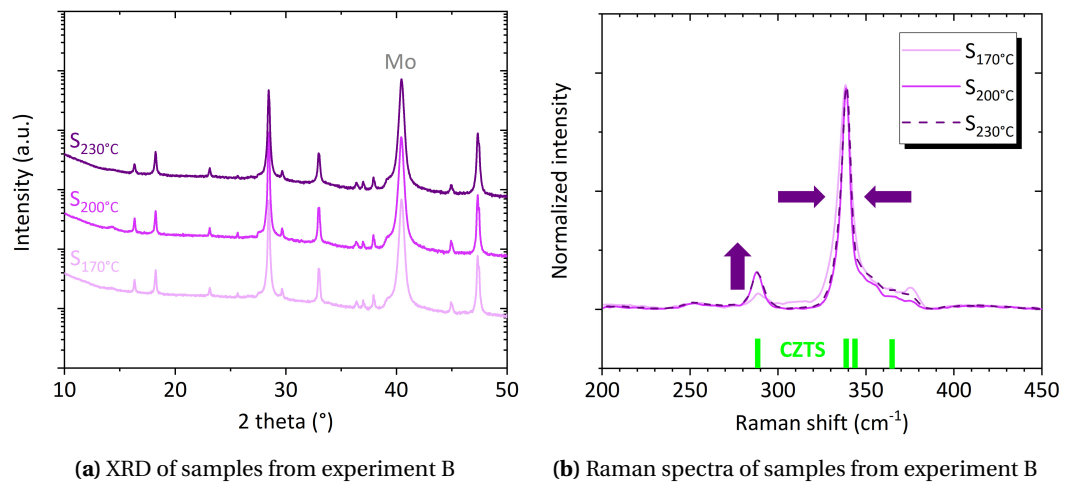


**Figure 4.24:** XRD and Raman spectra of samples from experiment B: XRD from different samples did not show any noticeable difference, but Raman spectrum showed lower intensity and peak broadening for lower sulfur vapor pressure.

#### 4.3.4 Device properties

The PV properties of the samples associated with experiment A and B measured under 1.5G illumination are shown in figure 4.25. The sample zone temperature of 550°C shows best PCE amongst all the samples from experiment A. Poor crystallization and Sn-S secondary phase is one of the reason for the lower PCE in the case of the CZTS<sub>520°C</sub> sample, due to the detrimental effect of the SnS<sub>2</sub> phase. Higher Sn loss and void formation near the back of the absorber is one of the reason for poor performance of the CZTS<sub>580°C</sub> sample, as has been confirmed by similar conclusions made in the literature [26,95].

During experiment B, sample S<sub>230°C</sub> showed the best performance in terms of  $V_{OC}$ ,  $J_{SC}$ , FF and efficiency. Conversely, sample S<sub>170°C</sub> did not work properly as a solar device.

The material and opto-electrical properties of sample S<sub>170°C</sub>, showed properties that can be related to the poor device properties, although it might not be the only reason. Recently, Kim et al. [106] pointed out that sulfur vacancy ( $V_S$ ) can facilitate non-radiative recombination, while lower sulfur pressure might increase the chance of having higher sulfur vacancy. However, a synchrotron-based experiment was performed to detect sulfur vacancy from these three samples but did not work properly.

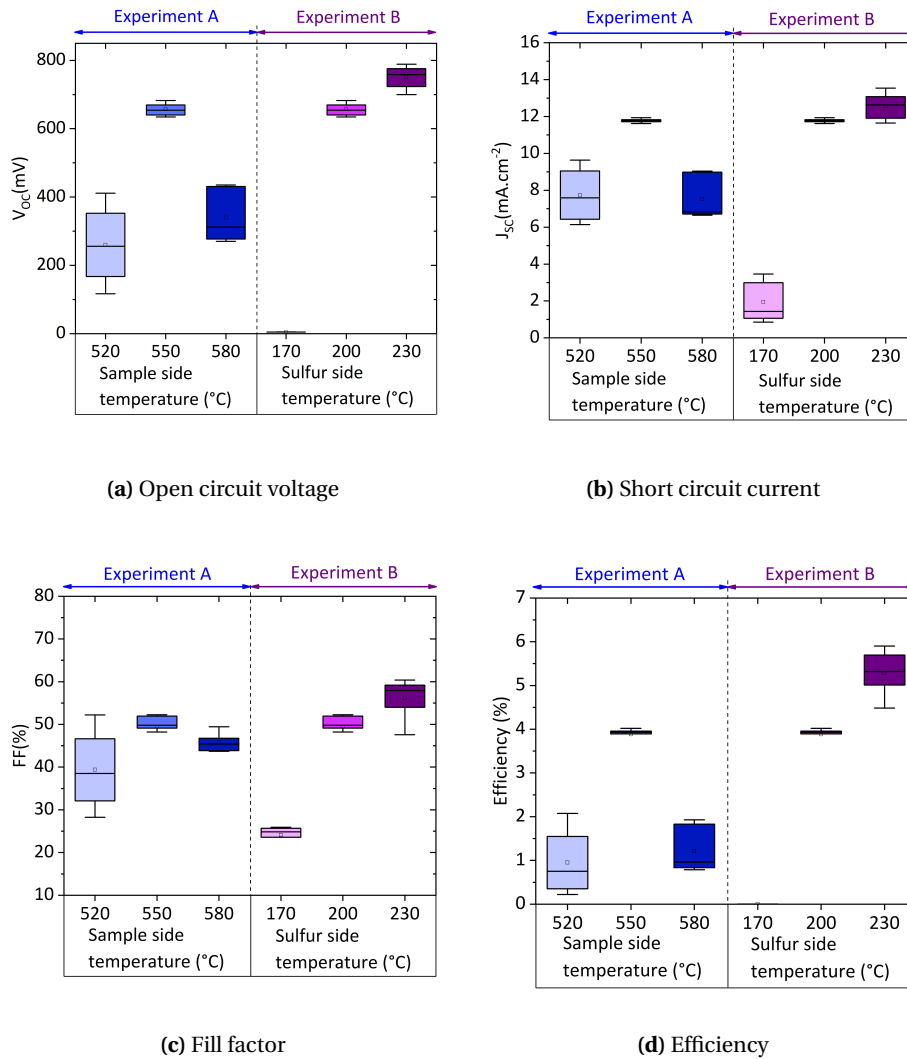
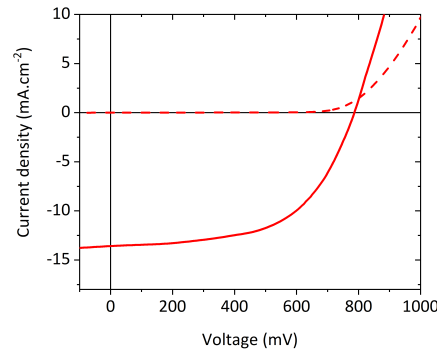
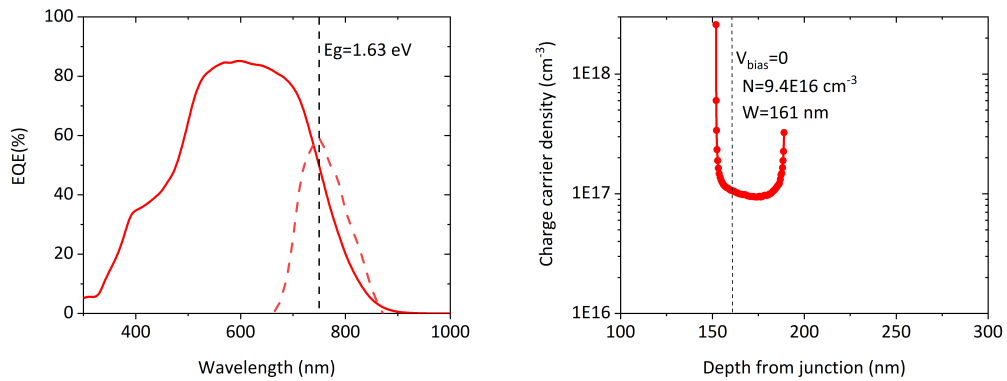


**Figure 4.25:** Light J-V parameters of the samples from experiment A and experiment B under 1.5G illumination condition.

The opto-electronic properties (dark J-V, illuminated J-V, EQE and C-V) of best CZTSe device from this work are illustrated in figure 4.26. The EQE in figure 4.26 (a) indicates a band-gap of 1.63 eV, deduced from the maximum of  $d(\text{EQE})/d(E)$  as a function of wavelength and a maximum EQE of 85%. The apparent carrier concentration is  $9.4\text{E}16 \text{ cm}^{-3}$ , with SCR width of 161 nm (at bias of 0V), measured by room temperature C-V.



(a) J-V measurement under 1.5G illumination and in dark



(b) EQE showing the band gap of 1.58 eV deduced from EQE edge (c) Charge carrier concentration profiles vs depletion width

**Figure 4.26:** J-V measurement under 1.5G illumination and in dark(a), EQE spectrum (b) and charge carrier concentration profiles as a function of the depletion width derived from C-V measurements (110 kHz, 300 K, dark) (c) of the best CZTS based solar cell.

**Table 4.7:** All the opto-electrical parameters of the best CZTS-based solar cells.

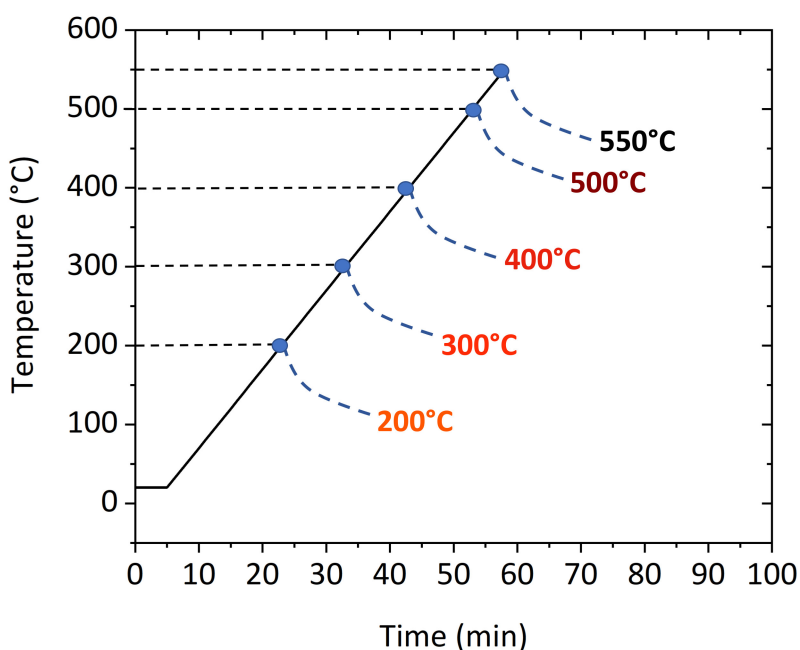
Light J-V				Dark J-V		C-V		EQE		
V <sub>oc</sub> (mV)	J <sub>sc</sub> (mA.cm <sup>-2</sup> )	FF (%)	Efficiency (%)	R <sub>s</sub> (ohm.cm <sup>2</sup> )	R <sub>sh</sub> (ohm.cm <sup>2</sup> )	N <sub>C-V</sub> (cm <sup>-3</sup> )	W (nm)	J <sub>sc</sub> (EQE) (mA.cm <sup>-2</sup> )	E <sub>g</sub> (eV)	V <sub>oc</sub> deficit (mV)
776	13.5	56	5.9	10.5	5600	1.1E+17	161	15.85	1.63	854

In summary, the best PCE achieved from this process is 6%, which is one of the highest efficiency, considering the use of elemental metal precursor using sputtering process. The optimized temperature for the sample zone was found to be 550°C and the sulfur zone was 230°C. Although, this efficiency could be improved by higher sulfur side temperature (higher sulfur vapor pressure), the setup of this reactor could not process higher sulfur vapor pressure

higher during the process. An experiment with a temperature higher than 230°C in sulfur side resulted in the condensation of sulfur in the extractor, thus prohibiting the argon flow completely.

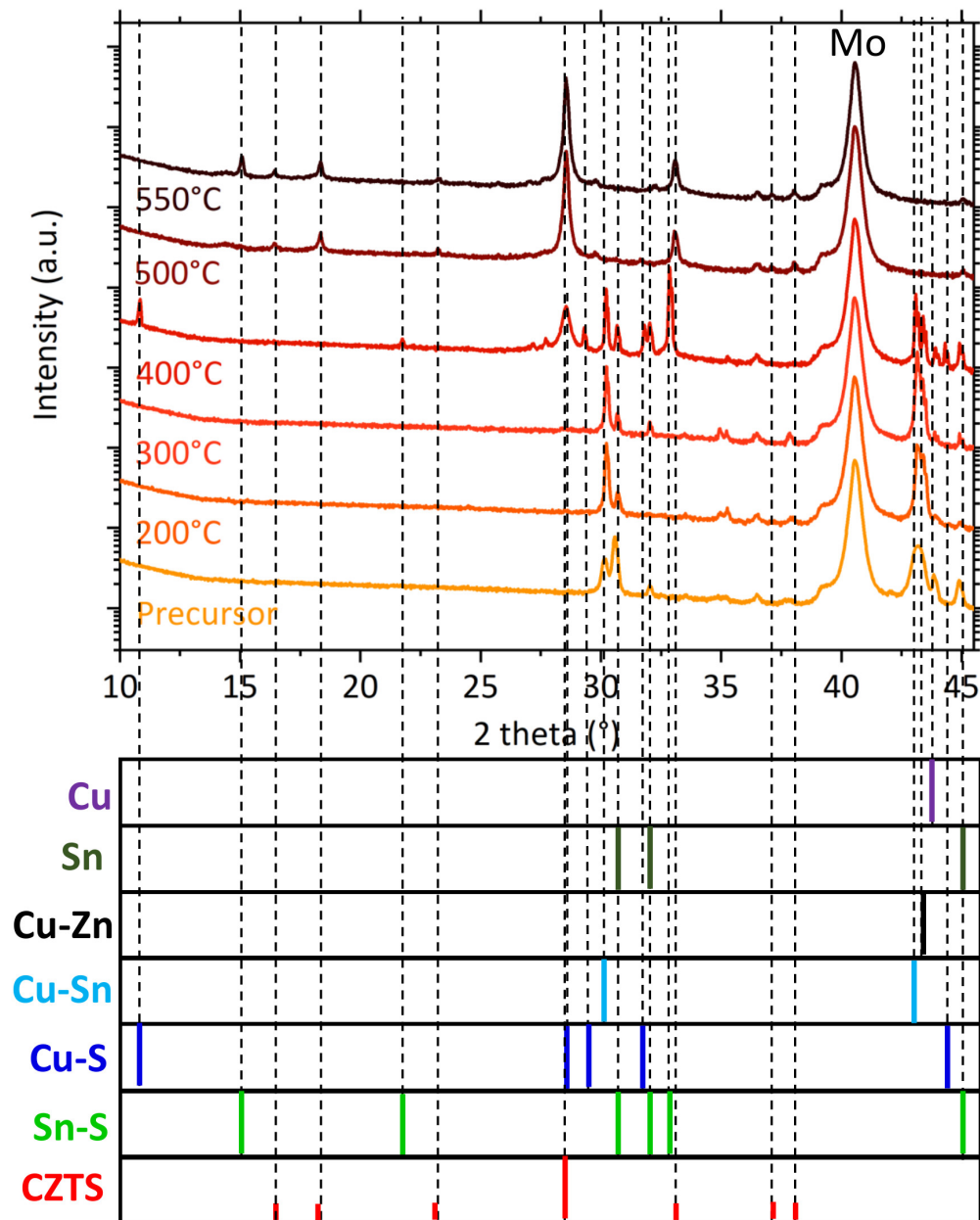
### 4.3.5 Formation mechanism of CZTS

To study the reaction mechanism during sulfurization, samples are annealed at different temperatures (200°C - 550°C) followed by a natural cooling for ex-situ analysis (see figure 4.27).



**Figure 4.27:** Temperature profile with the different points where the annealing was stopped for ex-situ characterization to determine the formation mechanism of CZTS absorber.

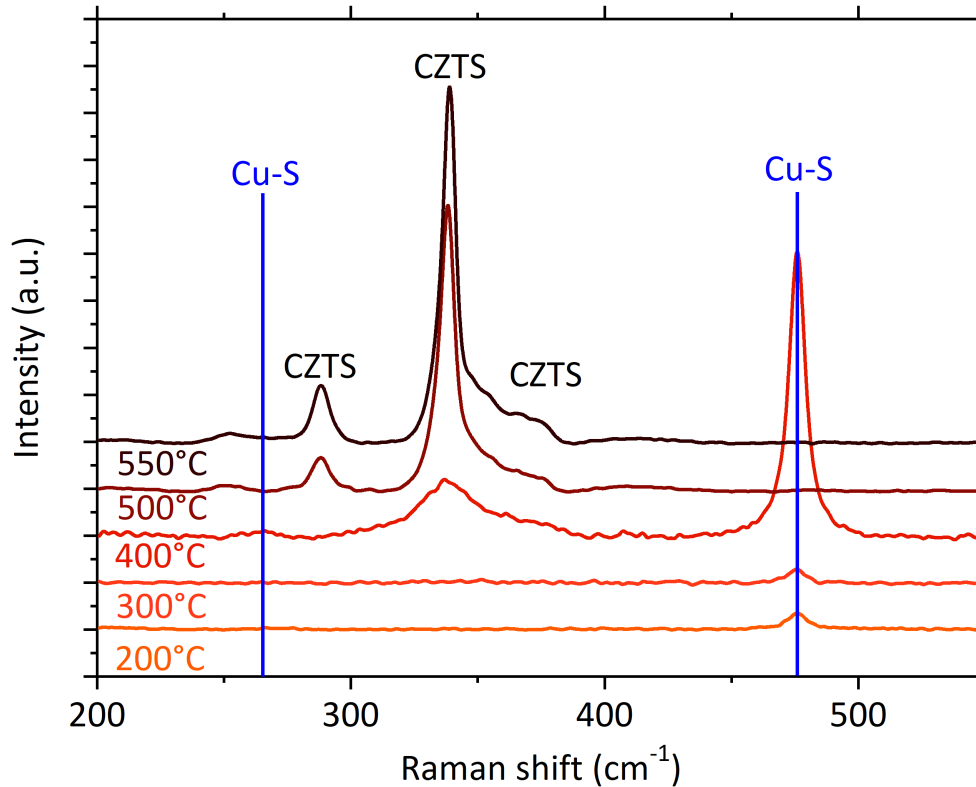
The presence of bronzes (Cu-Sn alloy) and brasses (Cu-Zn alloy) along with the presence of elemental metal (Cu and Sn) can be detected at the beginning of the reaction (from the precursor till 400°C), from XRD measurement (see figure 4.28). But, Zn cannot be detected, due to its possible presence as an amorphous form and/or present as an oxide. No indication of Cu-S or Sn-S phase is observed until 400°C. Later, the Sn-S secondary phase remains until the process temperature of 550°C, while CZTS phase starts to appear from 500°C. Therefore, the 30 minutes plateau of 550°C is necessary for a complete reaction from all the binary phases to highly crystallized CZTS compound.



**Figure 4.28:** XRD diffractogram of samples annealed with different temperatures to analyze the formation mechanism of the CZTS absorber.

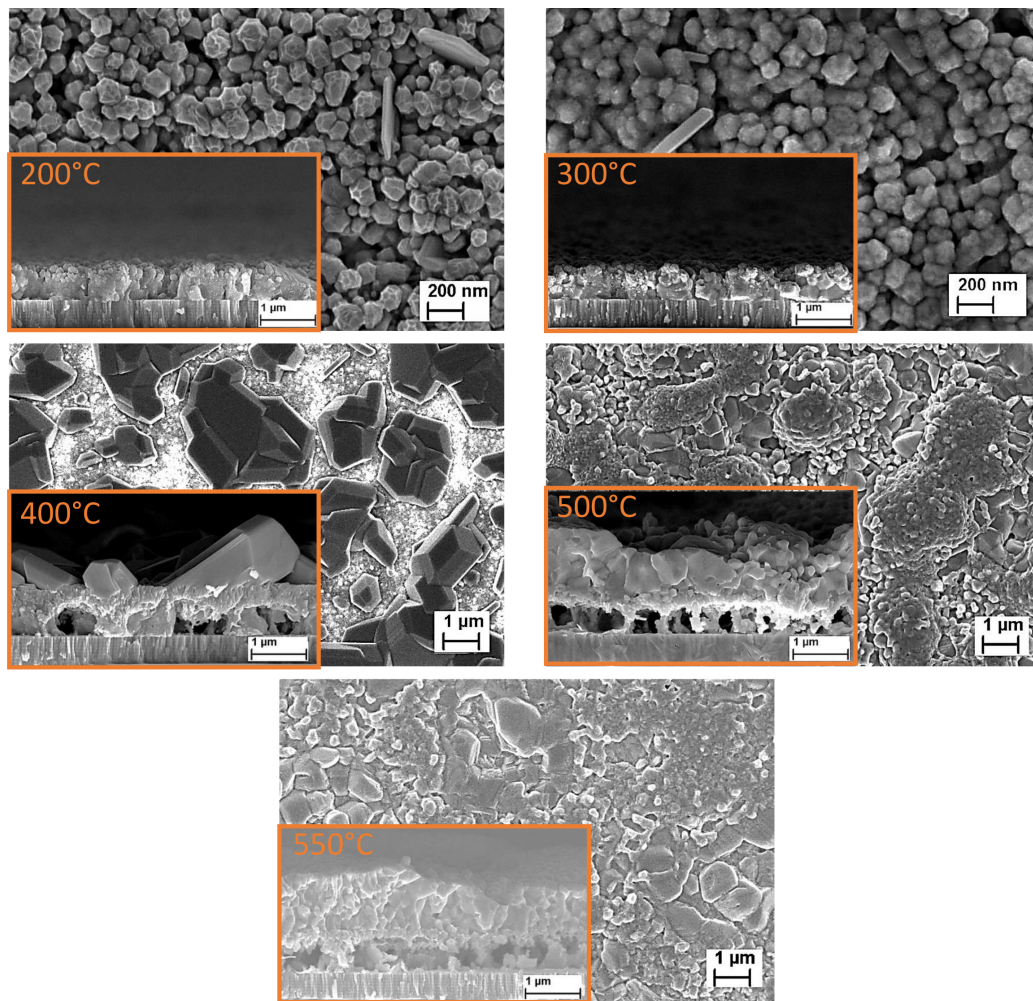
Figure 4.29 shows the Raman spectra of the same samples. Cu-S secondary phase can be detected until 400°C and disappears at a higher temperature. Although, a CZTS phase can be seen at 500°C, improved crystallization is achieved at 550°C, as can be detected by narrower main A mode CZTS peak at  $288\text{ cm}^{-1}$  and  $339\text{ cm}^{-1}$ . Furthermore, the Cu-S phase can be detected at 200°C, a contradiction with the XRD result. The reason could be that only a small

amount of Cu-S phase is formed at low temperature (below 400°C) mainly on the surface and cannot be detected by the XRD.



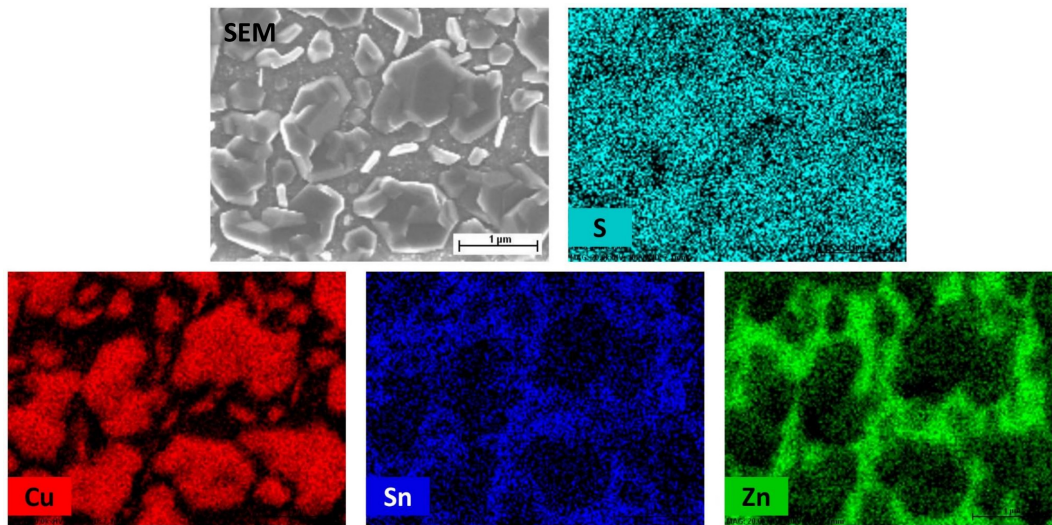
**Figure 4.29:** Raman spectra of the samples annealed with different temperatures to analyze the formation mechanism of the CZTS absorber.

Figure 4.30 is showing the SEM surface and cross-section (in the inset) of each sample corresponding to the above discussion. At 400°C, a very pronounced bilayer can be observed with big and highly crystallized grains on the top layer and small grains at the bottom. At 500°C, those highly crystallized grains can not be seen anymore. Also, the morphology seems more amorphous, while at 550°C it is more crystallized.



**Figure 4.30:** SEM image of surface and cross-section in the inset of the samples prepared with different temperatures to determine the CZTS formation mechanism.

To identify the nature of big grains present at 400°C, an EDX color mapping has been done on the sample(see figure 4.31). Thus, the highly crystallized growth at 400°C can be identified as a Cu-S secondary phase.



**Figure 4.31:** EDX mapping of the sample annealed up to 400°C under sulfur atmosphere, which clearly indicates the formation of a Cu-S secondary phase at this temperature.

Furthermore, the EDX color mapping on the sample annealed at 500°C shows the presence of CZTS phase, along with Zn-S secondary phase on the surface (see figure 4.32).

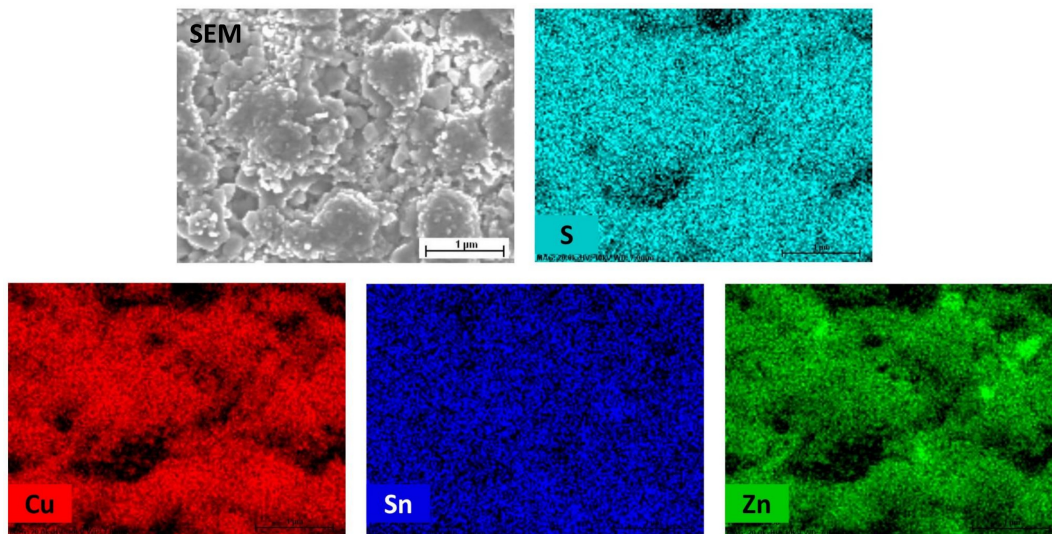


**Figure 4.32:** EDX mapping of the sample annealed up to 500°C under sulfur atmosphere, which clearly indicates the formation of a Zn-Se secondary phase at this temperature.

Lastly, from the EDX, the atomic percentage of anion and cation are deducted for this ex-situ samples. S to metal ratio is shown in figure 4.33 as a function of temperature. Most of the sulfur needed for the reaction is seen to be already present at 400°C (as ideally the ratio should be 1). That is the reason why the sample grown at 400°C has a similar average thickness as the

complete absorber.

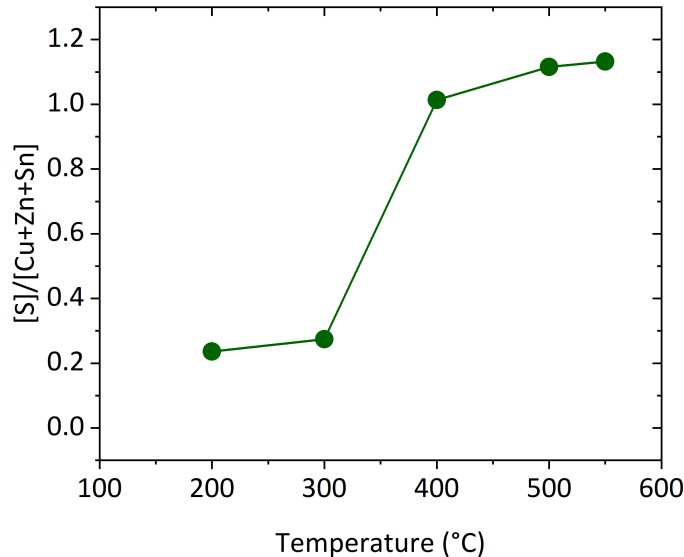


**Figure 4.33:** Sulfur to metal ratio as a function of the temperature deduced from the EDX measurement showing sulfur incorporation during annealing process.

**In summary**, this section describes the synthesis of the CZTS absorber using a two zone open reactor. The reaction temperature of both zones have been optimized to achieve the best performance of the CZTS based solar cell. The importance of sulfur pressure during the sulfurization was discussed experimentally. It has been shown that higher sulfur pressure during annealing improves material and optoelectrical properties. The reaction mechanism of sulfurization process has also been analyzed. It was demonstrated that the formation of CZTS using this method occurs from the reaction between the binary phases, similar to the reaction mechanism of a CZTSe absorber.

## 4.4 Conclusion

The procedure to synthesize CZTS and CZTSe based absorber has been established with nearly state of art efficiency. Best efficiency of 7.6% for 5.9% has been achieved for CZTSe and CZTS based solar cell respectively. The experimental work of this study showed that chalcogen vapor pressure has a significant role in terms of the microstructural and electrical properties of the CZTSe/CZTS absorber, where higher Se/S pressure is beneficial for the complete device. Similar conclusion also showed the importance of chalcogen vapor pressure to increase the

#### **Chapter 4. Development of CZTSe and CZTS absorber**

---

device performance of the complete device [26, 88]. The reaction mechanism from metallic precursor towards kesterite absorber is analyzed using ex-situ characterization. Although the characterization used during this study was not sufficient to detect the ternary phases (CTSe), combining both experimental results and literature review, it can be stated that the kesterite absorber has been grown from the reaction between the binaries.

# 5 Strategies and effects of Na and Sb incorporation on CZTS absorber

## Contents

---

<b>5.1 State of the art</b> . . . . .	<b>92</b>
5.1.1 Effects of Na and Sb incorporation . . . . .	92
5.1.2 Na and Sb incorporation method from literature . . . . .	94
<b>5.2 Na and Sb incorporation strategy</b> . . . . .	<b>96</b>
<b>5.3 Experimental results on Na and Sb incorporation</b> . . . . .	<b>97</b>
5.3.1 ToF-SIMS analysis . . . . .	97
5.3.2 Effect on material properties . . . . .	105
5.3.3 Effects of Na and Sb on device properties . . . . .	114
<b>5.4 Simulation using e-ARC</b> . . . . .	<b>120</b>
5.4.1 Effect of Na incorporation on Carrier Diffusion Length . . . . .	125
<b>5.5 Conclusion</b> . . . . .	<b>126</b>

---

Compared to CZTSe absorbers, CZTS absorbers exhibit a smaller grain size, which could be one of the reasons for their lower efficiency. In case of CIGS technology, alkali and Sb incorporation into the absorber layer leads to better crystallinity with bigger grains [107, 108]. Absorber doping with alkali and crystallization control with Sb (antimony) enhances the performance of CIGS-based solar cells thanks to the defect passivation and surfactant ability of these dopants [42, 109].

Therefore, investigating on alkali (Na) and Sb incorporation might be an effective procedure towards enhancing the performance of CZTS-based solar cell. It is worth noting that SLG substrate already contains alkali elements (Na, K), which diffuse naturally in the absorber during the high temperature (550° C) synthesis process. However, relying solely on SLG for alkali impedes the controllability, as different SLG substrates may have varying amounts of

alkali content. Incorporating Na from a controllable source will, therefore, be key for an accurate control and reproducibility of the absorber synthesis process.

As of today, few works have focused on clearly defining the effects of alkali and antimony on pure sulfur-based CZTS absorber. Thus, the current chapter will address the best suitable strategies for the doping, as well as its effect on the electrical, micro-structural and material properties of CZTS-based absorbers and solar cells. Moreover, this study will discuss the effect of Na on the possible decoupling of optoelectronic properties to structural properties. Additionally, we expect that findings from this study will also prove beneficial for absorber synthesis on alkali-free substrates, by defining the best route to apply external doping (Na, Sb) in the synthesis process.

### 5.1 State of the art

#### 5.1.1 Effects of Na and Sb incorporation

The beneficial effect of sodium "contamination" on CIGS was discovered by Hedström and co-workers in 1993 [41]. Since then, numerous works have been done (and are still going on) on the electrical and structural impact of impurities on CIGS and CZTSSe materials. Doping with alkali (Na, K) [110, 111] and antimony [108, 112] were investigated for CIGS solar cell, which recently led to an improved efficiency for CIGS-based thin-film solar cell.

The effect of Na for CIGS are commonly related to an increase in p-type conductivity via higher net hole concentration [113], enhanced grain growth, texturing with preferential orientation [114] and a direct impact on band-gap grading by lower inter-diffusion between In and Ga [111]. These characteristics results in an increased opto-electrical performance [109] and an improved crystallinity [114]. The enhanced electrical performance is mainly related to an increased  $V_{OC}$  and FF [109]. Although the precise role of Na towards the higher performance of the absorber has not been understood, defect passivation in the grain boundaries (GB) is considered to be one of the main reasons. [109].

The use of thin Sb layer during CIGS absorber synthesis was found to promote grain growth, which leads to enhanced EQE value for longer wavelength and improved power conversion efficiency (PCE) [42]. Moreover, Sb doping in CIGS material showed enhanced grain growth and increased  $V_{OC}$  only in the presence of Na [115].

Due to the similar properties of CIGS and CZTS(e), there has been an increased amount of interest towards exploring the potential of contamination (alkali or Sb) on kesterite absorber to improve its electrical and microstructural properties. Few works have been done to fully understand the effect of Na and Sb on Kesterite absorber. The reported effects are similar to

the ones observed for CIGS material. Doping by sodium has a positive effect on grain growth and texturization of kesterite based absorber [43–45]. An increase in device efficiency values, mainly increase in  $V_{OC}$ , FF and in some cases  $J_{SC}$  [116–120] is observed. An increase in the hole density and mobility, shallower acceptor level and reduction of certain deep trap center were linked to this improvement in electrical performance [119, 121, 122]. Although, there have been contradictory results on the effect of sodium on  $J_{SC}$  of kesterite absorber, a reduction in  $J_{SC}$  was also observed due to the decrease of space charge region [119]. A decrement in minority carrier lifetime was also noted [119], but the opposite was also observed when comparing an Na containing CZTSSe absorber to an one without Na [123, 124]. Furthermore, the passivation of GB by Na resulting in lower non-radiative GB recombination, it was considered one of the reason for an improvement of performances similar to the CIGS one [123, 125]. Similarly, hybrid-functional calculation showed the defect passivation nature of Na, by working as substitutional defects in the copper sub-lattice [126]. Moreover, it was pointed out by Haass et al., that the beneficial effect of Na doping was co-related with the Zn/Sn ratio in the absorber, as the higher the Zn/Sn ratio, the lower the effect of Na [127].

Using Sb has a similar effect on electronic properties of kesterite absorber as using sodium. According to Tiwari et al, co-doping of Na and Sb together provide better crystallization by lowering the energy requirement for the process and reducing the disorder between Cu and Sn site [128]. Solution-processed CZTSSe solar cell synthesized with  $SbCl_3$ , show improved PCE as a result of improved grain size and passivation of non-radiative recombination center in the band gap. But, too high an amount of  $SbCl_3$  is detrimental for the device [129]. Furthermore, it has been shown by 1<sup>st</sup> principle calculation that  $Sb_{Sn}$  defects have low formation energy under Cu-poor condition and low Sb concentration. This  $Sb_{Sn}$  antisite defect produces 1.1 eV deep level defects, which is detrimental for photovoltaic performances. On the other hand, Sb concentration beyond a critical point forms an isolated half-filled intermediate band at 0.5 eV above the valence band maximum which will increase the photo-current and as a result photovoltaic properties [130].

Some of the most recent works on Na and Sb incorporations are arranged in table 5.1. It clearly shows that sodium has a beneficial effect on electronic properties of kesterite based solar cell irrespective of synthesis method. Although, almost all the experiments shown in table 5.1 used SLG without barrier as a reference to compare with the sample with additionally added sodium, which might not give the clear picture on the effect of sodium doping. Na naturally out diffuses from SLG glass during the high-temperature synthesis process, which is the source of sodium doping for typical kesterite (CZTSSe) or chalcopyrite (CIGS) synthesis process [131]. The optimum sodium for the fabrication of CIGS-based material is often considered being equal to the amount of Na diffused from the glass, which is between 0.05 and 0.5 at(%) [132].

## Chapter 5. Strategies and effects of Na and Sb incorporation on CZTS absorber

But, Na diffusion from SLG is not controllable, which leads to the non-reproducibility of the process. Therefore, it is much beneficial to add sodium externally for better controllability and reproducibility of the process.

**Table 5.1:** Selection of works on the effect of sodium and antimony on Kesterite-based solar cell

Kesterite material	Synthesis method	Doping method	$V_{OC}$ (mV)	$J_{SC}$ (mA.cm <sup>-2</sup> )	FF (%)	PCE (%)	$R_S$ (Ohm.cm <sup>2</sup> )	$R_{Sh}$ (Ohm.cm <sup>2</sup> )
CZTS [116]	Co-sputtering+S	<b>Reference</b>	589	10.48	49.71	3.07	2.9	3073
		SS foil/Ti-10nm NaF(PAS)	638	13.38	48.01	4.1	3.93	3146
CZTS [117]	Co-evaporation	<b>Reference</b>	584	13.2	61.2	4.71		
		SLG-40 nm NaF(PAS)	603	13	66.8	5.23		
CZTS [128]	Spin-coating+S	<b>Reference</b>	550	16.3	47.1	4.2	4.9	930
		<b>Reference</b>	563	15.3	58.8	5.1	1.5	1320
		SLG+Sb(Oac <sub>3</sub> )+NaCl	610	14.9	63	5.7	1.3	1630
CZTSe [118]	Co-evaporation	<b>Reference</b>	315	35	58	6.4		147
		SLG+5nm NaF(PDT)	335	39	61	7.8		141
CZTSe [119]	Co-evaporation	<b>Reference</b>	274	35.9	51.8	1.94	0.74	
		SLG (ref.)	322	31.2	58.8	5.92	0.28	
		SLG+15 nm-NaF(PAS)	331	33.8	60.3	6.75	0.27	
CZTSSe [120]	Spin coating+Se	<b>Reference</b>	418	27.5	57	6.6		
		SLG+NaCl	450	30.77	59	8.3		
CZTSSe [129]	Spin coating+Se	<b>Reference</b>	439.1	28.1	47.2	5.8	2.8	
		SLG+SbCl <sub>3</sub>	463.9	29.3	58.2	7.9	1.7	

All the works listed in table 5.1, show that the addition of sodium leads to an improved of  $V_{OC}$  and FF. Moreover, for some works  $J_{SC}$  was also increased. There is no clear explanation on why  $J_{SC}$  was higher with sodium addition, even though the depletion region width gets smaller compared to the absorber without sodium doping because of higher net carrier concentration. This issue will be also addressed in this chapter.

### 5.1.2 Na and Sb incorporation method from literature

There are several ways to incorporate Na in the absorber during sequential process (sputtering based). Na naturally out diffuses from glass during annealing, which is shown in figure 5.1 (a). Moreover, three strategies can be adopted for external diffusion of alkali by sequential process. Compound of Na can be applied as source of Na before absorber synthesis (Pre-absorber synthesis (PAS)), which is shown in figure 5.1(b). Similar compound of Na can be applied after absorber synthesis prior to second annealing to assist Na diffusion in the absorber, commonly known as post deposition treatment (PDT) (see figure 5.1(c)). Lastly, Na doped Mo back contact can be used as the source of Na during absorber synthesis, shown in figure 5.1(d).

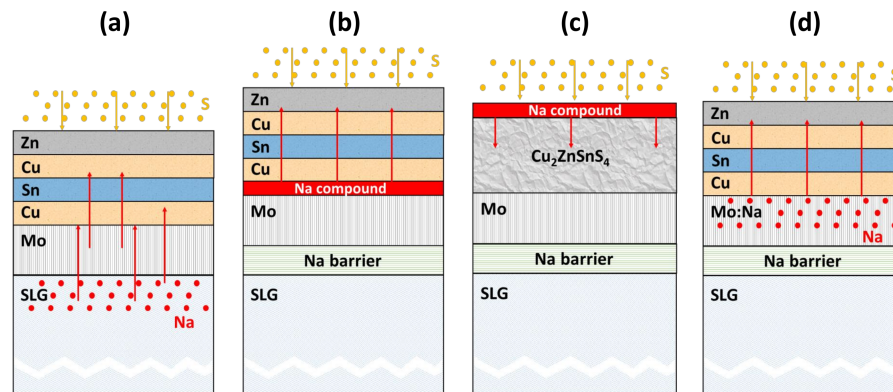


**Figure 5.1:** Schematic illustration of different methods for Na incorporation into absorber during sequential process. (a) Na is diffusing from the substrate (usually soda-lime glass) into absorber during growth. (b) A Na-diffusion barrier blocks transport of Na from the substrate, Na is supplied by a thin Na-containing precursor layer deposited prior to absorber growth (Pre-absorber synthesis (PAS)). (c) Na is diffused into as-grown absorbers using post-deposition treatment (Post-deposition treatment (PDT)). (d) Sodium is diffusing from sodium doped molybdenum during the absorber growth

Different processes of Na incorporation have been investigated until now, focusing mainly on selenium or sulfo-selenium based absorbers. For CIGS-based technology PDT, showed the best result in terms of electrical properties [107]. But, in the case of kesterite based technology, some work were done showing lower effectiveness of PDT [133, 134] compared to the process where Na was present during the synthesis (PAS). Although, by adopting process (d), complexity can arise from different back contact structure (different sheet resistance, temperature dependent diffusion of Na).

Moreover, solution-based processes have been found to be more efficient towards incorporation of alkali in kesterite absorber [120]. Nonetheless, as sequentially process (sputter deposition of precursor) can be easily industrialized, establishing successful Na incorporation strategy for CZTS-based absorber is of pure interest. However, to date no work has been done on CZTS-based absorber towards defining the best Na incorporation strategy. Therefore, later in this chapter, the best strategy for Na incorporation in CZTS absorber will be discussed.

Sb incorporation has been tested on CIGS technology by different methods, such as adding Sb-based compound ( $\text{Sb}_2\text{S}_3$ ) [112] as a solute for solution processed method or by evaporating Sb directly on Mo prior to the co-evaporation synthesis of the absorber [108, 115]. But, only solution based process was investigated in case of kesterite absorber, where  $\text{Sb}(\text{Oac}_3)$  and  $\text{SbCl}_3$  were used as a solute for Sb [128, 129]. Therefore, this study will be the first of a kind, which will bring some insight on Sb doping of CZTS material by sequentially processed (sputtering-based) absorber.

## 5.2 Na and Sb incorporation strategy

First of all, a  $\text{SiN}_x$  barrier is used between SLG and Mo to stop diffusion of Na and any other impurity from SLG, to study the effect of Na much more precisely. One CZTS sample is synthesized with  $\text{SiN}_x$  barrier and without any intentional doping to be used as a reference sample, which will be called 'undoped' in the following sections.

Na incorporation in CZTS has been tested using two strategies, that are applying Na before and applying Na after the synthesis of CZTS (similar to figure 5.1(b) and (c) respectively). Samples from both strategies will be addressed by PAS(NaXX) (PAS stands for pre-absorber synthesis and XX stands for the thickness of NaF used in nm) and PDT(NaXX) respectively in this chapter.

Sb incorporation has only been tested before absorber synthesis since the main expected result concerns the absorber crystallization. Sb can be deposited either on top of Mo or on top of the precursor. In the first case, delimitation occurs during the annealing process. Thus, Sb has been deposited only on top of precursor. As we want to study the effect of Sb, as well as the effect of Na and Sb co-doping on CZTS, two routes are used for this study. First route is the incorporation of Sb in CZTS without Na, which will be called PAS(SbYY) (YY stand for the thickness of Sb used in nm)(see figure 5.2(a)). And the second route is the incorporation of Sb in CZTS absorber with Na, which will be called PAS(NaXX+SbYY) (see figure 5.2(b)).

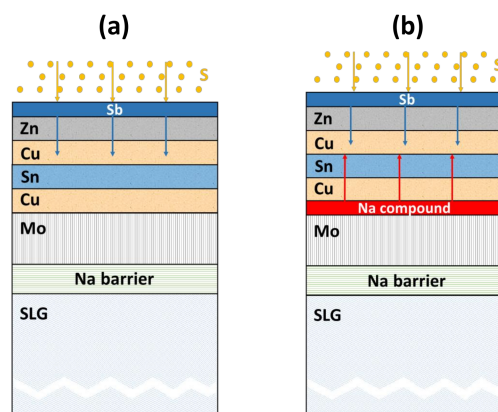


**Figure 5.2:** Schematic illustration of Sb incorporation into absorber during a sequential process. (a) Sb is supplied by a thin Sb-containing precursor layer deposited prior to absorber growth (PAS(Sb) (Pre-absorber synthesis)) and (b) Na and Sb are supplied by a thin Na and Sb-containing precursor layer deposited prior to absorber growth (PAS(Na+Sb)).

### 5.3. Experimental results on Na and Sb incorporation

**Table 5.2:** List of the samples and amount of dopant used for each samples.

Sample	Sb			NaF		
	Strategy	Deposition position	Thickness (nm)	Strategy	Deposition position	Thickness (nm)
Undoped	N/A	N/A	0	N/A	N/A	0
PAS(Na10)	N/A	N/A	0	PAS	before precursor	10
PAS(Na20)	N/A	N/A	0	PAS	before precursor	20
PAS(Na40)	N/A	N/A	0	PAS	before precursor	40
PDT(Na10)	N/A	N/A	0	PDT	after absorber	10
PDT(Na20)	N/A	N/A	0	PDT	after absorber	20
PDT(Na40)	N/A	N/A	0	PDT	after absorber	40
PAS(Sb5)	PAS	after precursor	5	N/A	N/A	0
PAS(Sb10)	PAS	after precursor	10	N/A	N/A	0
PAS(Sb20)	PAS	after precursor	20	N/A	N/A	0
PAS(Na10+Sb10)	PAS	after precursor	10	PAS	before precursor	10
PAS(Na40+Sb20)	PAS	after precursor	20	PAS	before precursor	40

For Na and Sb incorporation, 99.99% pure NaF and 99.998% pure elemental Sb have been deposited by evaporation. Sodium fluoride (NaF) of different thicknesses has been deposited by thermal evaporation using 730° C and 2nm/min deposition rate. Sb is deposited by thermal evaporation using 160° C and 2.5 nm/min deposition rate. All the samples are sulfurized using the standard procedure explained in section 4 (200° C are used in sulfur zone for this experiment). For Na incorporation after synthesis, NaF is applied on undoped CZTS absorber prior to a second annealing for 15 min and 350° C under Ar assisted sulfur flow.

### 5.3 Experimental results on Na and Sb incorporation

The first part of this section deals with the effectiveness of Na and Sb incorporation and their distribution in the absorber. The effect of structural and optoelectrical properties will then be discussed.

#### 5.3.1 ToF-SIMS analysis

Compositional depth profiles are performed on different samples by TOF-SIMS depth profiling to acquire the distribution of elements. The presence and distribution of Na and Sb throughout the experimental samples can be determined by this analysis due to its very low detection limits and excellent depth resolution.

Details on experimental procedure can be found in section 3.2.6. Complete solar devices (after finishing opto-electronic analysis) are used for this experiment after removing TCO and CdS

layer using 10% (v/v) HCl (Hydrochloric Acid). Therefore, the stacking order of all the samples used for SIMS analysis is CZTS/Mo (Molybdenum)/SiN<sub>x</sub>/SLG.

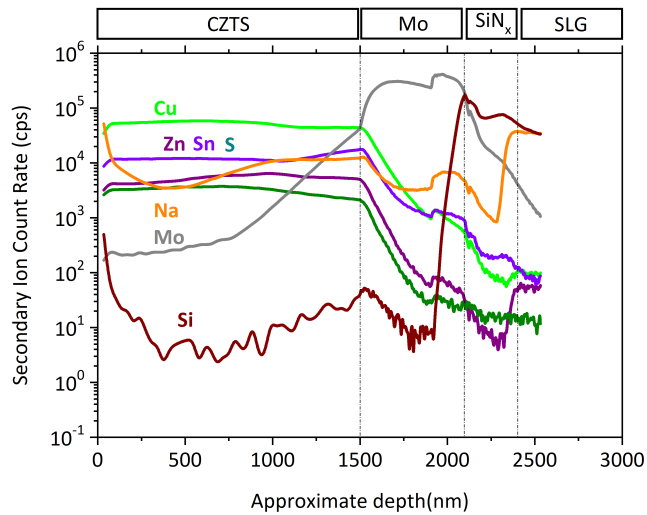
### 5.3.1.1 Evaluation of Na and Sb depth profile

TOF-SIMS profiling of the undoped sample is performed in positive secondary ion mode (figure 5.3(a)) and negative secondary ion mode (figure 5.3(b)). The approximate sputtering depth for all the samples are calculated as follows. First, for the simplicity of the analysis, the thickness of the layers for all the sample is assumed to be the same (e.g. CZTS (1500 nm)/Mo (600 nm)/SiN<sub>x</sub> (300 nm)/SLG). Second, for positive secondary ion mode, the signature of Mo back contact is used to provide depth perspective through the film. Thus, the crossover between the Mo and Cu (Copper) profile is determined to be CZTS/Mo interface and the crossover between the Si (Silicon) and Mo profile is determined to be Mo/SiN<sub>x</sub> interface. Furthermore, the interface between SiN<sub>x</sub> barrier and SLG is determined by an increment of Na profile. Since SiN<sub>x</sub> is used as a barrier for Na, it will contain a lower amount of Na compared to SLG. Third, for negative ion secondary mode, initial decrease of S (Sulfur) profile is used to indicate the position of CZTS/Mo interface. Mo/SiN<sub>x</sub> and SiN<sub>x</sub>/SLG interfaces are determined by O (Oxygen) profile. Since the barrier layer contains lower amount of O than Mo and SLG, that can be seen as a decrement between Mo and SLG glass interface (see figure 5.3(b)).

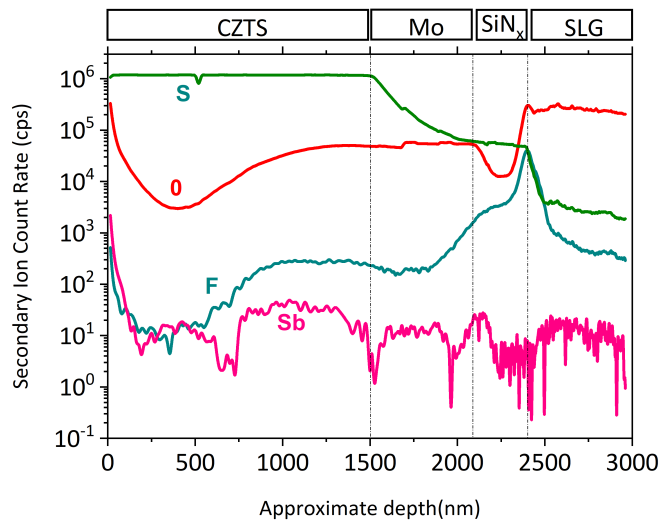
Figure 5.3(a) shows that Cu and S are distributed homogeneously throughout the absorber, while Zn has a slight increase in the middle of the absorber and Sn has a slight increase in the CZTS/Mo interface. These could give us a hint about the presence and position of Zn and Sn-based secondary phase in the absorber. It is worth to note that Na in the surface and the bulk can still be detected in the undoped sample due to the high sensitivity of Na during the positive secondary mode. However, the role of SiN<sub>x</sub> as the Na diffusion barrier confirmed by comparing this with a Na doped sample (see figure 5.5 (a)). Si showed a sharp rise in Mo/SiN<sub>x</sub> interface followed by a steady decrease, which is expected due to the difference in atomic (%) of Si in SiN<sub>x</sub> and SiO<sub>2</sub>. In negative secondary ion mode, S profile exhibits too high intensity counts to use for analysis. Therefore, S profile from positive secondary ion mode will be used to compare S profile of different samples. An increased amount of O can be seen in the back of CZTS absorber and inside Mo with a decrease in SiN<sub>x</sub> and increase again in SLG (as SLG contains a high amount of oxygen). Interestingly, F (Fluorine) profile can be detected successfully using negative secondary ion mode, where it increased sharply near SiN<sub>x</sub>/SLG interface. This is still not clear for the F to be found on the surface of SLG, but it might be related to the surface de-alkalization treatment done by the manufacturer using HF (hydrofluoric acid) to increase the transmittance and corrosion resistance [135, 136]. Furthermore, detection of

### 5.3. Experimental results on Na and Sb incorporation

Sb is near the detection limit of SIMS analysis, which indicates that no Sb was found in the undoped sample.



(a) SIMS analysis of the undoped sample done by positive secondary ion mode using  $O_2^+$  ion sputtering.



(b) SIMS analysis of the undoped sample done by negative secondary ion mode using  $Cs^+$  ion sputtering.

**Figure 5.3:** SIMS analysis of the undoped sample.

Five samples (undoped(ref.), PAS(Na10), PDT(Na40), PAS(Sb10) and PAS(Na10+Sb10)) will be considered from each kind of experiment for the analysis using TOF-SIMS. To have a closer inspection on the elements distribution of CZTS compound throughout the depth,

enlarged profiles of Cu, Zn, Sn and S are shown in figure 5.4. At first glance, the Cu, Zn, Sn and S profiles appear similar. However, upon closer inspection (see figure 5.4(b)) it can be seen that increased amount of Zn is present in the bulk of the undoped sample compared to front or back interface of the absorber, while increased amount of Zn is found near the back interface for other samples. Since all the samples are nominally Cu-poor and Zn-rich, it is not surprising to observe segregated ZnS. Also, the presence of Na and Sb in the absorber may have influenced the location of the precipitated ZnS. This phenomenon is in agreement with the literature [125]. A closer look at Sn profile of all the sample shows a slight increase in Sn intensity near the Mo interface, indicating that possible secondary phases of Sn might be present at the back side of the absorber. However, no corresponding peaks are detected by XRD associated with Sn secondary phase, which leads to the conclusion that the amount of this secondary phase is lower than 2% [137].

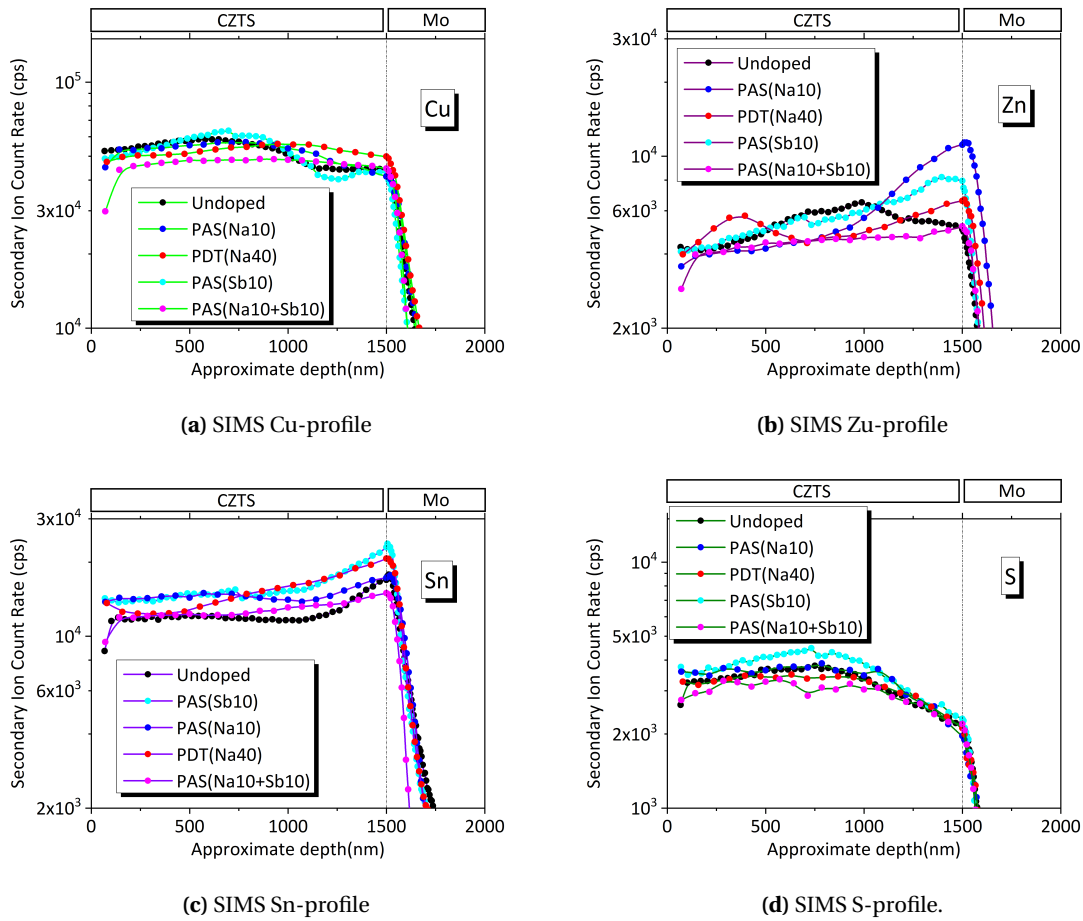


**Figure 5.4:** Enlarged view of Cu, Zn, Sn and S for different doping procedures.

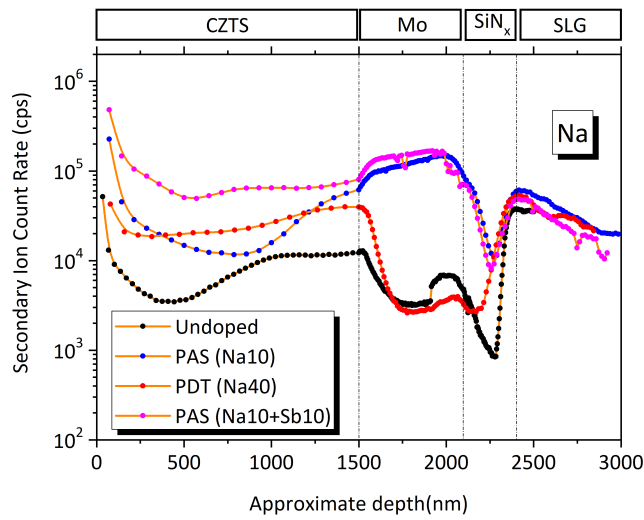
### 5.3. Experimental results on Na and Sb incorporation

---

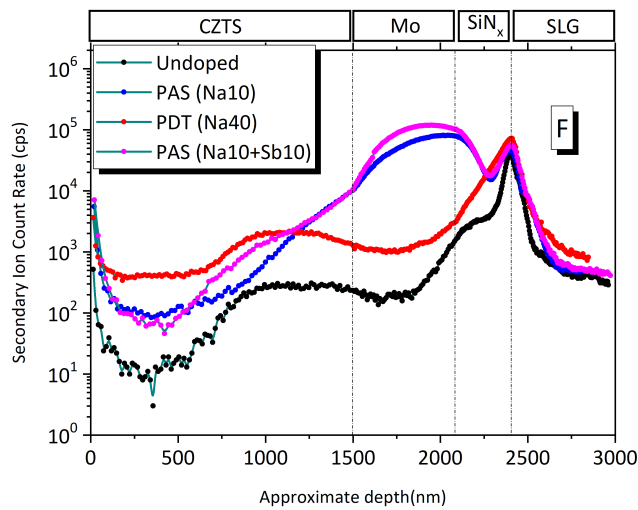
The distribution of Na, Sb and F for all the samples is shown in figure 5.5. All the Na incorporated samples show higher intensity counts of Na compared to the undoped sample (see figure 5.5(a)), which confirms the role of  $\text{SiN}_x$  as barrier. In the case of the PAS(Na10) sample, higher Na counts are found near the surface and rear of the absorber, in accordance with the literature, explaining that Na segregates at the kesterite surface and grain boundaries [131, 138, 139]. In the case of the PDT(Na40) sample, a more homogeneous distribution of Na is found. The PDT sample showed smaller grains with higher density of grain boundaries and since Na tends to accumulate in the grain boundaries (see figure 5.5), Na distribution appears to be more flat. This is also consistent with the literature [132, 140]. In the case of the PAS(Na10+Sb10) sample, the Na profile is similar to that of the PAS(Na10) sample with higher intensity. Na profile is found to be higher inside Mo back contact for the sample synthesized with Na(PAS(Na10) and PAS(Na10+Sb10)), while the opposite has been observed for undoped and PDT sample. It proves that Na diffused inside Mo during synthesis process at  $550^\circ\text{C}$  for PAS(Na10) and PAS(Na10+Sb10) sample, while second annealing at  $350^\circ\text{C}$  is not enough for Na to diffuse inside Mo back contact in the case of PDT(Na40) sample.

F distribution profiles show similar characteristics as Na distribution (see figure 5.5(b)). The lower intensity of F can be seen in the undoped sample compared to the sample treated with NaF. On the other hand, PAS(Na10) sample and PAS(Na10+Sb10) sample have a higher amount of F near CZTS/Mo interface and in Mo, while PDT(Na40) sample has relatively less variation. Although many works have been done regarding Na incorporation via NaF, no work emphasized the distribution of F throughout the CZTS absorber. This study demonstrates that F is present in the completed solar cell (as these samples are the same samples used as solar devices). Also, the position of F is found to be near the Mo interface and inside the Mo back contact.

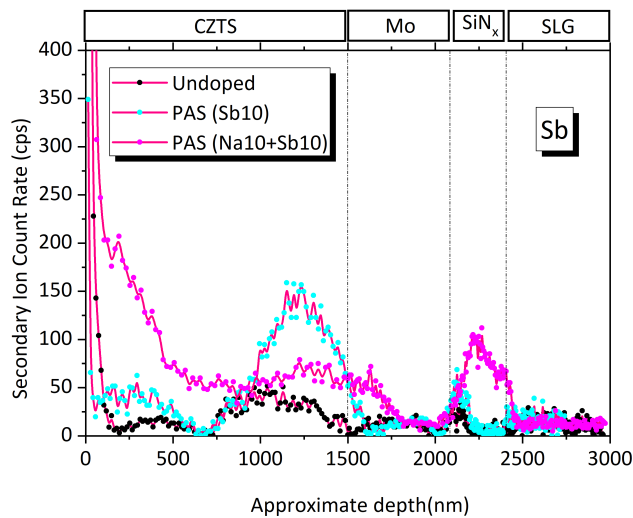
Sb distribution for different samples is shown in figure 5.5(d). In all the cases, Sb is detected near the detection limit of SIMS profiling. Here, the undoped sample shows the absence of Sb, while PAS(Sb10) and PAS(Na10+Sb10) shows some trace amount of Sb. Interestingly, when Sb is used without Na, it can only be seen near the CZTS/Mo interface, while Sb is detected mainly on the front and rear of the absorber for PAS(Na10+Sb10) sample.



(a) SIMS Na profile.



(b) SIMS F profile.



(c) SIMS Sb profile.

Figure 5.5: SIMS signal of the dopant for different doping procedures.

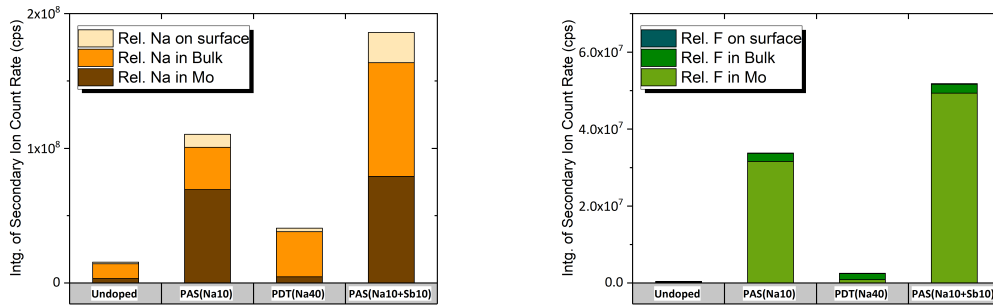
### 5.3. Experimental results on Na and Sb incorporation

---

Integration of Na and F profiles have been done by separating the profile in three parts (surface (0 nm-100 nm), bulk (100 nm-1500 nm) and Mo (1500 nm-2100 nm), in order to have a relatively quantitative view on the distribution of those elements in CZTS (see figure 5.6). Mo profiles from SIMS analysis for these samples are also given in figure 5.6(c) as a reference, to validate this analysis, as the relative intensity of Mo signal for all these samples is similar.

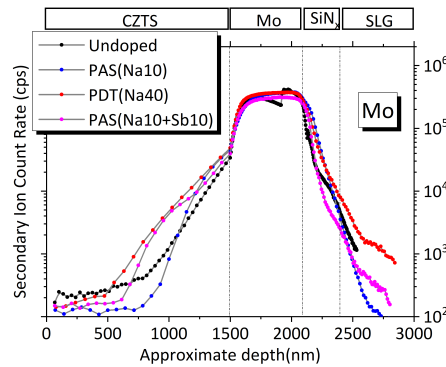
The PDT(Na40) sample has a lower amount of Na compared to the PAS(Na10) and PAS(Na10+Sb10) samples, although a higher amount of NaF is used for this sample. Some NaF from the surface of CZTS absorber might be re-evaporated during second annealing or did not diffuse inside the absorber and got removed during CdS process. As a result it shows low amount of Na in the absorber, similar to the literature [141]. Also, Na on the surface is relatively higher for PAS(Na10) sample, compared to PDT(40) sample, while the amount of Na in the bulk is similar. On the other hand, the amount of Na is higher in both the surface and bulk for PAS(Na10+Sb10) sample compared to the PAS(Na10) one, although a similar amount of NaF was used in both cases. Therefore, in comparison Na in one absorber is enhanced in the presence of Sb. Lastly, a similar integration is done on fluorine profile shown in figure 5.6(b), which agrees with the previous discussion that higher fluorine is found inside Mo when NaF is present during the synthesis. But, it is still unclear if F has any effect on material properties of CZTS absorber, even though most of F seems to reside in Mo. Ab-initio calculation could provide information on whether F intercalates in the lattice and makes additional defects in the absorber.

## Chapter 5. Strategies and effects of Na and Sb incorporation on CZTS absorber



(a) Comparison of the Na distribution in different regions of the samples.

(b) Comparison of the F distribution in different regions of the samples.



(c) Mo signal from SIMS analysis as a reference for the samples.

**Figure 5.6:** Comparison of Na and F distribution in different regions of the samples based on integrated raw SIMS data for different doping procedures (a, b) and Mo SIMS profile for these sample (c).

**In summary**, the effects of Na and Sb incorporation on the material properties of CZTS-based absorber are investigated using ToF-SIMS profiling:

1. The presence of Na and Sb is identified compared to the undoped sample, which proves the effectiveness of doping strategy.
2. The Position of the Zn based secondary phase shows dependency on the presence of Na in the absorber. Higher amount of Zn are found in the bulk of the absorber in the case of the undoped sample, while the Na doped sample showed higher Zn at the interface of the absorber.
3. Na applied before absorber synthesis showed higher amount of Na inclusion in the absorber compared to PDT one.
4. F has been detected in the absorber using NaF as the source of Na. Further, Ab-initio

calculation could provide information on whether F intercalates in the lattice and make additional defects in the absorber.

#### 5.3.2 Effect on material properties

##### 5.3.2.1 Effect on macro structural properties

Optical microscope images of absorber surface after different external doping strategies are shown in Figure 5.7. The pictures are arranged according to the different absorbers prepared with NaF and/or Sb using PAS method.

The first observation is that the PAS(Na40) sample shows some dark spots on the surface, which peels off during the CdS deposition process required to make a complete device. Based on this observations, we concluded that 40 nm of NaF is the highest usable amount for PAS(Na) method (otherwise, further degradation would occur in the finished device). Similarly, Sb also experiences some peeling off while using 20 nm of Sb. Hence, we limit our Sb usage to 20 nm during this experiment. Moreover, the incorporation of both Na and Sb (PAS(Na40+Sb20)) shows the same peeling off defect. Thus we will only consider PAS(Na10+Sb10) sample for material and electrical characterization in the following discussions. Secondly, the surface of the undoped sample shows some inhomogeneity, while PAS(Na10) and PAS(Na40) samples appear to exhibit reduced inhomogeneity, only due to differences in contrast. But, using both Na and Sb together for PAS(Na10+Sb10), the absorber surface appears to be truly homogeneous judging by the surface color. Lastly, the PDT(Na) sample (not shown in the figure) did not show any macroscopic degrading like the PAS(Na) sample, even with 40 nm NaF usage.

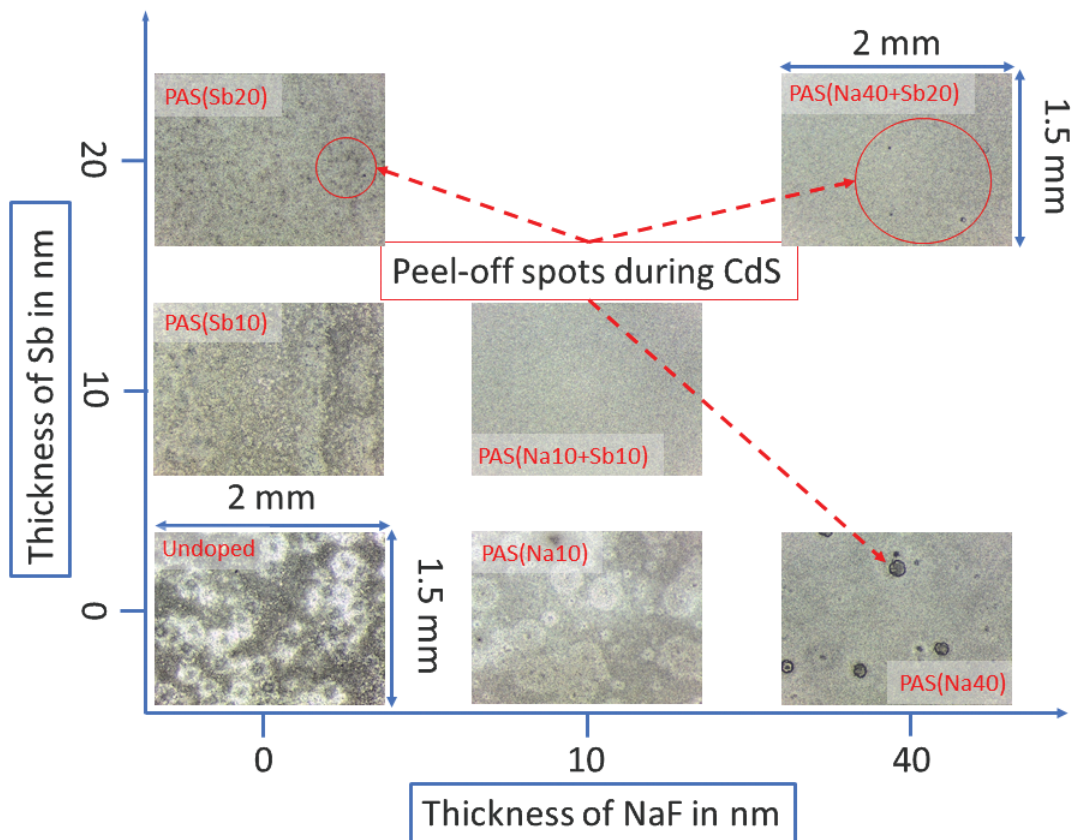


**Figure 5.7:** Optical microscopic image of absorber surface for various doping treatments via optical microscope. Red circle indicates the spots that peeled off during CdS deposition.

Figure 5.8 details a peel-off spot from the PAS(Na40) sample with an optical zoom on the dark spot(5.8(a)) along with top and cross-section SEM images of the same spot (figure 5.8(b) and (c) respectively). It is then identified that this region is forming a bubble between Mo and absorber. Indeed, this bubble formation between Mo and the absorber is the reason behind the peeling off happening during CdS deposition process whenever a higher amount of NaF(more than 40 nm) or Sb(more than 20 nm) is used.

### 5.3. Experimental results on Na and Sb incorporation

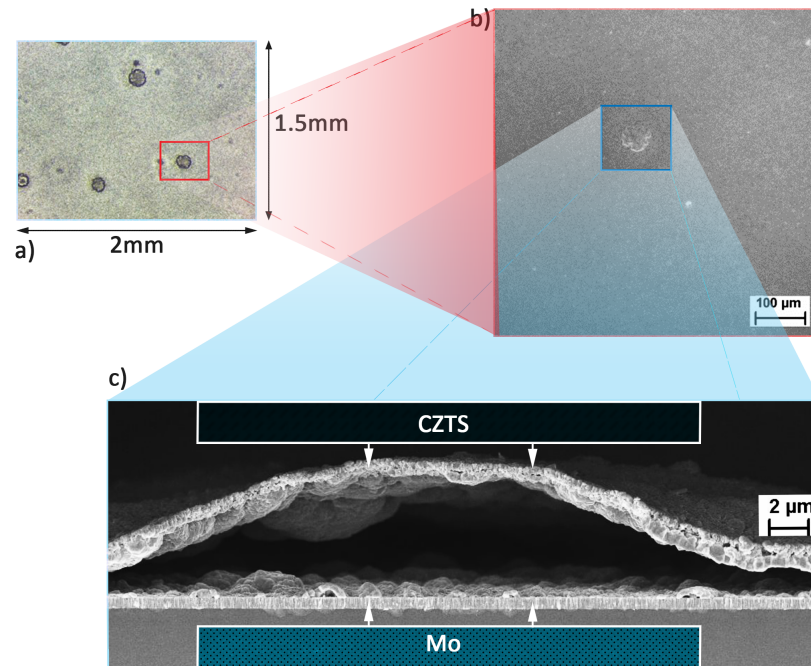


**Figure 5.8:** Formation of bubble on the PAS(Na40) sample via optical microscope (a), SEM top view of a bubble (b), SEM cross-section of a bubble (c).

#### 5.3.2.2 Effect on micro-structural properties

The surface SEM images of the different samples are shown in figure 5.9. The morphology of PDT(Na10) (figure 5.9(a)) is similar to that of PDT(Na10) (figure 5.9(c)). For the PDT(Na10) sample, some white dot-like particle can be seen on the grains of the absorber, where similar particle is identified as the residue of alkali (Na, K) fluoride after PDT by Khatri et al, [142]. In addition to these particle on the surface, both the undoped and PDT(Na10) samples show a non-homogeneous distribution of grains, where some show sharp and angular grain in micro size and other show more spherical grains with sizes below 300 nm. Both undoped and the PDT(Na10) samples are synthesized without Na, which is the reason for having similar morphologies. The second annealing (350° C for 15 minutes) with NaF, applied to the PDT(Na10) sample has no apparent effect on the morphology of the absorber, in agreement with the literature [111, 143]. In contrast, Na used during the synthesis process has a noticeable effect on the morphology of the absorber, as can be seen in figure 5.9. The PAS(Na10) sample exhibits sharper and more faceted grains than the undoped sample.

Absorber synthesized with Sb and without Na (in figure 5.9(d)) shows a similar morphology as the undoped sample. Thus, no effect of Sb on crystallization is observed. Interestingly, using

Na and Sb together during CZTS fabrication has a significant effect on the morphology (5.9(e)). The SEM image of the surface for the PAS(Na10+Sb10) sample reveals grains bigger than 1  $\mu\text{m}$ . It can be concluded that Sb facilitates grain growth only in the presence of Na during synthesis, as has already been observed with CIGS technology [115].

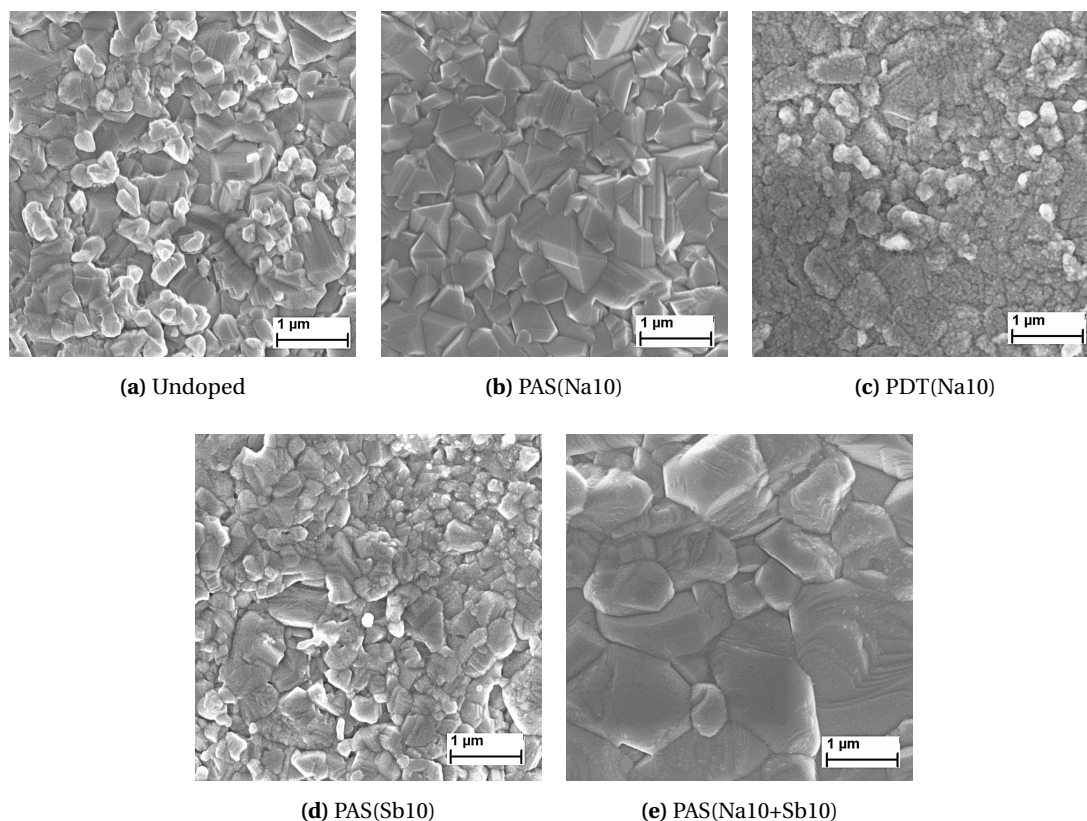


**Figure 5.9:** SEM surface images of CZTS absorber with different doping methods. SEM surface of undoped (a), PDT(Na10) (c) and PAS(Sb10) (d) shows similar morphology, where PAS(Na10) (b) shows more faceted grains and PAS(Na10+Sb10) (e) shows increased grain growth

These observations are further confirmed by the SEM cross-section images in figure 5.10. Here, non-homogeneous grain distribution ranging from 200 nm to 500 nm in the undoped sample is visible. When Na is present during absorber synthesis in the PAS(Na10) sample (5.10(b)), the grain size increased partially up to 800 nm. But, using higher amount of Na during this strategy leads to opposite results: smaller grain size and lower adhesion between CZTS and Mo (figure 5.10(c)). A similar effect with higher Na resulting in smaller grain size is also observed with CIGS absorbers by D. Rudmann [132]. Conversely, no apparent change of grain size is observed in the case of the PDT sample, whatever the amount of Na used. No apparent change is observed in the morphology of PAS(Sb10)(figure 5.10(f)), while a degradation of the

### 5.3. Experimental results on Na and Sb incorporation

---

morphology observed with higher Sb amount (PAS(Sb20) (figure 5.10(g)).

Finally, incorporation of Na in conjunction with Sb (figure 5.10(h)) shows noticeable grain size change compared to the undoped sample, confirming what had been observed with the surface SEM images. The grain size of this sample is bigger than  $1\ \mu\text{m}$ , the same thickness as that of the absorber itself.

**In summary**, the effects of Na and Sb incorporation on the morphology of CZTS-based absorber are:

1. The inclusion of **Na before synthesis** leads to sharp grains with facet and slight increase of grain size compared to the undoped sample. On the contrary, an 'overdose' of Na degrades the grain size.
2. The inclusion of **Na after synthesis** does not increase the grain size even with a higher amount of Na used in the process. Thus, no change of morphology is observed.
3. The inclusion of **Sb has no apparent effect** on the absorber except having slightly round shaped grains, while 'overdose' of Sb degrades the morphology of the absorber.
4. The inclusion of **Sb in the presence of Na** increased the grain size to more than  $1\ \mu\text{m}$ , which is the highest grain size achieved during this study for CZTS-based absorber. The co-doping of Na and Sb must have triggered the effectiveness of Sb as surfactant. Also, this can be related to the similar distribution profile of Na and Sb observed during SIMS analysis on this sample. (figure 5.5).

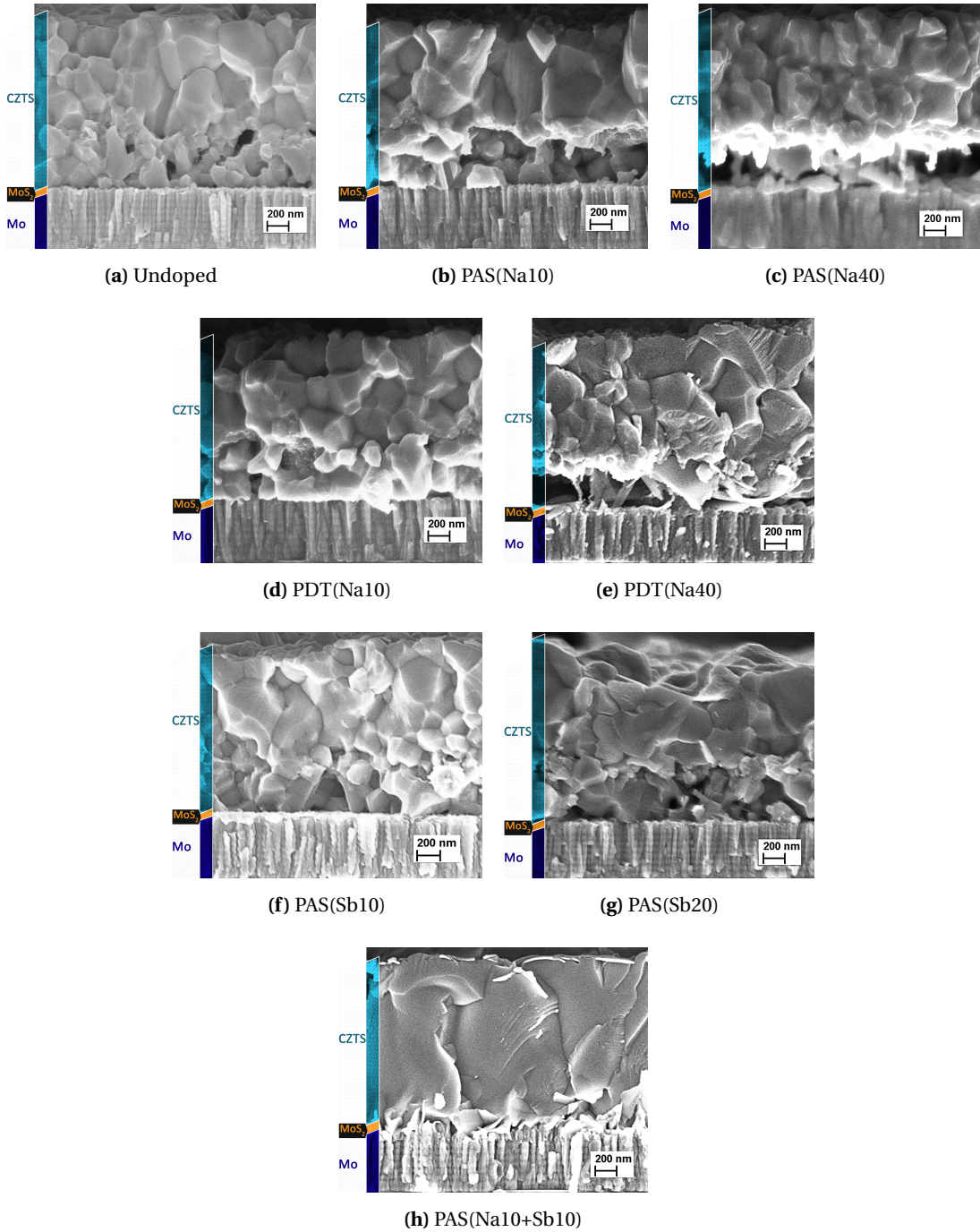
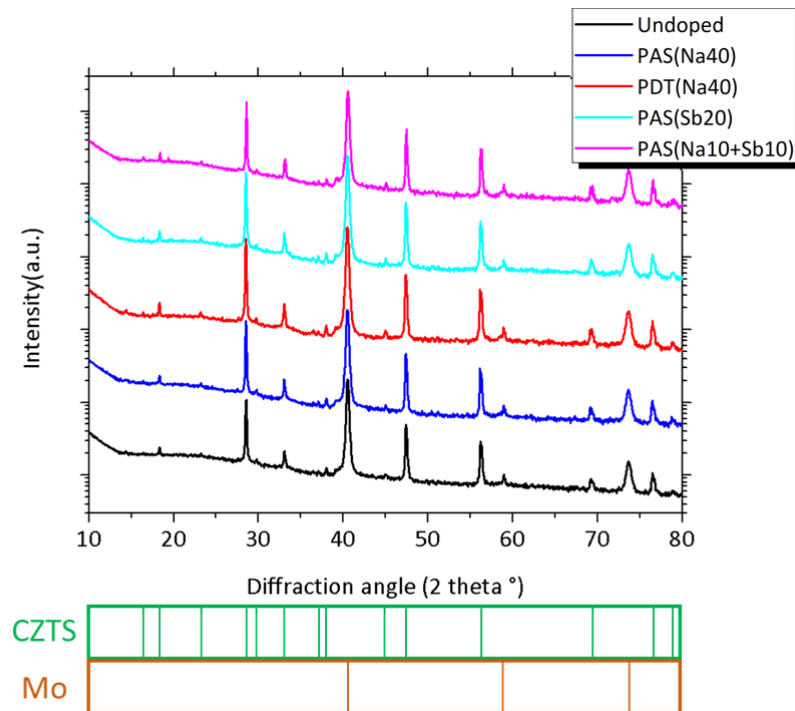


Figure 5.10: SEM cross-section images of CZTS absorber with different doping methods.

5.3.2.3 XRD analysis

The room temperature XRD of the CZTS absorber with the highest amount of Na and/or Sb used is shown in figure 5.11. XRD pattern from each experiment exhibit major peaks corresponding to the CZTS crystal structure. No noticeable peaks of secondary phases can be observed from figure 5.11. The diffraction peaks from (112), (220,204) and (312) planes are clearly observed at 28.44°, 47.33° and 56.09, which indicates the presence of a kesterite phase.



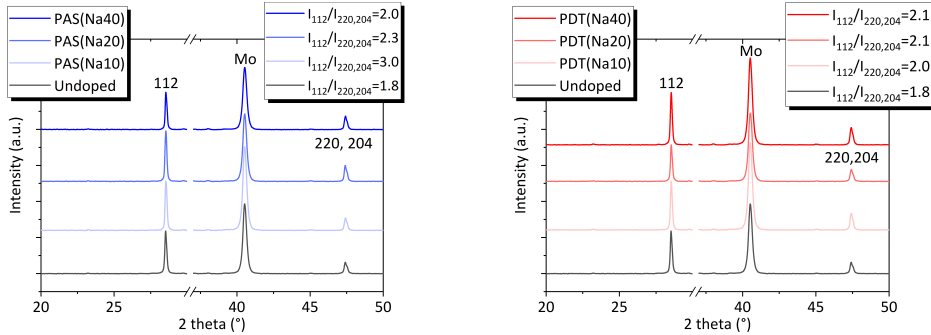
**Figure 5.11:** X-ray diffraction patterns of CZTS layers grown with various Na and Sb incorporation strategies.

**Effect on texturization:** The enlarged XRD diffractogram of all the samples are shown in figure 5.12, focusing the (112) and (220,204) peaks. The (112) and (220,204) reflection intensities have been determined by integrating the area below those peaks. The ratios of the intensity is shown in the inset of each respective XRD pattern.

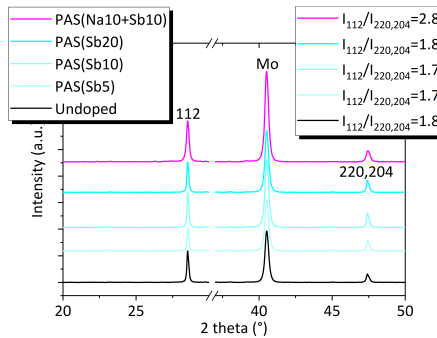
The PAS(Na) samples show preferential (112) orientation by having higher  $I_{112}/I_{220,204}$  value compared to undoped one (see figure 5.12 (a)), although, this value is decreasing with increasing amount of Na used. On the other hand, the PDT(Na) samples shows less pronounced preferential orientation (figure 5.12(b)) no and noticeable change using higher amount of Na is observed. For the PAS(Sb) samples (112) texturization is not favored compared to the undoped sample (figure 5.12(c)). But, samples with Na and Sb doping shows higher (112)

texturization, where  $I_{112}/I_{220,204}$  ratio is higher than the ratio of the undoped sample and similar to the PAS(Na10) one. Likewise, Rudmann et al., show similar properties of Na in the case of CIGS-based absorbers [132, 143].

From this analysis, it can be inferred that the texture of the CZTS compound is influenced by the presence of Na during synthesis (PAS(Na)), rather than added after synthesis (PDT(Na)). Furthermore, Sb incorporation did not show any preferential texturization.



(a) XRD diffractogram of all the PAS(Na) samples and undoped sample as a reference. (b) XRD diffractogram of all the PDT(Na) samples and undoped sample as a reference.



(c) XRD diffractogram of all the samples with Sb and undoped sample as a reference

**Figure 5.12:** XRD diffractogram of CZTS absorbers grown with various amount of Na and Sb under different experimental conditions. In the inset, the ratio of the intensity of peak (112) and peak (220) is indicated to demonstrate the preferred orientation due to Na and Sb incorporation.

**Effect on crystallite size:** XRD diffractograms are also used to calculate the average crystallite size of each sample from (112) peak by Scherrer's equation [144]. The detailed procedure for extracting crystallite size using Scherrer's equation is explained in section 3.2.4. The mean crystallite sizes of all the samples are shown in figure 5.13(b). Here, Na incorporation during the synthesis clearly increases the crystallite size compared to the undoped sample from 70 nm to 130 nm as confirmed by Prabhakar et al [145]. On the other hand, Na added after

### 5.3. Experimental results on Na and Sb incorporation

the synthesis has a small effect on the crystallite size, which is coherent with the grain size observed by SEM. Furthermore, the addition of Sb increases the crystallite size, while the grain size seen from SEM is unchanged compared to the reference sample. Therefore, the relation between mean crystallite size and morphology is not properly understood.

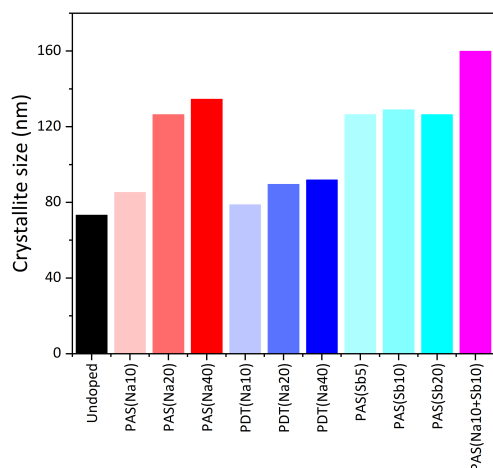


**Figure 5.13:** Crystallite size deduced from XRD diffractograms of Na and Sb incorporated samples.

#### 5.3.2.4 Raman analysis

The formation of a CZTS phase is further confirmed by Raman scattering (532 nm laser wavelength used) in figure 5.14, where all the spectra shows significant peaks associated with A mode symmetry of CZTS at  $288\text{ cm}^{-1}$  and  $338\text{ cm}^{-1}$  [58]. No obvious peaks associated with secondary phases can be detected from these spectra, which indicates good formation of CZTS compounds. From figure 5.14(a), it can be seen that the intensity and the width of both A mode peaks improved with Na doping for PAS(Na40) and PDT(Na40) sample compared to the undoped sample. In the case of the peak at  $338\text{ cm}^{-1}$ , the FWHM of the undoped sample was found to be  $7.2\text{ cm}^{-1}$ , while the FWHM of PAS(Na40) and PDT(Na40) was found to be  $5\text{ cm}^{-1}$  and  $4.6\text{ cm}^{-1}$  respectively. Narrower FWHM compared to the undoped sample indicates better crystallinity in the presence of Na.

On the contrary, Sb doping (PAS(Sb20)) showed similar Raman spectra as the undoped sample. Here, the FWHM of the PAS(Sb20) sample is found to be  $7.1\text{ cm}^{-1}$  for the peak at  $338\text{ cm}^{-1}$ , which is similar to the undoped one. Na and Sb incorporation (PAS(Na10+Sb10)) showed similar Raman scattering as the Na doped sample, with similar values of FWHM for the peak at  $338\text{ cm}^{-1}$ .

Hence, Na incorporation results in better crystallinity for CZTS compound seen by Raman

scattering. These effects can be also clearly seen in figure 5.14(b), which is an enlarged image of A mode symmetry peak of CZTS at  $338\text{ cm}^{-1}$ .

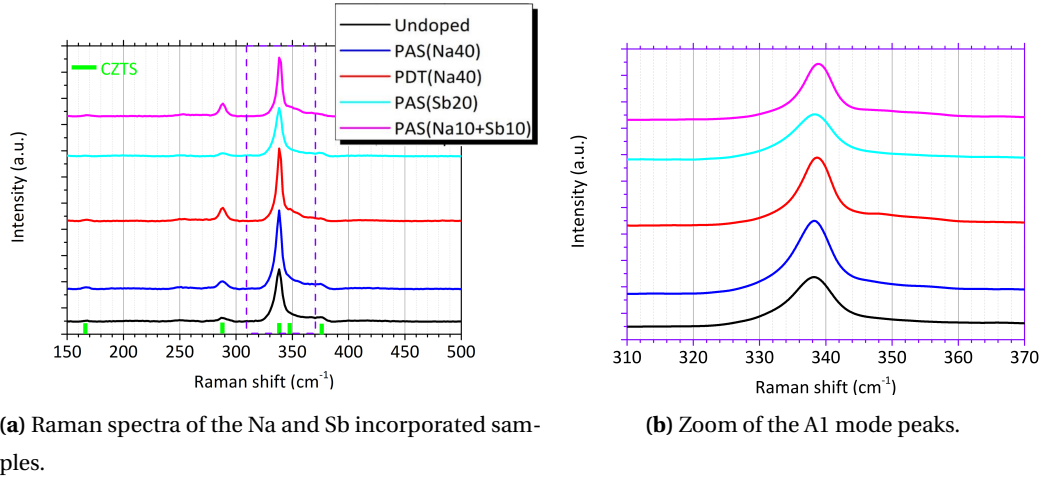


Figure 5.14: Effect of Na and Sb on CZTS absorber observed by Raman spectroscopy.

### 5.3.3 Effects of Na and Sb on device properties

In this section, several issues have been pointed out by the result obtained from light J-V, dark J-V, capacitance-voltage measurement and EQE.

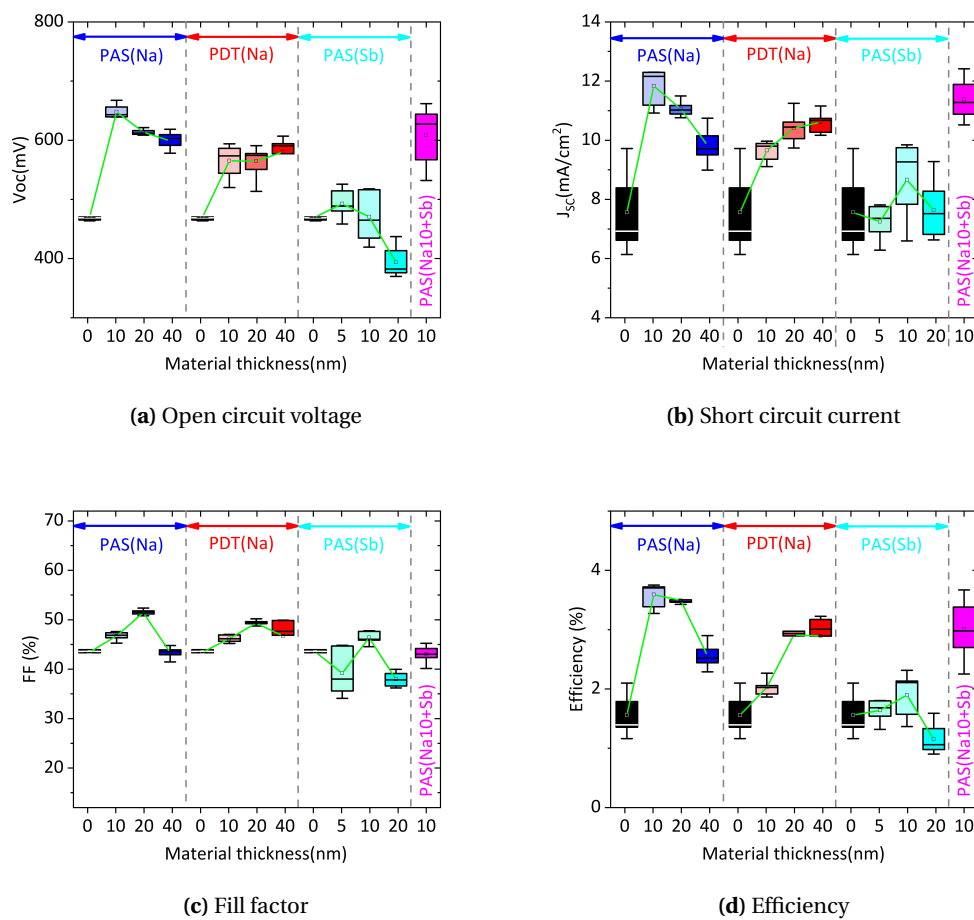
#### 5.3.3.1 Light J-V Measurements

The electrical parameter ( $V_{OC}$ ,  $J_{SC}$ , FF and PCE) of complete solar cells using all the experimental samples under AM 1.5G light illumination is shown in figure 5.15. For each sample, 6 to 9 solar cells are measured and the maximum, minimum, mean (dots connected by green line for representation of trend), median (horizontal line in the box) and interquartile range (colored box showing from 75th percentile to 25th percentile) is shown as a box plot.

First of all, the undoped sample showed low efficiency ( $<2\%$ ) with limited  $V_{OC}$  ( $\sim 530\text{ mV}$ ),  $J_{SC}$  ( $\sim 7\text{ mA/cm}^2$ ) and FF ( $\sim 42\%$ ). A significant improvement in efficiency is brought by the introduction of Na, particularly because of a  $V_{OC}$  gain of about  $100\text{ mV}$ -  $150\text{ mV}$ . Second, the PAS(Na) strategy shows better device properties compared to PDT(Na). PCE decrement can be observed while using higher amount (40 nm) of NaF using PAS(Na) strategy, mainly due to the reduction in FF and  $J_{SC}$ . But, higher amount of NaF shows better efficiency using the PDT(Na) strategy. Third, Sb incorporation seems to have no or negative effect in terms of PCE compared to the undoped sample. But, the PAS(Na10+Sb10) sample showed similar increase in PCE as PAS(Na10) sample, irrespective of the grain size increment in the case

### 5.3. Experimental results on Na and Sb incorporation

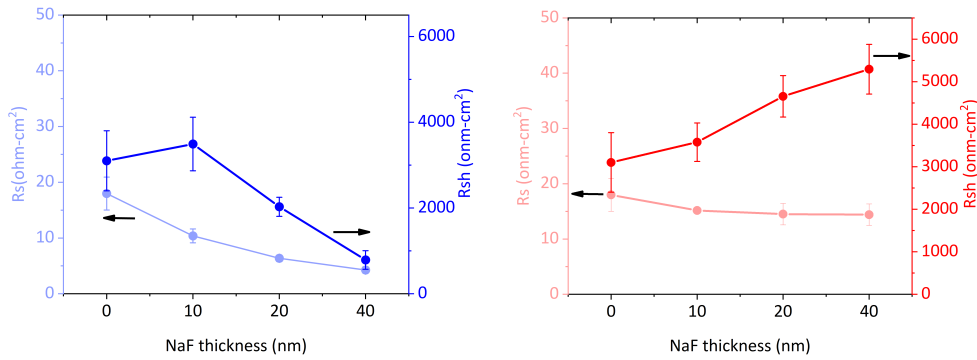
of PAS(Na10+Sb10). Since Sb shows no improvement in device properties alone, the PCE improvement of PAS(Na10+Sb10) compared to undoped sample is, therefore from Na only. Thus, later in this chapter, Sb doped samples will not be considered and some additional characterization can be found in appendix.



**Figure 5.15:** PV parameter of all the samples doped with different thicknesses of NaF using PAS(Na) and PDT(Na) methods and different thicknesses of Na and Sb using PAS(Sb) and PAS(Na+Sb) methods.

#### 5.3.3.2 Dark J-V measurements:

Series resistance ( $R_S$ ) and shunt resistance ( $R_{Sh}$ ) data are extracted from dark J-V curve of Na doped samples and shown in figure 5.16.



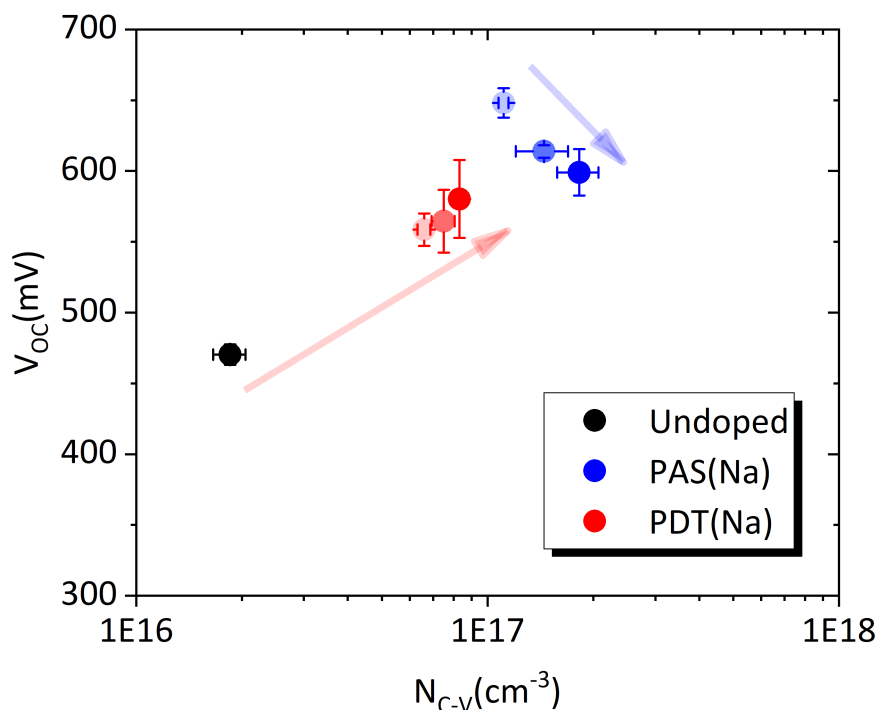
(a) Series( $R_S$ ) and shunt resistance( $R_{Sh}$ ) of the PAS(Na) samples. (b) Series( $R_S$ ) and shunt resistance( $R_{Sh}$ ) of the PDT(Na) samples.

Figure 5.16: Electrical parameter (series resistance, shunt resistance) of samples doped with Na.

In figure 5.16(a), in the case of the PAS(Na) strategy, increasing the amount of Na shows a decrease in both  $R_S$  and  $R_{Sh}$ , compared to the undoped sample. The general tendency of doping is known to reduce the series resistance [46], which explains this tendency. And the reason for  $R_{Sh}$  decrement is related to the bubble formation in the absorber. An alternative current path is created through peeled off (due to bubble formation) part of the absorber, which reduces the  $R_{Sh}$ . In the case of the PDT(Na) strategy (figure 5.16(b)), increasing amount of Na shows little decrease in  $R_S$  (overall high  $R_S$ ) and increase in  $R_{Sh}$ , compared to undoped sample.  $R_S$  and  $R_{Sh}$  value of PV device mainly affects the FF, which can explain the FF variation shown in figure 5.15. But, it can not explain the increase of PCE, as the main contribution is from the increase in  $V_{OC}$ .

5.3.3.3 C-V measurements:

In figure 5.17, the evolution of average  $V_{OC}$  is presented as a function of apparent carrier concentration  $N_{C-V}$ . Here, the colored circles are representing the average value of respective samples, error bars are representing the standard deviation and arrow is representing the increment of Na used for each procedure.



**Figure 5.17:** The evolution of  $V_{OC}$  as a function of  $N_{C-V}$ . The arrow is indicating the increasing amount of Na used in each case.

First of all, Na incorporation increased the apparent carrier concentration of CZTS device in an order of magnitude compared to the undoped sample (see figure 5.17(a)). A tendency of increased  $V_{OC}$  can be observed by the increase of  $N_{C-V}$ . Second,  $N_{C-V}$  of PAS(Na) samples are higher compared to the PDT(Na) samples. Thus, the PAS(Na) method appeared to be much effective for Na incorporation compared to the PDT(Na) method. Third, a decrement of  $V_{OC}$  is observed for PAS(Na) samples, while higher amount of Na used, even though the  $N_{C-V}$  increased. This can be related to the poor microstructural properties explained earlier. Generally Na incorporation leads to higher hole concentration in the bulk of the kesterite absorber [122], which explains the increase in  $N_{C-V}$ . Also, the composition of bulk material is also reported to affect the hole concentration in the bulk [146]. Therefore, to know the effect of external doping, we made sure that the reference sample and the sample with external doping have similar cation composition. The average cation values found from EDX measurement is of  $\text{Cu}/\text{Zn}+\text{Sn}=0.73(\pm 0.03)$ ,  $\text{Zn}/\text{Sn}=1.11(\pm 0.04)$  and  $\text{Cu}/\text{Sn}=1.56(\pm 0.06)$ .

The  $V_{OC}$  increment due to the increase in  $N_{C-V}$  can be explained by the following equation

[147],

$$\Delta V_{OC} = \frac{kT}{q} \ln\left(\frac{N_{C-V}}{N_0}\right) \quad (5.1)$$

Here,  $k$  is the Boltzmann constant,  $T$  is the temperature during the experiment (300K),  $q$  is the charge of the electron,  $N_{C-V}$  is the net carrier concentration of the doped sample and  $N_0$  is the net carrier concentration of the undoped sample. However, this equation alone can not explain the 100-150 mV of  $V_{OC}$  increase. Therefore, some other effect might be associated with this increment of  $V_{OC}$  along with the increased net carrier concentration.

Another possible reason for the increased  $V_{OC}$  could be the increase of diffusion length ( $L_D$ ). The relation between  $J_{Ph}$  and  $V_{OC}$  was found from Green et al., [148],

$$V_{OC} = \frac{kT}{q} \ln\left(\frac{J_{Ph}}{J_0}\right) \quad (5.2)$$

Here,  $J_0$  is saturation current, which can be described by,

$$J_0 = \frac{qDn_i^2}{L_D N} \quad (5.3)$$

Where  $n_i$  stands for the intrinsic carrier concentration and  $N$  stands for the majority carrier concentration. By using equation 5.2 and 5.3, considering  $n_i$ ,  $N$  and  $D$  is constant for the samples, one can deduce,

$$V_{OC} \propto \ln L_D \quad (5.4)$$

Thus, the increase of  $V_{OC}$  and  $J_{SC}$  can be partially explained by diffusion length. This point will be further discussed in a later section.

#### **5.3.3.4 EQE measurements**

Figure 5.18, shows the EQE spectra of Na incorporated samples. First, incorporation of Na (any strategy) shows improves EQE for all wavelength due to reduced interface recombination and increased carrier collection length [149]. The EQE of PAS(Na) showed the highest EQE

### 5.3. Experimental results on Na and Sb incorporation

response in the case of the PAS(Na10) sample and gradually decrease with the increased amount of Na used. Although the EQE response of PDT(Na40) sample is higher compared to PAS(Na10) sample, due to the higher series resistance of PDT(Na40) sample, the  $J_{SC}$  of this sample is found to be lower [46].

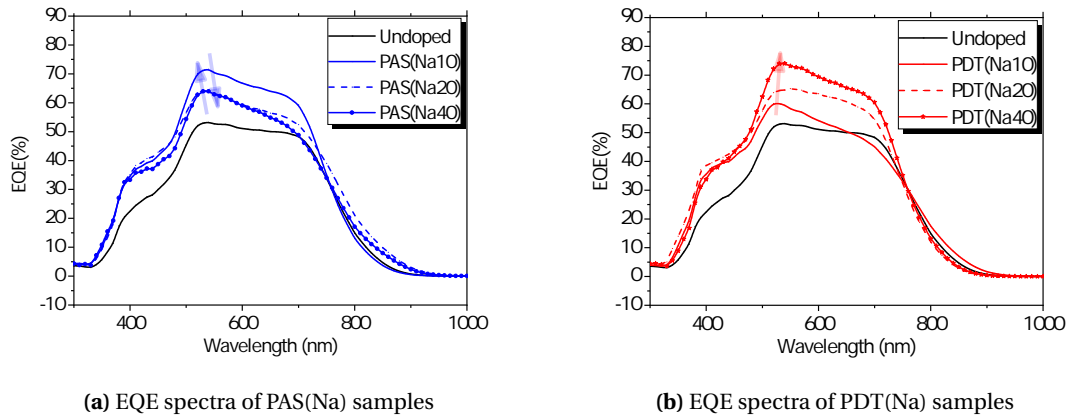


**Figure 5.18:** EQE spectra of samples with different amount of Na doping.

**Finally**, it is clear that for PAS(Na) strategy, 10nm NaF showed the best device properties and it started to decrease with increased amount of NaF used (use of 20 nm NaF). Therefore, a value between 10nm and 20nm (in this case 15 nm is used) of NaF is used to prepare another sample. PDT(Na) strategy got saturated in terms of device properties using 40nm of NaF, therefore no further sample is prepared. The light and dark J-V curve of PAS(Na15) sample are shown in figure 5.19. Also, the detailed electrical parameters of the PAS(Na15) and PDT(Na40) sample are shown along with undoped sample in table 5.3 (for the cell with the best efficiency).

Indeed, further improvement is achieved using 15 nm NaF for PAS(Na) strategy. Highest  $V_{OC}$  of 678 mV is achieved with voltage deficit of 802 mV. Increased  $J_{SC}$ , FF and efficiency is achieved due to decrease of  $R_S$  and increase of  $R_{Sh}$  and  $N_{C-V}$ . Although, the difference of  $V_{OC}$  between PAS(Na15) and PAS(Na40) is 94 mV, the net carrier concentration only accounts for 8 mV. Therefore, the minority carrier lifetime must be increased for PAS(Na15) sample, which showed higher  $V_{OC}$  and  $J_{SC}$ .

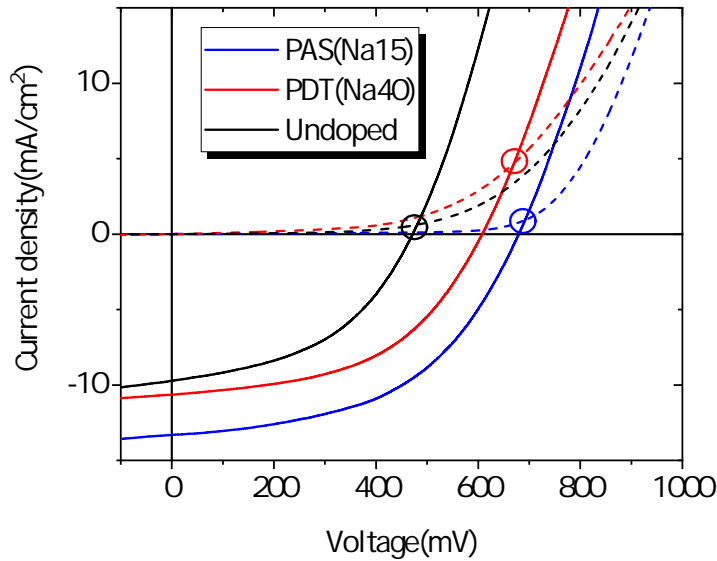


**Figure 5.19:** light J-V (solid line) and dark J-V (dashed line) curve of the optimized PAS(Na) method using 15 nm NaF along with the PDT(Na40) sample and undoped sample (circles are showing the crossover point for each method)

**Table 5.3:** All electrical parameters of PAS(Na15) and PDT(Na40) sample compared to undoped sample

Sample	Light IV				Dark IV		C-V			EQE		
	$V_{OC}$ mV	$J_{SC}$ $\text{mA}\cdot\text{cm}^{-2}$	FF %	Efficiency %	$R_S$ $\text{ohm}\cdot\text{cm}^2$	$R_{Sh}$ $\text{ohm}\cdot\text{cm}^2$	$N_{C-V}$ $\text{cm}^{-3}$	W nm	$\Delta V_{OC}$ mV	$J_{SC}(\text{EQE})$ $\text{mA}\cdot\text{cm}^{-2}$	$E_g$ eV	$V_{OC}$ deficit mV
Undoped	470	9.7	46	2.1	18	3101	$1.85\text{E}+16$	304		10.3	1.52	1050
PAS(Na15)	678	13.3	50	4.5	9.1	3320	$1.13\text{E}+17$	157	47	15.5	1.48	802
PDT(Na40)	584	11	50	3.2	14.4	5294	$8.31\text{E}+16$	218	39	13.2	1.52	936

## 5.4 Simulation using e-ARC

e-ARC<sup>1</sup> is a simulation software that can be used to estimate physical parameters of the solar cells (carrier collection length, recombination losses etc) using EQE analysis. Details on the simulation process is explained in section 3.3.4. From carrier collection length, we could have an estimation of carrier diffusion length according to following equation 5.5.

$$L_C = L_D + W \quad (5.5)$$

<sup>1</sup><https://unit.aist.go.jp/rcpv/cie>

Here,  $L_C$ ,  $L_D$  and  $W$  denote the carrier collection length, carrier diffusion length and width of the depletion region. Width of the depletion region ( $W$ ) can be extracted from C-V measurements.

First, the experimental and simulated EQE (calculated using e-ARC) of undoped sample are shown in figure 5.20, along with the absorption in different layers of solar cell. For this fitting, carrier collection length of 165 nm is found to be optimum. Figure 5.20 shows a fitting mismatch at short wavelength (500 nm-600 nm), where the calculated EQE is higher than experimental EQE. The current loss in ( $J_{loss}$ ) each layer is listed in table 5.4 and 5.4, along with the optimum thickness found for each layer.

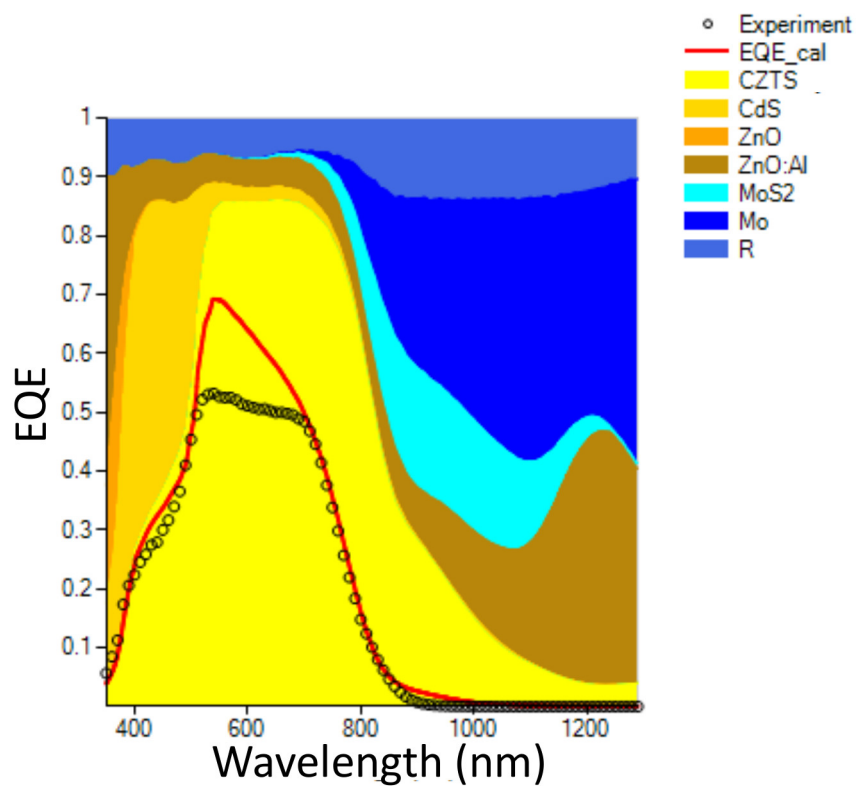


**Figure 5.20:** Fitting representation of experimental EQE from undoped sample with simulated EQE.

One of the main reason evoked for limited EQE at all wavelengths in thin film solar cell is surface recombination at the heterojunction interface [149]. It can explain the mismatch between experimental and simulated value. To into account this front interface recombination, another layer with same optical properties as absorber (CZTS) is introduced in the calculation. This layer is be called dead layer, which will not allow carrier extraction in the interface and as a result calculated EQE will be lower for short wavelength side. Although, this way of considering

## Chapter 5. Strategies and effects of Na and Sb incorporation on CZTS absorber

**Table 5.4:** List of current losses ( $J_{\text{absorption}}$ ) and the optimized thickness of the layers of solar cell using undoped sample.

Layer	Thickness (nm)	$J_{\text{absorption}}$ (mA/cm <sup>2</sup> )
ZnO:Al	400	3.8
ZnO	50	0.2
CdS	86	3.6
CZTS	1500	25.0
Mo		4.3
MoS <sub>2</sub>	50	2.4

**Table 5.5:** Absorption in CZTS ( $J_{\text{CZTS}}$ ) along with the loss by reflection ( $J_{\text{Reflection}}$ ), recombination ( $J_{\text{Recombination}}$ ) and  $J_{\text{EQE}}$  derived from undoped sample.

$J_{\text{CZTS}}$	$J_{\text{Reflection}}$	$J_{\text{recombination}}$ (mA/cm <sup>2</sup> )	$J_{\text{EQE}}$
25.0	4.0	13.3	11.8

interface recombination is purely mathematical, the thickness of the dead layer accounts for the recombination velocity at the front interface.

The schematic of this new layer, which is placed between CdS and CZTS layer, is illustrated in figure 5.21.



**Figure 5.21:** Schematic of thin film layers used for the EQE calculation with a dead layer to consider as front interface recombination.

Finally, after optimizing carrier collection length and dead layer thickness, the error (MSE) value decreased, indicating higher degree of matching between experimental and simulated EQE. The EQE spectra and associated data are shown in figure 5.22 and table 5.6 and 5.7. Using dead layer, we can have a quantitative comparison on interface recombination by the thickness or the current density loss of this layer from sample to sample, where higher thickness will indicate high interface recombination.

**Table 5.6:** List of current losses ( $J_{\text{absorption}}$ ) and the optimized thickness of the layers of solar cell using undoped sample considering dead layer.

Layer	Thickness (nm)	$J_{\text{absorption}}$ (mA/cm <sup>2</sup> )
ZnO:Al	400	3.8
ZnO	50	0.2
CdS	50	2.4
Dead layer	31	4.6
CZTS	1500	25.0
Mo		4.5
MoS <sub>2</sub>	50	2.5

**Table 5.7:** Absorption in CZTS ( $J_{\text{CZTS}}$ ) along with the loss by reflection ( $J_{\text{Reflection}}$ ), interface recombination from dead layer ( $J_{\text{Interface}}$ ), bulk recombination ( $J_{\text{Bulk}}$ ) and  $J_{\text{EQE}}$  derived from undoped sample considering dead layer.

$J_{\text{CZTS}}$	$J_{\text{Reflection}}$	$J_{\text{Interface}}$	$J_{\text{Bulk}}$	$J_{\text{EQE}}$
(mA/cm <sup>2</sup> )				
21.3	4.0	4.6	9.4	12.0

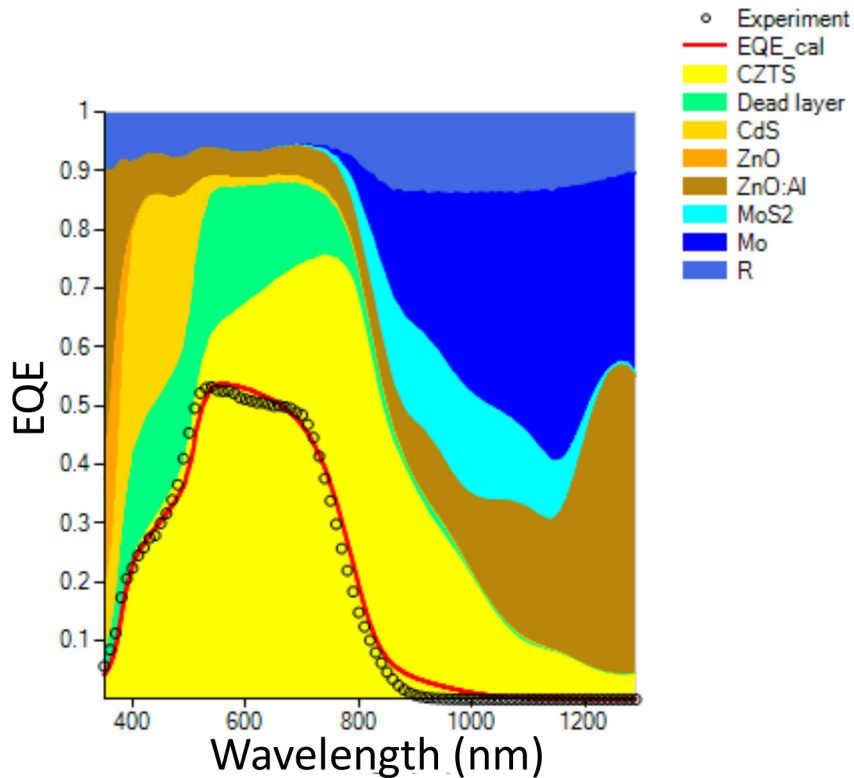


**Figure 5.22:** Fitting representation of experimental EQE from undoped sample with simulated EQE considering a dead layer(front interface recombination)

With this fitting, the carrier collection length for undoped sample determined to be 285 nm,

which is less than the depletion region width of 300 nm estimated from C-V measurement. That means the value of  $L_D$  is negative. However, due to the uncertainty of both  $W$  estimated by C-V and  $L_C$  by EQE, it can be assumed that  $L_D$  for undoped sample is close to 0. There is a slight mismatch for longer wavelength in the fitting (see figure 5.22), which might be due to the fact that, optical parameter used for CZTS absorber is taken from a source which used 789 nm thick CZTS material [65], where experimental sample consists of about 1500 nm thick absorber. Nonetheless, this fitting is fairly good to make a comparison between different devices with same layer construction.

A similar simulation has been done on PAS(Na15) sample, which is shown in figure 5.23 and table 5.8 and 5.9. A carrier collection length of 425 nm is found, which is significantly higher than the collection length of undoped one. Furthermore, dead layer thickness is found to be 4 nm, which is lower than the dead layer thickness of undoped sample (31 nm). Therefore, compared to the undoped sample, the PAS(Na15) sample has a reduced front surface recombination loss (reduced from 4.6 mA/cm<sup>2</sup> to 0.7 mA/cm<sup>2</sup>), as well as a reduced bulk recombination loss (from 13.3 mA/cm<sup>2</sup> to 5.4 mA/cm<sup>2</sup>)

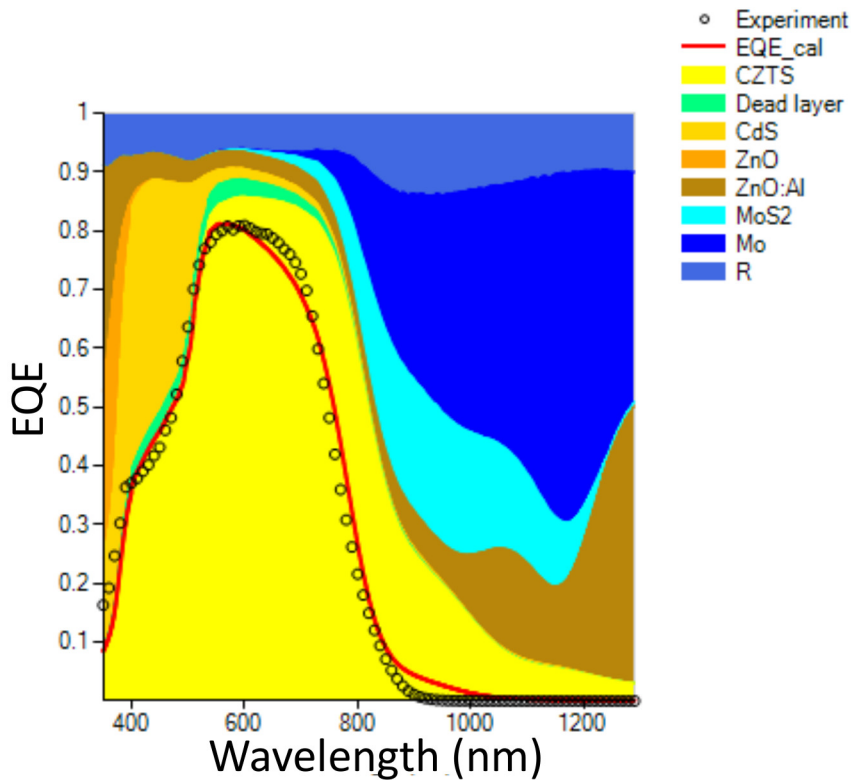


**Figure 5.23:** Fitting representation of experimental EQE from PAS(Na15) sample with simulated EQE considering a dead layer (front interface recombination), along with the contribution from all the layer and reflection.

**Table 5.8:** List of current losses ( $J_{\text{absorption}}$ ) and the optimized thickness of the layers of solar cell using PAS(Na15) sample.

Layer	Thickness (nm)	$J_{\text{absorption}}$ (mA/cm <sup>2</sup> )
ZnO:Al	350	2.7
ZnO	50	0.2
CdS	59	2.9
Dead layer	4	0.7
CZTS	1500	23.3
Mo		6
MoS <sub>2</sub>	50	3.7

**Table 5.9:** Absorption in CZTS ( $J_{\text{CZTS}}$ ) along with the loss by reflection ( $J_{\text{Reflection}}$ ), interface recombination from dead layer ( $J_{\text{Interface}}$ ), bulk recombination ( $J_{\text{Bulk}}$ ) and  $J_{\text{EQE}}$  derived from PAS(Na15) sample.

$J_{\text{CZTS}}$	$J_{\text{Reflection}}$	$J_{\text{Interface}}$ (mA/cm <sup>2</sup> )	$J_{\text{Bulk}}$	$J_{\text{EQE}}$
23.3	3.9	0.7	5.6	17.7

Using similar procedure, all the sample for this study are analyzed to obtain carrier collection length and the result is discussed in following section.

#### 5.4.1 Effect of Na incorporation on Carrier Diffusion Length

From the simulation described in section 3.3.4, carrier collection length of all Na incorporated samples are calculated. As the depletion region width ( $W$ ) of all the samples are estimated from capacitance-voltage measurement, equation 5.5 can be applied to deduce the value of minority carrier diffusion length ( $L_D$ ). The  $L_D$  and  $W$  of all Na incorporated samples are shown in figure 5.24. For PAS(Na) samples, while the  $W$  is decreasing due to increased  $N_{C-V}$ , the  $L_D$  first increased until PAS(NaF15) and than decreased again. On the other hand, PDT(Na) sample showed lower  $L_D$ , due to the lack of Na incorporation described before. Also, from this figure, we can see that, for Na incorporated samples, carrier collection lengths are more dependent on  $L_D$ , than on  $W$ . It explains that  $J_{\text{SC}}$  still increases even with reduced  $W$ .

$V_{\text{OC}}$  of all samples as a function of the carrier diffusion length ( $L_D$ ) and interface recombination loss ( $J_{\text{Interface}}$ ) are shown in figure 5.25. A clear correlation can be seen between  $L_D$  and  $J_{\text{Interface}}$  with  $V_{\text{OC}}$ . A reduced interface recombination and increased carrier diffusion length can be observed as a result of Na doping. A similar conclusion was made by Gershon et al, [125] showing the effect of Na as suppressor of non-radiative recombination. Thus, it can explain the increase of  $V_{\text{OC}}$  as well addition to the contribution of net carrier concentration.

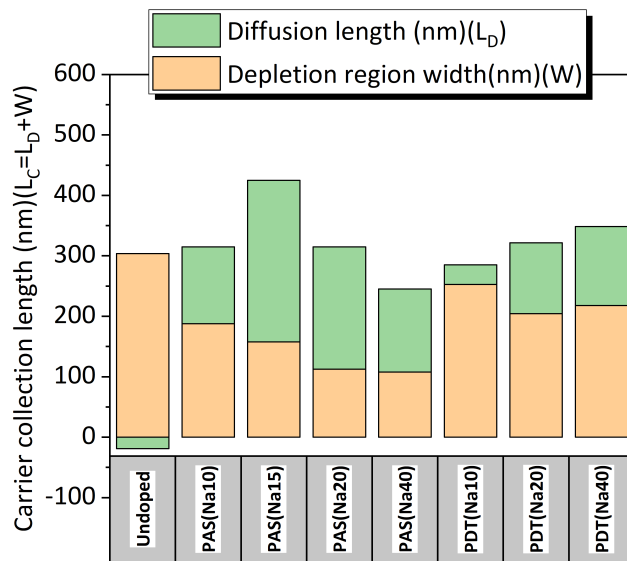
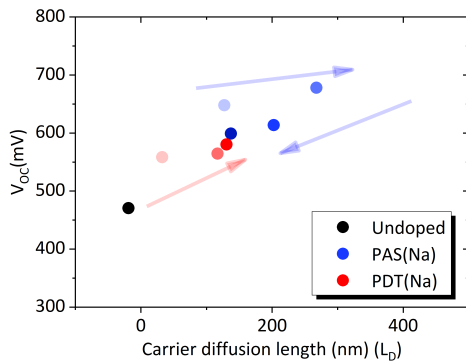
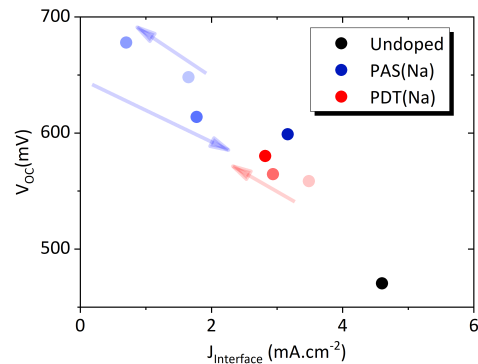


**Figure 5.24:** Estimated collection length, diffusion length and depletion region width of all samples. Here, arrow is indicating the increasing amount of Na.



(a) Carrier diffusion length vs  $V_{OC}$ .



(b) Estimated interface recombination loss ( $J_{Interface}$ ) vs  $V_{OC}$ .

**Figure 5.25:**  $V_{OC}$  as a function of carrier collection length and interface recombination loss ( $J_{Interface}$ ) for samples with different Na incorporation strategy.

## 5.5 Conclusion

This study reveals the effects of intentional Na and Sb contamination/incorporation on CZTS-based absorber. Different strategies are applied for Na and Sb incorporation process. Na showed beneficial effect on the morphology of the CZTS absorber, mainly inducing faceted big grains, although overdose of Na degrades the morphology. The application of Na during

synthesis is found to be the most effective way of doping, in terms of CZTS absorber morphology and device performance. On the other hand, Sb doping does not show any morphological or electrical improvement on CZTS absorber, without the presence of Na. When Na is present in the absorber Sb incorporation results in improved crystallization.

Finally, Na incorporation enhanced the PCE of solar cell by improving not only  $V_{OC}$  and FF but also  $J_{SC}$ . But the most significant improvement came from the increase in  $V_{OC}$ . Increase in carrier concentration and reduction in recombination (interface and bulk) are the reasons for this improvement.

# 6 Bandgap grading

## Contents

---

<b>6.1 State of the Art</b> . . . . .	<b>129</b>
<b>6.2 Front Grading</b> . . . . .	<b>131</b>
6.2.1 Experimental Procedure . . . . .	131
6.2.2 Results and discussions . . . . .	133
<b>6.3 Back Grading</b> . . . . .	<b>146</b>
6.3.1 Experimental Procedure . . . . .	146
6.3.2 Result and discussion . . . . .	147
<b>6.4 General discussion and conclusion</b> . . . . .	<b>154</b>

---

The objective of this chapter is to examine the fabrication process of a front graded and back graded CZTSSe absorber. A detailed characterization towards the realization of bandgap grading will be also analyzed and discussed.

## 6.1 State of the Art

The best efficiency for selenium-based kesterite absorber is 11.6% [67] (with a bandgap of  $\sim 1$  eV) and 11% [78] for sulfur-based kesterite absorber (with a bandgap of  $\sim 1.5$  eV). A higher bandgap gives a higher  $V_{OC}$  at the expense of  $J_{SC}$ , while a lower bandgap does the opposite. The bandgap tuning ability is induced by the change in the ratio of sulfur and selenium. Therefore, the bandgap of kesterite absorber can be tuned for best  $V_{OC}$  in terms of best possible  $J_{SC}$ . Indeed, the best certified efficiency achieved experimentally by kesterite based absorber is 12.6% [14], with a bandgap of 1.13 eV due to the presence of both sulfur and selenium. But, this efficiency is still lower than that of CIGS technology. The high-efficiency CIGS technology

applies In-Ga gradient throughout the thickness of the absorber. This produces a bandgap graded absorber, resulting in reduced recombination and improved performances [47, 150]. Similarly, the bandgap grading for kesterite absorbers appeared to be an interesting topic of research concerning efficiency improvement of this technology.

The change of bandgap by changing the chalcogen ratio is nearly linear and the main change can be seen in the conduction band [36]. A higher to lower sulfur content from absorber-buffer interface towards the bulk of the absorber (front grading) will give improved  $V_{OC}$ . And a lower to higher sulfur content from the bulk of the absorber towards Mo/absorber interface (back grading) will increase  $J_{SC}$  and FF due to improved carrier collection. Several simulations associated with bandgap grading of kesterite-based absorber already proved its beneficial effect by improving the performance [151, 152]. They reported, however, that the device performance was very sensitive to the grading placement within the absorber, as well as to the type and the degree of the grading.

Experimentally, it has been proven that having different S/Se vapor pressure during the annealing of elemental precursors is sufficient to tune the bandgap of a kesterite absorber, but using this process, the S/Se ratio was constant throughout the absorber [153]. On the other hand, using a compound precursor shows higher sulfur content at the back and lower at the front of the absorber [154]. Nonetheless, realizing and controlling a variable S/Se ratio throughout the absorber is complicated due to the fact that diffusion of Se in kesterite is rapid with an activation energy of  $0.5 \pm 0.1$  eV [155], which is one of the main challenge towards realizing S/Se grading. Experimentally, at 500°C, half of the sulfur was replaced by Se during a sulfo-selenization process in 10 seconds [156].

Different synthesis strategies have been tested in the literature to control the anion composition throughout the depth of the absorber. A front grading was realized recently, by surface sulfurization of a sputter-deposited CZTSe absorber and the device properties were analyzed in depth without emphasizing on the reaction mechanism of the process [157]. Yang et al, [158] synthesized a CZTSSe sample with front grading using a different mixture of  $SeS_2/Se$  and achieved a PCE of 12.3%. This is one of the highest efficiency achieved by bandgap grading, but it is still lower than the highest efficiency achieved by a CZTSSe-based absorber without any gradient. In another case, the CZTSe nano-particle annealed under S and Se environment, showed replacement of the Se by S at a temperature lower than 500°C, due to the differences of vapor pressure at a this temperature. A defect layer was also created on the surface of such a sample during this process, due to the expansion of the volume [159].

Ross et al, [160] selenized a pre-sulfurized absorber to achieve back grading. This experiment did not show a continuous distribution of Se throughout the absorber, but rather larger CZTS grains restraining the nucleation and the growth of selenide grains at low-temperature selenization. However, it showed that selenization for a longer time resulted in grain growth of selenide grains at the expense of sulfur grains. In addition, the relation of Na with Se diffusion in CZTS sample was pointed out showing that sodium selenide facilitates the Se incorporation in the absorber. On the other hand, Kato et al, [161] showed a successful application of back grading obtaining 11% PCE for submodule, although lack of sufficient experimental details and analysis made this result hard to replicate.

All the above-mentioned works mostly used compound precursor for realizing bandgap grading. However, it has been pointed out that CZTS inhibits the diffusion of Se compared to elemental metal [156]. Using elemental precursor for bandgap grading is therefore interesting to gain some valuable insights. Bandgap grading also requires knowledge on the effect of anion composition in terms of structural and microstructural properties of the absorber, for better controllability of the reaction. According to Dimitrievska et al [57], a sulfur-rich absorber shows a decrease of domain size from the surface to the rear of the film, whereas selenium-rich absorber shows a homogeneous domain size with lower values of strains compared to sulfur-rich one.

In this chapter, the fabrication process of a CZTSSe absorber with front and back bandgap grading using elemental metal precursor will be presented. Also different characterization processes will be performed in order to better understand the reaction mechanism associated with bandgap grading.

## 6.2 Front Grading

### 6.2.1 Experimental Procedure

This section aims at producing a CZTSSe absorber and solar cell with a wider bandgap close to the front surface (CdS/CZTS interface). The strategy is to create a [S]/[S+Se] grading from the surface of the absorber towards the bulk by sulfurizing a CZTSe absorber- starting from an absorber synthesized with the standard procedure explained in chapter 4. Different sulfurization conditions (temperature, duration) have been tested to control the position and the range of the gradient composition.

The schematic of the annealing procedure is shown in figure 6.1. First, a standard selenization

is done on all the samples (figure 6.1(a)). Later, these samples are annealed under sulfur environment at different temperatures (200°C-550°C) for 10 minutes and two more samples are prepared at a 550°C annealing temperature but for the duration of 1 minute and 30 minutes respectively (figure 6.1(b)). The name of each sample is given according to the selenization and sulfurization profile used for the annealing. For instance, in  $Se_{Std.S550(1\ min)}$ ,  $Se_{Std.}$  stands for standard selenization and  $S_{550(1\ min)}$  stands for sulfurization at 550°C for 1 min prior to natural cooling.

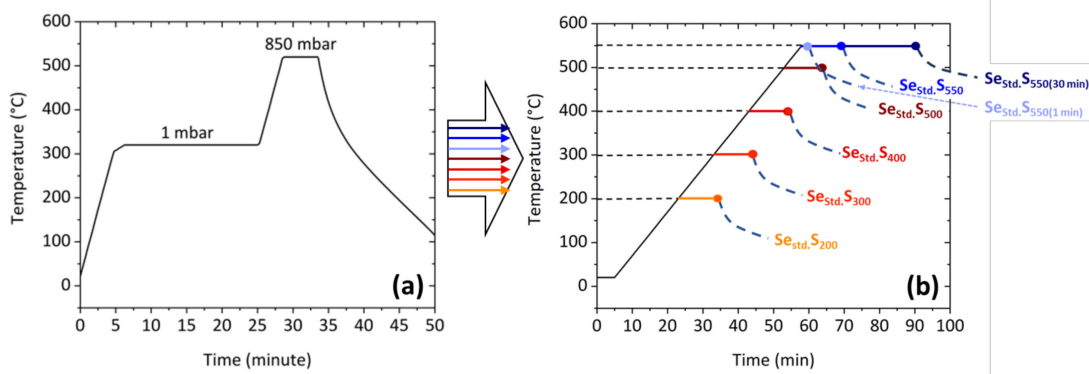


**Figure 6.1:** Temperature profile of the precursor selenization to synthesize the CZTSe absorber(a) and temperature profile showing different temperatures points used for sulfurization of the CZTSe absorber(b) to achieve front grading.

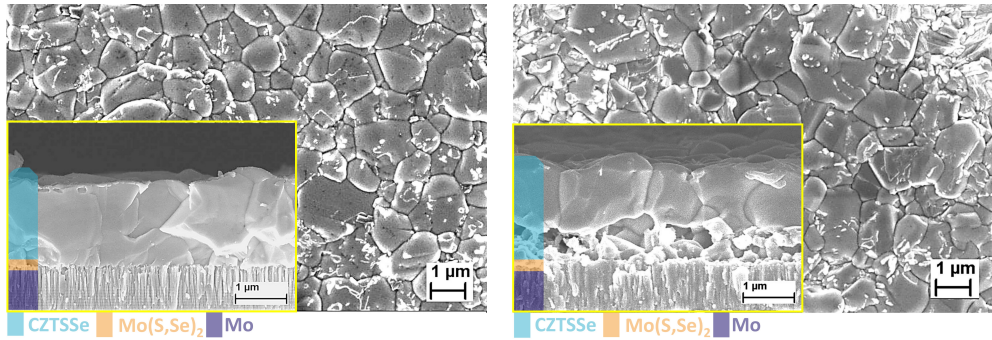
The name of each sample and annealing details are also shown in table 6.1 along with the anion and cation composition of the material. These compositions will be discussed briefly in section 6.2.2.

**Table 6.1:** The composition ratio of anion and cation measured by EDX along with the annealing conditions of each sample.

Sample name	Selenization	Sulfurization temp.(°C)	Sulfurization duration (min)	Cu(at%)	Zn(at%)	Sn(at%)	[S]/[S+Se]
$Cu_2ZnSnSe_4$	Standard	N/A	N/A	41.5±0.5	31.8±0.5	26.7±0.5	0
$Se_{Std.S200}$	Standard	200	10	41.6±0.5	31.8±0.5	26.4±0.5	0.05±0.02
$Se_{Std.S300}$	Standard	300	10	41.7±0.5	31.9±0.5	26.4±0.5	0.07±0.02
$Se_{Std.S400}$	Standard	400	10	41.7±0.5	32.1±0.5	26.1±0.5	0.09±0.02
$Se_{Std.S500}$	Standard	500	10	41.7±0.5	32.1±0.5	26.2±0.5	0.16±0.02
$Se_{Std.S550(1\ min)}$	Standard	550	1	41.7±0.5	32.1±0.5	26.1±0.5	0.18±0.02
$Se_{Std.S550(10\ min)}$	Standard	550	10	42.2±0.5	32.4±0.5	25.4±0.5	0.25±0.02
$Se_{Std.S550(30\ min)}$	Standard	550	30	43.6±0.5	32.8±0.5	23.6±0.5	0.95±0.02

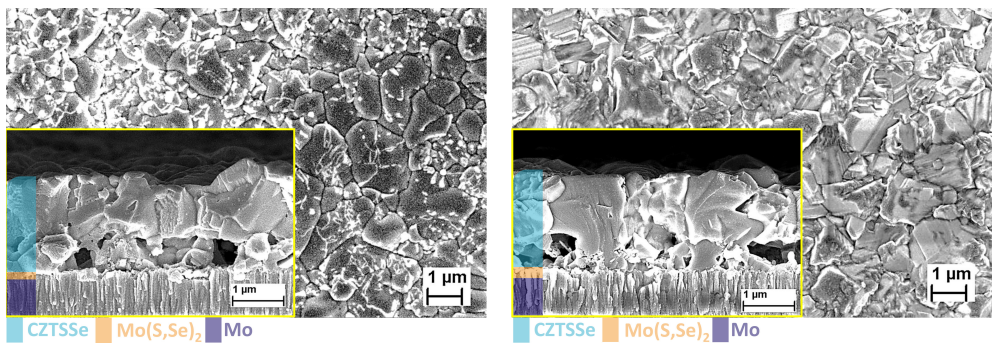
6.2.2 Results and discussions

6.2.2.1 Effects on morphology



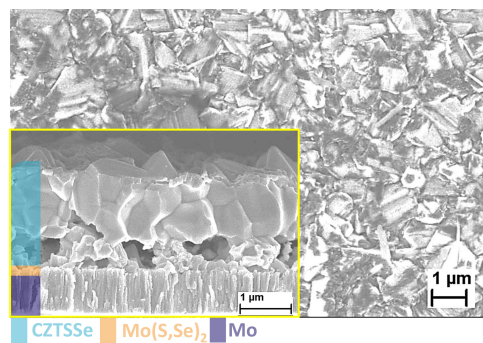
(a) Surface and cross-section(inset) of the Se<sub>Std.S200</sub> sample

(b) Surface and cross-section(inset) of Se<sub>Std.S300</sub> sample



(c) Surface and cross-section(inset) of Se<sub>Std.S400</sub> sample

(d) Surface and cross-section(inset) of Se<sub>Std.S500</sub> sample



(e) Surface and cross-section(inset) of the Se<sub>Std.S550</sub> sample

**Figure 6.2:** SEM image of samples sulfurized under different temperatures for 10 minutes after standard selenization process explained in Table 6.1. In the cross-section, all the different layers of the sample are identified.

The morphology of the resulting CZTSSe films examined by SEM, are depicted in figure 6.2 (as a function of different sulfurization temperatures under fixed duration(10 minutes)) and figure 6.3 (as a function of different sulfurization time at fixed temperature(550°C)). Both the images of the surface and the cross-section (inset with yellow border) are shown for each sample.

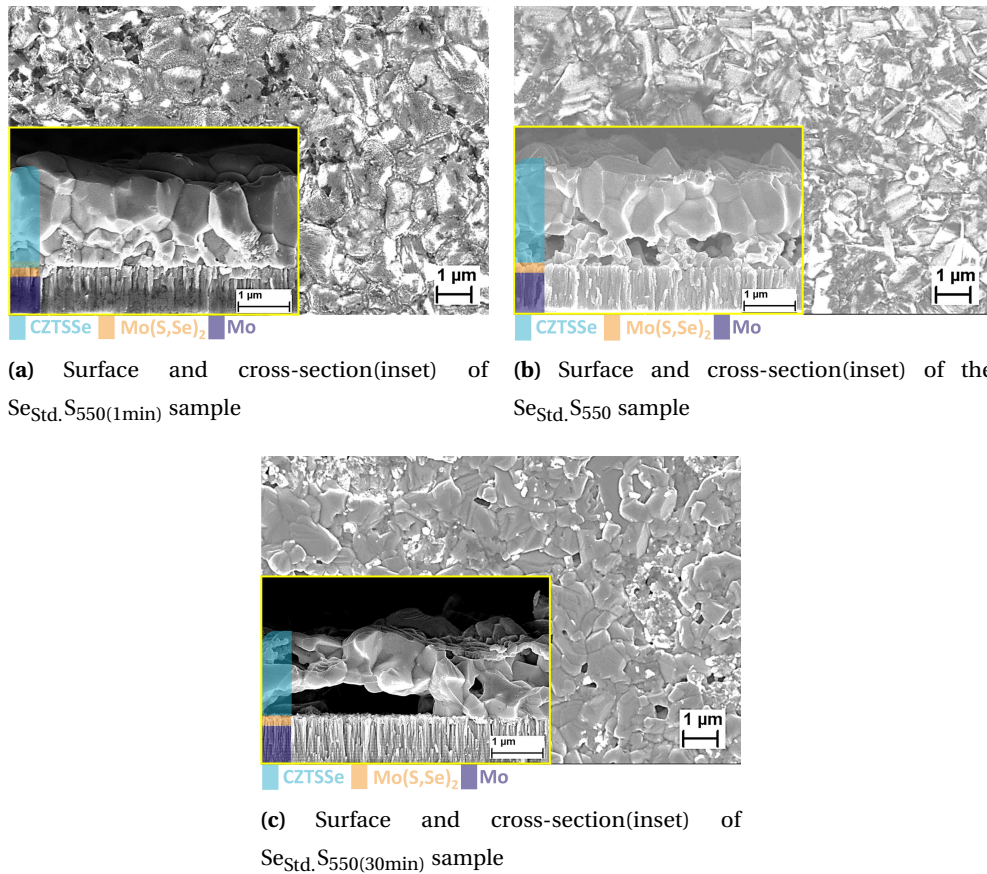


**Figure 6.3:** SEM image of the samples sulfurized under 550°C for different durations after a standard selenization process. In the cross-section all the different layers of the sample are identified.

Several observations can be made from the image 6.2 and 6.3,

1.  $Se_{Std.S200}$  shows compact grains and an almost similar morphology to the standard CZTSe sample showed in chapter 4 and it started to change with higher sulfurization temperature;
2. For all the other samples, bimodal grain distribution can be observed, where larger grains are located near the surface and smaller grains are situated near the back contact;
3. Increasing the sulfurization temperature increases the void at the back (CZTS/Mo inter-

- face) of the absorber, as can be seen from the cross-section images;
4. Furthermore, increasing sulfurization temperature shows more faceted grains and a peculiar brighter layer on the surface can be seen from the surface of the absorber;
  5. Sulfurization for 30 minutes shows decreased thickness of the absorber observed from the cross-section of sample  $Se_{Std. S_{550(30min)}}$ . Also, pinholes are visible from the surface of the sample.

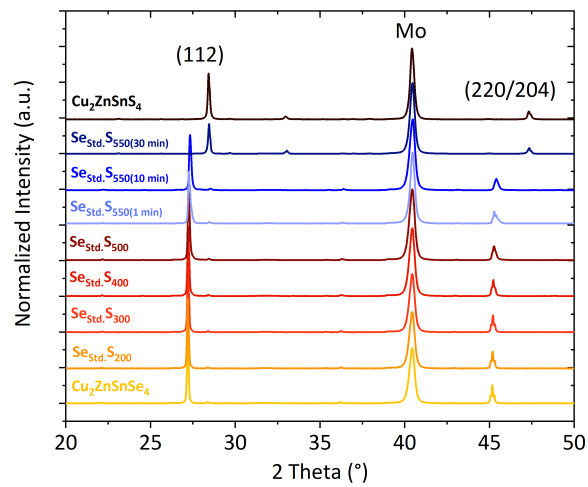
### 6.2.2.2 Effects on material properties

The effects of this sulfo-selenization process are investigated using EDX, XRD and Raman for bulk material properties, and GIXRD, GDOES for material properties as a function of depth.

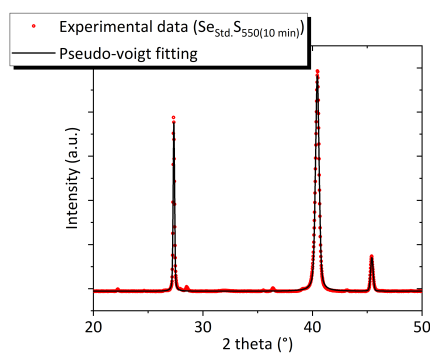
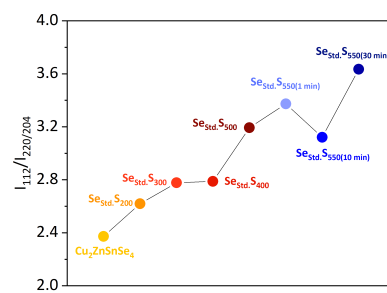
**EDX** is used to measure the cation and anion composition following the procedure explained in 3.2.2 (see table 6.1). The cation composition of a pure CZTSe sample synthesized with the precursor from the same run is also shown as reference for comparison. No noticeable effect of sulfurization can be seen for any of the sample except  $S_{Std. Se_{550(30 min)}}$ . Here, the  $S_{Std. Se_{550(30 min)}}$  sample shows higher Cu and Zn atomic concentration and lower Sn concentration compared to the reference sample, although all the samples were made with the same precursor configuration. Thus, Sn loss must have occurred during high temperature sulfurization process. Sugimoto et al., also found a similar effect of sulfurization temperature while using CZTSe nano-particles as precursor [159]. Also  $S_{Std. Se_{550(30 min)}}$  sample showed reduced thickness (figure 6.3) which proves the material loss during sulfurization.

The anion composition is also shown as the ratio of anions ( $[S]/[S+Se]$ ) in table 6.1, where 0 corresponds to pure Se based sample and 1 corresponds to pure sulfur based sample. Sulfur can be identified starting from sulfurization temperature of 200°C with an anion ratio of 0.05 and the amount of sulfur increased with the increase of temperature. Likewise, longer sulfurization duration increases the anion ratio, such as 30 minutes of annealing almost completely replaces the Se by S.

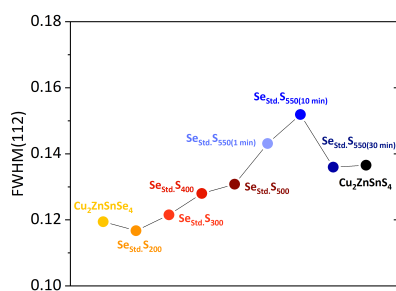
**XRD** analysis of these samples is shown in figure 6.4. The XRD pattern of all the samples are presented in figure 6.4(a). The analysis has been done by fitting the peak(112), (220/204) and Mo via pseudo-voigt function according to the equation 3.2. An example of the fitting is shown in figure 6.4(b).



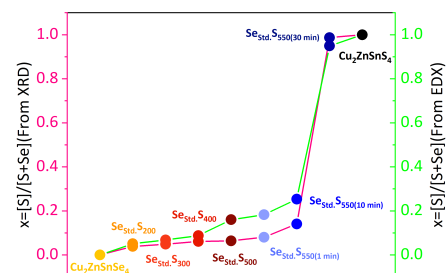
(a) XRD diffractogram of the samples prepared for front grading

(b) Fitting of  $\text{Se}_{\text{Std.S550(10 min)}}$ , as an example of the fitting used for the analysis.

(c) Ratio of area under peak (112) and peak (220/204).



(d) FWHM of peak (112) as a function of all the sample.



(e) Anion composition deduced from the XRD peak (112) position (pink line) and EDX measurement (green line).

**Figure 6.4:** XRD analysis of the samples used for front grading.

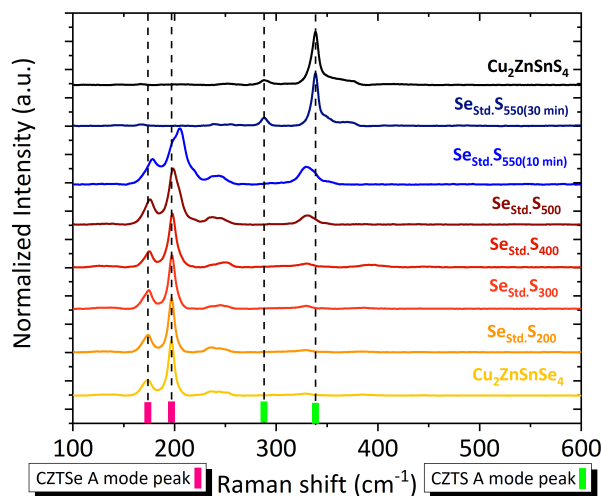
Different data (area, height, position and FWHM) are extracted from the fitting of the peak for analysis. The ratio of area under peak (112) and peak (220/204) as a function of the different samples are shown in figure 6.4(c). Additionally, FWHM of peak (112) as a function of different samples is shown in figure 6.4(d). Lastly, figure 6.4(e) shows the anion composition calculated using Vegard's law (explained in section 3.2.4) from the position of the XRD peak (112) (pink line) along with the anion composition extracted from EDX (Green line) as a function of different samples. The following comments can be made from analyzing the XRD data:

1. Figure 6.4(a) shows the diffraction peaks (112 and 220/204) of kesterite as well as the diffraction peaks of Mo. Mo peak is used for peak position correction of all the samples by comparing with the reference sample. The XRD diffractograms of pure CZTSe and CZTS are also shown as a reference for comparison. Shifting of peaks (112, 220/204) can be seen compared to the CZTSe reference. It is shifted from the CZTSe peak position to the CZTS one, with increased temperature and duration. This shows the successful incorporation of S in the CZTSe absorber. Also,  $Se_{Std. S_{550}(30 \text{ min})}$  shows peak position similar to that of CZTS, indicating complete replacement of Se by S;
2. Figure 6.4(c) shows the ratio of area under peak (112) and peak (220/204) as a function of different samples. Although, all the samples exhibit preferential (112) texturization, the degree of 112 texturization increases with increasing amount of S inclusion. This can be related to the SEM image shown in figure 6.2 and 6.3, showing higher degree of faceted grains with increased temperature and duration;
3. Figure 6.4(d) shows the FWHM of peak (112) as a function of samples. The FWHM is increased with increased amount of S incorporation in the presence of Se and it is decreased again as all the Se is replaced by S. As FWHM is inversely proportional to the domain size of the material according to Scherrer equation [46], the global domain size of CZTSSe absorber decreases with increasing amount of S inclusion. A similar conclusion was also made by Dimitrievska et al, [57];
4. Finally, the anion composition calculated from peak position of each sample is shown in figure 6.4(e) along with the anion composition achieved from EDX analysis. The anion composition calculated using both method indicates the increase of S content with increased temperature and duration;

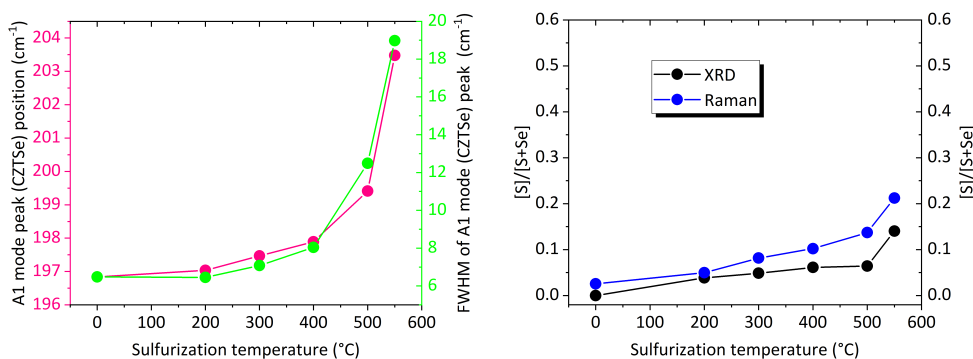
The Raman spectra using green laser (532 nm) of these samples are shown in figure 6.5(a). All the peaks appearing in the spectra agree with the Raman peaks characteristics of CZTSSe thin films, as was previously reported [58, 98, 122]. Here, with increasing ( $[S]/[S+Se]$ ) ratio, Raman peaks in the high frequency region corresponding to S vibration are gradually increasing

in intensity. Fitting A1 mode peak at around  $196\text{ cm}^{-1}$  reveals some facts towards realizing front grading. The peak position and FWHM of A1 mode peak are shown as a function of temperature in figure 6.5(b). The peak position is shifting towards higher frequency indicating higher S content according to Grossberg et al, [58]. Furthermore, FWHM of A1 mode peak is also increasing with increased temperature. This broadening is related to the convolution of Se and S/Se vibration around  $200\text{ cm}^{-1}$  and might be phonon confinement effects due to the poorer crystal quality, discussed briefly by Dimitrievska et al, [162]. It is also possible to estimate the anion composition by calculating  $\text{Area}_{\text{CZTS}} / (\text{Area}_{\text{CZTS}} + \text{Area}_{\text{CZTSe}})$ . Here,  $\text{Area}_{\text{CZTS}}$  corresponds to area of Raman spectra in the region of  $270\text{ cm}^{-1}$  and  $380\text{ cm}^{-1}$ , mainly related to vibration from S atom and  $\text{Area}_{\text{CZTSe}}$  corresponds to area of Raman spectra in the region of  $150\text{ cm}^{-1}$  and  $260\text{ cm}^{-1}$ , mainly related to vibration from Se atom described by Dimitrievska et al, [162].

From the anion composition ratio deduced from Raman spectra and XRD analysis (6.5(c)), it can be detected that the anion ratio of pure CZTSe is little higher than 0 from Raman analysis, which is due to the fact that the  $\text{Area}_{(270\text{ cm}^{-1}-380\text{ cm}^{-1})}$  overlaps with the second order peaks of the CZTSe, located around  $360\text{ cm}^{-1}$ . Since all the samples have similar second order peak, it should not affect the calculation of anion composition. Comparing the anion composition deduced from XRD and Raman, it can be said that the overall anion composition calculated using Raman spectra is higher than that of XRD. The reason for this higher overall anion composition from Raman analysis may be due to the fact that Raman analysis has been performed using a green laser, which have a limited penetration depth. Therefore, the spectra from this analysis is mainly from the upper part of the bulk, while XRD shows the integral of total bulk. This can indicate the presence of front grading in these samples, by having higher S on the surface.



(a) Raman spectra using green laser (532 nm) of all the CZTSSe absorber towards realizing front grading using different temperatures and durations.



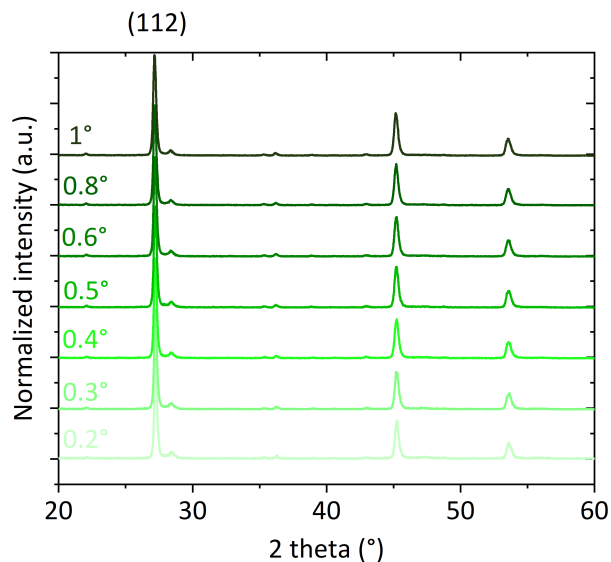
(b) Peak position along with FWHM of A1 mode (CZTSe) peak of all the samples prepared for this experiment is showing as a function of temperature.

(c) Chalcogen composition ratio ( $x=S/S+Se$ ) deduced from the XRD peak (112) position (pink line) and Raman measurement (green line) as function of temperature.

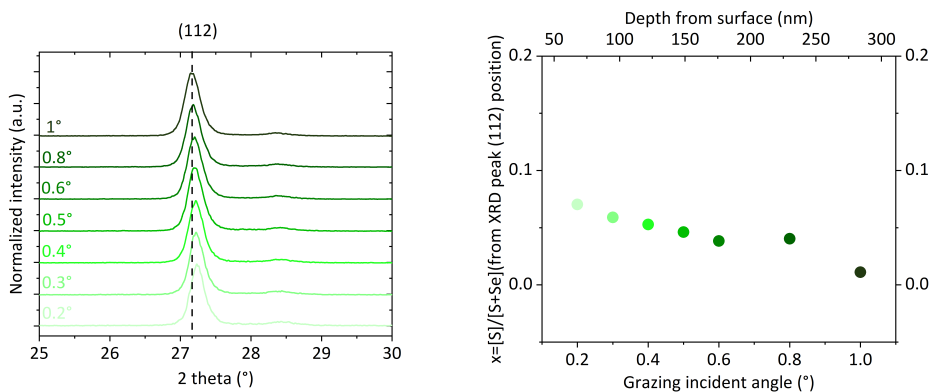
**Figure 6.5:** Raman analysis of the samples used for front grading.

**GIXRD** has been performed for microstructural analysis, where incident angle of X-ray is fixed to obtain XRD data from a certain thickness of the sample. More details on the principle of this process can be found in 3.2.4. Different incident angle from  $0.2^\circ$  to  $5^\circ$  are used as incident angle during this analysis. Two particular samples,  $Se_{Std.S500}$  and  $Se_{Std.S550(10\ min)}$  are selected for this experiment, due to the presence of highest amount of sulfur to selenium ratio. The GIXRD performed with similar incident angle on a pure CZTSe sample to calibrate the measurement as a function of incident angle is also included.

The GIXRD analysis of the  $\text{Se}_{\text{Std. S500}}$  sample is shown in figure 6.6. The diffractograms using different incident angle starting from  $0.2^\circ$  to  $1^\circ$  are shown in figure 6.6(a).



(a) GIXRD representation of the  $\text{Se}_{\text{Std. S500}}$  sample.



(b) Enlarged peak (112) representation of figure 6.6 (a).

(c) Anion composition as a function of grazing incident angle calculated from the peak(112) position of the  $\text{Se}_{\text{Std. S500}}$  sample.

**Figure 6.6:** XRD analysis of the  $\text{Se}_{\text{Std. S500}}$  sample used for front grading.

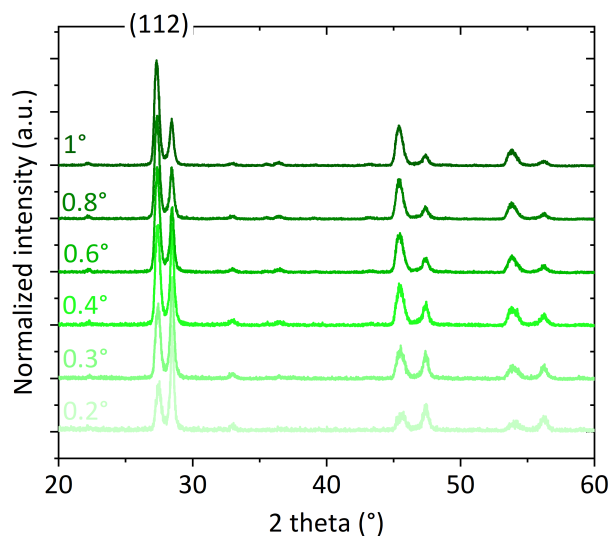
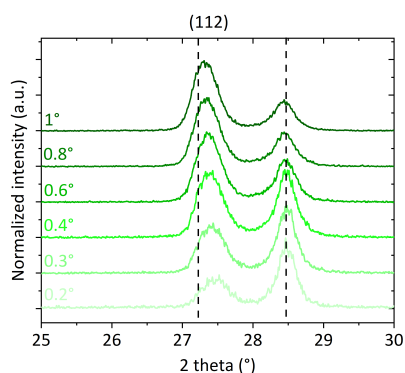
While XRD shows global crystalline phase of the bulk, GIXRD is highly sensitive for detecting crystalline phases of the absorber surface. It can therefore be said that no noticeable Sn or Cu based secondary phases are induced by this synthesis method since no peak corresponding to Sn or Cu based secondary phases could be detected using either XRD or GIXRD. An enlarged image of figure 6.6(a) emphasizing peak (112) is shown in figure 6.6(b). A slight shift of peak

can be observed from  $0.2^\circ$  to  $1^\circ$  incident angle. To get a clearer picture on this peak shifting, the anion ratio is calculated using Vegard's law shown in figure 6.6(c), along with the depth from the surface. The depth from surface of GIXRD experiment is calculated from the X-ray penetration depth for each incident angle and anion ratio, as described in 3.2.4. From figure 6.6(c), we can see that a small gradient is present in the front of the absorber, where the anion ratio varies from around 0.07 to 0.01 for incident angle  $0.2^\circ$  to  $1^\circ$ .

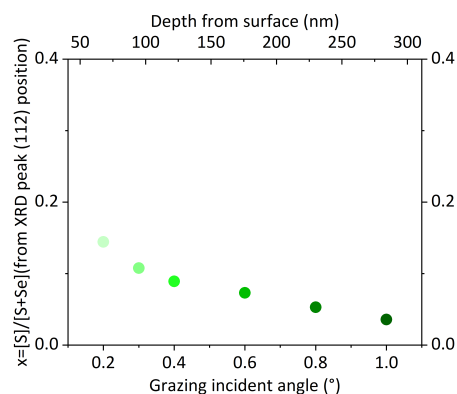
Similar characterization is also done on the sample  $\text{Se}_{\text{Std. S}_{550(10 \text{ min})}}$  shown in figure 6.7. From figure 6.7(a), a bimodal behavior can be observed showing peaks for CZTSSe (as it was detected by XRD and Raman analysis) at around  $27.5^\circ$ ,  $45.5^\circ$  and  $53.9^\circ$ , while peaks could also be detected at around  $28.5^\circ$ ,  $47.4^\circ$  and  $56.2^\circ$ . Further argument can be made from figure 6.7(b), where the peak around  $27.5^\circ$  shifted with increased incident angle while the peak around  $28.5^\circ$  is constant. This indicates that the first peak is related to graded CZTSSe, while the other could be ZnS/CZTS/CTS. Ross et al, [160] described this peak as CZTS, while Sugimoto et al, [159] proved it was ZnS using TEM-EDS. Furthermore, the peak related to sulfur-based phase shows higher intensity compared to CZTSSe at  $0.2^\circ$  incident angle, which starts to decrease with increased incident angle and was not observed during XRD. This means that this pure sulfur-based phase is limited to the near surface of the absorber. The anion composition calculated from the CZTSSe peak position achieved from GIXRD is shown as a function of the incident angle and depth from the surface in figure 6.7(c). This shows a higher degree of grading compared to the  $\text{Se}_{\text{Std. S}_{500}}$  sample. Furthermore, the anion composition shows lower S content at higher incident angle compared to the measurement from XRD, due to the presence of higher sulfur at the back as well.

To summarize, using GIXRD, the presence of front grading using this synthesis process was demonstrated. The degree of grading is also increased with increased temperature, which can be used to control the front grading for best optimization. Furthermore, a pure sulfur-based phase was observed on the surface of  $\text{Se}_{\text{Std. S}_{550(10 \text{ min})}}$  using GIXRD.

**GDOES** analysis is performed on these samples to further analyze this achieved gradient and to understand the characteristics of this sulfur based peak. The sulfur and selenium profile of  $\text{Se}_{\text{Std. S}_{400}}$ ,  $\text{Se}_{\text{Std. S}_{500}}$  and  $\text{Se}_{\text{Std. S}_{550}}$  sample along with CTZSe sample as reference are shown in figure 6.8. In this figure, the dashed line represents the Se distribution and the solid line represents the S distribution. Several statements can be made from figure 6.8.

(a) GIXRD representation of the  $\text{Se}_{\text{Std. S550}}$  sample.

(b) Enlarged peak (112) representation of figure 6.6 (a).

(c) Anion composition as a function of grazing incident angle calculated from the peak(112) position of the  $\text{Se}_{\text{Std. S550}}$  sample.**Figure 6.7:** XRD analysis of the  $\text{Se}_{\text{Std. S550}}$  samples used for front grading.

First of all, clear indication of sulfo-selenium grading can be observed from 0-500 nm by having higher to lower amount of sulfur from the surface towards the bulk, and vice versa for the selenium. Therefore, we could say that the front grading was successfully implemented using this method. Secondly, the degree of grading increased with increasing sulfurization temperature. Third, at the surface of the  $\text{Se}_{\text{Std. S500}}$  and the  $\text{Se}_{\text{Std. S550}}$  sample, an absence of Se can be observed, which gives the indication of a S only based phase limited to the surface (within 10-20 nm). Fourth, comparing S and Se profiles of  $\text{Se}_{\text{Std. S550}}$  sample, the grading is

## Chapter 6. Bandgap grading

present until 200 nm from the surface and after the grading, both profile showed a flat line. For  $\text{Se}_{\text{Std. S}_{500}}$ , the gradient is until 150 nm. It can therefore be concluded that, it is possible to control the cross-over point of grading from the surface. Finally, when comparing the profile of S and Se of all the sulfo-selenized samples with the CZTSe sample, a slight decrease of Se content at the back of the absorber and an increase of overall S throughout the absorber can be observed. This leads to the conclusion that, although these samples showed front grading, some S is still diffusing at the back of the absorber.

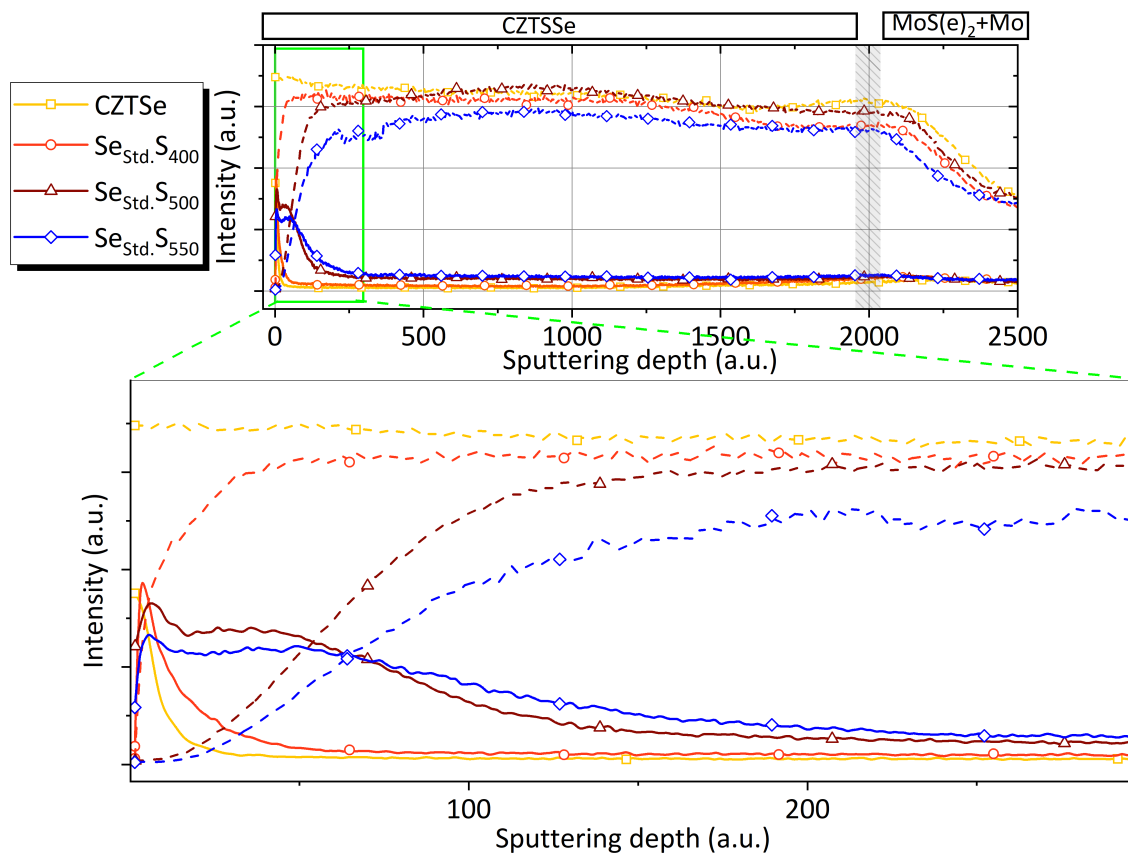
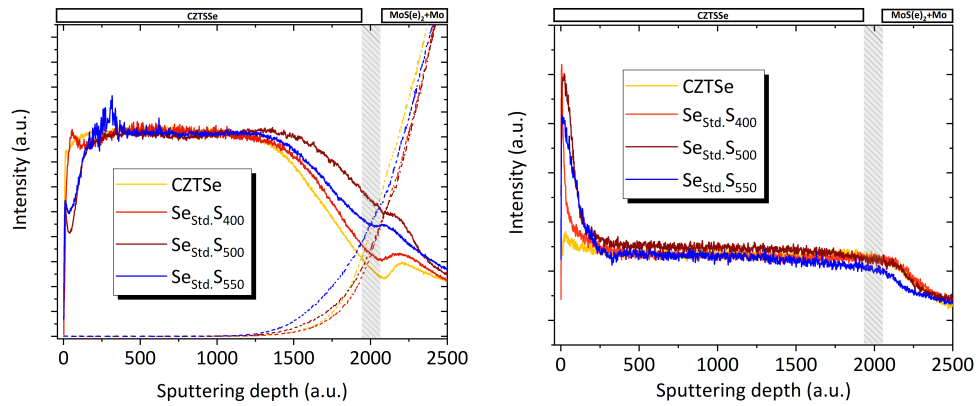
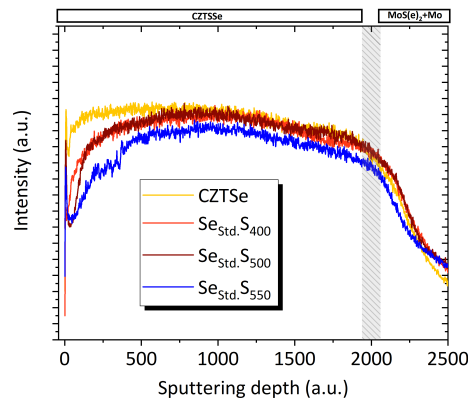


**Figure 6.8:** S and Se distribution throughout the depth of the samples prepared for front grading measured by GDOES, where dashed line corresponds to Se profile and solid line corresponds to sulfur profile. The enlarged distribution of S and Se near the surface are shown in the image below.

Figure 6.9 shows the Cu and Mo profile(a), Zn profile(b) and Sn profile (c) for all the samples analyzed in figure 6.8. From the profile of Cu, Zn and Sn, there is a sudden decrease in Cu and Sn profile at the surface. The Zn profile, on the contrary, showed opposite characteristics. This indicates that the sulfur rich phase on surface seen from GIXRD and S/Se GDOES profiles is ZnS, rather than CZTS or CTS.



(a) Cu and Mo (dashed lines) distribution throughout the depth of the samples prepared for front grading by GDOES. (b) Zn distribution throughout the depth of the samples prepared for front grading by GDOES.



(c) Sn distribution throughout the depth of the samples prepared for front grading by GDOES.

**Figure 6.9:** Cation distribution throughout the depth of the samples prepared for front grading by GDOES.

### 6.2.2.3 Device properties

Complete photovoltaic devices are fabricated using sample  $Se_{Std.S500}$  with and without an additional HCl etching similar to Fairbrother et al, [102]. The etching is done using 10%(v/v) HCl at 75°C temperature for 10 minutes to remove the ZnS phase detected at the surface. Figure 6.10(a) shows the light and dark J-V curves with and without HCl etching.

While, the sample without etching shows poor electrical properties, an increase in all the electrical properties can be observed after the HCl etching procedure. Furthermore, figure 6.10(b) shows the EQE of these samples. The bandgap of 1.07 eV is derived from the 1st

## Chapter 6. Bandgap grading

derivative of EQE spectra of the etched sample (see figure 6.10(b) green dashed line). This bandgap is slightly higher than the bandgap of pure CZTSe (1.02 eV) used during this study. This also indicates the inclusion of sulfur in the absorber using this process. However, the increase in bandgap could arise from Cu/Zn ordering due to the second annealing [25]. The 427 mV  $V_{OC}$  of the  $Se_{Std.}S_{500}$  sample is higher than the 410 mV  $V_{OC}$  obtained from the reference CZTSe sample. The  $J_{SC}$  and FF decreased substantially, therefore the efficiency of the final device was found to be lower compared to the reference CZTSe sample.

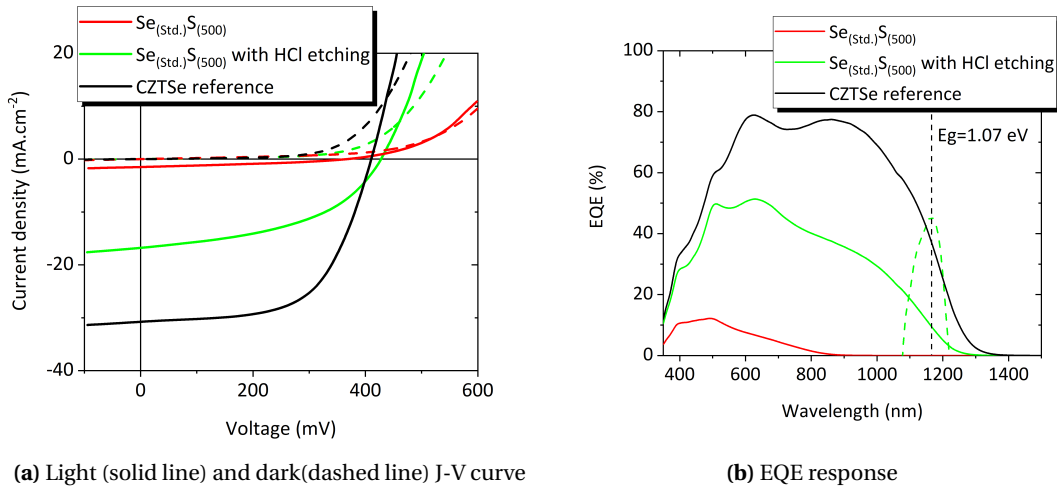


**Figure 6.10:** Optoelectronic properties of the  $Se_{Std.}S_{500}$  sample before and after HCl etching. Light J-V (measured under AM 1.5G illumination) (solid line) and dark J-V (dashed line) (a) EQE reveals a bandgap of 1.07 eV derived from 1<sup>st</sup> derivative of EQE spectra (b)

**Table 6.2:** Electrical parameter of the  $Se_{Std.}S_{500}$  sample after HCl etching.

Light J-V				Dark J-V		EQE	
$V_{OC}$	$J_{SC}$	FF	Efficiency	$R_S$	$R_{Sh}$	$E_g$	$V_{OC}$ deficit
(mV)	(mA.cm <sup>-2</sup> )	(%)	(%)	(ohm.cm <sup>2</sup> )	(ohm.cm <sup>2</sup> )	(eV)	(mV)
427	16.8	47	3.4	1.81	748	1.07	643

**In summary**, front grading is successfully implemented using pure metallic precursor and subsequent sulfo-selenization process. Different material characterizations were performed to realize the anion composition in the bulk of the absorber globally and as a function of depth. The presence of front grading is proved using GIXRD and GDOES depth profiling. Temperature higher than 400°C was found to be effective to have a noticeable sulfur inclusion in the absorber. Additionally, increasing the temperature increased the amount of sulfur inclusion in the absorber resulting in a higher degree of front grading. A layer of ZnS forms

on the surface during the sulfurization of the CZTSe absorber, which can be removed using HCl etching. The device property, however, did not show improvement compared to best CZTSe absorber from this work. Further optimization of temperature and etching procedure may result in better device properties, and further studies are therefore required towards optimizing this procedure to have the beneficial effect of front grading.

## 6.3 Back Grading

### 6.3.1 Experimental Procedure

One possible way to implement back grading for kesterite absorber is to introduce Se on an already sulfurized kesterite absorber. In this section, the effects and limitations of this strategy will be discussed briefly with the help of different characterization procedures. Three samples were prepared by doing the sulfurization of the metallic precursor under different temperatures (400°C, 500°C and 550°C shown in figure 6.11(a)) for 10 minute, before the standard selenization process (shown in figure 6.11(b)). The sulfurization temperature range upward from 400°C was selected because most of sulfur incorporation with the precursor happened at 400°C, as explained in chapter 4.

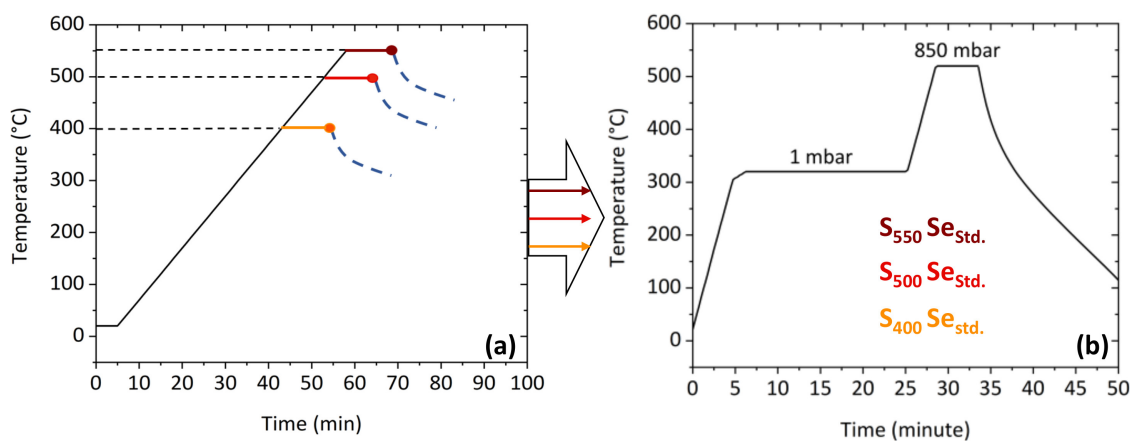


**Figure 6.11:** Temperature profile for sulfurization of metallic precursor under different temperatures pointed by different color(a) and temperature profile of pure selenization used for selenizing, previously sulfurized sample(b) to achieve back grading.

The name of each sample were given according to the sulfurization and selenization profile used for the annealing. For example in S<sub>400</sub>Se<sub>Std.</sub>, S<sub>400</sub> stands for sulfurization at 400°C for 10 min prior to natural cooling and Se<sub>Std.</sub> stands for standard selenization which is done after sulfurization. Details for each sample are also in table 6.3, along with the anion and cation

## Chapter 6. Bandgap grading

composition of the finished absorber. These compositions will be discussed briefly in section 6.3.2.

**Table 6.3:** The composition ratio of anion and cation measured by EDX along with the annealing condition of each sample.

Sample name	Sulfurization temp.(°C)	Sulfurization duration (min)	Selenization	Cu(at%)	Zn(at%)	Sn(at%)	[S]/[S+Se]
Cu <sub>2</sub> ZnSnSe <sub>4</sub>	N/A	N/A	Standard	41.5±0.5	31.8±0.5	26.7±0.5	0
S <sub>400</sub> SeStd.	400	10	Standard	42.0±0.5	32.4±0.5	25.6±0.5	0.20±0.02
S <sub>500</sub> SeStd.	500	10	Standard	42.5±0.5	32.7±0.5	24.8±0.5	0.25±0.02
S <sub>550</sub> SeStd.	550	10	Standard	43.7±0.5	33.3±0.5	23.0±0.5	0.37±0.02

### 6.3.2 Result and discussion

#### 6.3.2.1 Effects on morphology

The morphology of the resulting CZTSSe films examined by SEM, are shown in figure 6.12. For each sample, both the SEM image of the surface and cross-section (inset with yellow border) are given. S<sub>400</sub>SeStd. shows irregular grains and pinholes on surface and voids at the rear side of the absorber. Further degradation of morphology can be observed with increased sulfurization temperature. Using a 550°C sulfurization temperature for sample S<sub>550</sub>SeStd. results in grains lower than 500 nm with higher degree of pinholes and surface irregularity.

#### 6.3.2.2 Effects on material properties

**Cation and anion compositions** measured by EDX following the procedure explained in 3.2.2 are shown in table 6.3. The cation composition of pure CZTSe sample synthesized with the precursor from same run is also given in table 6.3, as reference for comparison. From this figure, it can be noted that increasing sulfurization temperature resulted in higher Cu and Zn atomic concentration and lower Sn concentration compared to reference sample, although all the samples used the same precursor configuration. Therefore, samples are losing Sn during the first annealing or more precisely during the sulfurization step, where the loss is proportional to the annealing temperature. Furthermore, the anion composition is given as the ratio of anion([S]/[S+Se]). Here, the sample made with a lower temperature sulfurization step showed lower S concentration while the maximum S content obtained for S<sub>550</sub>SeStd. is 0.37.

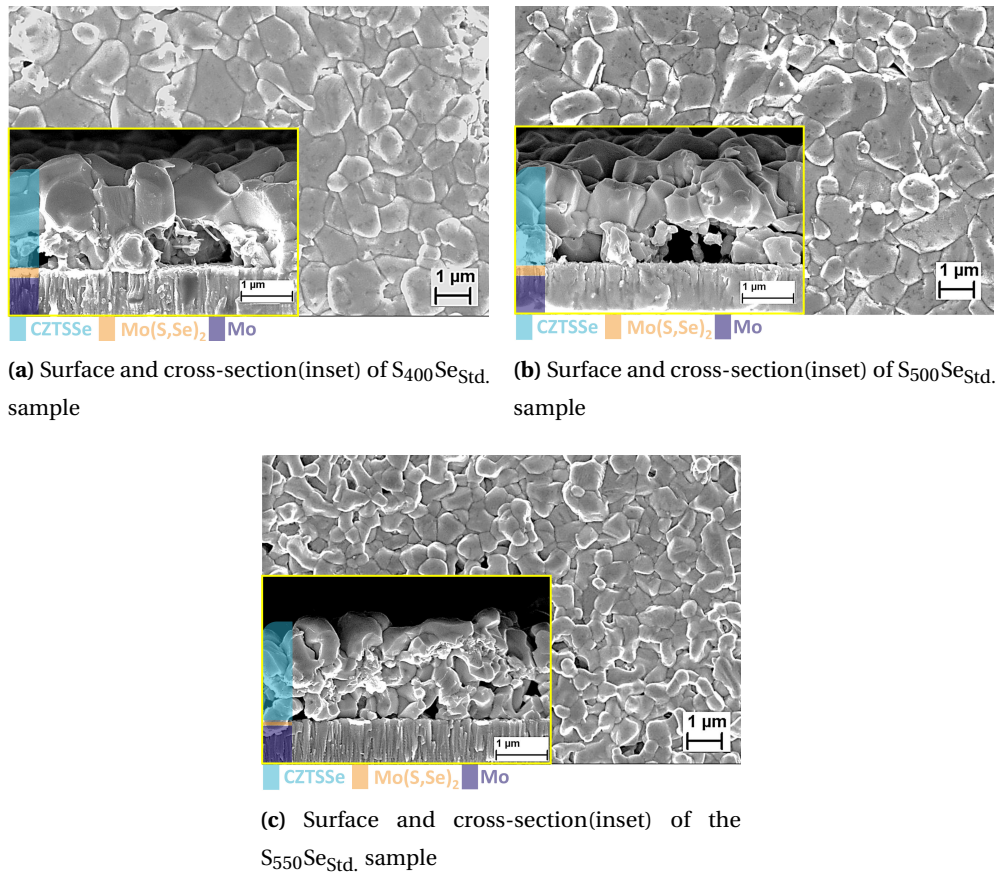
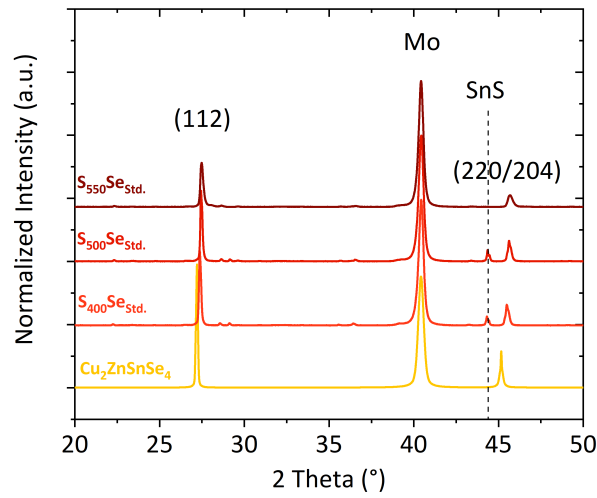
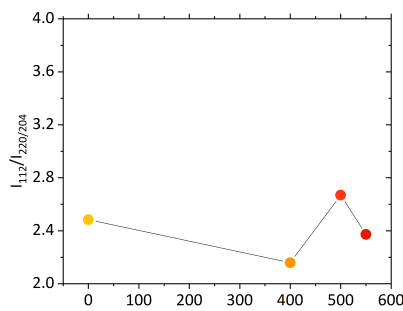


**Figure 6.12:** SEM images of samples sulfurized under different temperatures prior to standard selenization process.

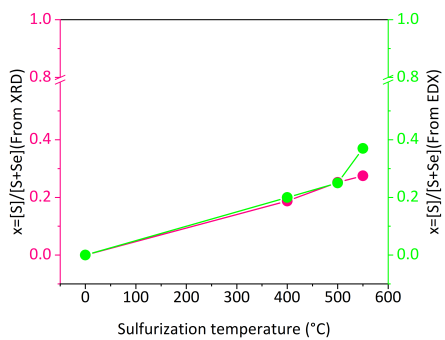
**XRD pattern analysis** is shown in figure 6.13, with figure 6.13(a) showing the XRD pattern indicating peak (112) and (220/204). From the data extracted from the fitting, the ratio of area under peak (112) and peak (220/204) is shown in figure 6.13(b) and FWHM of peak (112) is shown in figure 6.13(d) as a function of the different samples. Additionally, figure 6.13(c) shows the anion composition (pink line), which is calculated using Vegard's law from the position of peak (112) along with anion composition extracted from EDX (Green line) as function of different samples. From figure 6.13(a), a SnS secondary phase [26] can be detected from sample  $S_{400}Se_{Std.}$  and  $S_{500}Se_{Std.}$ , but it is not observed anymore for sample  $S_{550}Se_{Std.}$ . Also, main kesterite peaks (112, 220/204) shifting can be seen from CZTSe reference towards higher diffraction angle with increased temperature. Therefore, it points out at the successful inclusion of S in CZTSe absorber. Figure 6.13(b) shows the ratio of area under peak (112) and peak (220/204) as a function of different samples to investigate the preferential texturization of the sample due to this particular sulfo-selenization process.



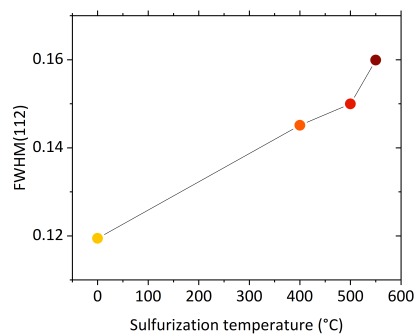
(a) X-ray diffraction of all the samples prepared for rear grading



(b) Ratio of area under peak (112) and peak (220/204) of all the samples.



(c) Chalcogen composition ratio ( $x = \text{S}/(\text{S} + \text{Se})$ ) deduced from the XRD peak (112) position and EDX measurement.

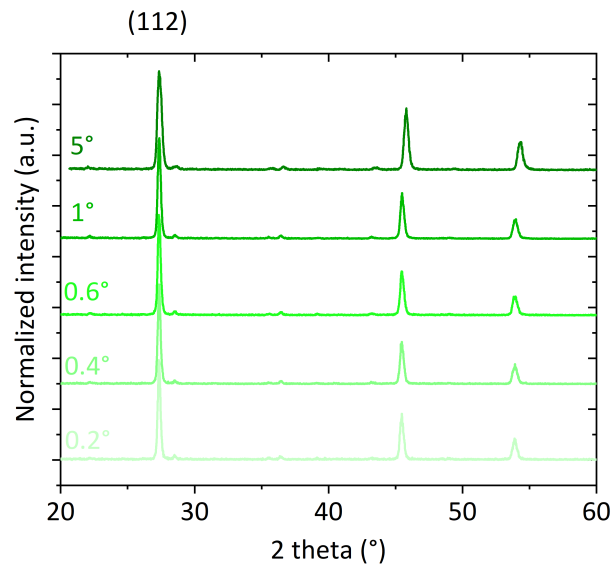


(d) FWHM of peak (112) as a function of all the samples.

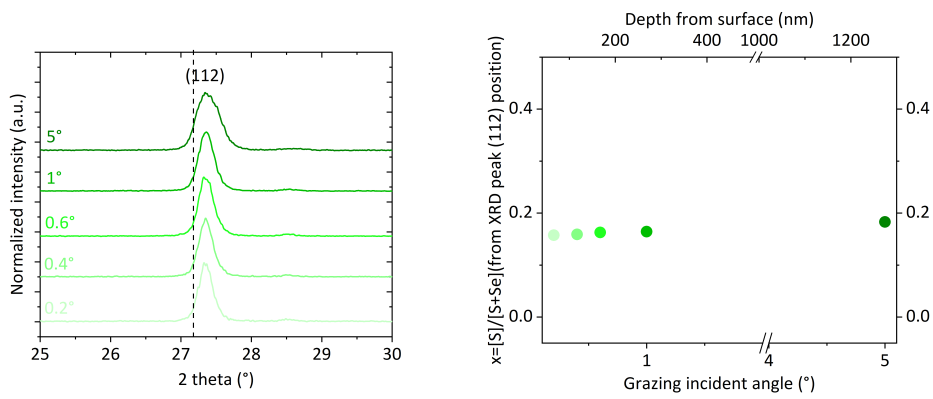
**Figure 6.13:** XRD analysis of samples used for rear grading.

Although, all the samples showed preferential (112) texturization, the degree of 112 texturization did not show any trend with increasing S content or temperature. Figure 6.13(d) highlights the FWHM of peak (112) as a function of different samples, exhibiting that the FWHM is increased with increased amount of S incorporation, similar to the front grading experiment. Finally, the anion composition calculated from peak position of each sample is shown in figure 6.13(e) along with the anion composition achieved from EDX analysis.

**GIXRD** characterization was performed on samples  $S_{400}Se_{Std.}$  and  $S_{550}Se_{Std.}$  to have an overview of the anion composition as a function of depth. A similar procedure of data treatment is used for these sample as described for front grading. Figure 6.14 shows the GIXRD analysis of  $S_{400}Se_{Std.}$  sample. In 6.14(a), the diffractogram is showing different incident angle starting from  $0.2^\circ$  to  $5^\circ$ . No Sn or Cu based secondary phases can be detected from figure 6.14(a), although the XRD showed SnS secondary phase formation for this sample. Therefore, we can say that the SnS secondary phase must be at the rear side of the absorber. An enlarged image of figure 6.14(a), emphasizing peak (112) is shown in figure 6.14(b). No noticeable peak shift can be observed for this sample. To have a clearer understanding, the anion ratio is calculated from peak (112) using Vegard's law shown in figure 6.14(c), along with the depth from the surface. From figure 6.14(c), we can see that, instead of having a graded anion composition from the bulk towards the back, it has a constant mixture of S and Se throughout the absorber. The anion composition value from the XRD is nearly similar to the anion composition value found for different incident angle, which also suggests a constant anion composition throughout the absorber.



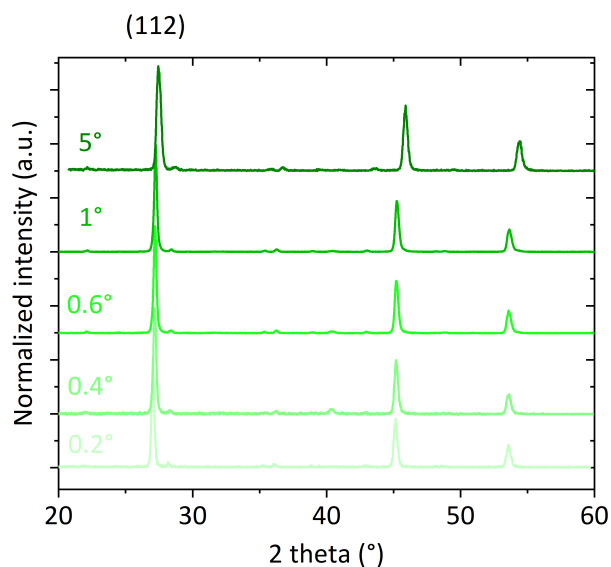
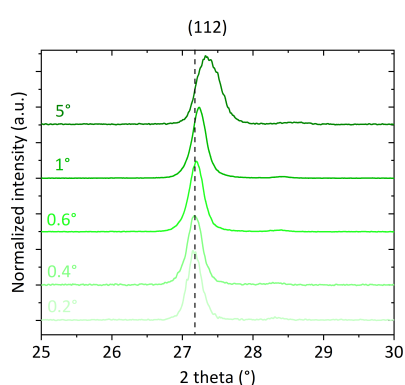
(a) GIXRD pattern of  $S_{400}Se_{Std.}$  sample.



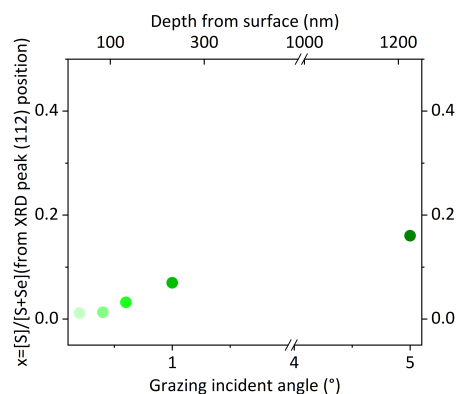
(b) Enlarged peak (112) representation of figure 6.14 (a).

(c) Anion composition as a function of grazing incident angle calculated from the peak(112) position of  $S_{400}Se_{Std.}$  sample.

**Figure 6.14:** GIXRD analysis of  $S_{400}Se_{Std.}$  sample used for rear grading.

(a) GIXRD pattern of the  $S_{550}Se_{Std.}$  sample.

(b) Enlarged peak (112) representation of figure 6.15 (a).

(c) Anion composition as a function of grazing incident angle calculated from the peak(112) position of the  $S_{550}Se_{Std.}$  sample.**Figure 6.15:** GIXRD analysis of the  $S_{550}Se_{Std.}$  sample used for rear grading.

Similar characterization was also done on sample  $S_{550}Se_{Std.}$  (figure 6.15). Figure 6.15(a) shows the XRD pattern for different incident angles. Peak shifting of all the peaks as a function on incident angle can be noticed from the figure. To have a clear view, the enlarged image of peak (112) is shown in figure 6.15(b), which also confirms the peak shifting and presence of higher sulfur at the back of the absorber. The anion composition calculated from the CZTSSe peak position achieved from GIXRD is shown as a function of incident angle and depth form surface in figure 6.15(c). This shows a back grading, where more sulfur could be found at the

back of the absorber.

In summary, using GIXRD the presence of back grading is shown, where only the sample synthesized with higher sulfurization temperature (550°C) shows back grading and sample with lower sulfurization temperature (400°C) shows a constant S to Se ratio throughout the absorber.

**GDOES** analysis is performed on these samples to further validate the result obtained from GIXRD. The sulfur and selenium profile of the  $S_{400}Se_{Std.}$  and  $S_{550}Se_{Std.}$  samples along with CZTSe sample as reference are shown in figure 6.16. Here dotted line represents the Se distribution and solid line represents the S distribution. Several statements can be made from figure 6.16. First of all the overall intensity of Se for CZTSe samples are lower than CZTSe sample proving the inclusion of S in the absorber. Also, Se profile of  $S_{400}Se_{Std.}$  is showing a flat distribution while Se profile of  $S_{550}Se_{Std.}$  is showing higher to lower selenium distribution from surface to the back of the absorber. Therefore, the back grading can be also realized from sample  $S_{550}Se_{Std.}$ .

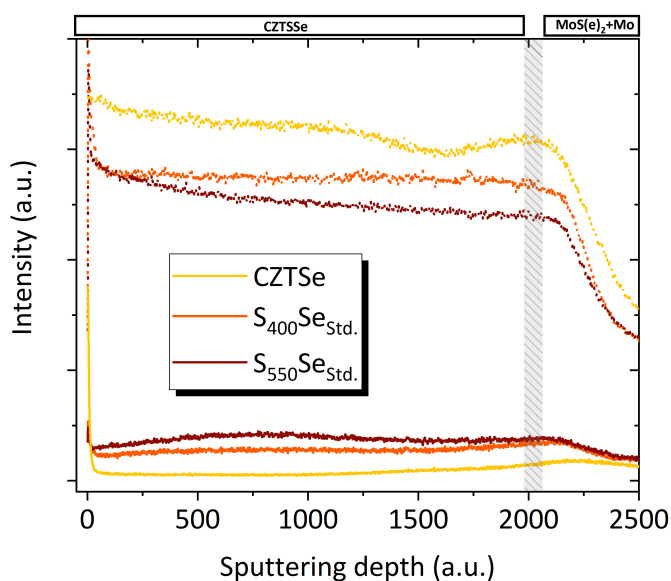


**Figure 6.16:** S and Se (dot line) distribution throughout the depth of the samples prepared for rear grading by GDOES.

To understand the reason of S and Se homogeneous mixing for  $S_{400}Se_{Std.}$ , a sample is prepared to analyze the intermediate step of reaction mechanism. For this purpose, the sample was prepared by sulfurizing at 400°C followed by a selenization step with a 320°C temperature plateau only. **EDX mapping** of this sample is shown in figure 6.17. First of all, 400°C sulfuriza-

tion temperature shows secondary phase of Cu, Zn and Sn as shown in chapter 4. Selenization of this sample replaced the S mainly from Cu secondary phase as this is thermodynamically more feasible, according to figure 6.17. Later, the intermixing of Cu-Se, Zn-S and Sn-S reacts together to form CZTSSe at a higher temperature plateau, using Cu-Se as the main fluxing agent for the grain growth. This can be the reason for having homogeneous anion composition throughout the absorber for this sample.

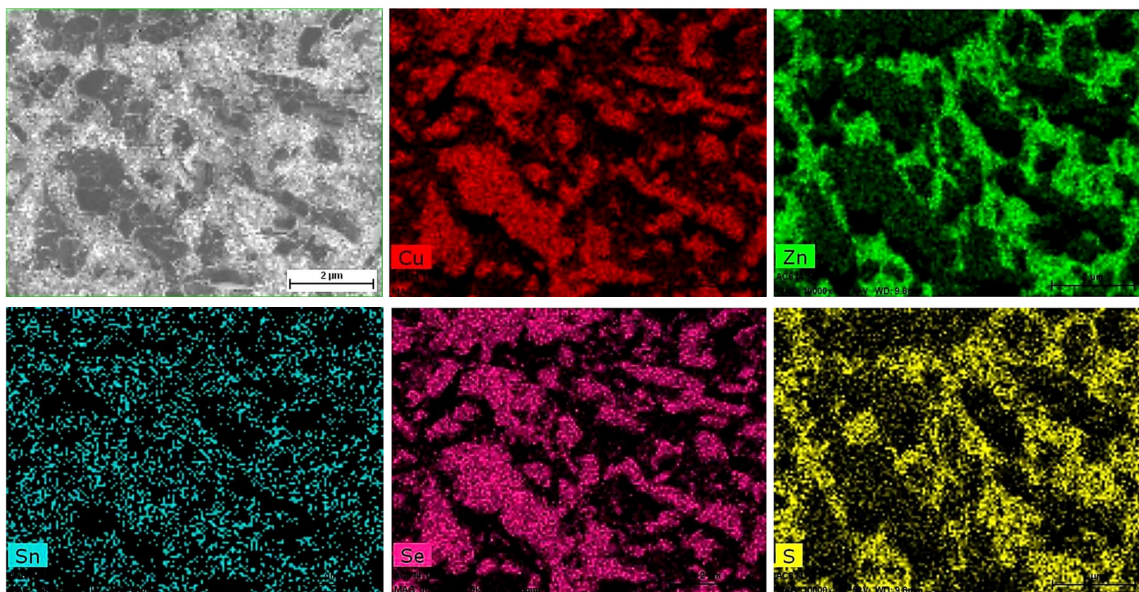


**Figure 6.17:** EDX mapping (using 10 keV excitation voltage) of sample sulfurized at 400°C followed by a selenization with 320°C plateau only, showing distribution of Cu, Zn, Sn, S and Se distribution from surface.

To summarize, sample sulfurized at lower temperature (400°C) did not show any back grading, instead a homogeneous distribution of S and Se can be observed throughout the depth, whereas, sample sulfurized at higher temperature (550°C) showed back grading but at a price of deteriorating morphology, resulting in a non working device.

## 6.4 General discussion and conclusion

In this chapter, the fabrication process of CZTSSe absorber with front and back grading was explained. In the first case, a standard selenization process followed by a sulfurization process at different temperatures and duration was performed. This process is summarized by the schematic, shown in figure 6.18.

Here, a high temperature sulfurization has been done on a CZTSe sample. Front grading was

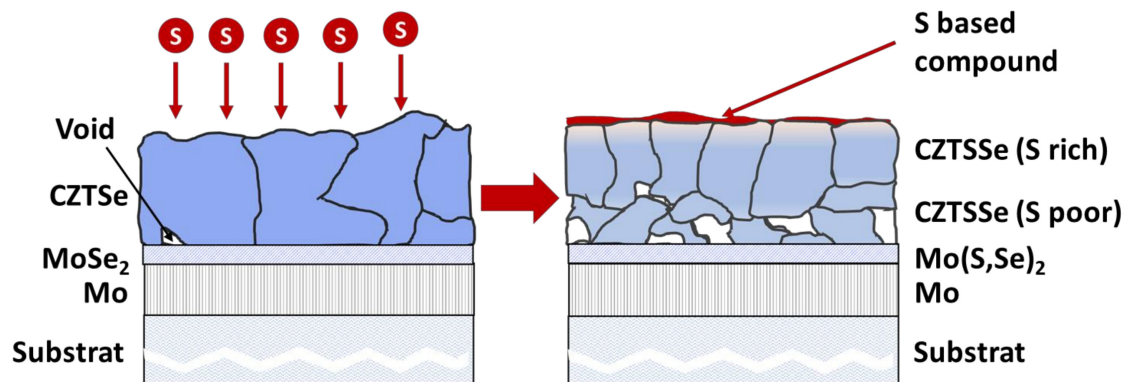


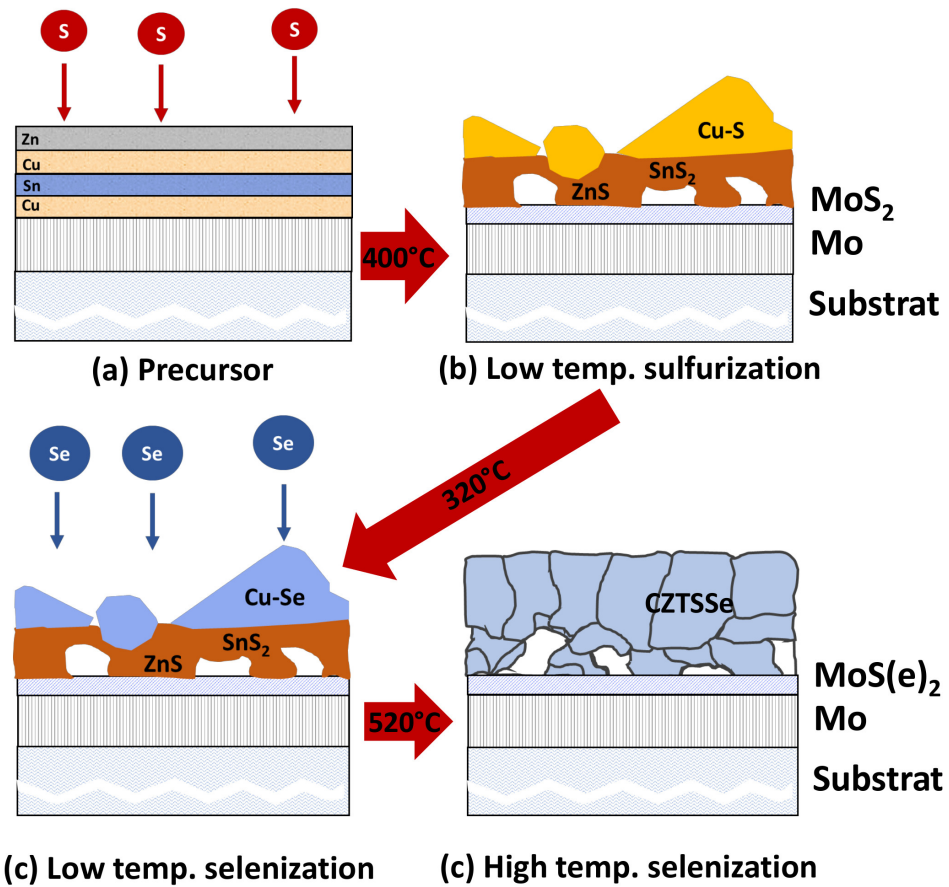
**Figure 6.18:** Schematic illustration of sulfo-selenization process to achieve front grading. A standard CZTSe absorber (in left) is sulfurized at high temperature to achieve front graded CZTSSe absorber (in right). Also, a highly sulfur rich surface can be observed on CZTSSe sample.

demonstrated using this process, which is confirmed by GIXRD and GDOES analysis. However, bimodal grains with smaller grain size and higher amount of void was observed on the finished CZTSSe samples, compared to the starting CZTSe sample. Furthermore, this process also induces a S based compound limited to the surface of CZTSSe absorber, which is concluded as ZnS secondary phase by GDOES analysis. Solar cell fabricated using  $Se_{Std.S500}$  sample showed highest PCE of 3.4% after a HCl etching while sample without etching showed 0.7%.

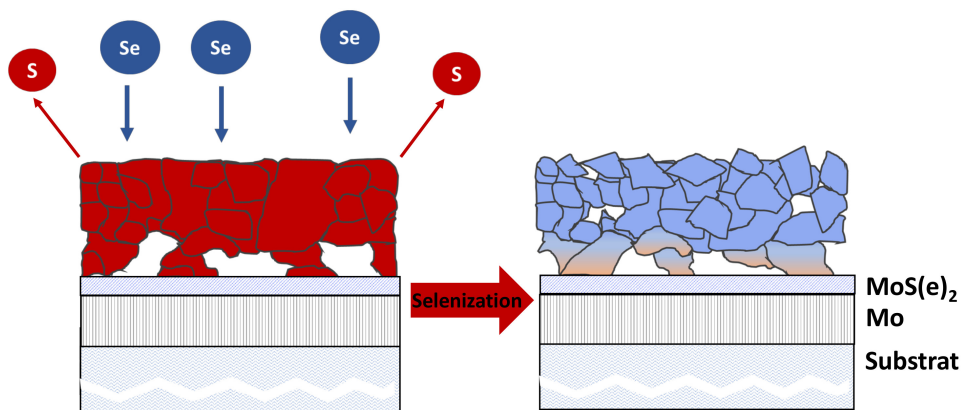
For back grading, samples prepared with sulfurization at different temperatures were selenized using a standard recipe. Two different effects were observed during this analysis, shown in figure 6.19.

Low sulfurization temperature used during this process was found to be ineffective towards realizing a back grading : At a 400°C sulfurization temperature, mainly binary phases are formed. When selenization is done on the sample with binary compounds, the S in CuS replaced by Se and become CuSe. Later, this CuSe phase works as fluxing agent and increases the grain size, as well as equalize the S/Se ratio throughout the absorber (figure 6.19). On the other hand, higher sulfurization temperature shows back grading to some extent at the expense of microstructural properties. The lack of CuSe phase of this sample during annealing must be the reason for not having an enhanced grain growth.

From this work many insights on bandgap grading are revealed. Successful bandgap grading at the front side is demonstrated along with the working solar cell. However, back side grading did not work properly. Therefore, further work is required to apply the findings of this work and overcome the difficulties encountered during this study.



(a) Illustration of the back grading process using low temperature sulfurization prior to standard selenization. Sulfurization of the precursor (a) at 400°C shows a CuS binary phase, which is completely replaced by Se during the first low temperature step of selenization.



(b) Illustration of the back grading process using high temperature sulfurization prior to standard selenization. During high temperature Se is replacing sulfur.

**Figure 6.19:** Schematic illustration of sulfo-selenization process to achieve back grading.

## 7 Conclusion and Perspective

This thesis had one main ambition : Achieve improved performance for kesterite absorbers. With this endeavour in mind, we explored and analyzed the best ways to reach this goal. First and foremost, it was crucial to establish and explain the relationships between the synthesis conditions of kesterite based absorbers (CZTS, CZTSe), its physical properties and the performance of photovoltaic devices. The very first step was to understand the formation mechanism of the material in relation to the growth conditions. Both CZTS and CZTSe are synthesized by a two-step annealing process, where precursor deposition by DC sputtering is followed by a second step of annealing. A careful study of the different annealing conditions was key to apprehend in depth the reaction mechanism that lead to the final kesterite-based absorber. A strong emphasis was put on the material characterization at each step of the synthesis. The results clearly demonstrate that our selenization process - two-step annealing along with the improved Mo back contact and HCl etching - was beneficial to achieve a PCE of 7.6%. A highest PCE of 5.9% was achieved as well using an open reactor for sulfurization. Experimental work also highlighted the importance of chalcogen vapor pressure on microstructural and electrical properties of CZTSe/CZTS absorber, higher chalcogen vapor pressure being beneficial for the complete device.

Some attention was, subsequently devoted to other ways of enhancing performances, which led to explore the possible benefits from incorporation of Na and Sb in CZTS. Experiments were carried out by applying Na and Sb, during and after the synthesis of CZTS in order to choose the best strategy in terms of material and electrical properties. Results demonstrate that, as with CIGS technologies, sodium is beneficial for CZTS to achieve an increase of the open circuit voltage, fill factor and short circuit current. Additional favorable effects on the morphology of the CZTS absorber - such as faceted big grains - arise from Na incorporation ; but conversely

Na 'overdose' degrades the morphology. Na being present during the synthesis process has been determined to be the best strategy to achieve higher PCE (double PCE compared to sample without Na). 15 nm of NaF was observed to be the optimum amount for obtaining best resulting devices, an excessive amount of Na resulting in the degradation of the absorber. EQE analysis and simulation were performed on samples with intentional Na contamination and indication of surface passivation properties induced by Na were identified. Contrary to Na, Sb incorporation did not show any improvement in terms of electrical properties despite the big grains it allows.

Finally, we sought to improve efficiency even further with bandgap engineering, a powerful tool which may increase the performances of CZTSSe based solar cells without changing the absorber material quality. A focus was placed on bandgap engineering based on the control of  $[S]/([S]+[Se])$  ratio in the absorber, which revealed many interesting insights : Front side grading was realized and the defect layer at the surface of the absorber induced by this process was removed successfully using HCl etching. A resulting solar cell, produced with this absorber showed 3.5% efficiency. Two pathways which hint at the limitations of the front side grading were explored. One is the use of binary compounds as the intermediate precursor resulting in a constant bandgap due to the formation of Cu-Se from Cu-S at the beginning of the reaction. The second is the poor crystallinity while using ternary compound as the intermediate precursor, due to the lack of surfactant as Cu based binaries at this stage.

## 7.1 Perspectives

Kesterite being a complex material, it requires a high degree of understanding. This work sought to give some lights on different aspects. Several other research topics may be identified that would speed up the development of kesterite and push it to same level as other thin-film technologies such as CIGS and CdTe. To achieve this, theoretical studies on the understanding of defects will be but one step; a higher degree of understanding of the processes, correlation of device characteristics with processing conditions and knowledge on secondary phases will be required.

This work highlighted the importance of chalcogen vapor pressure during annealing. The low process controllability is the biggest research challenge as it makes the analysis complicated. Thus, a new process using  $H_2S/H_2Se$  as chalcogen source may prove beneficial by providing higher degree of controllability.

Na was found to be beneficial to increase the device properties; A deeper study on other alkali,

## Chapter 7. Conclusion and Perspective

---

or any other relevant elements could help with defects passivation. Work on replacement of cations would be able to address the order-disorder issue, such as- Sn can be replaced by Ge or Cu can be replaced by Ag etc. But care need to be taken as these inclusion of different elements might face criticism because of the potential use of toxic/scarce material.

Graded bandgap holds interesting promises of improvements for kesterite absorber, but these are still out of reach due to the lack of process control and knowledge. A new design of furnace that can utilize both sulfur and selenium simultaneously during annealing procedure might be a good way to reliably achieve graded kesterite. A deep study of the front and back interfaces will also be indispensable to get the most benefits from a graded absorber. Furthermore, suitable nano-characterization process should be developed to identify the atomic distribution of S and Se and apply the knowledge back to the process.

Kesterite solar cell was destined to replace other thin-film technologies. This technology has yet to reach its climax. Its performance are still not up to par with its predecessors but it certainly hasn't reached its full potential. There is little doubt that, with the constant improvements brought forth by the many research groups (most of whom achieved more than 10% efficiency), it will soon catch up with the other mature thin-film technologies.



## Bibliography

- [1] D. Wuebbles, D. Fahey, K. Hibbard, B. DeAngelo, S. Doherty, K. Hayhoe, R. Horton, J. Kossin, P. Taylor, A. Waple, and C. Weaver, “Executive summary. climate science special report: Fourth national climate assessment, volume i,” *U.S. Global Change Research Program*, 2017.
- [2] NASA, “Global climate change: Vital signs of the planet,” 2018. [Online; accessed 24-July-2018].
- [3] European Commission, “2030 climate and energy framework,” 2014. [Online; accessed 24-July-2018].
- [4] International Energy Agency, “Statistics:total primary energy supply (TPES) by source,” 2017. [Online; accessed 24-July-2018].
- [5] C. Kost, S. Shammugam, V. Jülch, H.-T. Nguyen, and T. Schlegl, “Levelized cost of electricity- renewable energy technologies (Fraunhofer Institute),” *Fraunhofer Institute*, p. 42, 2018.
- [6] Fraunhofer Institute, “Photovoltaics report,” 2018. [Online; accessed 24-July-2018].
- [7] M. A. Green, Y. Hishikawa, E. D. Dunlop, D. H. Levi, J. Hohl-Ebinger, and A. W. Ho-Baillie, “Solar cell efficiency tables (version 52),” *Progress in Photovoltaics: Research and Applications*, vol. 26, no. 7, pp. 427–436, 2018.
- [8] M. A. Green, “Commercial progress and challenges for photovoltaics,” *Nature Energy*, vol. 1, p. 15015, 2016.
- [9] USGS, “Usgs minerals information: Commodity statistics and information,” 2017. [Online; accessed 24-July-2018].
- [10] WebElements Periodic Table, “Abundance in earth’s crust,” 2017. [Online; accessed 24-July-2018].

## Bibliography

---

- [11] V. Fthenakis, W. Wang, and H. C. Kim, "Life cycle inventory analysis of the production of metals used in photovoltaics," *Renewable and Sustainable Energy Reviews*, vol. 13, no. 3, pp. 493 – 517, 2009.
- [12] D. Cozza, C. M. Ruiz, D. Duché, S. Giraldo, E. Saucedo, J. J. Simon, and L. Escoubas, "Optical modeling and optimizations of Cu<sub>2</sub>ZnSnS<sub>4</sub> solar cells using the modified transfer matrix method," *Opt. Express*, vol. 24, pp. A1201–A1209, Sep 2016.
- [13] S. G. Haass, "Alkali treatment of solution processed kesterite solar cells," 2017.
- [14] W. Wang, M. T. Winkler, O. Gunawan, T. Gokmen, T. K. Todorov, Y. Zhu, and D. B. Mitzi, "Device characteristics of CZTSSe thin film solar cells with 12.6% efficiency," *Advanced Energy Materials*, vol. 4, no. 7, p. 1301465, 2014.
- [15] N. Naghavi, D. Abou-Ras, N. Allsop, N. Barreau, S. Bücheler, A. Ennaoui, C. Fischer, C. Guillen, D. Hariskos, J. Herrero, R. Klenk, K. Kushiya, D. Lincot, R. Menner, T. Nakada, C. Platzer-Björkman, S. Spiering, A. Tiwari, and T. Törndahl, "Buffer layers and transparent conducting oxides for chalcopyrite Cu(In,Ga)S<sub>2</sub> based thin film photovoltaics: present status and current developments," *Progress in Photovoltaics: Research and Applications*, vol. 18, no. 6, pp. 411–433, 2010.
- [16] U. Rau, P. O. Grabitz, and J. H. Werner, "Resistive limitations to spatially inhomogeneous electronic losses in solar cells," *Applied Physics Letters*, vol. 85, no. 24, pp. 6010–6012, 2004.
- [17] W. Aron, C. Shiyou, W. Su-Huai, and G. Xin-Gao, "Kesterite thin-film solar cells: Advances in materials modelling of Cu<sub>2</sub>ZnSnS<sub>4</sub>," *Advanced Energy Materials*, vol. 2, no. 4, pp. 400–409, 2012.
- [18] S. Siebentritt and S. Schorr, "Kesterites—a challenging material for solar cells," *Progress in Photovoltaics: Research and Applications*, vol. 20, no. 5, pp. 512–519, 2012.
- [19] S. Schorr, "The crystal structure of kesterite type compounds: A neutron and x-ray diffraction study," *Solar Energy Materials and Solar Cells*, vol. 95, no. 6, pp. 1482 – 1488, 2011. Special Issue : Thin film and nanostructured solar cells.
- [20] S. Chen, X. G. Gong, A. Walsh, and S.-H. Wei, "Crystal and electronic band structure of Cu<sub>2</sub>ZnSnX<sub>4</sub> (x=s and se) photovoltaic absorbers: First-principles insights," *Applied Physics Letters*, vol. 94, no. 4, p. 041903, 2009.

- [21] A. Lafond, L. Choubrac, C. Guillot Deudon, P. Fertey, M. Evain, and S. Jobic, "X-ray resonant single-crystal diffraction technique, a powerful tool to investigate the kesterite structure of the photovoltaic  $\text{Cu}_2\text{ZnSnS}_4$  compound," *Acta Crystallographica Section B Structural Science, Crystal Engineering and Materials*, vol. 70, no. 2, pp. 390–394, 2014-04-01.
- [22] K. Rudisch, Y. Ren, C. Platzer-Björkman, and J. Scragg, "Order-disorder transition in B-type  $\text{Cu}_2\text{ZnSnS}_4$  and limitations of ordering through thermal treatments," *Applied Physics Letters*, vol. 108, no. 23, p. 231902, 2016.
- [23] J. J. Scragg, L. Choubrac, A. Lafond, T. Ericson, and C. Platzer Björkman, "A low-temperature order-disorder transition in  $\text{Cu}_2\text{ZnSnS}_4$  thin films," *Applied Physics Letters*, vol. 104, no. 4, p. 041911, 2014.
- [24] G. Rey, A. Redinger, J. Sendler, T. P. Weiss, M. Thevenin, M. Guennou, B. El Adib, and S. Siebentritt, "The band gap of  $\text{Cu}_2\text{ZnSnSe}_4$ : Effect of order-disorder," *Applied Physics Letters*, vol. 105, no. 11, p. 112106, 2014.
- [25] S. Bourdais, C. Choné, B. Delatouche, A. Jacob, G. Larramona, C. Moisan, A. Lafond, F. Donatini, G. Rey, S. Siebentritt, A. Walsh, and G. Dennler, "Is the Cu/Zn disorder the main culprit for the voltage deficit in kesterite solar cells?," *Advanced Energy Materials*, vol. 6, no. 12, p. 1502276, 2016.
- [26] J. J. Scragg, J. T. Wätjen, M. Edoff, T. Ericson, T. Kubart, and C. Platzer-Björkman, "A detrimental reaction at the molybdenum back contact in  $\text{Cu}_2\text{ZnSn}(\text{S},\text{Se})_4$  thin-film solar cells," *Journal of the American Chemical Society*, vol. 134, no. 47, pp. 19330–19333, 2012. PMID: 23146047.
- [27] J. Scragg, *Studies of  $\text{Cu}_2\text{ZnSnSe}_4$  films prepared by sulfurisation of electrodeposited precursors*. PhD thesis, University of Bath, 5 2010.
- [28] H. Katagiri, K. Jimbo, M. Tahara, H. Araki, and K. Oishi, "The influence of the composition ratio on CZTS-based thin film solar cells," *MRS Proceedings*, vol. 1165, pp. 1165–M04–01, 2009.
- [29] M. Kumar, A. Dubey, N. Adhikari, S. Venkatesan, and Q. Qiao, "Strategic review of secondary phases, defects and defect-complexes in kesterite CZTS–Se solar cells," *Energy Environ. Sci.*, vol. 8, pp. 3134–3159, 2015.
- [30] S. Siebentritt, "Why are kesterite solar cells not 20% efficient?," *Thin Solid Films*, vol. 535, pp. 1–4, 2013.

## Bibliography

---

- [31] S. Chen, A. Walsh, X.-G. Gong, and S.-H. Wei, "Classification of lattice defects in the kesterite  $\text{Cu}_2\text{ZnSnS}_4$  and  $\text{Cu}_2\text{ZnSnSe}_4$  earth-abundant solar cell absorbers," *Advanced Materials*, vol. 25, no. 11, pp. 1522–1539, 2013.
- [32] D. Han, Y. Y. Sun, J. Bang, Y. Y. Zhang, H.-B. Sun, X.-B. Li, and S. B. Zhang, "Deep electron traps and origin of  $p$ -type conductivity in the earth-abundant solar-cell material  $\text{Cu}_2\text{ZnSnS}_4$ ," *Phys. Rev. B*, vol. 87, p. 155206, Apr 2013.
- [33] M. Dimitrievska, A. Fairbrother, E. Saucedo, A. Pérez-Rodríguez, and V. Izquierdo-Roca, "Secondary phase and Cu substitutional defect dynamics in kesterite solar cells: Impact on optoelectronic properties," *Solar Energy Materials and Solar Cells*, vol. 149, pp. 304–309, 2016.
- [34] J. Márquez, M. Neuschitzer, M. Dimitrievska, R. Gunder, S. Haass, M. Werner, Y. Romanuk, S. Schorr, N. Pearsall, and I. Forbes, "Systematic compositional changes and their influence on lattice and optoelectronic properties of  $\text{Cu}_2\text{ZnSnSe}_4$  kesterite solar cells," *Solar Energy Materials and Solar Cells*, vol. 144, pp. 579–585, 2016.
- [35] L. Grenet, M. A. A. Suzon, F. Emieux, and F. Roux, "Analysis of failure modes in kesterite solar cells," *ACS Applied Energy Materials*, vol. 1, no. 5, pp. 2103–2113, 2018.
- [36] S. Chen, A. Walsh, J. H. Yang, X. G. Gong, L. Sun, P. X. Yang, J. H. Chu, and S. H. Wei, "Compositional dependence of structural and electronic properties of  $\text{Cu}_2\text{ZnSn}(\text{S},\text{Se})_4$  alloys for thin film solar cells," *Phys. Rev. B*, vol. 83, p. 125201, Mar 2011.
- [37] G. Altamura, "Development of CZTSSe thin films based solar cells."
- [38] C. Platzer-Björkman, "Kesterite compound semiconductors for thin film solar cells," *Current Opinion in Green and Sustainable Chemistry*, vol. 4, pp. 84–90, 2017. 4 Novel materials for energy production and storage 2017.
- [39] S. Giraldo, E. Saucedo, M. Neuschitzer, F. Oliva, M. Placidi, X. Alcobé, V. Izquierdo-Roca, S. Kim, H. Tampo, H. Shibata, A. Perez-Rodriguez, and P. Pistor, "How small amounts of Ge modify the formation pathways and crystallization of kesterites," *Energy Environ. Sci.*, vol. 11, pp. 582–593, 2018.
- [40] E. Chagarov, K. Sardashti, A. C. Kummel, Y. S. Lee, R. Haight, and T. S. Gershon, " $\text{Ag}_2\text{ZnSn}(\text{S},\text{Se})_4$ : A highly promising absorber for thin film photovoltaics," *The Journal of Chemical Physics*, vol. 144, no. 10, p. 104704, 2016.

- [41] J. Hedstrom, H. Ohlsen, M. Bodegard, A. Kylner, L. Stolt, D. Hariskos, M. Ruckh, and H. W. Schock, "ZnO/CdS/Cu(In,Ga)Se<sub>2</sub> thin film solar cells with improved performance," in *Conference Record of the Twenty Third IEEE Photovoltaic Specialists Conference - 1993* (Cat. No.93CH3283-9), pp. 364–371, May 1993.
- [42] L. Van Puyvelde, J. Lauwaert, A. Tempez, W. Devulder, S. Nishiwaki, F. Pianezzi, C. Detavernier, A. N. Tiwari, and H. Vrielinck, "Electronic defect study on low temperature processed Cu(In,Ga)Se<sub>2</sub> thin-film solar cells and the influence of an Sb layer," *Journal of Physics D: Applied Physics*, vol. 48, no. 17, p. 175104, 2015.
- [43] W. Hlaing Oo, J. Johnson, A. Bhatia, E. Lund, M. Nowell, and M. Scarpulla, "Grain size and texture of Cu<sub>2</sub>ZnSnS<sub>4</sub> thin films synthesized by cosputtering binary sulfides and annealing: Effects of processing conditions and sodium," *Journal of Electronic Materials*, vol. 40, no. 11, pp. 2214–2221, 2011.
- [44] C. M. Sutter-Fella, J. A. Stückelberger, H. Hagendorfer, F. La Mattina, L. Kranz, S. Nishiwaki, A. R. Uhl, Y. E. Romanyuk, and A. N. Tiwari, "Sodium assisted sintering of chalcogenides and its application to solution processed Cu<sub>2</sub>ZnSn(S,Se)<sub>4</sub> thin film solar cells," *Chemistry of Materials*, vol. 26, no. 3, pp. 1420–1425, 2014.
- [45] M. Johnson, S. V. Baryshev, E. Thimsen, M. Manno, X. Zhang, I. V. Veryovkin, C. Leighton, and E. S. Aydil, "Alkali-metal-enhanced grain growth in Cu<sub>2</sub>ZnSnS<sub>4</sub> thin films," *Energy Environ. Sci.*, vol. 7, pp. 1931–1938, 2014.
- [46] R. Scheer and H. W. Schock, *Chalcogenide Photovoltaics: Physics, Technologies, and Thin Film Devices*. Wiley-VCH, 2011.
- [47] M. A. Contreras, J. Tuttle, A. Gabor, A. Tennant, K. Ramanathan, S. Asher, A. Franz, J. Keane, L. Wang, J. Scofield, and R. Noufi, "High efficiency Cu(In,Ga)Se<sub>2</sub> based solar cells: processing of novel absorber structures," in *Proceedings of 1994 IEEE 1st World Conference on Photovoltaic Energy Conversion - WCPEC (A Joint Conference of PVSC, PVSEC and PSEC)*, vol. 1, pp. 68–75 vol.1, 1994.
- [48] H. Sugimoto, C. Liao, H. Hiroi, N. Sakai, and T. Kato, "Lifetime improvement for high efficiency Cu<sub>2</sub>ZnSnS<sub>4</sub> submodules," in *2013 IEEE 39th Photovoltaic Specialists Conference (PVSC)*, pp. 3208–3211, June 2013.
- [49] H. Huang, K. Winchester, A. Suvorova, B. Lawn, Y. Liu, X. Hu, J. Dell, and L. Faraone, "Effect of deposition conditions on mechanical properties of low-temperature PECVD

## Bibliography

---

- silicon nitride films,” *Materials Science and Engineering: A*, vol. 435-436, pp. 453 – 459, 2006.
- [50] D. Abou Ras, T. Kircharzt, and U. Rau, *Advanced characterization techniques for thin film solar cells*. John Wiley and sons, 2011.
- [51] T. P. Dhakal, C. Peng, R. R. Tobias, R. Dasharathy, and C. R. Westgate, “Characterization of a CZTS thin film solar cell grown by sputtering method,” *Solar Energy*, vol. 100, pp. 23 – 30, 2014.
- [52] P. Fernandes, P. Salomé, and A. da Cunha, “Study of polycrystalline  $\text{Cu}_2\text{ZnSnS}_4$  films by raman scattering,” *Journal of Alloys and Compounds*, vol. 509, no. 28, pp. 7600 – 7606, 2011.
- [53] A. R. Denton and N. W. Ashcroft, “Vegard’s law,” *Phys. Rev. A*, vol. 43, pp. 3161–3164, Mar 1991.
- [54] P. M. P. Salomé, P. A. Fernandes, J. P. Leitão, M. G. Sousa, J. P. Teixeira, and A. F. d. Cunha, “Secondary crystalline phases identification in  $\text{Cu}_2\text{ZnSnSe}_4$  thin films: contributions from raman scattering and photoluminescence,” *Journal of Materials Science*, vol. 49, no. 21, pp. 7425–7436, 2014.
- [55] A. Redinger, K. Hönes, X. Fontané, V. Izquierdo-Roca, E. Saucedo, N. Valle, A. Pérez Rodríguez, and S. Siebentritt, “Detection of a ZnSe secondary phase in coevaporated  $\text{Cu}_2\text{ZnSnSe}_4$  thin films,” *Applied Physics Letters*, vol. 98, no. 10, p. 101907, 2011.
- [56] A. Hernández Martínez, M. Placidi, L. Arqués, S. Giraldo, Y. Sánchez, V. Izquierdo Roca, P. Pistor, M. Valentini, C. Malerba, and E. Saucedo, “Insights into the formation pathways of  $\text{Cu}_2\text{ZnSnSe}_4$  using rapid thermal processes,” *ACS Applied Energy Materials*, 2018.
- [57] M. Dimitrievska, A. Fairbrother, R. Gunder, G. Gurieva, H. Xie, E. Saucedo, A. Pérez Rodríguez, V. Izquierdo Roca, and S. Schorr, “Role of S and Se atoms on the microstructural properties of kesterite  $\text{Cu}_2\text{ZnSn}(\text{S},\text{Se})_4$  thin film solar cells,” *Phys. Chem. Chem. Phys.*, vol. 18, no. 12, pp. 8692–8700, 2016.
- [58] M. Grossberg, J. Krustok, J. Raudoja, K. Timmo, M. Altosaar, and T. Raadik, “Photoluminescence and raman study of  $\text{Cu}_2\text{ZnSn}(\text{Se}_x\text{S}_{1-x})_4$  monograins for photovoltaic applications,” *Thin Solid Films*, vol. 519, no. 21, pp. 7403 – 7406, 2011.
- [59] J. C. Vickerman, “Secondary ion mass spectrometry—basic concepts, instrumental aspects, applications and trends,” *Surface and Interface Analysis*, vol. 10, no. 8, pp. 435–435, 1987.

- [60] S. Merdes, B. Johnson, R. Sáez-Araoz, A. Ennaoui, J. Klaer, I. Lauermaun, R. Mainz, A. Meeder, and R. Klenk, "Current transport in CuInGaS<sub>2</sub> based solar cells with high open circuit voltage - bulk vs. interface," *MRS Proceedings*, vol. 1165, pp. 1165-M05-15, 2009.
- [61] S. S. Hegedus and W. N. Shafarman, "Thin film solar cells device measurements and analysis," *Progress in Photovoltaics: Research and Applications*, vol. 12, no. 2, pp. 155-176, 2004.
- [62] P. A. Fernandes, A. F. Sartori, P. M. P. Salomé, J. Malaquias, A. F. da Cunha, M. P. F. Graça, and J. C. González, "Admittance spectroscopy of Cu<sub>2</sub>ZnSnS<sub>4</sub> based thin film solar cells," *Applied Physics Letters*, vol. 100, no. 23, p. 233504, 2012.
- [63] T. Hara, T. Maekawa, S. Minoura, Y. Sago, S. Niki, and H. Fujiwara, "Quantitative assessment of optical gain and loss in submicron-textured CuIn<sub>1-x</sub>Ga<sub>x</sub>Se<sub>2</sub> solar cells fabricated by three-stage coevaporation," *Phys. Rev. Applied*, vol. 2, p. 034012, Sep 2014.
- [64] C. Yim, M. O'Brien, N. McEvoy, S. Winters, I. Mirza, J. G. Lunney, and G. S. Duesberg, "Investigation of the optical properties of MoS<sub>2</sub> thin films using spectroscopic ellipsometry," *Applied Physics Letters*, vol. 104, no. 10, p. 103114, 2014.
- [65] S.-Y. Li, C. Hägglund, Y. Ren, J. J. Scragg, J. K. Larsen, C. Frisk, K. Rudisch, S. Englund, and C. Platzer-Björkman, "Optical properties of reactively sputtered Cu<sub>2</sub>ZnSnS<sub>4</sub> solar absorbers determined by spectroscopic ellipsometry and spectrophotometry," *Solar Energy Materials and Solar Cells*, vol. 149, pp. 170 - 178, 2016.
- [66] K. Ito and T. Nakazawa, "Electrical and optical properties of stannite-type quaternary semiconductor thin films," *Japanese Journal of Applied Physics*, vol. 27, no. 11R, p. 2094, 1988.
- [67] Y. S. Lee, T. Gershon, O. Gunawan, T. K. Todorov, T. Gokmen, Y. Virgus, and S. Guha, "Cu<sub>2</sub>ZnSnSe<sub>4</sub> thin-film solar cells by thermal co-evaporation with 11.6% efficiency and improved minority carrier diffusion length," *Advanced Energy Materials*, vol. 5, no. 7, p. 1401372, 2015.
- [68] T. Teoman, N. Janet, S. Johannes, P. Devendra, S. Vincent, P. Jürgen, and G. Levent, "Device characteristics of an 11.4% Cu<sub>2</sub>ZnSnSe<sub>4</sub> solar cell fabricated from sputtered precursors," *Advanced Energy Materials*, vol. 0, no. 0, p. 1703295, 2018.

## Bibliography

---

- [69] G. Zoppi, I. Forbes, R. W. Miles, P. J. Dale, J. J. Scragg, and L. M. Peter, "Cu<sub>2</sub>ZnSnSe<sub>4</sub> thin film solar cells produced by selenisation of magnetron sputtered precursors," *Progress in Photovoltaics: Research and Applications*, vol. 17, no. 5, pp. 315–319, 2009.
- [70] G. Brammertz, M. Buffière, S. Oueslati, H. ElAnzeery, K. Ben Messaoud, S. Sahayaraj, C. Köble, M. Meuris, and J. Poortmans, "Characterization of defects in 9.7% efficient Cu<sub>2</sub>ZnSnSe<sub>4</sub>-CdS-ZnO solar cells," *Applied Physics Letters*, vol. 103, no. 16, p. 163904, 2013.
- [71] M. Neuschitzer, Y. Sanchez, S. López-Marino, H. Xie, A. Fairbrother, M. Placidi, S. Haass, V. Izquierdo-Roca, A. Perez-Rodriguez, and E. Saucedo, "Optimization of CdS buffer layer for high performance Cu<sub>2</sub>ZnSnSe<sub>4</sub> solar cells and the effects of light soaking elimination of crossover and red kink," *Progress in Photovoltaics: Research and Applications*, vol. 23, no. 11, pp. 1660–1667, 2015.
- [72] S. Oueslati, G. Brammertz, M. Buffière, H. ElAnzeery, O. Touayar, C. Köble, J. Bekaert, M. Meuris, and J. Poortmans, "Physical and electrical characterization of high-performance Cu<sub>2</sub>ZnSnSe<sub>4</sub> based thin film solar cells," *Thin Solid Films*, vol. 582, pp. 224 – 228, 2015. E-MRS 2014 Spring Meeting, Symposium A, Thin-Film Chalcogenide Photovoltaic Materials.
- [73] J. Li, H. Wang, L. Wu, C. Chen, Z. Zhou, F. Liu, Y. Sun, J. Han, and Y. Zhang, "Growth of Cu<sub>2</sub>ZnSnSe<sub>4</sub> film under controllable Se vapor composition and impact of low Cu content on solar cell efficiency," *ACS Applied Materials & Interfaces*, vol. 8, no. 16, pp. 10283–10292, 2016.
- [74] C. Andres, S. Haass, Y. Romanyuk, and A. Tiwari, "9.4% efficient Cu<sub>2</sub>ZnSnSe<sub>4</sub> solar cells from co-sputtered elemental metal precursor and rapid thermal annealing," *Thin Solid Films*, vol. 633, pp. 141 – 145, 2017. E-MRS 2016 Spring Meeting, Symposium V, Thin-Film Chalcogenide Photovoltaic Materials.
- [75] L. Vauche, L. Risch, Y. Sánchez, M. Dimitrievska, M. Pasquinelli, M. T. Goislard, P. P. Grand, F. S. Jaime, and E. Saucedo, "8.2% pure selenide kesterite thin film solar cells from large area electrodeposited precursors," *Progress in Photovoltaics: Research and Applications*, vol. 24, no. 1, pp. 38–51, 2016.
- [76] Y. Yang, G. Wang, W. Zhao, Q. Tian, L. Huang, and D. Pan, "Solution-processed highly efficient Cu<sub>2</sub>ZnSnSe<sub>4</sub> thin film solar cells by dissolution of elemental Cu, Zn, Sn, and Se powders," *ACS Applied Materials & Interfaces*, vol. 7, no. 1, pp. 460–464, 2015.

- [77] H. Katagiri, N. Sasaguchi, S. Hando, S. Hoshino, J. Ohashi, and T. Yokota, "Preparation and evaluation of  $\text{Cu}_2\text{ZnSnS}_4$  thin films by sulfurization of eb evaporated precursors," *Solar Energy Materials and Solar Cells*, vol. 49, no. 1, pp. 407 – 414, 1997.
- [78] M. Green, Y. Hishikawa, E. D. Dunlop, D. H. Levi, J. Hohl-Ebinger, and A. W. Ho-Baillie, "Solar cell efficiency tables (version 51)," *Progress in Photovoltaics: Research and Applications*, vol. 26, no. 1, pp. 3–12, 2017.
- [79] C. Malerba, C. L. Azanza Ricardo, M. Valentini, F. Biccari, M. Müller, L. Rebuffi, E. Esposito, P. Mangiapane, P. Scardi, and A. Mittiga, "Stoichiometry effect on  $\text{Cu}_2\text{ZnSnS}_4$  thin films morphological and optical properties," *Journal of Renewable and Sustainable Energy*, vol. 6, no. 1, p. 011404, 2014.
- [80] T. P. White, N. N. Lal, and K. R. Catchpole, "Tandem solar cells based on high-efficiency C-Si bottom cells: Top cell requirements for more than 30% efficiency," *IEEE Journal of Photovoltaics*, vol. 4, no. 1, pp. 208–214, 2014.
- [81] W. Weihuang, W. Guohui, C. Guilin, C. Shuiyuan, and H. Zhigao, "The effect of sulfur vapor pressure on  $\text{Cu}_2\text{ZnSnS}_4$  thin film growth for solar cells," *Solar Energy*, vol. 148, pp. 12 – 16, 2017.
- [82] K. Jimbo, R. Kimura, T. Kamimura, S. Yamada, W. S. Maw, H. Araki, K. Oishi, and H. Katagiri, " $\text{Cu}_2\text{ZnSnS}_4$ -type thin film solar cells using abundant materials," *Thin Solid Films*, vol. 515, no. 15, pp. 5997 – 5999, 2007. Proceedings of Symposium O on Thin Film Chalcogenide Photovoltaic Materials, EMRS 2006 Conference.
- [83] H. Katagiri, K. Jimbo, S. Yamada, T. Kamimura, W. S. Maw, T. Fukano, T. Ito, and T. Motohiro, "Enhanced conversion efficiencies of  $\text{Cu}_2\text{ZnSnS}_4$  -based thin film solar cells by using preferential etching technique," *Applied Physics Express*, vol. 1, no. 4, p. 041201, 2008.
- [84] M. Green, K. Emery, Y. Hishikawa, W. Warta, and E. D. Dunlop, "Solar cell efficiency tables (version 46)," *Progress in Photovoltaics: Research and Applications*, vol. 23, no. 7, pp. 805–812, 2013.
- [85] T. Shin, U. Mitsutaro, H. Masaki, M. Takahiro, and I. Tadayoshi, " $\text{Cu}_2\text{ZnSnS}_4$  photovoltaic cell with improved efficiency fabricated by high temperature annealing after CdS buffer layer deposition," *Progress in Photovoltaics: Research and Applications*, vol. 25, no. 1, pp. 14–22, 2016.

## Bibliography

---

- [86] D. Nam, S. Cho, J. H. Sim, K. J. Yang, D. H. Son, D. H. Kim, J. K. Kang, M. S. Kwon, C. W. Jeon, and H. Cheong, "Solar conversion efficiency and distribution of ZnS secondary phase in  $\text{Cu}_2\text{ZnSnS}_4$  solar cells," *Solar Energy Materials and Solar Cells*, vol. 149, pp. 226 – 231, 2016.
- [87] Y. Feng, T.-K. Lau, G. Cheng, L. Yin, Z. Li, H. Luo, Z. Liu, X. Lu, C. Yang, and X. Xiao, "A low-temperature formation path toward highly efficient se-free  $\text{Cu}_2\text{ZnSnS}_4$  solar cells fabricated through sputtering and sulfurization," *CrystEngComm*, vol. 18, pp. 1070–1077, 2016.
- [88] Y. Ren, N. Ross, J. K. Larsen, K. Rudisch, J. J. S. Scragg, and C. Platzer-Björkman, "Evolution of  $\text{Cu}_2\text{ZnSnS}_4$  during Non-Equilibrium annealing with Quasi-in situ monitoring of sulfur partial pressure," *Chemistry of Materials*, vol. 29, no. 8, pp. 3713–3722, 2017.
- [89] A. Moholkar, S. Shinde, G. Agawane, S. Jo, K. Rajpure, P. Patil, C. Bhosale, and J. Kim, "Studies of compositional dependent CZTS thin film solar cells by pulsed laser deposition technique: An attempt to improve the efficiency," *Journal of Alloys and Compounds*, vol. 544, pp. 145 – 151, 2012.
- [90] K. Woo, Y. Kim, and J. Moon, "A non-toxic, solution-processed, earth abundant absorbing layer for thin-film solar cells," *Energy Environ. Sci.*, vol. 5, pp. 5340–5345, 2012.
- [91] T. Yuan, Y. Li, M. Jia, Y. Lai, J. Li, F. Liu, and Y. Liu, "Fabrication of  $\text{Cu}_2\text{ZnSnS}_4$  thin film solar cells by sulfurization of electrodeposited stacked binary Cu–Zn and Cu–Sn alloy layers," *Materials Letters*, vol. 155, pp. 44 – 47, 2015.
- [92] M. Mousel, T. Schwarz, R. Djemour, T. P. Weiss, J. Sandler, J. C. Malaquias, A. Redinger, M. O. Cojocar, P. P. Choi, and S. Siebentritt, "Cu-rich precursors improve kesterite solar cells," *Advanced Energy Materials*, vol. 4, no. 2, p. 1300543, 2014.
- [93] P. A. Fernandes, M. G. Sousa, P. M. P. Salomé, J. P. Leitão, and A. F. d. Cunha, "Thermodynamic pathway for the formation of SnSe and SnSe<sub>2</sub> polycrystalline thin films by selenization of metal precursors," *Royal Society of Chemistry*, vol. 15, no. 47, pp. 10278–10286, 2013.
- [94] W. C. Hsu, I. Repins, C. Beall, C. DeHart, B. To, W. Yang, Y. Yang, and R. Noufi, "Growth mechanisms of co-evaporated kesterite a comparison of Cu-rich and Zn-rich composition paths," *Progress in Photovoltaics: Research and Applications*, vol. 22, no. 1, pp. 35–43, 2013.

- [95] L. Vauche, L. Risch, M. Arasimowicz, Y. Sánchez, E. Saucedo, M. Pasquinelli, T. Goisard de Monsabert, P. Grand, and S. Jaime-Ferrer, "Detrimental effect of sn-rich secondary phases on  $\text{Cu}_2\text{ZnSnSe}_4$  based solar cells," *Journal of Renewable and Sustainable Energy*, vol. 8, no. 3, p. 033502, 2016.
- [96] D. B. Mitzi, O. Gunawan, T. K. Todorov, K. Wang, and S. Guha, "The path towards a high-performance solution-processed kesterite solar cell," *Solar Energy Materials and Solar Cells*, vol. 95, no. 6, pp. 1421 – 1436, 2011. Special Issue : Thin film and nanostructured solar cells.
- [97] A. Fairbrother, L. Fourdrinier, X. Fontané, V. Izquierdo Roca, M. Dimitrievska, A. Pérez Rodríguez, and E. Saucedo, "Precursor stack ordering effects in  $\text{Cu}_2\text{ZnSnSe}_4$  thin films prepared by rapid thermal processing," *The Journal of Physical Chemistry C*, vol. 118, no. 31, pp. 17291–17298, 2014.
- [98] A. Fairbrother, X. Fontané, V. I. Roca, M. E. Rodríguez, S. L. Marino, M. Placidi, L. C. Barrio, A. P. Rodríguez, and E. Saucedo, "On the formation mechanisms of Zn-rich  $\text{Cu}_2\text{ZnSnS}_4$  films prepared by sulfurization of metallic stacks," *Solar Energy Materials and Solar Cells*, vol. 112, pp. 97 – 105, 2013.
- [99] J. J. Scragg, T. Ericson, T. Kubart, M. Edoff, and C. Platzer Björkman, "Chemical insights into the instability of  $\text{Cu}_2\text{ZnSnS}_4$  films during annealing," *Chemistry of Materials*, vol. 23, no. 20, pp. 4625–4633, 2011.
- [100] S. López Marino, M. Placidi, A. Pérez Tomás, J. Llobet, V. Izquierdo Roca, X. Fontané, A. Fairbrother, M. Espíndola Rodríguez, D. Sylla, A. Pérez Rodríguez, and E. Saucedo, "Inhibiting the absorber/mo-back contact decomposition reaction in  $\text{Cu}_2\text{ZnSnSe}_4$  solar cells: the role of a ZnO intermediate nanolayer," *Journal of Materials Chemistry A*, vol. 1, no. 29, 2013.
- [101] A. Fairbrother, X. Fontané, V. Izquierdo-Roca, M. Placidi, D. Sylla, M. Espindola-Rodriguez, S. López-Mariño, F. A. Pulgarín, O. Vigil-Galán, A. Pérez-Rodríguez, and E. Saucedo, "Secondary phase formation in Zn rich  $\text{Cu}_2\text{ZnSnSe}_4$  based solar cells annealed in low pressure and temperature conditions," *Progress in Photovoltaics: Research and Applications*, vol. 22, no. 4, pp. 479–487, 2014.
- [102] A. Fairbrother, E. García-Hemme, V. Izquierdo-Roca, X. Fontané, F. A. Pulgarín-Agudelo, O. Vigil-Galán, A. Pérez-Rodríguez, and E. Saucedo, "Development of a selective chemical etch to improve the conversion efficiency of Zn-rich  $\text{Cu}_2\text{ZnSnS}_4$  solar cells," *Journal of the American Chemical Society*, vol. 134, no. 19, pp. 8018–8021, 2012. PMID: 22545682.

## Bibliography

---

- [103] L. Grenet, M. A. A. Suzon, F. Emieux, and F. Roux, "Comparing strategies for improving efficiencies in vacuum processed  $\text{Cu}_2\text{ZnSnSe}_4$  solar cells," *Journal of Renewable and Sustainable Energy*, vol. 10, no. 4, p. 043503, 2018.
- [104] R. A. Wibowo, S. Moeckel, H. Yoo, A. Hoelzing, R. Hock, and P. J. Wellmann, "Formation of  $\text{Cu}_2\text{SnSe}_3$  from stacked elemental layers investigated by combined in situ X-ray diffraction and differential scanning calorimetry techniques," *Journal of Alloys and Compounds*, vol. 588, pp. 254 – 258, 2014.
- [105] M. F. Carolin, R. U. Alexander, H. Ceri, H. Ive, E. R. Yaroslav, and N. T. Ayodhya, "Formation mechanism of  $\text{Cu}_2\text{ZnSnSe}_4$  absorber layers during selenization of solution deposited metal precursors," *Journal of Alloys and Compounds*, vol. 567, pp. 102 – 106, 2013.
- [106] S. Kim, J.-S. Park, and A. Walsh, "Identification of killer defects in kesterite thin-film solar cells," *ACS Energy Letters*, vol. 3, no. 2, pp. 496–500, 2018.
- [107] J. Philip, W. Roland, H. Dimitrios, L. Erwin, W. Wolfram, and P. Michael, "Effects of heavy alkali elements in  $\text{Cu}(\text{In,Ga})\text{Se}_2$  solar cells with efficiencies up to 22.6," *physica status solidi (RRL) – Rapid Research Letters*, vol. 10, no. 8, pp. 583–586, 2016.
- [108] T. Nakada, Y. Honishi, Y. Yatsushiro, and H. Nakakoba, "Impacts of Sb and Bi incorporations on CIGS thin films and solar cells," in *2011 37th IEEE Photovoltaic Specialists Conference*, pp. 003527–003531, June 2011.
- [109] K. Granath, M. Bodegård, and L. Stolt, "The effect of naf on  $\text{Cu}(\text{In,Ga})\text{Se}_2$  thin film solar cells," *Solar Energy Materials and Solar Cells*, vol. 60, no. 3, pp. 279 – 293, 2000.
- [110] P. Reinhard, B. Bissig, F. Pianezzi, E. Avancini, H. Hagendorfer, D. Keller, P. Fuchs, M. Döbeli, C. Vigo, P. Crivelli, S. Nishiwaki, S. Buecheler, and A. N. Tiwari, "Features of kf and naf postdeposition treatments of  $\text{Cu}(\text{In,Ga})\text{Se}_2$  absorbers for high efficiency thin film solar cells," *Chemistry of Materials*, vol. 27, no. 16, pp. 5755–5764, 2015.
- [111] D. Rudmann, D. Brémaud, A. da Cunha, G. Bilger, A. Strohm, M. Kaelin, H. Zogg, and A. Tiwari, "Sodium incorporation strategies for cigs growth at different temperatures," *Thin Solid Films*, vol. 480-481, pp. 55 – 60, 2005. EMRS 2004.
- [112] M. Yuan, D. B. Mitzi, O. Gunawan, A. J. Kellock, S. J. Chey, and V. R. Deline, "Antimony assisted low-temperature processing of cigs solar cells," *Thin Solid Films*, vol. 519, no. 2, pp. 852 – 856, 2010. Special Section: Romanian Conference on Advanced Materials 2009.

- [113] T. Nakada, H. Ohbo, M. Fukuda, and A. Kunioka, "Improved compositional flexibility of Cu(In,Ga)Se<sub>2</sub>-based thin film solar cells by sodium control technique," *Solar Energy Materials and Solar Cells*, vol. 49, no. 1, pp. 261 – 267, 1997.
- [114] M. B. Ård, K. Granath, and L. Stolt, "Growth of Cu(In,Ga)Se<sub>2</sub> thin films by coevaporation using alkaline precursors," *Thin Solid Films*, vol. 361-362, pp. 9 – 16, 2000.
- [115] Y. Yatsushiro, H. Nakakoba, T. Mise, T. Kobayashi, and T. Nakada, "Effects of antimony doping on Cu(In<sub>1-x</sub>Ga<sub>x</sub>)Se<sub>2</sub> thin films and solar cells," *Japanese Journal of Applied Physics*, vol. 51, no. 10, p. 10NC25, 2012.
- [116] K. Sun, F. Liu, C. Yan, F. Zhou, J. Huang, Y. Shen, R. Liu, and X. Hao, "Influence of sodium incorporation on kesterite Cu<sub>2</sub>ZnSnS<sub>4</sub> solar cells fabricated on stainless steel substrates," *Solar Energy Materials and Solar Cells*, vol. 157, pp. 565 – 571, 2016.
- [117] T. Mise, S. Tajima, T. Fukano, K. Higuchi, T. Washio, K. Jimbo, and H. Katagiri, "Improving the photovoltaic performance of co-evaporated Cu<sub>2</sub>ZnSnS<sub>4</sub> thin-film solar cells by incorporation of sodium from naf layers," *Progress in Photovoltaics: Research and Applications*, vol. 24, no. 7, pp. 1009–1015, 2016.
- [118] G. Rey, F. Babbe, T. Weiss, H. Elanzeery, M. Melchiorre, N. Valle, B. E. Adib, and S. Siebentritt, "Post-deposition treatment of Cu<sub>2</sub>ZnSnSe<sub>4</sub> with alkalis," *Thin Solid Films*, vol. 633, pp. 162 – 165, 2017. E-MRS 2016 Spring Meeting, Symposium V, Thin-Film Chalcogenide Photovoltaic Materials.
- [119] J. V. Li, D. Kuciauskas, M. R. Young, and I. L. Repins, "Effects of sodium incorporation in co-evaporated Cu<sub>2</sub>ZnSnSe<sub>4</sub> thin-film solar cells," *Applied Physics Letters*, vol. 102, no. 16, p. 163905, 2013.
- [120] M. Werner, C. Sutter-Fella, Y. Romanyuk, and A. Tiwari, "8.3% efficient Cu<sub>2</sub>ZnSn(S,Se)<sub>4</sub> solar cells processed from sodium-containing solution precursors in a closed reactor," *Thin Solid Films*, vol. 582, pp. 308 – 312, 2015. E-MRS 2014 Spring Meeting, Symposium A, Thin-Film Chalcogenide Photovoltaic Materials.
- [121] Y.-R. Lin, V. Tunuguntla, S.-Y. Wei, W.-C. Chen, D. Wong, C.-H. Lai, L.-K. Liu, L.-C. Chen, and K.-H. Chen, "Bifacial sodium-incorporated treatments: Tailoring deep traps and enhancing carrier transport properties in Cu<sub>2</sub>ZnSnS<sub>4</sub> solar cells," *Nano Energy*, vol. 16, pp. 438 – 445, 2015.

## Bibliography

---

- [122] A. Nagaoka, H. Miyake, T. Taniyama, K. Kakimoto, Y. Nose, M. A. Scarpulla, and K. Yoshino, "Effects of sodium on electrical properties in  $\text{Cu}_2\text{ZnSnS}_4$  single crystal," *Applied Physics Letters*, vol. 104, no. 15, p. 152101, 2014.
- [123] H. Zhou, T.-B. Song, W.-C. Hsu, S. Luo, S. Ye, H.-S. Duan, C.-J. Hsu, W. Yang, and Y. Yang, "Rational defect passivation of  $\text{Cu}_2\text{ZnSn}(\text{S},\text{Se})_4$  photovoltaics with solution-processed  $\text{Cu}_2\text{ZnSnS}_4\text{:Na}$  nanocrystals," *Journal of the American Chemical Society*, vol. 135, no. 43, pp. 15998–16001, 2013.
- [124] H. Tampo, K. M. Kim, S. Kim, H. Shibata, and S. Niki, "Improvement of minority carrier lifetime and conversion efficiency by na incorporation in  $\text{Cu}_2\text{ZnSnSe}_4$  solar cells," *Journal of Applied Physics*, vol. 122, no. 2, p. 023106, 2017.
- [125] T. Gershon, B. Shin, N. Bojarczuk, M. Hopstaken, D. B. Mitzi, and S. Guha, "The role of sodium as a surfactant and suppressor of non-radiative recombination at internal surfaces in  $\text{Cu}_2\text{ZnSnS}_4$ ," *Advanced Energy Materials*, vol. 5, no. 2, pp. 1400849–n/a, 2015.
- [126] E. Ghorbani, J. Kiss, H. Mirhosseini, M. Schmidt, J. Windeln, T. D. Kühne, and C. Felser, "Insights into intrinsic defects and the incorporation of Na and K in the  $\text{Cu}_2\text{ZnSnSe}_4$  thin-film solar cell material from hybrid-functional calculations," *The Journal of Physical Chemistry C*, vol. 120, no. 4, pp. 2064–2069, 2016.
- [127] S. G. Haass, C. Andres, R. Figi, C. Schreiner, M. Bürki, Y. E. Romanyuk, and A. N. Tiwari, "Complex interplay between absorber composition and alkali doping in high-efficiency kesterite solar cells," *Advanced Energy Materials*, pp. 1701760–n/a, 2017. 1701760.
- [128] D. Tiwari, T. Koehler, X. Lin, R. Harniman, I. Griffiths, L. Wang, D. Cherns, R. Klenk, and D. J. Fermin, " $\text{Cu}_2\text{ZnSnS}_4$  thin films generated from a single solution based precursor: The effect of na and sb doping," *Chemistry of Materials*, vol. 28, no. 14, pp. 4991–4997, 2016.
- [129] K. F. Tai, D. Fu, S. Y. Chiam, C. H. A. Huan, S. K. Batabyal, and L. H. Wong, "Antimony doping in solution-processed  $\text{Cu}_2\text{ZnSn}(\text{S},\text{Se})_4$  solar cells," *ChemSusChem*, vol. 8, no. 20, pp. 3504–3511, 2015.
- [130] X. Zhang, M. Han, Z. Zeng, and Y. Duan, "The role of Sb in solar cell material  $\text{Cu}_2\text{ZnSnS}_4$ ," *J. Mater. Chem. A*, vol. 5, pp. 6606–6612, 2017.
- [131] D. W. Niles, M. Al-Jassim, and K. Ramanathan, "Direct observation of na and o impurities at grain surfaces of  $\text{CuInSe}_2$  thin films," *Journal of Vacuum Science & Technology A: Vacuum, Surfaces, and Films*, vol. 17, no. 1, pp. 291–296, 1999.

- [132] D. Rudmann, *Effects of sodium on growth and properties of CIGS thin films and solar cells*. PhD thesis, ETH Zurich, <http://e-collection.library.ethz.ch/eserv/eth:27376/eth-27376-02.pdf>, 2004.
- [133] C. Andres, T. Schwarz, S. G. Haass, T. P. Weiss, R. Carron, R. Caballero, R. Figi, C. Schreiner, M. Bürki, A. N. Tiwari, and Y. E. Romanyuk, “Decoupling of optoelectronic properties from morphological changes in sodium treated kesterite thin film solar cells,” *Solar Energy*, 2018.
- [134] S. López Marino, Y. Sánchez, M. Espíndola Rodríguez, X. Alcobé, H. Xie, M. Neuschitzer, I. Becerril, S. Giraldo, M. Dimitrievska, M. Placidi, L. Fourdrinier, V. Izquierdo Roca, A. Pérez-Rodríguez, and E. Saucedo, “Alkali doping strategies for flexible and light-weight  $\text{Cu}_2\text{ZnSnSe}_4$  solar cells,” *Journal of Materials Chemistry A*, vol. 4, no. 5, pp. 1895–1907, 2016.
- [135] T. Yoneda and T. Morimoto, “Mechanical durability of water repellent glass,” *Thin Solid Films*, vol. 351, no. 1, pp. 279 – 283, 1999.
- [136] Dealkalization, “DealkalizationWikipedia, the free encyclopedia,” 2018. [Online; accessed 25-March-2018].
- [137] H. Toraya and S. Tsusaka, “Quantitative phase analysis using the whole-powder-pattern decomposition method: Solution from knowledge of chemical compositions,” *Journal of Applied Crystallography*, vol. 28, no. 4, pp. 392–399, 1995.
- [138] L. Kronik, D. Cahen, and H. W. Schock, “Effects of sodium on polycrystalline  $\text{Cu}(\text{In,Ga})\text{Se}_2$  and its solar cell performance,” *Advanced Materials*, vol. 10, no. 1, pp. 31–36, 1999.
- [139] R. Haight, X. Shao, W. Wang, and D. B. Mitzi, “Electronic and elemental properties of the  $\text{Cu}_2\text{ZnSn}(\text{S,Se})_4$  surface and grain boundaries,” *Applied Physics Letters*, vol. 104, no. 3, p. 033902, 2014.
- [140] A. Rockett, J. Britt, T. Gillespie, C. Marshall, M. Al Jassim, F. Hasoon, R. Matson, and B. Basol, “Na in selenized  $\text{Cu}(\text{In,Ga})\text{Se}_2$  on Na-containing and Na-free glasses: Distribution, grain structure, and device performances,” *Thin Solid Films*, vol. 372, pp. 212–217, 9 2000.
- [141] H. Xie, S. López-Marino, T. Olar, Y. Sánchez, M. Neuschitzer, F. Oliva, S. Giraldo, V. Izquierdo-Roca, I. Lauer mann, A. Pérez-Rodríguez, and E. Saucedo, “Impact of Na

## Bibliography

---

- dynamics at the  $\text{Cu}_2\text{ZnSn(S,Se)}_4/\text{CdS}$  interface during post low temperature treatment of absorbers,” *ACS Applied Materials & Interfaces*, vol. 8, no. 7, pp. 5017–5024, 2016.
- [142] I. Khatri, H. Fukai, H. Yamaguchi, M. Sugiyama, and T. Nakada, “Effect of potassium fluoride post-deposition treatment on  $\text{Cu(In,Ga)Se}_2$  thin films and solar cells fabricated onto sodalime glass substrates,” *Solar Energy Materials and Solar Cells*, vol. 155, pp. 280–287, 2016.
- [143] D. Rudmann, A. F. da Cunha, M. Kaelin, F. Kurdesau, H. Zogg, A. N. Tiwari, and G. Bilger, “Efficiency enhancement of  $\text{Cu(In,Ga)Se}_2$  solar cells due to post-deposition Na incorporation,” *Applied Physics Letters*, vol. 84, no. 7, pp. 1129–1131, 2004.
- [144] A. L. Patterson, “The scherrer formula for X-Ray particle size determination,” *Phys. Rev.*, vol. 56, pp. 978–982, Nov 1939.
- [145] T. Prabhakar and N. Jampana, “Effect of sodium diffusion on the structural and electrical properties of  $\text{Cu}_2\text{ZnSnS}_4$  thin films,” *Solar Energy Materials and Solar Cells*, vol. 95, no. 3, pp. 1001–1004, 2011.
- [146] A. Nagaoka, H. Miyake, T. Taniyama, K. Kakimoto, and K. Yoshino, “Correlation between intrinsic defects and electrical properties in the high-quality  $\text{Cu}_2\text{ZnSnS}_4$  single crystal,” *Applied Physics Letters*, vol. 103, no. 11, p. 112107, 2013.
- [147] F. Pianezzi, P. Reinhard, A. Chirilă, B. Bissig, S. Nishiwaki, S. Buecheler, and A. N. Tiwari, “Unveiling the effects of post-deposition treatment with different alkaline elements on the electronic properties of CIGS thin film solar cells,” *Physical Chemistry Chemical Physics*, vol. 16, no. 19, pp. 8843–8851, 2014.
- [148] M. A. Green, *Solar cells: Operating principles, technology, and system applications*. Prentice-Hall, Inc., 1982.
- [149] C. J. Hages, N. J. Carter, and R. Agrawal, “Generalized quantum efficiency analysis for non-ideal solar cells: Case of  $\text{Cu}_2\text{ZnSnSe}_4$ ,” *Journal of Applied Physics*, vol. 119, no. 1, p. 014505, 2016.
- [150] C. Frisk, C. P. Björkman, J. Olsson, P. Szaniawski, J. T. Wätjen, V. Fjällström, P. Salomé, and M. Edoff, “Optimizing Ga profiles for highly efficient  $\text{Cu(In,Ga)Se}_2$  thin film solar cells in simple and complex defect models,” *Journal of Physics D: Applied Physics*, vol. 47, no. 48, p. 485104, 2014.

- [151] D. Hironiwa, M. Murata, N. Ashida, Z. Tang, and T. Minemoto, "Simulation of optimum band-gap grading profile of  $\text{Cu}_2\text{ZnSn}(\text{S},\text{Se})_4$  solar cells with different optical and defect properties," *Japanese Journal of Applied Physics*, vol. 53, no. 7, p. 071201, 2014.
- [152] S. Mohammadnejad and A. Baghban Parashkoush, "CZTSSe solar cell efficiency improvement using a new band-gap grading model in absorber layer," *Applied Physics A*, vol. 123, no. 12, 2017.
- [153] A. Fairbrother, X. Fontané, V. Izquierdo Roca, M. Espindola Rodriguez, S. López Marino, M. Placidi, J. López García, A. Pérez Rodríguez, and E. Saucedo, "Single-step sulfoselenization method to synthesize  $\text{Cu}_2\text{ZnSn}(\text{S},\text{Se})_4$  absorbers from metallic stack precursors," *ChemPhysChem*, vol. 14, no. 9, pp. 1836–1843, 2013.
- [154] S. Temgoua, R. Bodeux, and N. Naghavi, "A better understanding of the reaction pathways in the formation of  $\text{Cu}_2\text{ZnSn}(\text{S},\text{Se})_4$  thin films," *Solar Energy Materials and Solar Cells*, vol. 172, pp. 160–167, 2017.
- [155] S. P. Harvey, I. Repins, and G. Teeter, "Defect chemistry and chalcogen diffusion in thin-film  $\text{Cu}_2\text{ZnSnSe}_4$  materials," *Journal of Applied Physics*, vol. 117, no. 7, p. 074902, 2015.
- [156] N. Ross, J. Larsen, S. Grini, L. Vines, and C. Platzer Björkman, "Practical limitations to selenium annealing of compound co-sputtered  $\text{Cu}_2\text{ZnSnS}_4$  as a route to achieving sulfur-selenium graded solar cell absorbers," *Thin Solid Films*, vol. 623, pp. 110–115, 2017.
- [157] K. C. Wang, H. R. Hsu, and H. S. Chen, "Study of surface sulfurization of  $\text{Cu}_2\text{ZnSn}(\text{S},\text{Se})_4$  thin film solar cell by sequential  $\text{H}_2\text{Se}$  selenization/ $\text{H}_2\text{S}$  sulfurization," *Solar Energy Materials and Solar Cells*, vol. 163, pp. 31–37, 2017.
- [158] K. J. Yang, D. H. Son, S. J. Sung, J. H. Sim, Y. I. Kim, S.-N. Park, D. H. Jeon, J. Kim, D. K. Hwang, C. W. Jeon, D. Nam, H. Cheong, J. K. Kang, and D. H. Kim, "A band-gap-graded CZTSSe solar cell with 12.3% efficiency," *J. Mater. Chem. A*, vol. 4, no. 26, pp. 10151–10158, 2016.
- [159] K. Sugimoto, N. Suyama, K. Nakada, and A. Yamada, "Crystal growth mechanism of  $\text{Cu}_2\text{ZnSn}(\text{S},\text{Se})_4$  thin films fabricated from nanoparticles," *Japanese Journal of Applied Physics*, vol. 56, no. 3, p. 035502, 2017.
- [160] N. Ross, J. Larsen, S. Grini, E. Sarhammar, L. Vines, and C. Platzer Björkman, " $\text{Cu}_2\text{ZnSn}(\text{S},\text{Se})_4$  solar cell absorbers from diffusion of selenium into annealed

## Bibliography

---

- Cu<sub>2</sub>ZnSnS<sub>4</sub> absorbers,” in *2016 IEEE 43rd Photovoltaic Specialists Conference (PVSC)*, pp. 0492–0497, 2016.
- [161] T. Kato, N. Sakai, and H. Sugimoto, “Efficiency improvement of Cu<sub>2</sub>ZnSn(S,Se)<sub>4</sub> sub-module with graded bandgap and reduced backside ZnS segregation,” in *2014 IEEE 40th Photovoltaic Specialist Conference (PVSC)*, pp. 0844–0846, 2014.
- [162] M. Dimitrievska, G. Gurieva, H. Xie, A. Carrete, A. Cabot, E. Saucedo, A. Pérez Rodríguez, S. Schorr, and V. Izquierdo Roca, “Raman scattering quantitative analysis of the anion chemical composition in kesterite Cu<sub>2</sub>ZnSn(S,Se)<sub>4</sub> solid solutions,” *Journal of Alloys and Compounds*, vol. 628, pp. 464–470, 2015.

# Appendix

## .1 Sensitivity analysis of e-ARC

This sensitivity analysis is done by changing one parameter during simulation, while keeping all the other parameter constant. First of all, ZnO:Al layer thickness can affect all the wavelength that is effective for absorber, but the amount of change is relatively low (17% average change in MSE value is observed for 100% change of thickness). On the other hand, thickness of Zn layer has effects only on the wavelength less than 400 nm, but the amount of change is relatively higher than ZnO:Al (22% average change in MSE value is observed for 100% change of thickness). Secondly, CdS thickness have huge impact on the calculated EQE for the wavelength of 300nm-600nm (87% average change in MSE value is observed for 100% change of thickness). Therefore, CdS thickness should be optimized carefully to have the best fitting of experimental data. Thirdly, the MoS<sub>2</sub> thickness has low (7% average change in MSE value is observed for 100% change of thickness) effect on calculated EQE, which is mainly on the wavelength greater than 800nm. Finally, the carrier collection length has the highest impact (93% average change in MSE is observed for 100% change of thickness) on the calculation of EQE by this modeling.

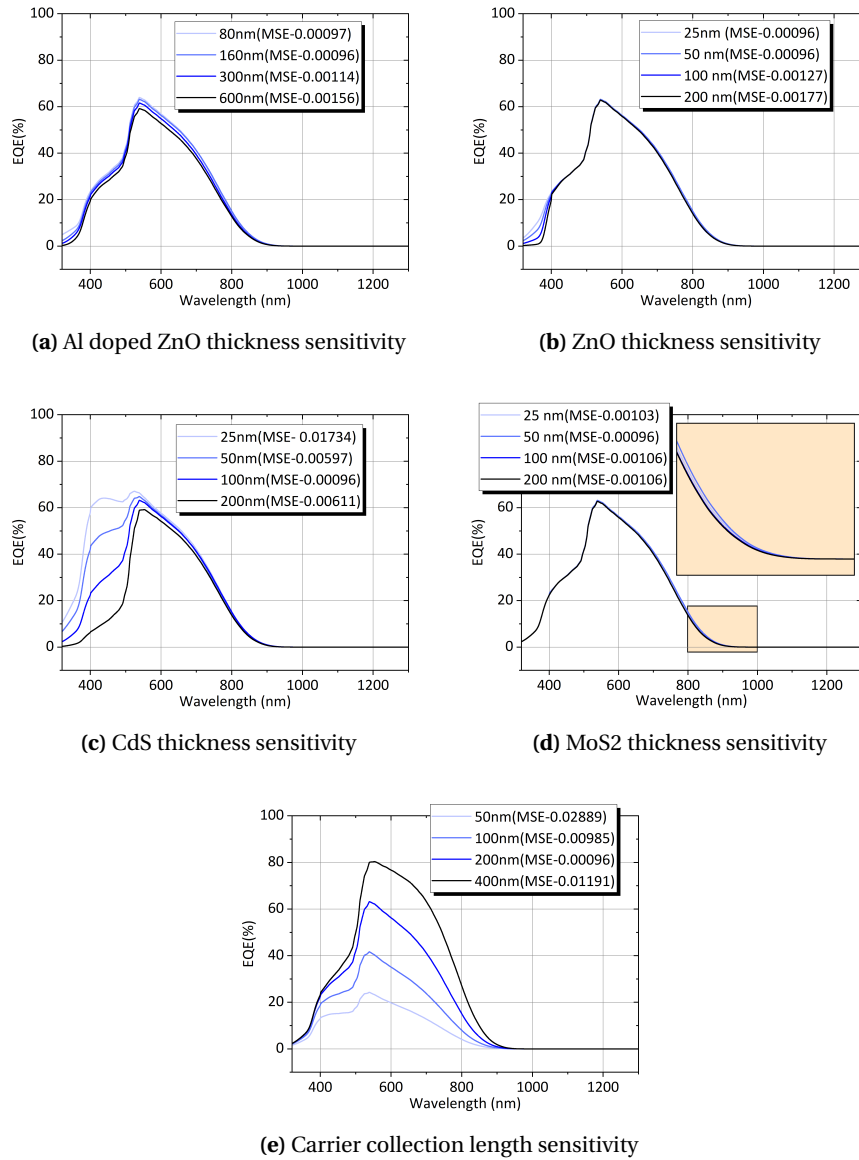


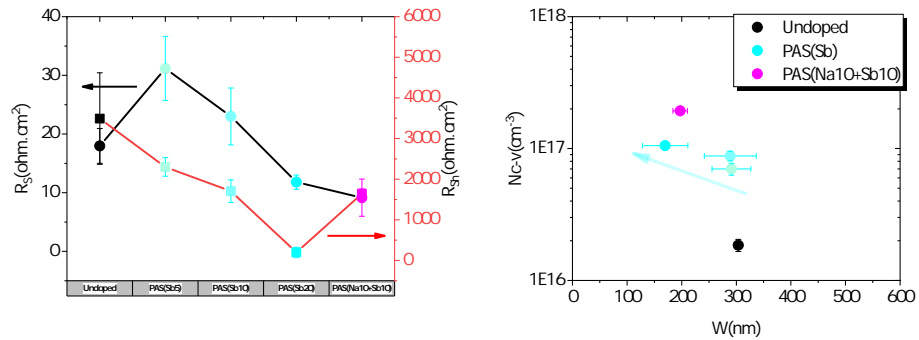
Figure 1: Effect of different parameter as a representation of sensitivity analysis in simulation.

## .2 Dark J-V and C-V measurements of Sb-doped CZTS device

Figure 2 is showing the  $R_s$  and  $R_{sh}$  deduced from dark J-V measurement and net carrier concentration ( $N_{C-V}$ ) and depletion region width ( $W$ ) deduced from capacitance-voltage measurement for all Sb-incorporated sample.

The  $R_s$  of Sb-doped sample increased noticeably compared to undoped sample, which can be the reason to have decreased  $J_{SC}$  for PAS(Sb5) sample. Although  $R_s$  value decreased with

## .2. Dark J-V and C-V measurements of Sb-doped CZTS device



(a) Series ( $R_S$ ) and shunt resistance ( $R_{Sh}$ ) of PAS(Sb) samples compared to undoped samples. (b) Carrier concentration ( $N_{C-V}$ ) vs Depletion region width ( $W$ ) of PAS(Sb) samples, where arrow indicates the increasing amount of Sb used

**Figure 2:** Electrical parameter (series resistance, shunt resistance, net carrier concentration and depletion region width extracted from dark IV curve and C-V measurement) of sample doped with Sb.

increased amount of Sb due to slightly higher net carrier concentration, but the  $J_{SC}$  remain similar to undoped sample. Furthermore, PAS(Na10+Sb10) sample showed lower  $R_{Sh}$  compared to PAS(Na10) sample (figure 5.17), which can be the reason for PAS(Na10+Sb10) sample having 40mV (mean.) lower  $V_{OC}$ . Interestingly, the  $R_{Sh}$  of PAS(Na10+Sb10) sample is somewhat closer to the  $R_{Sh}$  of PAS(Na20) sample. From the result of SIMS, we learned that the amount of Na for PAS(Na10+Sb10) sample is higher than PAS(Na10) sample. Therefore, this higher Na content can be responsible for lower  $R_{Sh}$  in case of PAS(Na10+Sb10) sample.

## **Abstract**

The goal of this work is to study and to develop the routes toward efficiency improvement of Kesterite-based solar cells. First, a baseline process has been developed leading to a maximum power conversion efficiency of 7.6% and 5.9% for CZTSe and CZTS-based solar cells, respectively. Second, the incorporation of Na and Sb in the CZTS absorber has been tested as a first strategy to enhance the performance of CZTS devices. Results show that Na improves efficiency by passivating the surface and reduce recombination on the surface and at the bulk. Power conversion efficiency with optimized Na content is doubled compared to the reference sample without Na, but has no effect on device performances. Sb improved the morphology of the absorber in the presence of Na. It has been expected to increase efficiency, which is not the case. Third, the efficiency of Kesterite solar cells was studied with the introduction of S/Se gradient as a function of its depth in the absorber. No enhance of efficiency was reach by S/Se grading as was not possible to obtain simultaneously a good grain morphology and a smooth S/Se gradient along the absorber depth.

## **Resumé**

Le but de ce travail est d'étudier et de développer des voies pour améliorer l'efficacité des cellules solaires à base de Kesterite. Tout d'abord, un processus de référence a été mis au point pour obtenir un rendement de conversion d'énergie maximal de 7.6% et 5.9% pour les cellules solaires CZTSe et CZTS respectivement. Dans un deuxième temps, l'incorporation de Na et de Sb dans l'absorbeur CZTS a été testée comme première stratégie pour améliorer les performances des dispositifs CZTS. Les résultats montrent que le Na améliore l'efficacité en passivant la surface et en réduisant les recombinaisons de surface et dans le volume de l'absorbeur. L'efficacité de conversion photovoltaïque avec une teneur en Na optimisée est doublée par rapport à l'échantillon de référence sans Na. Le Sb a amélioré la morphologie de l'absorbeur en présence de Na mais sans impact sur les performances des dispositifs. Enfin, l'introduction de gradient d'énergie de bande interdite créé par un gradient de composition S/Se en fonction de la profondeur dans l'absorbeur a été testée pour améliorer d'avantage le rendement des cellules solaires. Les caractérisations matériaux ont montré l'obtention de gradient proche de la surface de l'absorbeur mais ne se traduisant pas par un gain en performance. En effet, la fabrication de gradient S/Se vers l'interface arrière et dans une moindre mesure proche de la surface se fait au détriment de la cristallisation du matériau masquant le bénéfice du gradient d'énergie.